Quantum optical metrology using two-photon interference

Kyle Jordan

Thesis submitted to the University of Ottawa in partial fulfillment of the requirements for the degree of Doctorate in Philosophy, Physics

Department of Physics
Faculty of Science
University of Ottawa

Supervised by
Jeff S. Lundeen

uOttawa

Abstract

Optical quantum metrology uses specially-prepared states of light to probe sensitive samples. Choosing a suitable probe state allows one to extract more information per probe photon about an unknown parameter than is possible using any classical technique. In effect, these techniques improve the sensitivity of the measurement whenever the number of probe photons is constrained in some way.

This thesis presents experimental and theoretical results on the use of pairs of time-frequency entangled photons in precision measurements. It begins with an overview of necessary background knowledge about quantum optics and quantum information. This is followed by a theoretical discussion on the estimation of a single delay using two-photon interference. We show that constraints on the probe photon's bandwidth complicate the measurement problem, requiring suitable optimization of the two-photon quantum state to avoid losing precision.

We then consider the use of two-photon interference for linear spectroscopic measurements. Linear spectroscopy relates the absorption and phase spectrum of a sample to unknown electronic parameters. We describe a proof-of-principle experiment demonstrating that two-photon interferometric spectroscopy can be used for simultaneously measurement of both absorption and phase. This is followed by an information-theoretic discussion of the precision of this technique. For low losses, we show that the method provides phase sensitivity similar to classical interferometry while approaching the optimal absorption precision of any possible measurement. If the absorption and phase values are both related to a single unknown parameter, then our technique provides improved sensitivity to this parameter compared to both classical measurements and other quantum techniques in the presence of realistic levels of loss.

We conclude with a discussion of quantum-optical coherence tomography, which is a two-photon interferometric method for determining the material structure of a sample. We present an ongoing experiment which aims to apply the method to tissue-like samples, where the quantum measurement is limited by a poor signal-to-noise ratio. Preliminary results demonstrate that this noise can be largely reduced by suitable frequency-domain filtering. This allows us to precisely determine the position of a scattering center using a few hundred detected photon pairs despite the presence of large amounts of noise. We follow this with a theoretical discussion of signal artifacts which are known to complicate the measured interferogram. We show these artifacts are due to a distinct interferometric effect, which can be distinguished from the signal of interest using the relative time delay between detected photons. We conclude with a brief discussion on possible techniques for artifact removal.

Acknowledgements

First and foremost, I would like to express my deepest gratitude to my thesis supervisor, Jeff Lundeen. Jeff's efforts in guiding the direction of my research, and his blend of encouragement and helpful criticism, are greatly appreciated. His approach to physics research, which places a strong emphasis on understanding the fundamentals of any given problem, has had a great impact on my own view of physics. Jeff has fostered a friendly and collaborative research environment at the University of Ottawa, and I have certainly been lucky to be a part of the Lundeen lab during my graduate studies.

I wish to express my thanks to my fellow labmates. In particular, I thank Raphael Abrahao and Andrew Proppe for the training they provided in experimental optics. I thank Arman Mansouri, Thomas Bailey, and Jinghui Huang for helpful discussions and for making lab work so enjoyable. I thank Simon Lamontagne and Angéline Lafleur for their efforts and good spirits during the challenges of experimental research. I have been fortunate to work alongside Aldo Martinez, Brayden Freitas, Timothy Lee, Manuel Ferrer, and Colin Veevers. I am also greatful to the researchers at the National Research Council for their insights regarding quantum optics: Yingwen Zhang, Frédéric Bouchard, Alicia Sit, Duncan England, Ben Sussman, and Phil Bustard.

Last, but certainly not least, I thank my parents and my partner Victoria, for their love and encouragement. Without their support, this thesis would not be possible.

Author Contributions

The work presented in this thesis is the result of collaboration. Each project was carried out under the guidance of Jeff Lundeen.

The model and calculations discussed in Chapter 2 were developed largely through discussion with Jeff Lundeen and Raphael Abrahao.

The experiment described in Chapter 3 was conceived of by Andrew Proppe, Jeff Lundeen, and Ben Sussman. The experiment design was carried out by Andrew Proppe and KJ, with significant feedback from Yingwen Zhang and Frédéric Bouchard. Spectroscopic samples were prepared by Andrew Proppe, and data collection was performed by both KJ and Andrew Proppe. Data analysis was carried out by KJ, with significant feedback from Andrew Proppe, Jeff Lundeen, and Ben Sussman.

The calculations of Chapter 4 were largely carried out by KJ, with significant feedback from Andrew Proppe and Jeff Lundeen.

The experiment described in Chapter 5 conceived of by KJ, Andrew Proppe, and Yingwen Zhang. The experiment was built by Angéline Lafleur, KJ, and Andrew Proppe. Data collection was done by KJ and Angéline Lafleur, and analysis was performed by KJ.

List of Publications

The following manuscripts were published during my time as a PhD student. Not all of these works are related to the content of this thesis.

- Jing-Hui Huang, Xiang-Yun Hu, Adetunmise C. Dada, Jeff S. Lundeen, Kyle M. Jordan, Huan Chen, and Jianqi An. "Autocorrelative weak-value amplification and simulating the protocol under strong Gaussian noise." Phys. Rev. A 106, 053704 (2022).
- Kyle M. Jordan, Raphael A. Abrahao, and Jeff S. Lundeen. "Quantum metrology timing limits of the Hong-Ou-Mandel interferometer and of general two-photon measurements." Phys. Rev. A 106, 063715 (2022).
- Jing-Hui Huang, Jeff S. Lundeen, Kyle M. Jordan, Adetunmise C. Dada, Guang-Jun Wang, and Xiang-Yun Hu. "Weak-value-amplification enhancement of the Magneto-optical Kerr effect in nanoscale layered structures." Phys. Rev. A 108, 033724 (2023).
- Jing-Hui Huang, Kyle M. Jordan, Adetunmise C. Dada, Xiang-Yun Hu, and Jeff S. Lundeen. "Enhancing interferometry using weak value amplification with real weak values." Phys. Rev. A 134, 080802 (2025).

Contents

List of Figures

1

Introduction

The precision of any measurement is limited primarily by the noises affecting the measured signal. Historically, most noises are due to the technical limitations of the instruments used. For instance, if one wishes to measure the duration of an event using the motion of sand in an hourglass, the precision with which the time can be determined is limited by the stochastic behaviour of the falling sand. The time required to drain the hourglass is therefore different during different measurement trials, so that the time recorded by the hourglass has a finite uncertainty. In making a measurement, then, a primary goal is to reduce the various noises affecting a signal, thereby increasing the measurement's precision.

The same principle applies to optical measurements. In this case, one can make a distinction between technical noises and quantum noises. Technical noises are due to the imperfect behaviour of the optical setup, which may be due to background light, to excess noise in electronic detectors, and to fluctuations in the refractive index through which the beam propagates. Quantum noises, on the other hand, are present even in an ideal setup, and are due to the random behaviour of light itself. Any sufficiently precise measurement is limited by quantum noises; reducing these noises is the goal of quantum metrology.

This chapter lays out the prerequisite knowledge needed to understand experiments in quantum optical metrology. First, Section 1.1 presents a broad overview of research on two photon interference and quantum metrology. Section 1.2 summarizes some results from quantum optics which are required to understand the origins of quantum noise in optical systems and the techniques to avoid it. Then, Section 1.3 describes the theoretical formalism of quantum metrology, which provides a mathematical framework for predicting the precision of arbitrary measurements. It ends with a discussion in Section 1.4 of spontaneous

parametric down-conversion (SPDC), which allows one to create quantum-correlated photon pairs (also called *biphotons*) from an intense classical light source. The work described in this thesis focuses on interferometric measurements of spectral and temporal parameters using two-photon interference; in discussing the mechanism responsible for these photon pairs, many of the spectral and temporal properties of these pairs become apparent.

1.1 Overview

The work described in the following chapters lies at the intersection of two broad topics in quantum optics. The first studies the phenomena of two photon interference. This line of research was initiated largely in search of optical phenomena which were uniquely quantum mechanical, having no classical counterpart. Nevertheless, these interference effects have been recognized as a tool for precision measurement even in the first exploratory papers, and this practical utility has been a major reason for continued interest over the past few decades.

Interference has been recognized as a key phenomena in quantum science since its inception. In the case of electrons and other material particles, interference, *e.g.* from a double slit, is distinctly nonclassical and a key indication of wave-particle duality. A single photon sent through two slits similarly reveals interference fringes. In this case, however, the distribution of fringes is exactly predicted by the classical Maxwell equations. Similarly, single photons sent through other interferometer geometries reproduce classical intensity distributions, as in the experiments by Grangier *et al.* [1]. Even the stochastic nature of photodetections, which was the original inspiration for optical wave-particle duality, is completely explained by the quantum mechanical properties of the detector itself, with no need for a quantum theory of light [2]. The first challenge for the field quantum optics was thus the need to justify its existence, to identify optical phenomena which are uniquely quantum in origin.

Two photon interference was not the first nonclassical phenomena to be experimentally observed. Years earlier, the photon antibunching effect, which has no explanation in terms of fluctuating classical

fields [3], was demonstrated in experiments by Kimble *et al.* using radiation from resonance fluorescence [4]. Still, research continued to look for more nonclassical effects. Ghosh *et al.* demonstrated, first theoretically [5] and then experimentally [6], that two photon interference was another genuinely quantum effect. Ordinarily, measurement of two photons requires that one produce a photon pair and look for two time-correlated detector clicks (*i.e.*, coincidences). In two photon interference, each of the photons can arrive at either detector. There are then two possible pairings of source photon to detector click; the detector click can be triggered by two possible paired-photon-paths, and under certain indistinguishability constraints, the corresponding amplitudes will interfere. This leads to a measurable variation in the probability of seeing a pair of clicks. However, no interference fringes are seen in the optical intensity, which is sensitive only to single photon interference [6].

The most well-studied two photon interference effect was first reported on by Hong, Ou, and Mandel [7], and is therefore referred to as the Hong-Ou-Mandel effect. Here, the two photons of equal frequency and polarization are produced in distinct beams, typically by parametric down conversion. Each photon enters one port of a beamsplitter, and partial reflection of each photon provides the two possible paths. A pair of detectors, one at each beamsplitter output, records the rate of coincidences. Hong *et al.* varied the relative delay between the two photons, and found that when the relative delay was sufficiently small, the rate of coincidence counts was entirely suppressed [7]. Monitoring this coincidence rate therefore allowed for precise measurement of the relative delay, with a reported accuracy of 50 fs (corresponding to 15 μm of path length).

This seminal work was followed quickly by further experiments in a variety of new configurations. When the two photons each may have one of two initial wavevectors [5], or the photons each may have one of two frequencies [8, 9], beat fringes in the coincidence rate appear. Steinberg *et al.* demonstrated that the width of the interference (the so-called "Hong-Ou-Mandel dip") is insensitive to all even orders of dispersion of the optical medium before the beamsplitter [10, 11]. At a fundamental level, Hong-Ou-Mandel interference became re-interpreted as a measurement of the *distinguishability* of the two photons at the beamsplitter [12], where this distinguishability could be due to temporal differences, as in the original experiment, or

could come from frequency, spatial, or polarization differences. In this way, Hong-Ou-Mandel interference can be used to measure changes in any optical degree of freedom.

More exotic variations of two photon interference were also studied as a means of testing quantum nonlocality. The most well-known of these is the *induced coherence* effect, demonstrated by Zou *et al.*, in which one photon of a pair is provided only one path, while the other still takes two paths; the latter photon is found to exhibit intensity fringes similar to classical (single photon) interference, though the physical origin remains an interference of two-photon paths [13]. A second noteworthy example is the interferometer proposed by Franson [14] and demonstrated by Kwiat *et al.* [15], in which the two photons travel through separate, highly imbalanced Mach-Zehnder interferometers. Interference in this case, occurring between the pair of short paths and the pair of long paths, can be used to violate a Bell-like inequality holding for any theory of local hidden variables.

At the same time, the second foundational topic for this work, the quantum theory of measurement precision, was in development. Research in this field, which has come to have the name "quantum metrology", takes as inspiration the mathematical theory of classical statistics, particularly in regards to detection theory and parameter estimation. Understanding that the final limitation to measurement precision comes from quantum mechanical noise, *e.g.* arising from quantum indeterminacy, quantum metrology relates the ultimate precision limits of any measurement to the physical properties of the probe and detector apparatus. Applying this theory to specific measurement tasks allows one to rigorously quantify the sensitivity of various experimental approaches, and to identify the physical resources most important in improving precision. For this reason, the theory of quantum metrology has become the standard framework for studies of precise optical measurements.

The quantum generalization of classical parameter estimation was formulated in a series of articles by Helstrom [16, 17, 18]. His motivation was to generalize familiar results about optimal decision and estimation from classical statistics to the type of statistics generated by quantum measurements. Importantly, this generalization included a quantum version of the Cramér-Rao bound. In classical statistics, the Cramér-Rao inequality sets the minimum uncertainty (maximum precision) with which an unknown

parameter can be estimated from a noisy signal. The quantum theory related the precision of an estimate to a particular expectation value calculated from the probe system's quantum state — the precision of a measurement was now determined by a physical property of the measurement apparatus, with some physical states being more sensitive to the value of the parameter than others. Alas, the primary applications Helstrom considered, such detection of a signal in a noisy background [16] and measurement of a coherent field's amplitude [19], yielded relatively unsurprising results, and were mostly ignored by experimenters at the time.

More than a decade later, the issue of quantum noise in optical measurements was highlighted again. In an effort to detect gravitational waves, the LIGO project proposed the construction of large Michelson-type interferometers, with path lengths of many kilometers and using optical powers of hundreds of watts. The precision of the interferometer would be fundamentally limited by shot noise which is observed in any classical state of light. This problem was addressed by Caves, who showed that quadrature-squeezed light, injected into the unused input port of a classical interferometer, could suppress shot noise in the resulting phase measurement [20]. This paper contained a revolutionary insight: quantum mechanics not only dictated the noise limit of measurements, but also provided tools to reduce noise by way of nonclassical effects such as squeezing. Yurke *et al.* soon followed with a proposal for a new nonlinear (*SU(1,1)*) interferometer which could also evade shot noise [21]. Common to both the squeezed state interferometer and the nonlinear interferometer was an error that scaled as N^{-1} when N photons are used, rather than the $N^{-1/2}$ scaling familiar from classical statistics. Whereas the $N^{-1/2}$ scaling had been named the "standard quantum limit" for phase measurements, the N^{-1} scaling was named the "Heisenberg limit" [22].

The discovery of Heisenberg-limited measurements became the basis for a renewed study of quantum metrology. This effort was aided by simultaneous developments in quantum information theory. Helstrom had once sought to generalize the theory of classical parameter estimation and optimal decision theory to quantum-enabled contexts. The new theory, inspired by the discovery of super-dense coding [23] and quantum teleportation [24], aimed to quantify the resource of quantum entanglement using various operationally-defined metrics such as capacity of communication channels [25]. Similarly, the problem of

parameter estimation was reinterpreted by Wooters [26], and then by Braunstein and Caves [27], as a type of quantum state discrimination. Estimation of a parameter θ from a probe state $\rho(\theta)$ was equivalent to discrimination between the nearby states $\rho(\theta)$ and $\rho(\theta + d\theta)$. The task of quantum metrology was then to design probe states which varied quickly with θ, and also to determine a suitable measurement strategy for accessing this information. Furthermore, entanglement was found to also play a key role in quantum metrology. Not only were entangled states able to reach the Heisenberg limit [21, 28]; Giovannetti *et al.* pointed out that entangled probes played a crucial role in any Heisenberg-limited measurement [29].

A pedagogical example is the interferometer proposed by Bollinger *et al.* [30]. Consider the maximally entangled N-photon state $|N\rangle|0\rangle + |0\rangle|N\rangle$ (termed a "N00N state" by Lee, Kok, and Dowling [31]), being a superposition of states with all photons in one interferometer arm and with all photons in the other. A phase shift applied to one arm will perform the transformation $|n\rangle \mapsto e^{in\phi}|n\rangle$ to the portion of the state in the affected arm, so that the probe evolves into the state $|N\rangle|0\rangle + e^{iN\phi}|0\rangle|N\rangle$. The use of N photons leads to a phase shift enhanced by a factor of N; applying the quantum Cramér-Rao bound to this example shows that the phase uncertainty (assuming the right measurement is performed) is $\Delta\phi = 1/N$, exactly the Heisenberg limit. Such an interferometer is theoretically interesting, but faces severe practical difficulties. Not only are N00N states exceedingly difficult to generate for states containing more than a few photons [32], even the measurement stage requires state-of-the-art detection techniques [33]. However, a more fundamental difficulty is the interferometer's sensitivity to optical loss. A single photon scattering out of the interferometer is enough to completely decohere the N00N state, resulting in the loss of all phase information. In a state containing N photons, this loss sensitivity is $\sqrt{N}$ times larger than that of classical interferometers, comparable to the $\sqrt{N}$ times enhancement in precision for ideal experiments.

Similar considerations apply to more general entangled probe states. For phase measurements using probe states with a fixed number of photons, losses generally prevent saturation of the Heisenberg limit [34]. Even in measurements of other quantities, any amount of decoherence (of which loss is one example) generally restores $N^{-1/2}$ scaling, though quantum metrology can still improve measurement precision by a N-independent factor [35]. One of the main challenges of modern metrological research is thus to design

probe states and measurements which are least degraded by optical losses.

Another major thread of research in quantum metrology is that of multiparameter estimation. The problem in this case is to precisely estimate the value of multiple unknown parameters using a single probe system. Multiparameter estimation was first treated shortly after the advent of quantum metrology by Holevo [36] and Helstrom [37], who took a special interest in simultaneous estimation of complementary variables such as position and momentum. In classical estimation theory, results in the single- and multiparameter theories are largely the same; for example, the same procedure (maximum likelihood estimation) allows one to saturate both the single- and multiparameter Cramér-Rao bounds [38]. This is not the case in the quantum theory. Quantum metrology allows one to construct an optimal measurement for estimation of any single parameter [39], but the optimal measurements for different parameters may be incompatible, so that no single measurement is optimal for all parameters of interest [40]. The two theories also differ in the resources of interest. For example, collective measurements provide no benefit in single parameter estimation [29], yet a well-known result shows that collective measurements are optimal in some multiparameter estimation problems [41]. Measurement incompatibility leads to radical changes even in the conceptual understanding of metrology. Since the work of Braunstein and Caves, single parameter estimation has been understood in terms of distance metrics in the space of quantum states [27, 42]. The precision of multiparameter estimation, however, cannot be faithfully described by any distance metric [43], so that some new, as-yet-unknown mathematical interpretation is needed. The multiparameter theory is thus much less developed than the single parameter theory, with many key results being proved only in the last few years, and many fundamental questions remaining unanswered at present. Reviews summarizing these recent developments are available in Refs [44, 45, 46].

At the same time as these theoretical developments, multiparameter metrology has seen a renewed push on the experimental front as well. This is driven by the recognition that many measurement tasks of practical interest feature multiple unknown parameters. These parameters may provide mutually beneficial information, such as the measurement of multiple phases which are spatially distributed [47], measurement of a 3D rotation [48, 49], or measurement of phase and loss in spectroscopy [50] (see also Chapters 3 and

4). Additional parameters may appear in the form of nuisance parameters, which are unknown but whose values are not of interest [51, 52]. Multiparameter estimation also appears in an extreme form when one considers continuous measurements [53], such as the measurement of an unknown waveform function [54, 55, 56].

The field of quantum metrology is currently characterized by a large body of theoretical work establishing relevant precision bounds, together with a relative scarcity of experimental demonstrations. One major reason for this is technical difficulty. As mentioned above, entanglement is a crucial ingredient in many quantum-enhanced sensing schemes, but the generation of large entangled states is still challenging [57]. Furthermore, entangled states are more sensitive not only to parameter shifts, but also to noise, so that the use of entangled sensors becomes increasingly difficult in applications which feature uncontrolled environmental effects. In optics this noise is largely due to loss [58]. Development of high-efficiency optical sources and detectors is therefore crucial for any successful applications of optical quantum metrology.

For the reasons outlined above, optical demonstrations of quantum metrology have largely focused on the use of low numbers of entangled photons, with the most common sources of entanglement being quadrature squeezing [59] and entangled photon pairs (*e.g.*, by two-mode squeezing in the low-gain regime). Quadrature squeezing is a relatively well-developed technology [60], it can be implemented in high-power systems, and it is nearly optimal for phase sensing under many noise models [61]. For these reasons, it has been the technique of choice in most practical applications, the most prominent of which is a Caves-style enhancement of LIGO's phase sensitivity [62], but also in laboratory measurements of optical properties [63].

Entangled photon pairs (*biphotons*), on the other hand, are common in proof-of-principle experiments. Since by definition only two particles are entangled, Heisenberg-limited scaling is not possible. Precision is typically enhanced by a factor of $\sim \sqrt{2}$ compared to classical techniques (for example, in $N = 2$ N00N interferometers), though in some specific tasks such as absorption estimation photon pairs are optimal [64]. The benefit to using photon pairs is twofold: first, coincidence measurements allow one to extract two-photon signals even in the presence of large backgrounds and loss, so that biphotons allow for easy

proof-of-principle demonstrations without the technical challenge of other measurements; second, photon pairs are usually hyperentangled, showing strong correlations in all of their degrees of freedom. A single probe state can then provide quantum-enhanced sensitivity in many variables at once. For this reason, photon pairs are commonly applied to quantum-enhanced imaging [65].

As discussed above, two photon interference has been identified since its conception as a possible tool for metrology. This is due in part to some technical advantages compared to classical (single photon) interferometry, including improved sensitivity, dispersion cancellation and the aforementioned signal improvements in coincidence counting. For example, quantum optical coherence tomography replicates classical coherence tomography using two photon interference, promising greater resolution at low photon fluxes [66]. Two photon interference has also been a tool of choice in the measurement of small quantum-optical effects, such as the single photon tunneling time [67] and the spatial mode-induced group delay [68]. A second motivation is the potential to use two photon interference to perform tasks which have no classical counterpart, such as imaging with undetected photons [69]. For these reasons, photon pair experiments have remained a major focus in the search for quantum-enhanced measurement techniques.

Despite this long-held interest in two photon interferometry, and the simultaneous application of quantum metrological theory to optical tasks such as phase measurement, the metrological performance of two photon interferometry has only recently become a topic of significant study. This may be due in part to the historical focus on Heisenberg-limited measurements, which require large numbers of entangled photons. The earliest metrological study to explicitly consider the use of entangled photon pairs as a resource was that of K. Lyons *et al.*, who in 2016 showed an enhancement in beam displacement measurements due to the entirely quantum resource of position-momentum entanglement [70]. The same year, another study by A. Lyons *et al.* quantified the precision of a Hong-Ou-Mandel interferometer using classical estimation theory. This latter study did not focus on a quantum enhancement in precision, but rather sought to use metrological theory to optimize the precision of a practical measurement technique. The use of frequency entanglement as a means of enhancing interferometric precision was demonstrated by Chen *et al.* [71]. Using quantum estimation theory, Nair examined the precision of arbitrary optical states for absorption

measurements [72]. As absorption naturally leads to decoherence, Heisenberg scaling is not possible in this measurement. As a consequence, photon pairs were found to be the optimal measurement probe, and the use of highly entangled multiparticle states is unnecessary.

Due to the wide range of possible measurement techniques utilizing photon pairs as probes, metrological understanding of many tasks such as coherence tomography is still incomplete. Except in simple cases such as absorption metrology, the optimal choices of probe state and measurement technique are op. In particular, multiparameter estimation has been considered only in select contexts [73, 74]. Applications of two photon interferometry to more complicated practical tasks such as spectroscopy are still mostly speculative [75, 76, 77].

This thesis examines the use of two photon interference for three measurement tasks. In Chapter 2, Hong-Ou-Mandel-based timing measurements are examined from the perspective of multiparameter quantum metrology. Chapters 3 and 4 considers two photon interferometry as a means of enhancing the precision of spectroscopic measurements. Finally, Chapter 5 examines two problems in quantum optical coherence tomography: first, the use of frequency correlations to suppress uncorrelated background noise, and second, the removal of artifact peaks through measurement of the joint temporal state.

1.2 Quantum optics

The classical theory of optics, as described by Maxwell, centers on three related quantities: the distribution of charges in space, and the electric and magnetic field vectors. The fields may in turn be divided into two components, with one contribution coming from the electrostatic fields due to the instantaneous positions of the charges and the other describing self-sustaining propagating waves (*i.e.*, light). The latter component dominates at positions far from any charges, so that it is sufficient to consider only the fields of propagating electromagnetic waves. However, the six components of a free electromagnetic field are highly interrelated due the conditions imposed by Maxwell's equations. A description in terms of the electric and magnetic fields, while experimentally relevant, therefore has a great redundancy due to the number

of vector components that must be described. A much simpler method relies on the vector potential $\boldsymbol{A}$, which is a single transverse field that encodes the physics of both the propagating electric and magnetic fields. For similar reasons, the quantum theory of light begins with a description of the vector potential.

The quantum mechanical operator describing the vector potential is the field operator $\hat{\boldsymbol{A}}(\boldsymbol{r},t)$, which in free space has the form [2]

$$\hat{\boldsymbol{A}}(\boldsymbol{r},t) = \frac{1}{\sqrt{2\pi^3\epsilon_0}} \sum_s \int d^3\boldsymbol{k} \left(\frac{\hbar}{2\omega}\right)^{1/2} \Big(\hat{a}_s(\boldsymbol{k})\boldsymbol{\varepsilon}_s(\boldsymbol{k}) e^{i(\boldsymbol{k}\cdot\boldsymbol{r}-\omega t)} + \text{h.c.}\Big). \tag{1.1}$$

The electric and magnetic fields can be calculated from $\hat{\boldsymbol{A}}$ using the usual relations from classical electrodynamics,

$$\begin{aligned}
\hat{\boldsymbol{E}}(\boldsymbol{r},t) &= -\frac{\partial}{\partial t}\hat{\boldsymbol{A}}(\boldsymbol{r},t) \\
&= \frac{i}{\sqrt{2\pi^3\epsilon_0}} \sum_s \int d^3\boldsymbol{k} \left(\frac{\hbar\omega}{2}\right)^{1/2} \Big(\hat{a}_s(\boldsymbol{k})\boldsymbol{\varepsilon}_s(\boldsymbol{k}) e^{i(\boldsymbol{k}\cdot\boldsymbol{r}-\omega t)} - \text{h.c.}\Big), \qquad (1.2a) \\
\hat{\boldsymbol{B}}(\boldsymbol{r},t) &= \nabla \times \hat{\boldsymbol{A}}(\boldsymbol{r},t) \\
&= \frac{i}{\sqrt{2\pi^3\epsilon_0}} \sum_s \int d^3\boldsymbol{k} \left(\frac{\hbar}{2\omega}\right)^{1/2} \Big(\hat{a}_s(\boldsymbol{k})\boldsymbol{k} \times \boldsymbol{\varepsilon}_s(\boldsymbol{k}) e^{i(\boldsymbol{k}\cdot\boldsymbol{r}-\omega t)} - \text{h.c.}\Big). \qquad (1.2b)
\end{aligned}$$

Here, s labels the two orthonormal polarization vectors $\boldsymbol{\varepsilon}_s(\boldsymbol{k})$ for a given wave vector $\boldsymbol{k}$. In all three expressions, $\omega = c|\boldsymbol{k}|$ is the angular frequency corresponding to wave vector $\boldsymbol{k}$, and $\hbar$ and ε_0 are Planck's constant and the permittivity of free space, respectively. The quantum mechanical annihilation operator $\hat{a}_s(\boldsymbol{k})$ corresponds to the classical plane wave amplitude, and obeys the canonical commutation relation

$$\Big[\hat{a}_s(\boldsymbol{k}),\, \hat{a}^\dagger_{s'}(\boldsymbol{k}')\Big] = \delta_{ss'}\delta^3(\boldsymbol{k}-\boldsymbol{k}'), \tag{1.3}$$

where the creation operator $\hat{a}^\dagger_s(\boldsymbol{k})$ adds a single photon to the plane wave mode corresponding to $\boldsymbol{k}$ and s; the abbreviation h.c. denotes the Hermitian conjugate of the preceding terms. Any optical state may be written in terms of the vacuum state $|0\rangle$, containing no photons, and the various creation operators

$\hat{a}_s^\dagger(\boldsymbol{k})$. It can be verified by direct computation that the fields $\hat{\boldsymbol{E}}$ and $\hat{\boldsymbol{B}}$ given by (1.2a) and (1.2b) satisfy Maxwell's equations in free space, so that many of the familiar results of classical optics have close analogues in the quantum theory.

1.2.1 Mode transformations

The expressions (1.1), (1.2a) and (1.2b) are similar in form to the plane wave decomposition of a classical electromagnetic field, where the operators $\hat{a}_s(\boldsymbol{k})$ and $\hat{a}_s^\dagger(\boldsymbol{k})$ are replaced by the complex amplitudes $\alpha_s^*(\boldsymbol{k})$ and $\alpha_s(\boldsymbol{k})$ of each plane wave. This leads to a heuristic method of quantization, in which any linear relationship between the classical amplitudes $\alpha_s(\boldsymbol{k})$ has a quantum analogue in terms of the creation operators $\hat{a}_s^\dagger(\boldsymbol{k})$ [78, 79]. More specifically, if a linear optical device implements the transformation

$$\alpha_s(\boldsymbol{k}) \mapsto \beta_s(\boldsymbol{k}) = \sum_{s'} \int d^3\boldsymbol{k}'\, M_{ss'}(\boldsymbol{k},\boldsymbol{k}')\, \alpha_{s'}(\boldsymbol{k}'), \tag{1.4}$$

then the same device, after quantization, implements the transformation

$$\hat{a}_s^\dagger(\boldsymbol{k}) \mapsto \hat{b}_s^\dagger(\boldsymbol{k}) = \sum_{s'} \int d^3\boldsymbol{k}'\, M_{ss'}(\boldsymbol{k},\boldsymbol{k}')\, \hat{a}_{s'}^\dagger(\boldsymbol{k}'). \tag{1.5}$$

Of particular importance is the case where

$$\sum_{s''} \int d^3\boldsymbol{k}''\, M_{ss''}(\boldsymbol{k},\boldsymbol{k}'')\, M^*_{s's''}(\boldsymbol{k}',\boldsymbol{k}'') = \delta_{ss'}\delta^3(\boldsymbol{k}-\boldsymbol{k}'), \tag{1.6}$$

so that the operators $\hat{b}_s(\boldsymbol{k})$ satisfy the commutation relations

$$\left[\hat{b}_s(\boldsymbol{k}),\, \hat{b}_{s'}^\dagger(\boldsymbol{k}')\right] = \delta_{ss'}\delta^3(\boldsymbol{k}-\boldsymbol{k}'). \tag{1.7}$$

Transformations of this type may be considered a unitary transformation of the optical modes [79]; furthermore, if this transformation does not change the frequencies of the modes and hence the energies of

the associated photons, then it describes a lossless linear optical device. A lossy linear device can be described by a lossless linear device which is followed by one or more modes being discarded [80]. It is convenient to consider any operator $\hat{b}^\dagger$ which is related to the plane wave operators $\hat{a}_s^\dagger(\boldsymbol{k})$ by such a unitary transformation to be a creation operator on account of the commutation relation (1.7). This text uses the term *mode operator* to describe the creation operator corresponding to an arbitrary optical mode. Two creation operators $\hat{b}_1^\dagger$ and $\hat{b}_2^\dagger$ which satisfy $\left[\hat{b}_1,\, \hat{b}_2^\dagger\right] = 0$ are said to be *orthogonal*.

Two special cases are frequently used in this work and deserve mention. First, consider a single photon state, which is described at a fixed time t_0 by $\hat{b}^\dagger(t_0)\,|0\rangle$. The operator $\hat{b}^\dagger(t_0)$ may be decomposed into a collection of plane wave operators $\hat{a}_s^\dagger(\boldsymbol{k})$, through an expression of the form

$$\hat{b}^\dagger(t_0) = \sum_s \int d^3k\, \beta_s(\boldsymbol{k}; t_0)\, \hat{a}_s^\dagger(\boldsymbol{k}). \tag{1.8}$$

Each plane wave operator will evolve as $\hat{a}_s^\dagger(\boldsymbol{k})e^{-i\omega t}$ on account of (1.5), so that the state of the photon at a later time t is $b^\dagger(t)\,|0\rangle$, where

$$\hat{b}^\dagger(t) = \sum_s \int d^3k\, \beta_s(\boldsymbol{k}; t_0) e^{-i\omega(t-t0)}\, \hat{a}_s^\dagger(\boldsymbol{k}). \tag{1.9}$$

According to (1.8) and (1.9), the propagation of a single photon can be described by decomposing the initial state into a set of plane wave amplitudes $\beta_s(\boldsymbol{k})$, each of which evolve in time as $\beta_s(\boldsymbol{k})e^{-i\omega t}$. This is the same procedure by which one calculates the propagation of a classical electromagnetic wave. In other words, a single photon propagates through free space in a manner analogous to a classical wave [79].

As a second example, we consider a lossless beamsplitter, the quantum theory of which was first worked out by Prasad *et al.* [78]. This device (Figure 1.1) consists of two input ports described by mode operators $\hat{a}^\dagger$ and $\hat{b}^\dagger$, and two output ports described by mode operators $\hat{c}^\dagger$ and $\hat{d}^\dagger$. We will assume that all four

mode operators are orthogonal. The beamsplitter implements the transformation

$$\hat{c}^\dagger = u_{ca}\hat{a}^\dagger + u_{cb}\hat{b}^\dagger, \tag{1.10a}$$

$$\hat{d}^\dagger = u_{da}\hat{a}^\dagger + u_{db}\hat{b}^\dagger. \tag{1.10b}$$

Requiring that the beamsplitter is lossless (and hence unitary), we have the requirements

$$|u_{ca}|^2+|u_{cb}|^2 = 1, \tag{1.11a}$$

$$|u_{da}|^2+|u_{db}|^2 = 1, \tag{1.11b}$$

$$u_{ca}u_{da}^* + u_{cb}u_{db}^* = 0. \tag{1.11c}$$

After choosing suitable phases for the creation operators, then,

$$\hat{c}^\dagger = \sqrt{\eta}\,\hat{a}^\dagger + \sqrt{1-\eta}\,\hat{b}^\dagger, \tag{1.12a}$$

$$\hat{d}^\dagger = \sqrt{1-\eta}\,\hat{a}^\dagger - \sqrt{\eta}\,\hat{b}^\dagger, \tag{1.12b}$$

for some $0 \leq \eta \leq 1$. Other phase conventions are sometimes useful, so long as the constraints (1.11) are satisfied. Of particular importance is the case of a 50:50 beamsplitter, for which $|u_{ca}|= |u_{da}|= |u_{cb}|= |u_{db}|$; this is obtained by taking $\eta = 1/2$. Beamsplitters of this type are the foundation of many interferometric effects, one of which is discussed in the following section.

For readability, it is helpful to drop the hats $\hat{}$ over operators. In the rest of the text, we will use the same symbol to label a mode and to denote the corresponding annihilation operator, with the meaning being clear from context.

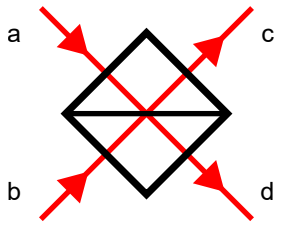

Figure 1.1: Diagram of a beamsplitter. The device takes two input modes a and b, which mix to form two output modes c and d.

1.2.2 Hong-Ou-Mandel interference

A single photon, incident at one port of a beamsplitter, leads to two distinguishable outcomes: the photon may reflect from the beamsplitter, leaving one port; or, it may be transmitted, and leave the other. For a 50:50 beamsplitter, each of these outcomes are equally likely. One may also consider a situation in which two photons are incident at a 50:50 beamsplitter, with one photon entering each of the two input ports. This situation leads to one of four outcomes, since each photon may separately leave one of two output ports. In the two-photon case, however, the four outcomes are not equally likely, and the respective probabilities depend strongly on the properties (*e.g.*, polarization, frequency, time-of-arrival, and spatial mode) of the two photons. This effect is called *Hong-Ou-Mandel interference*, after the authors of Ref. [7], and it provides a relatively simple way of comparing the properties of one photon to that of another.

Evolution of the two-photon state

For simplicity, we suppose that the two photons begin in a separable state; the next subsection considers a similar interference effect occurring for entangled photon pairs. The initial state of the photons is then

$$|\psi\rangle = a_1^\dagger b_2^\dagger |0\rangle \,, \tag{1.13}$$

where we use the same labeling of the beamsplitter ports as in Figure 1.1. The indices 1 and 2 are used to indicate the degrees of freedom of the two photons other than input port; for instance, they may possess different polarizations. The state after the beamsplitter can be obtained from the inverse relationship to (1.12),

$$a_i^\dagger = \frac{1}{\sqrt{2}}\left(c_i^\dagger + d_i^\dagger\right), \tag{1.14a}$$

$$b_i^\dagger = \frac{1}{\sqrt{2}}\left(c_i^\dagger - d_i^\dagger\right), \tag{1.14b}$$

leading to the state

$$|\psi'\rangle = \frac{1}{2}\left[c_1^\dagger + d_1^\dagger\right]\left[c_2^\dagger - d_2^\dagger\right]|0\rangle\,. \tag{1.15}$$

Expanding this out, we have

$$|\psi'\rangle = \frac{1}{2}\left[\underbrace{c_1^\dagger c_2^\dagger - d_1^\dagger d_2^\dagger}_{\text{exit same port}} - \underbrace{c_1^\dagger d_2^\dagger + c_2^\dagger d_1^\dagger}_{\text{exit opposite ports}}\right]|0\rangle\,. \tag{1.16}$$

As indicated, the first two terms describe a pair which leaves via a single output port, either c or d. The final two terms describe outcomes in which the two photons leave via opposite output ports.

Distinguishable photons

Suppose first that the modes with indices 1 and 2 are orthogonal, so that

$$\left[c_1,\, c_2^\dagger\right] = \left[d_1,\, d_2^\dagger\right] = 0. \tag{1.17}$$

The four terms in the state (1.16) then correspond to distinct outcomes, with each outcome having a probability of $(\frac{1}{2})^2 = \frac{1}{4}$. This is the same result that one would anticipate if one supposed that each

photon scattered from the beamsplitter independently.

Indistinguishable photons

Now consider the case in which the photons have identical degrees of freedom before the beamsplitter. More specifically, the case in which

$$c_1^\dagger = c_2^\dagger, \qquad d_1^\dagger = d_2^\dagger, \tag{1.18}$$

so that the output modes cannot be used to determine which photon came from which input port. In this case, the outcome in which both photons transmit through the beamsplitter is indistinguishable from that in which both photons reflect from the beamsplitter, leading to quantum interference between these two outcomes. Labeling $c_1 = c_2 = c$ and $d_1 = d_2 = d$, the state is

$$|\psi'\rangle = \frac{1}{2}\left[\left(c^\dagger\right)^2 - \left(d^\dagger\right)^2\right]|0\rangle\,, \tag{1.19}$$

and one finds that the two photons always exit a single output port together, with each of the two output ports being equally likely [7]. The outcomes in which photons exit opposite ports interfere destructively and are never observed; this is a consequence of the sign difference between the two transformations (1.14), which is a consequence of the beamsplitter being lossless. This destructive interference is the Hong-Ou-Mandel effect, and the increased probability of a pair leaving via a single output port is termed *photon bunching*.

In practice, the two photons may have degrees of freedom which are similar despite not being identical. As the degrees of freedom of the two photons are made more distinguishable, the probabilities of the four outcomes approach $\frac{1}{4}$. Conversely, as the degrees of freedom are made more indistinguishable, the opposite-output-ports outcome becomes less probable [12].

A common experimental setup involves a photodetector placed at each output port (Figure 1.2). If

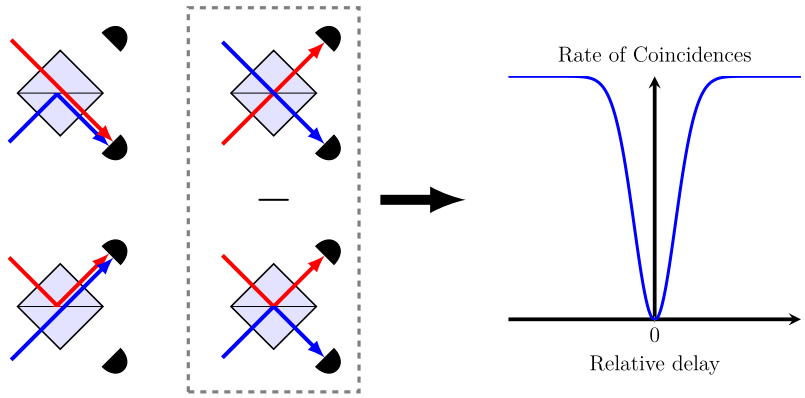

Figure 1.2: Schematic diagram of a Hong-Ou-Mandel interferometer. One photon enters each of the two input ports of a 50:50 beamsplitter, which results in one of four possible scatterings. If the two photons are distinguishable on the basis of some auxiliary degree of freedom, such as time-of-arrival, then all four outcomes are equally likely. If the two photons are indistinguishable, then the two outcomes leading to a coincidence detection interfere destructively, leading to a "HOM dip".

the two detectors click simultaneously, one counts a "coincidence" click. The photons are prepared with identical degrees of freedom, except for one which can be varied (such as the relative time-of-arrival at the beamsplitter). When this degree of freedom is tuned such that the two photons possess identical properties, the rate of coincidence clicks decreases to zero [7].

1.2.3 Phase-sensitive two-photon interference

Classical interferometers, such as the Michelson and Mach-Zehnder interferometer, may be regarded as the interference of a single photon with itself [81]. Each photon in a beam is placed in a superposition of two paths which are later recombined, so that an interference signal depending on the relative phases acquired in each path is observed. Analogous two-photon interferometers can be built, in which a photon pair is placed in a superposition of two states, which are later recombined [8, 9]. This leads to a phase-sensitive two-photon interference pattern.

A notable example is Franson interference [14], which occurs when a pair of photons, detected at a fixed moment in time, may have been emitted from the source at one of two possible times. Franson

interference is briefly discussed in Section 5.3 in comparison with a related effect. Another example, of significant interest in Chapters 3 and 4, uses the same geometry and detection scheme as a Hong-Ou-Mandel interferometer, with the difference that the initial state is entangled, rather than separable. We shall refer to this type of interferometer as an "entangled state Hong-Ou-Mandel interferometer" for simplicity.

Consider again two photons, with one photon incident on each of the two input ports of the beamsplitter. The initial state is now

$$|\psi\rangle = \frac{1}{\sqrt{2}}\left[e^{i\phi/2}a_1^\dagger b_2^\dagger + e^{-i\phi/2}a_2^\dagger b_1^\dagger\right]|0\rangle\,. \tag{1.20}$$

Indices 1 and 2 are used to label degrees of freedom other than the input port; in later chapters, this degree of freedom will be the frequency of the two photons. We use ϕ to denote a relative phase that may exist between the two terms in the superposition. As was discussed in the previous subsection, a state consisting of only one of these two terms would show no interference after the beamsplitter, due to the distinguishably provided by the other degrees of freedom. We will find, however, that interference still exists between the two terms in the original superposition state.

The action of the beamsplitter is once again given by (1.14). After the beamsplitter, the photon pair is in the state

$$\begin{aligned}|\psi'\rangle &= \frac{1}{2\sqrt{2}}\left[e^{i\phi/2}\left(c_1^\dagger + d_1^\dagger\right)\left(c_2^\dagger - d_2^\dagger\right) + e^{-i\phi/2}\left(c_2^\dagger + d_2^\dagger\right)\left(c_1^\dagger - d_1^\dagger\right)\right]|0\rangle \\ &= \frac{1}{\sqrt{2}}\left[\cos\frac{\phi}{2}c_1^\dagger c_2^\dagger - \cos\frac{\phi}{2}d_1^\dagger d_2^\dagger - i\sin\frac{\phi}{2}c_1^\dagger d_2^\dagger + i\sin\frac{\phi}{2}c_2^\dagger d_1^\dagger\right]|0\rangle\,.\end{aligned} \tag{1.21}$$

Similar to Hong-Ou-Mandel interference with a separable state, this interference can be observed if one measures the fraction of pairs which leave the beamsplitter via a single output port (bunched pairs) and those in which a single photon leaves each output port (antibunched pairs). Pairs tend to bunch when $\phi \approx 2n\pi$ for $n \in \mathbb{Z}$, and tend to antibunch when $\phi \approx (2n+1)\pi$. Unlike in the separable case, photons leaving the beamsplitter are always distinguishable, in the sense that the two photons always possess

different values for some degree of freedom (corresponding to the indices 1 and 2). Nevertheless, the interference is still due to indistinguishability of the fields in the two input modes a and b; the photon at each input port has equal probability of possessing the index 1 or 2. A more detailed calculation (discussed in Section 3.4) shows that the interference visibility decreases when the probability distribution at the two ports are not equal.

Our discussion highlights a crucial difference between the separable- and entangled-state HOM interferometers. In the former, the interference always tends to decrease the coincidence probability; this is due to a sign difference in (1.14), which is a consequence of unitarity. The separable-state interferometer is therefore always phase-insensitive. In the latter, the phase ϕ determines the type of interference (constructive or destructive), and this phase is under the control of the experimenter, being determined entirely by the initial state of the photon pair. This fact is used in Chapter 3 to construct a phase-sensitive spectroscopy technique.

1.3 Quantum metrology

The field of quantum metrology is concerned with the ultimate limits to the precision of physical measurements, as dictated by the laws of quantum mechanics. This study originated in the understanding that quantum indeterminism acts as a fundamental source of noise in physical measurements, so that a quantum mechanical description of the measurement process is needed for a complete understanding of measurement precision. Efforts to merge classical statistical theory with quantum mechanics, lead primarily by Helstrom [39] and Holevo [40], resulted in a set of theoretical tools relating measurement precision to the physical properties of a probe system — in particular, the quantum Fisher information [18], which quantifies the sensitivity of a probe system in measurements of some unknown parameter. Following experimental advances in the control of quantum systems, it was realized that quantum noise can be partially overcome by careful engineering of measurement devices. The first practical application was identified by Caves [20]: interferometric phase measurements, which are ordinarily limited by the shot noise arising from the

stochastic quantum nature of light, can be made to show greatly enhanced precision if one injects a small amount of optical power into the unused input port of the interferometer. This additional light can be prepared in a quadrature-squeezed state, whose phase uncertainty (over a small range of angles) is smaller than the phase uncertainty of an optical ground state. The effect of this is to introduce a small amount of entanglement between the two beams of the interferometer which reduces the shot noise observed at the photodetector.

Squeezed-state interferometers are now routinely applied to phase measurements, with experiments showing reductions in noise by a factor of more than 30 [60], and with the technique now being regularly applied to improve gravitational wave detection [82]. This success has launched a large research effort to investigate other techniques for quantum enhanced measurements. A common theme has been the use of entangled states, which feature strong correlations across multiple variables, to reduce measurement uncertainty [30, 41]. Often, one faces a constraint on the allowable types of measurement; for instance, the allowable energy or available bandwidth of the measurement device might have an upper bound. These constraints limit the possible precision in measurements of some quantities of interest [63]. Preparing the probe in an entangled state can allow one to more effectively utilize the available resources, resulting in improved sensitivity compared to classical techniques. In phase measurements, for instance, classical interferometers utilizing N probe photons have an uncertainty of $1/\sqrt{N}$, known as the *standard quantum limit*. If these same photons are instead prepared in a highly entangled N00N state, one finds the uncertainty scales as $1/N$ instead, known as the *Heisenberg limit* [31]. When N is large, the precision enhancement can be substantial. These quantum techniques come with some tradeoffs, as the quantum enhancement often quickly degrades when one introduces small imperfections to the measuring device.

The current task of quantum metrology is threefold: first, to find quantum systems which maximize the quantum Fisher information, enabling greater sensitivity to small shifts in unknown parameters; second, to design measurement schemes which can read out this additional information and use it to provide precise estimates of the values of these parameters; and third, to accomplish all of this in a manner which is resistant to common forms of experimental error. In the case of optical measurements, the most important

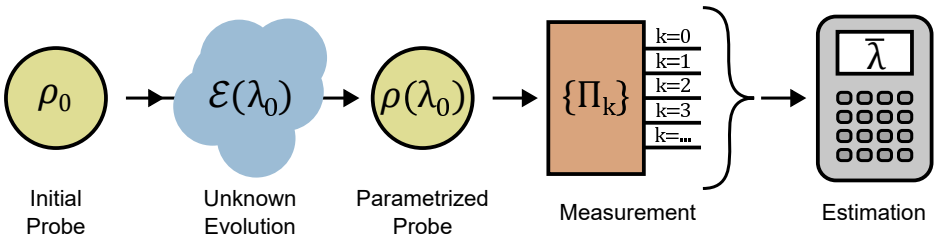

Figure 1.3: Schematic diagram of a typical measurement. A probe system is prepared in a known initial state ρ_0. This system undergoes an evolution which is parameterized by one or more unknown values $\boldsymbol{\lambda}_0$. Afterwards, the probe is measured by some apparatus, leading to a measurement outcome. This outcome is then used to estimate values $\overline{\boldsymbol{\lambda}}$ of the unknown parameters.

error to consider is optical loss, which serves to degrade many of the nonclassical properties of light which are used to enhance measurement precision in the first place.

1.3.1 The metrological problem

A reasonably general model of a physical measurement involves four main components (Figure 1.3): the *probe system*, an *evolution*, a *measurement*, and an *estimator* [57]. The purpose of the measurement is to determine one or more unknown parameters which characterize the evolution.

The probe is a quantum system which is prepared in a well-known initial state, described by a density matrix ρ_0. This system then undergoes some evolution, which is described by a quantum channel (a completely positive trace-preserving map) $\mathcal{E}$, which depends on a vector of unknown parameters $\boldsymbol{\lambda}$ with components λ_i, $i = 1, \ldots, N$. In the following discussion, it is sometimes useful to distinguish arbitrary parameter values from the "true" values in a particular measurement; when necessary, we will use a subscript $\lambda_{0,i}$ to denote the true values.

After undergoing this parameterized evolution, the probe is left in a final state

$$\rho(\boldsymbol{\lambda}) = \mathcal{E}_{\boldsymbol{\lambda}}(\rho_0). \tag{1.22}$$

The evolution often involves a coupling to another system, the *object* of the measurement, so that the dynamics of the probe are determined by the (possibly unknown) properties of the object. However, the theory does not require that the evolution have any particular form. The final step is a measurement of the probe, whose outcomes x have a corresponding probability $p(x;\boldsymbol{\lambda})$. These probabilities are given by the Born rule,

$$p(x;\boldsymbol{\lambda}) = \mathrm{Tr}\left[\rho(\boldsymbol{\lambda})\,\Pi(x)\right], \tag{1.23}$$

where $\Pi(x)$ is a positive operator-valued measure (POVM), normalized so that

$$\int dx\,\Pi(x) = \mathbb{1}. \tag{1.24}$$

The $\boldsymbol{\lambda}$-dependence of the measurement probabilities reflects the parameter-dependence of the post-evolution probe state. The final task of the experimenter is to infer the values of the unknown parameters from the observed measurement outcome x.

The general theory describing measurement precision, the quantum theory of parameter estimation, takes the form of an optimization problem. The goal is to minimize the difference between the true parameter values and the estimated values, as given by some cost function. Each of the stages in Figure 1.3 has an associated optimization problem and a corresponding bound. These bounds are most easily described in reverse order, that is, considering first the estimation of the parameters from a particular data set, and ending with the dynamical behaviour of the probe system. We proceed with a brief description of each of these stages before giving a more detailed discussion of the theoretical results.

Suppose first that a measurement has been conducted as described above, yielding an outcome x. We wish to find estimates $\overline{\lambda}_i$ of the parameters λ_i which are close to their true values. Since the outcome x in a given trial is random, we seek to minimize the average error when carrying out an ensemble of many measurement trials. The estimated values are determined by the observed outcome x, so that the estimates are determined using an *estimator* function $\overline{\lambda}_i(x)$. In the simplest case, the estimator may compute the

average outcome of multiple measurement trials. In more complicated situations, the estimator may consist of a numerical optimization procedure which infers the value of λ_i which is most likely to lead to the outcome x. The intent is to find a suitable set of estimators $\overline{\lambda}_i(x)$ which minimize the error in the estimated parameter values. Since the relationship between the outcomes x and the parameters $\boldsymbol{\lambda}$ is determined by the probability distribution $p(x;\boldsymbol{\lambda})$, the optimal choice of estimator will generally depend on the particular form of this distribution.

In a typical experiment, there is generally not a one-to-one relationship between the parameter values $\boldsymbol{\lambda}$ and the measurement outcome. As a simple example, most parameters of interest lie in a continuum of possible values; meanwhile, any real experiment has a finite number of possible outcomes set by the range of measurable values and the measurement device's resolution. It is therefore impossible to infer the parameter values with certainty; given a fixed probability distribution $p(x;\boldsymbol{\lambda})$, there is generally a minimum average error with which the values of the λ_i may be estimated. This minimum achievable error, which obviously depends on the particular distribution $p(x;\boldsymbol{\lambda})$, is given by the classical Cramér-Rao bound, which depends only on the distribution $p(x;\boldsymbol{\lambda})$, considered a function of $\boldsymbol{\lambda}$. The inverse of the classical Cramér-Rao bound is the classical Fisher information (CFI) [83], which we discuss in detail in Subsection 1.3.2. Measurements whose distributions have a large CFI can be used to estimate the unknown parameters with great accuracy and precision, since an estimator exists which has a small average error.

The amount of CFI associated with a particular experiment depends on the form of the $p(x;\boldsymbol{\lambda})$, and therefore on the choice of physical measurement which is made on the probe system. Certain measurements may have outcomes which are weakly correlated with the values of the λ_i, or may have outcomes whose distribution is highly sensitive to small changes in the parameter values. Consider now the choice of measurement $\Pi(x)$ which maximizes the CFI given a fixed form of the probe state $\rho(\boldsymbol{\lambda})$. If we assume the state $\rho(\boldsymbol{\lambda})$ depends continuously on the $\boldsymbol{\lambda}$, no choice of $\Pi(x)$ will lead to arbitrarily large values of the CFI for estimation of a continuous parameter. This is a consequence of the fact that states whose density matrices which are nearly equal cannot be distinguished with certainty (there are rare exceptions to this statement discussed below, but it is true in all measurements encountered in practice). There is

then generally a maximum value of the CFI for a given probe state $\rho(\boldsymbol{\lambda})$. This maximum value is given by the quantum Fisher information (QFI), whose value depends only on the state $\rho(\boldsymbol{\lambda})$ and its dependence on the $\boldsymbol{\lambda}$ [18]. The inverse of the QFI also provides a lower bound on the achievable error in estimates of the λ_i known as the quantum Cramér-Rao bound.

The general framework discussed so far applies both to estimation of a single parameter and to joint estimation of multiple parameters. However, some aspects of the theory differ between the two cases. For this reason, and for pedagogical reasons, we first give a more detailed description of the single parameter case before considering the more general situation.

1.3.2 Classical theory of single parameter estimation

Suppose that a probe system in an initial state ρ_0 evolves under some dynamics into an unknown state $\rho(\lambda)$, where λ is a single real parameter characterizing some unknown aspect of the dynamics. As discussed above, the final state is measured according to a POVM $\Pi(x)$ yielding an outcome x. The outcomes follow a probability distribution $p(x;\lambda)$. From the measured outcome, an estimate $\overline{\lambda}(x)$ of the unknown parameter is calculated.

The goal in estimating the unknown parameter is to produce an estimate $\overline{\lambda}$ which is on average close to the true value λ_0. The most common measure of this average error is the mean squared error,

$$\mathrm{MSE}_\lambda \equiv \langle(\overline{\lambda} - \lambda_0)^2\rangle, \tag{1.25}$$

where the angled brackets $\langle\cdot\rangle$ denotes an ensemble average over the estimated values $\overline{\lambda}$, which depends on the random measurement outcome. This may be rewritten in the form

$$\mathrm{MSE}_\lambda = \left\langle \left(\overline{\lambda} - \langle\overline{\lambda}\rangle\right)^2 \right\rangle + \left(\langle\overline{\lambda}\rangle - \lambda_0\right)^2. \tag{1.26}$$

The first term on the right is the variance of the estimator $\overline{\lambda}$, which quantifies the spread of values of the

estimator about the mean. Note that the distribution of measured values depends on the true value of the parameter, so that the variance has an implicit dependence on λ_0. The second term on the right is the square of the *bias*, $\langle\overline{\lambda}\rangle - \lambda_0$, that is, the difference between the average estimate and the true value. Estimators for which the bias vanishes are known as *unbiased estimators*; it is desirable for any estimator to be unbiased, since then a sufficiently large ensemble of estimates can be used to accurately determine the value λ_0. If the relationship between average estimates $\langle\overline{\lambda}\rangle$ and true values λ_0 is one-to-one, then the estimator may be made unbiased by adding some correction term which is found through calibration.

If the estimator in question is unbiased, then the mean squared error is equal to the variance of estimates, so that the optimal unbiased estimator is that which that minimizes the variance of estimates. The minimum attainable variance is determined by the distribution of measurement outcomes $p(x;\lambda)$. We now derive the lower bound on the variance of the estimator, following Kay [38]. For any estimator, we may write

$$\int dx\, p(x;\lambda_0)\ \left[\overline{\lambda}(x) - \langle\overline{\lambda}\rangle\right] = 0, \tag{1.27}$$

which follows from the definition of $\langle\overline{\lambda}\rangle$. Differentiating with respect to λ_0 gives

$$\int dx\, p(x;\lambda_0)\ \left[\overline{\lambda}(x) - \langle\overline{\lambda}\rangle\right]\ \frac{\partial \ln p(x;\lambda_0)}{\partial\lambda_0} - \frac{d\langle\overline{\lambda}\rangle}{d\lambda_0}\int dx\, p(x;\lambda_0) = 0, \tag{1.28}$$

where we have used the fact that $\partial p/\partial\lambda_0 = p\,\partial \ln p/\partial\lambda_0$. For an unbiased estimator, $d\langle\overline{\lambda}\rangle/d\lambda_0 = 1$ and so

$$\int dx\, p(x;\lambda_0)\ \left[\overline{\lambda}(x) - \langle\overline{\lambda}\rangle\right]\ \frac{\partial \ln p(x;\lambda_0)}{\partial\lambda_0} = 1. \tag{1.29}$$

The Cauchy-Schwarz inequality for expectation values $\langle X\rangle$ states that $\langle XY\rangle^2 \leq \langle X^2\rangle\langle Y^2\rangle$. Applying this to the functions $\left[\overline{\lambda}(x) - \langle\overline{\lambda}\rangle\right]$ and $\partial \ln p(x;\lambda_0)/\partial\lambda_0$ leads to the inequality

$$\left\langle \left(\overline{\lambda} - \langle\overline{\lambda}\rangle\right)^2 \right\rangle \geq \frac{1}{\mathcal{F}_\lambda}, \tag{1.30}$$

where $\mathcal{F}_\lambda$ is the classical Fisher information for the parameter λ, given by the expression

$$\mathcal{F}_\lambda \equiv \int dx\, p(x;\lambda_0)\, \left(\frac{\partial \ln p(x;\lambda_0)}{\partial \lambda_0}\right)^2. \tag{1.31}$$

This can also be written in the equivalent forms

$$\mathcal{F}_\lambda = \int dx\, \frac{1}{p(x;\lambda_0)}\, \left(\frac{\partial p(x;\lambda_0)}{\partial \lambda_0}\right)^2 \tag{1.32a}$$

$$= -\int dx\, p(x;\lambda_0)\, \frac{\partial^2 \ln p(x;\lambda_0)}{\partial \lambda_0^2}. \tag{1.32b}$$

The first expression follows from the familiar expression for the derivative of a logarithm; the second expression holds if $p(x,\lambda)$ satisfies some mild regularity conditions [44], and can be derived by writing $\mathcal{F}_\lambda$ as the integral of $(\partial p/\partial\lambda_0)(\partial \ln p/\partial\lambda_0)$ and performing an integration by parts. It is straightforward to show that if N trials of measurement are carried out such that the results are independent and identically distributed, then

$$\left\langle \left(\overline{\lambda} - \langle\overline{\lambda}\rangle\right)^2 \right\rangle \geq \frac{1}{N\mathcal{F}_\lambda}, \tag{1.33}$$

where $\mathcal{F}_\lambda$ is now calculated from the distribution of outcomes of a single trial. As promised, the minimum error of an unbiased estimator is inversely proportional to the CFI determined by the distribution of measurement outcomes. This inequality is the *classical Cramér-Rao bound*, and it is a consequence of classical statistics.

The classical Cramér-Rao bound sets a lower limit on the possible variance of an estimate of λ, but on its own it does not state whether any estimator actually reaches this bound. In the case of classical estimation, a general estimator is known which does saturate the bound, at least in the limit of many trials

N. Given an observed set of outcomes $x_1, \ldots, x_N$, define the *likelihood* of a particular λ by

$$\mathcal{L}(\lambda) = \prod_{i=1}^{N} p(x_i; \lambda). \tag{1.34}$$

That is, the likelihood function is the probability distribution evaluated at the observed measurement outcomes, treated as a function of the unknown parameter λ. The *maximum likelihood estimator* of λ is defined to be the value of λ for which the likelihood function for the observed outcomes is maximized. With the exception of a few simple distributions $p(x; \lambda)$, this optimization cannot be performed analytically. Typically, a maximum likelihood estimator is implemented by numerically optimizing the value of $\ln \mathcal{L}(\lambda)$ over possible values of λ, with the logarithm serving to broaden the sharp peaks which occur in a typical likelihood function.

In the limit $N \gg 1$, so long as $\mathcal{L}$ and $p(x; \lambda)$ satisfy some mild regularity conditions, one can show that the maximum likelihood estimator is unbiased and saturates the classical Cramér-Rao bound [38]. Specifically, in the large-N limit, the maximum likelihood estimate becomes normally distributed with mean λ_0 and variance $1/N\mathcal{F}_\lambda$. This does not guarantee any particular rate of convergence with N; in general, determining an optimal estimator given a finite number of trials is quite challenging [84]. Nevertheless, this result shows that the CFI is a useful description of the amount of information about the value of λ contained in the measurement distribution $p(x; \lambda)$.

1.3.3 Quantum theory of single parameter estimation

The quantum theory parallels the classical theory, in that it provides a lower bound on the possible variance in measurements of an unknown parameter λ. The classical bound is derived from the statistical distribution of measurement outcomes, which depends both on the post-evolution state $\rho(\lambda)$ and also on the choice of measurement. The quantum theory of parameter estimation performs an optimization over all possible measurements, any one of which is described by a POVM $\Pi(x)$. It provides a bound on the variance, and hence on the mean squared error, which is due only to the physical state $\rho(\lambda)$ of the probe

considered as a function of the unknown λ. This bound is known as the *quantum Cramér-Rao bound*, which is expressed as the inverse of the *quantum Fisher information* (QFI) of the state $\rho(\lambda)$. Since the classical Cramér-Rao bound describes the possible measurement precision given a particular POVM, the classical bound is itself lower bounded by the quantum Cramér-Rao bound; equivalently, the QFI is an upper bound on the CFI of any possible measurement scheme.

The quantum Cramér-Rao bound

The quantum Cramér-Rao bound was initially derived by Helstrom [18, 39] through a calculation which parallels the derivation of the classical bound. We give here an alternative derivation, due to Braunstein and Caves [27], in which the quantum Fisher information is obtained by optimizing the classical Fisher information over all possible POVMs $\Pi(x)$.

The derivation begins by writing the classical Fisher information in the form

$$\mathcal{F}_\lambda = \int dx \, \frac{1}{p(x;\lambda_0)} \left(\frac{\partial p(x;\lambda_0)}{\partial \lambda_0} \right)^2 . \tag{1.35}$$

For a given probe state $\rho(\lambda_0)$ and POVM $\Pi(x)$, the probability density can be written

$$p(x;\lambda_0) = \mathrm{Tr}\left\{ \Pi(x)\, \rho(\lambda_0) \right\} . \tag{1.36}$$

Then,

$$\begin{aligned} \mathcal{F}_\lambda &= \int dx \, \frac{1}{\mathrm{Tr}\left\{ \Pi(x)\, \rho(\lambda_0) \right\}} \left(\frac{\partial \, \mathrm{Tr}\left\{ \Pi(x)\, \rho(\lambda_0) \right\}}{\partial \lambda_0} \right)^2 \\ &= \int dx \, \frac{1}{\mathrm{Tr}\left\{ \Pi(x)\, \rho(\lambda_0) \right\}} \left(\mathrm{Tr}\left\{ \Pi(x)\, \rho'(\lambda_0) \right\} \right)^2 , \end{aligned} \tag{1.37}$$

where $\rho'(\lambda_0) = d\rho(\lambda_0)/d\lambda_0$. At this stage it is useful to introduce the *symmetric logarithmic derivative* L

for the parameter λ, which is implicitly defined by the expression [18, 39]

$$\rho'(\lambda_0) = \frac{1}{2}\left(\rho(\lambda_0)L + L\rho(\lambda_0)\right). \tag{1.38}$$

Note that L implicitly depends on the true value of the parameter λ_0. The symmetric logarithmic derivative is a generalization of the factor $\partial \ln p(x;\lambda_0)/\partial\lambda_0$ to the case of non-commuting quantum theory. Generally, both the eigenvalues and eigenbasis of the state $\rho(\lambda)$ will change with λ; in the special case where only the eigenvalues depend on λ, L simply encodes the classical derivative $\partial \ln p(x;\lambda_0)/\partial\lambda_0$. The operator L has an analogous role to this derivative in the quantum bound.

By definition, we have

$$\begin{aligned}\mathrm{Tr}\left\{\Pi(x)\,\rho'(\lambda_0)\right\} &= \frac{1}{2}\mathrm{Tr}\left\{\Pi(x)\,\rho(\lambda_0)\,L\right\} + \frac{1}{2}\mathrm{Tr}\left\{\Pi(x)\,L\,\rho(\lambda_0)\right\} \\ &= \mathrm{Tr}\left\{\rho(\lambda_0)\,\Pi(x)\,L\right\} + \frac{1}{2}\mathrm{Tr}\left\{\rho(\lambda_0)\,[L,\,\Pi(x)]\right\},\end{aligned} \tag{1.39}$$

where square brackets denote a commutator. Since $\Pi(x)$ and $\rho(\lambda_0)$ are both Hermitian, $\mathrm{Tr}\left\{\Pi(x)\,\rho(\lambda_0)\right\}$ is real. The term on the left is the derivative of a real function, so it is therefore real. By contrast, $[L,\,\Pi(x)]$ is anti-Hermitian, so that the final term on the right is purely imaginary. It follows that

$$\mathrm{Re}\,\mathrm{Tr}\left\{\rho(\lambda_0)\,\Pi(x)\,L\right\} = \mathrm{Tr}\left\{\Pi(x)\,\rho'(\lambda_0)\right\}. \tag{1.40}$$

The classical Fisher information can therefore be written

$$\mathcal{F}_\lambda = \int dx\, \frac{1}{\mathrm{Tr}\left\{\Pi(x)\,\rho(\lambda_0)\right\}}\Big(\mathrm{Re}\,\mathrm{Tr}\left\{\rho(\lambda_0)\,\Pi(x)\,L\right\}\Big)^2, \tag{1.41}$$

so that

$$\mathcal{F}_\lambda \leq \int dx\, \frac{1}{\mathrm{Tr}\left\{\Pi(x)\,\rho(\lambda_0)\right\}}\Big|\mathrm{Tr}\left\{\rho(\lambda_0)\,\Pi(x)\,L\right\}\Big|^2. \tag{1.42}$$

After some rearranging, this can be written

$$\mathcal{F}_\lambda \leq \int dx \left| \mathrm{Tr} \left\{ \frac{\rho^{1/2}(\lambda_0)\,\Pi^{1/2}(x)}{\sqrt{\mathrm{Tr}\left\{\rho(\lambda_0)\,\Pi(x)\right\}}}\,\Pi^{1/2}(x)\,L\,\rho^{1/2}(\lambda_0) \right\} \right|^2 . \tag{1.43}$$

The Cauchy-Schwarz inequality for the Hilbert-Schmidt inner product states that for any A and B, $|\mathrm{Tr}\{A^\dagger B\}|^2 \leq \mathrm{Tr}\{A^\dagger A\}\,\mathrm{Tr}\{B^\dagger B\}$. Applying this to the expression above gives

$$\mathcal{F}_\lambda \leq \int dx\,\mathrm{Tr}\left\{\Pi(x)\,L\,\rho(\lambda_0)\,L\right\}. \tag{1.44}$$

The operators $\Pi(x)$ form a POVM, so $\int dx\,\Pi(x) = \mathbb{1}$. The bound then takes the form

$$\mathcal{F}_\lambda \leq \mathcal{Q}_\lambda, \tag{1.45}$$

where we have defined the quantum Fisher information

$$\mathcal{Q}_\lambda = \mathrm{Tr}\left\{L\,\rho(\lambda_0)\,L\right\} = \mathrm{Tr}\left\{\rho(\lambda_0)\,L^2\right\}. \tag{1.46}$$

Whereas the CFI is the expectation value of the square of the logarithmic derivative $\partial \ln p(x;\lambda_0)/\partial\lambda_0$, the QFI is the expectation value of the square of the symmetric logarithmic derivative L.

Properties of the quantum Fisher information

As in the classical case, it can be shown that if N independent trials of the measurement are made, so that $\rho = \rho_0^{\otimes N}$ and $\Pi(x_1,\ldots,x_N) = \bigotimes_{i=1}^N \Pi_0(x_i)$, the QFI is given by $N\mathcal{Q}_\lambda$, where $\mathcal{Q}_\lambda$ is the QFI of a single trial. Including the factors of N, then, the quantum Cramér-Rao bound can be expressed by the chain of inequalities

$$\left\langle \left(\overline{\lambda} - \langle\overline{\lambda}\rangle\right)^2 \right\rangle \geq \frac{1}{N\mathcal{F}_\lambda} \geq \frac{1}{N\mathcal{Q}_\lambda}. \tag{1.47}$$

It is important to ask whether any choice of POVM $\Pi(x)$ actually saturates the quantum Cramér-Rao bound. A straightforward calculation shows that a projective measurement onto the eigenbasis of the symmetric logarithmic derivative L results in a CFI that equals the QFI for any probe state [39]. Since the operator L itself depends on the true parameter λ_0, this optimal measurement is not always known in advance; instead, one often starts with a guess of the value of λ and project onto the symmetric logarithmic derivative corresponding to this value. Of course, this guess can be updated based on the result of previous measurement trials so that the projection basis tends to the optimal value as $N \to \infty$, forming an adaptive measurement.

The framework developed so far allows for optimization of the parameter estimate from the observed measurement outcomes; it also allows for optimization of the measured observables in order to maximize the information obtained about the parameter. The remaining stages of the measurement process are the choice of initial probe state, and the evolution which transforms the probe into a parameter-dependent state. Typically, one assumes that the evolution is fixed, and the dynamical process which encodes the parameter in the probe state is outside of experimental control [42]. This leaves a final stage of optimization, which seeks to maximize the quantum Fisher information by choice of the initial probe state. The optimal probe state depends on the nature of the dynamical evolution. We now consider a common form of evolution and obtain the probe state which maximizes the sensitivity to the unknown parameter.

Unitary evolution and pure states

Under unitary evolution, the initial probe state ρ_0 evolves into the state

$$\rho_0 \mapsto \rho(\lambda) = U(\lambda)\rho_0 U^\dagger(\lambda), \tag{1.48}$$

where $U(\lambda)$ is a unitary operator. Differentiating this gives

$$\frac{d\rho(\lambda)}{d\lambda} = \frac{dU}{d\lambda}\rho_0 U^\dagger + U\rho_0\frac{dU^\dagger}{d\lambda} = \frac{dU}{d\lambda}U^\dagger\rho(\lambda) + \rho(\lambda)U\frac{dU^\dagger}{d\lambda}. \tag{1.49}$$

Suppose now that $U(\lambda)$ takes the form $U(\lambda) = \exp(i\lambda h)$, where the generator h is Hermitian. This form of unitary occurs in many contexts related to displacement of the state in some degree of freedom [85]; depending on the choice of h, λ can describe a displacement in time, frequency, space, momentum, angle, phase, or quadrature. In this case, the expression above implies that

$$\frac{1}{2}\left(L\rho(\lambda) + \rho(\lambda)L\right) = ih\rho(\lambda) - i\rho(\lambda)h. \tag{1.50}$$

We may calculate the matrix elements of each side in the eigenbasis of the density operator; this results in the expression [86]

$$L = \sum_j \sum_k \left[\frac{2i(p_j - p_k)}{p_j + p_k} \langle j| h |k\rangle\right] |j\rangle \langle k|, \tag{1.51}$$

where $\rho(\lambda) = \sum_i p_i |i\rangle \langle i|$ and the sum is taken over all pairs of indices for which the denominator is nonzero. It can be shown that the optimal state for estimation of a single parameter is always pure [45], so it is reasonable to focus on this case. If the probe state after evolution is $\rho = |\psi\rangle \langle\psi|$, then

$$L = 2ih |\psi\rangle \langle\psi| - 2i |\psi\rangle \langle\psi| h. \tag{1.52}$$

Explicit calculation then shows that

$$\mathcal{Q}_\lambda = 4 \langle\psi_0| h^2 |\psi_0\rangle - 4 \langle\psi_0| h |\psi_0\rangle^2, \tag{1.53}$$

so that the QFI is four times the variance of the observable h as calculated for the initial probe state $|\psi_0\rangle$, a result first shown by Helstrom [85]. The optimal initial probe state is then one that maximizes this variance, that is, an equal superposition of eigenstates of h with the largest and smallest eigenvalues [86].

Heisenberg scaling and quantum-enhanced precision

A unique feature of quantum metrology as compared to classical metrology is that the scaling of the precision with the number of probe states can be different. As discussed in Subsection 1.3.2, a measurement which uses N trials consisting of M probe systems has a classical Fisher information that scales as MN, so that the precision scales as $1/\sqrt{MN}$; this type of scaling is sometimes referred to as the *standard quantum limit*. This is not the only possible strategy: when quantum effects are considered, one can use in each trial M noninteracting probe systems that are prepared in an entangled state. If the probe systems evolve independently, then the unitary describing this evolution has the form

$$\prod_{j=1}^{M} e^{i\lambda h_j} = \exp\left(i\lambda \sum_{j=1}^{M} h_j\right), \tag{1.54}$$

where the generator h_j acts on the j^{th} probe system. The optimal probe state now consists of an equal superposition of two states: one state is the M-fold product of the lowest eigenstate of h, and the other is the M-fold product of the highest eigenstate of h. The variance in this case scales as M^2, so that $\mathcal{Q}_\lambda \propto M^2$ and the optimal precision scales as $1/M\sqrt{N}$, a $\sqrt{M}$ improvement on the standard quantum limit. This type of scaling is referred to as the *Heisenberg limit* [30], and highlights the advantage that entangled probe states can bring to precision measurements.

1.3.4 Multiparameter estimation problems

In practice, it can be advantageous to determine multiple unknown parameters using a single measurement scheme. The framework described above can be generalized to the case of multiparameter estimation, with some minor changes. Conceptually, the problem of multiparameter estimation is very similar to that of single parameter estimation, so we state some of the results of the theory without proof.

In the single parameter problem, the error in the parameter estimate was characterized by the mean squared error, which could be written in terms of the variance and the bias of the estimator. In the

multiparameter scenario, we wish to estimate a vector λ_i of unknown parameters using estimators $\overline{\lambda}_i$, where the true values of the parameters are $\lambda_{0,i}$. We then consider the quantities

$$\left\langle \left(\overline{\lambda}_i - \lambda_{0,i}\right)\left(\overline{\lambda}_j - \lambda_{0,j}\right)\right\rangle = \left\langle \left(\overline{\lambda}_i - \langle\overline{\lambda}_i\rangle\right)\left(\overline{\lambda}_j - \langle\overline{\lambda}_j\rangle\right)\right\rangle + \left(\langle\overline{\lambda}_i\rangle - \lambda_{0,i}\right)\left(\langle\overline{\lambda}_j\rangle - \lambda_{0,j}\right). \tag{1.55}$$

The first term on the right is just the covariance matrix of the estimator,

$$\boldsymbol{C}_{ij} = \left\langle \left(\overline{\lambda}_i - \langle\overline{\lambda}_i\rangle\right)\left(\overline{\lambda}_j - \langle\overline{\lambda}_j\rangle\right)\right\rangle, \tag{1.56}$$

while the second term vanishes when each of the estimators $\overline{\lambda}_i$ is unbiased, $\langle\overline{\lambda}_i\rangle = \lambda_{0,i}$. Taking $i = j$, (1.55) is again a statement that the mean squared error of each parameter is the variance plus the square of the bias. The off-diagonal components quantify correlations in the errors of different parameters. For an unbiased estimator, the covariance matrix C of the estimator can then be used as a measure of precision.

We again consider the problem of determining the optimal precision of the estimates $\overline{\lambda}_i$. In the multiparameter case, this bound takes the form of a matrix inequality which places a lower bound on the covariance matrix; the inverse of the bound is called the *classical Fisher information matrix*. The CFI matrix is determined by the probability distribution $p(x;\{\lambda_{0,k}\})$ of observed outcomes, which now depends on all of the unknown parameters λ_k. The classical Fisher information matrix has elements

$$\begin{aligned}\boldsymbol{\mathcal{F}}_{ij} &= \int dx\, p(x;\{\lambda_{0,k}\})\left(\frac{\partial \ln p(x;\{\lambda_{0,k}\})}{\partial\lambda_{0,i}}\right)\left(\frac{\partial \ln p(x;\{\lambda_{0,k}\})}{\partial\lambda_{0,j}}\right)\\ &= \int dx\, \frac{1}{p(x;\{\lambda_{0,k}\})}\left(\frac{\partial p(x;\{\lambda_{0,k}\})}{\partial\lambda_{0,i}}\right)\left(\frac{\partial p(x;\{\lambda_{0,k}\})}{\partial\lambda_{0,j}}\right)\end{aligned} \tag{1.57}$$

Note in particular that each diagonal element $\boldsymbol{\mathcal{F}}_{ii}$ of the CFI matrix is just the single parameter CFI of the corresponding element λ_i. The CFI matrix bounds the covariance via another classical Cramér-Rao bound [38],

$$\boldsymbol{C} \geq \frac{1}{N}\boldsymbol{\mathcal{F}}^{-1}, \tag{1.58}$$

where the matrix inequality $\boldsymbol{A} \geq \boldsymbol{B}$ should be interpreted as a statement that the matrix $\boldsymbol{A} - \boldsymbol{B}$ is positive semidefinite. In this inequality, N is again the number of identical, statistically independent trials which are performed. Just like in the single parameter case the maximum likelihood estimator, defined in the same way as in the single parameter case, asymptotically saturates this bound in the limit $N \to \infty$ [38].

The multiparameter generalization of the quantum Cramér-Rao bound also takes the form of a matrix inequality. It states that [45]

$$\boldsymbol{C} \geq \frac{1}{N}\boldsymbol{\mathcal{F}}^{-1} \geq \frac{1}{N}\boldsymbol{\mathcal{Q}}^{-1}, \tag{1.59}$$

where the *quantum Fisher information matrix* $\boldsymbol{\mathcal{Q}}$ is defined by

$$\boldsymbol{\mathcal{Q}}_{ij} = \frac{1}{2}\mathrm{Tr}\left[\rho(\{\lambda_{0,k}\})\ \{L_i, L_j\}\right], \tag{1.60}$$

where $\{\cdot,\cdot\}$ denotes the anticommutator, and the symmetric logarithmic derivatives L_i corresponding to parameters λ_i are again defined by

$$\frac{\partial\rho(\{\lambda_{0,k}\})}{\partial\lambda_i} = \frac{1}{2}\left(\rho(\{\lambda_{0,k}\})L_i + L_i\rho(\{\lambda_{0,k}\})\right). \tag{1.61}$$

As in the classical case, each diagonal element $\boldsymbol{\mathcal{Q}}_{ii}$ of the QFI matrix is just the single parameter QFI calculated for the corresponding element λ_i.

The question of the saturability of the quantum Cramér-Rao bound is more complicated in the multiparameter case than in the single parameter case. For a single parameter, the optimal measurement is a projection onto the eigenbasis of the symmetric logarithmic derivative. With multiple parameters come multiple operators L_i, which generally do not commute. If the symmetric logarithmic derivatives L_i do not commute, then the optimal measurements for different parameters cannot be performed on the same probe system.

If the every pair of operators L_i commute, then a projection onto the common eigenbasis of the operators

results in a CFI matrix equal to the QFI matrix. Generally, a slightly weaker condition is sufficient, which requires only that $\mathrm{Tr}\left(\rho(\{\lambda_{0,k}\})\,[L_i,\,L_j]\right) = 0$ for all pairs of operators [87]. In particular, if $\rho(\{\lambda_{0,k}\})$ is a pure state and the evolution is unitary, then this condition is satisfied if all generators associated with each pair of parameters commute. Otherwise, the quantum Cramér-Rao bound may not be attained by any measurement, and a stronger bound due to Holevo holds [40, 88]. Even in this case, however, it is possible to saturate the quantum Cramér-Rao bound for all unknown parameters, up to a constant factor. In particular, if there are M unknown parameters, one can alternate between projections onto the eigenbases of the M operators L_i, so that at least N/M trials will use the optimal projection for each parameter. It follows that the precision in each estimate will be within a factor of $M^{-1/2}$ of the corresponding quantum Cramér-Rao bound. Since the ratio between the realizable precision and the quantum bound does not depend on the number of trials, an optimal measurement's precision must have the same scaling with N as the QFI matrix. In fact, a more detailed study of the problem shows that the QFI matrix still gives the realizable bound to within a factor of two [89].

1.4 Spontaneous parametric down-conversion

Spontaneous parametric down-conversion (SPDC) is the most common technique for producing photon pairs, also called *biphotons*. It is particularly appealing for quantum optics experiments since it can be made to produce photon pairs which are highly entangled in essentially any degree of freedom. Photon pairs produced by SPDC tend to have some characteristic properties due to the particular physical mechanism by which they are produced. Since this thesis is primarily concerned with two-photon interference, these characteristics of SPDC-based photon pairs play a prominent role in all later discussions.

Spontaneous parametric down-conversion is a process by which light of a high frequency is converted, by means of a nonlinear optical interaction, into light of a lower frequency. The high-frequency light, referred to as the *pump*, is typically provided by a laser beam. The interaction is commonly provided by a nonlinear crystal; the anharmonic dielectric response of the crystal at high pump intensities effectively

couple optical modes of different frequencies, allowing energy to be exchanged between the high- and low-frequency modes. This process occurs far from any material resonance, so that the energy and momentum of the crystal are unchanged. It follows that energy and momentum conservation must hold for the initial and final states of the optical field alone. At low intensities, SPDC involves only a single pump photon and two down-converted photons. Each photon has an energy $\hbar\omega$ and a momentum $\hbar\boldsymbol{k}$, so that energy and momentum conservation impose the restrictions

$$\omega_p = \omega_s + \omega_i, \tag{1.62a}$$

$$\boldsymbol{k}_p = \boldsymbol{k}_s + \boldsymbol{k}_i. \tag{1.62b}$$

The subscript p here refers to the pump field, while s and i (short for *signal* and *idler*) are conventional names for the two lower-energy photons. The wavevector $\boldsymbol{k}$ describes the spatial dependence of each optical mode through a factor $e^{i\boldsymbol{k}\cdot\boldsymbol{r}}$, so that (1.62b) is often referred to as the *phase matching* condition [90].

In many experiments, one collects down-converted photons only along two fixed directions, in which case the frequencies and polarizations of the two photons are the only undetermined variables left in (1.62). Commonly, one uses a birefringent nonlinear medium; in this case, after fixing the propagation directions of the photons, (1.62) is typically satisfied for at most one choice of polarizations. Exceptions occur for very thin media [91], and for careful choices of material and geometry [92], where the phase matching condition for a fixed pair of angles may have multiple solutions corresponding to multiple choices of polarization. The process is classified according to the polarizations of the photons: type-0 and type-I SPDC involve pairs with identical polarizations (either parallel or orthogonal to the pump polarization, respectively), and type-II SPDC results in a pair of oppositely-polarized photons. We focus on those situations in which only a single pair of polarizations satisfy the phase matching condition, so that only the angles and frequencies of the photons may vary.

The wavevector $\boldsymbol{k}$ is related to the frequency by $|\boldsymbol{k}| = n(\omega)\omega/c$, so that (1.62) provides four constraints on the allowed frequency and direction of the down-converted photons. Considering a fixed pair of po-

larizations, these photons are described by six variables (one frequency and two angles for each photon), so that strict energy-momentum conservation still allows for an infinite number of solutions for possible down-conversion. In practice, the finite thickness of the nonlinear crystal provides a spatial inhomogeneity in the interaction, which loosens the requirement for longitudinal momentum conservation [93]. A single pump beam therefore leads to down-converted light across a wide range of frequencies and angles. Nevertheless, the energies and transverse momenta of the two photons are always related by (1.62).

If one down-converted photon's direction is fixed, transverse momentum conservation generally determines the direction of the other down-converted photon — the specific relationship between the angles depends on the polarizations of the three beams as well as the birefringence and dispersion relations describing the nonlinear crystal, but typically the two photons are emitted in opposite transverse directions relative to the pump beam (Figure 1.4a) [94]. Energy conservation (Figure 1.4b) specifies only the relationship between the signal and idler frequencies; the allowable range of frequencies (*i.e.*, the bandwidth of the down-converted beam) is determined by longitudinal momentum conservation. Define the momentum mismatch $\Delta\boldsymbol{k}$ by

$$\Delta\boldsymbol{k} \equiv \boldsymbol{k}_p - \boldsymbol{k}_s - \boldsymbol{k}_i. \tag{1.63}$$

Transverse momentum conservation corresponds to the condition $\Delta\boldsymbol{k}_\perp = 0$. As mentioned above, longitudinal phase matching is weakened due to the finite length of the crystal; one can expect that a crystal of length L will efficiently produce down-converted photons so long as

$$|\Delta k_z| \lesssim \frac{1}{L}, \tag{1.64}$$

where the pump beam is incident along the z-axis (Figure 1.4c). A more detailed calculation shows that the down-conversion efficiency is proportional to $\mathrm{sinc}^2\left(\Delta k_z L/2\right)$ [93]. Since Δk_z is roughly proportional to the range of allowed frequencies, it follows that the bandwidth of the radiation increases rapidly as the crystal thickness decreases.

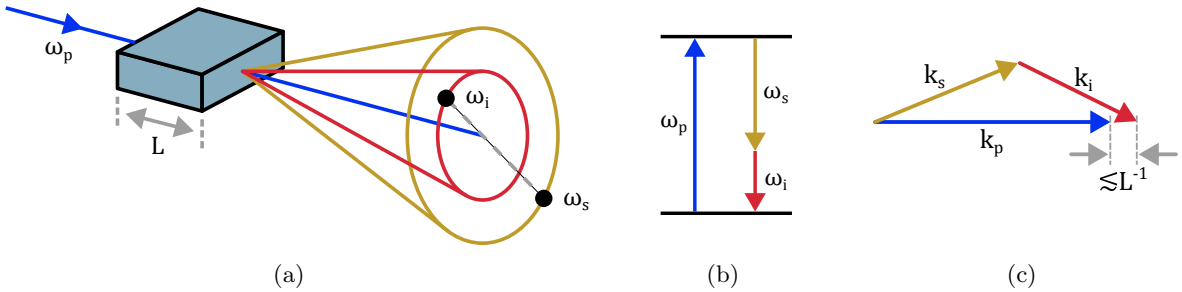

Figure 1.4: A typical SPDC source. (a) Photon pairs are produced by pumping a nonlinear crystal with a laser beam at frequency ω_p. Pairs of photons are produced in a cone centered on the pump beam. Due to momentum conservation, photons are found at opposite angles relative to the pump beam. (b) Condition for energy conservation. The frequencies of the two down-converted photons must add to the frequency of the pump photon. (c) Condition for momentum conservation. The wavevectors of the down-converted photons must add to the wavevector of the pump photon in the two transverse directions. Along the longitudinal direction, the initial and final wavevectors may differ by approximately the inverse of the crystal length.

The discussion so far has assumed a pump beam with a definite frequency ω_p. More realistically, the pump has some finite bandwidth $\delta\omega_p$. Each frequency in the pump beam will lead to its own set of down-converted photons whose frequencies satisfy (1.62a). A simple representation for the time-frequency state of a photon pair emitted along a fixed pair of directions is [95]

$$|\psi\rangle = \iint d\omega\, d\omega'\, \phi(\omega_s, \omega_i)\, a_s^\dagger(\omega_s) a_i^\dagger(\omega_i)\, |0\rangle\,, \tag{1.65}$$

where $a_s^\dagger(\omega)$ and $a_s^\dagger(\omega)$ are creation operators for modes along the signal and idler directions, respectively, with monochromatic frequency ω. The complex function $\phi(\omega_s, \omega_i)$, called the *joint spectral amplitude* (JSA), completely specifies the time-frequency state of the pair. The corresponding intensity $|\phi(\omega_s, \omega_i)|^2$ is called the *joint spectral intensity* (JSI). Since each pump frequency is assumed independently generate pairs consistent with (1.62a), the joint spectral amplitude can generally be written in the form [95]

$$\phi(\omega_s, \omega_i) = \alpha(\omega_s + \omega_i) f(\omega_s, \omega_i). \tag{1.66}$$

Here, $\alpha(\omega)$ is just the spectral amplitude of the pump beam, while $f(\omega_s, \omega_i)$, called the *phase matching*

function, is set by the crystal properties.

A typical form for the JSI is shown in Figure 1.5a, where we have assumed a narrowband pump and employed a Gaussian approximation for the spectrum, which suppresses the side lobes arising from the $\mathrm{sinc}^2(\Delta k_z L/2)$ contribution to the phase matching function. Supposing that the phase matching function varies slowly with frequency near its peak, (1.66) shows that the width along the diagonal is equal to the pump bandwidth $\delta\omega_p$. The width along the antidiagonal, which we will call the *biphoton bandwidth*, is determined by the crystal properties as encoded in the phase matching function. It is also sometimes convenient to introduce a *joint temporal amplitude* defined by

$$\widetilde{\phi}(t_s, t_i) = \frac{1}{2\pi} \iint d\omega_s \, d\omega_i \, \phi(\omega_s, \omega_i) \, e^{-i\omega_s t_s - i\omega_i t_i}, \tag{1.67}$$

which is normalized so that

$$\iint d\omega_s \, d\omega_i \, |\phi(\omega_s, \omega_i)|^2 = \iint dt_s \, dt_i \, |\widetilde{\phi}(t_s, t_i)|^2. \tag{1.68}$$

The JSA gives the complex amplitude of the down-converted photons having a particular pair of frequencies. The JTA gives the complex amplitude of the down-converted photons having a particular pair of time-of-arrivals, measured relative to an arbitrary but fixed time zero (typically taken to be the arrival time of the pump pulse at a detector). The *joint temporal intensity* (JTI) $|\widetilde{\phi}(t_s, t_i)|^2$ for the state depicted is shown in Figure 1.5b. From the general properties of the Fourier transform, the width of the JTI along the diagonal is approximately $1/\delta\omega_p$, while the width along the antidiagonal, called here the *biphoton coherence time*, is approximately the inverse of the biphoton bandwidth. From Figure 1.5b one observes that the tight frequency anticorrelations in the JSI correspond to tight timing correlations in the JTI. In common sources, the time-of-arrival of each of the two photons are equal to within a few femtoseconds, ignoring any dispersion.

The tight timing correlations indicated by Figure 1.5b give an experimental signature that can be used to identify pairs of photons which originate from a single down-conversion event, as opposed to

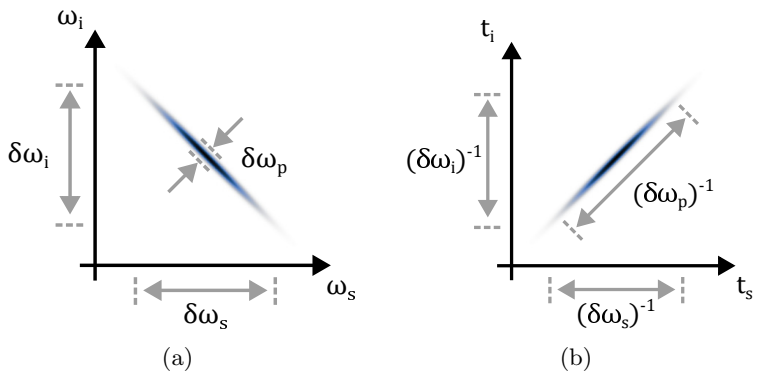

Figure 1.5: Joint spectral intensity (a) and joint temporal intensity (b) of a typical biphoton generated by SPDC. The width of the JSI along the diagonal direction is equal to the bandwidth of the pump beam. The width of the JSI along the antidiagonal is determined by the phase matching conditions of the crystal, and is larger for shorter crystals. The corresponding widths of the JTI are approximately the inverse of those of the JSI.

those originating from different down-conversion events. A typical setup involves two fast photodetectors connected to a digital time-tagger. At modest intensities, a pair of clicks that arrive at detectors within a short time interval, typically on the order of a nanosecond, are overwhelmingly likely to belong to a single biphoton.

2

Two-photon measurements of relative delay using Gaussian time-frequency states

2.1 Introduction

This chapter examines the theoretical precision bounds governing measurement of optical delays using photon pairs. A common example of a two-photon measurement of delay uses the shift in a Hong-Ou-Mandel interferometer as the readout. Focus therefore turns to the precision limits specific to such a measurement, and the conditions under which Hong-Ou-Mandel interference can optimally extract the delay information encoded in the state. Much of this chapter is based on the author's paper [96].

2.2 Two-photon measurements of delay

Measurements of delay are fundamental to many metrological and technological tasks. Optical delays can be used to infer material properties such as refractive index [97] and birefringence [98, 99]. Delay measurements play an important role in technologies such as optical ranging [100], clock synchronization [101], and optical coherence tomography [102]. They can also be used to answer fundamental questions

in quantum optics, for instance in measurements of quantum tunneling times [67] and of the gain-induced group delay in parametric down-conversion [103].

Traditional methods of obtaining quantum-enhanced delay measurements rely on increasing interferometric phase-sensitivity through the use nonclassical techniques such as N00N state interference or quadrature squeezing. In the case of negligible losses, these techniques provide Heisenberg limited scaling with the number of probe photons [33]. Nevertheless, these techniques have seen limited use in practice. One reason for this is the fragility of these measurements in situations with significant losses. Another drawback comes from the same enhanced phase sensitivity that makes these measurements theoretically appealing. In order to measure a phase shift, it is necessary that the interferometer be kept phase stable to within a fraction of an oscillation. In the case of N00N states, the period of oscillation is made smaller by a factor of N, which places much more stringent conditions on the necessary stabilization [33]. Quadrature squeezing does not change the oscillation period, but a reduction in noise occurs only over a small range of phases, which again requires stringent stabilization techniques [104].

Hong-Ou-Mandel (HOM) interference, by comparison, does not offer Heisenberg limited phase scaling. In fact, its precision in delay measurements is comparable to that of a classical interferometer utilizing a similar number of probe photons. Despite this, HOM interference has become the technique of choice in many recent experiments, including real-time measurements of delay [105] and scan-free profilometry [106]. The reason for this is due to technical advantages offered by HOM interference. First, the interference pattern is largely phase-insensitive, so that stabilization is usually unnecessary. In common experimental setups, the interferogram is also insensitive to all even orders of dispersion in either arm [10, 11]. As a result, measured changes in the interferogram can be attributed almost entirely to the group delay of interest, with third-order dispersion being the most common source of error. This makes it suitable for use in environments with relatively high amounts of dispersion, such as in fiber. Also, since HOM interference relies on coincidence measurements, the measurement is relatively insensitive to background light. Chapter 5, for instance, shows how the tight correlations between photon pairs can be used for significant noise reduction. Furthermore, broadband optical losses affect the measured interference pattern only through a

reduction in intensity, rather than interference visibility. HOM interferometry therefore avoids many of the experimental challenges associated with frequency-stabilized measurements and possesses useful features that make it more feasible than many other low-light methods.

Section 2.3 begins by considering the general precision limits applying to any measurement of relative delay which arise from the quantum theory of parameter estimation. It also examines the effect that an unknown mean delay has for the achievable precision of relative delay measurements. Section 2.4 then turns to the particular measurement scheme which infers relative delay from the HOM interferogram. For simplicity, it focuses on an approximation to the two-photon state in which the spectro-temporal properties are described by a Gaussian distribution. It considers the scenarios under which the HOM measurement saturates the quantum Cramér-Rao bound, indicating that the measurement efficiently extracts all delay information available in the two-photon state. A brief discussion of the role of detector time resolution is given in Appendix A.

2.3 Quantum limits to timing resolution

This section examines the precision limits arising from the quantum Cramér-Rao bound. We consider a probe state in which two photons are prepared in orthogonal spatial modes with arbitrary spectro-temporal properties. Taking $a_1^\dagger(\omega)$ and $a_2^\dagger(\omega)$ to be creation operators that add a photon with frequency ω into respective spatial modes labeled 1 and 2. We suppose that the probe is initialized in an arbitrary two-photon pure state, which has the form [95]

$$|\psi_0\rangle = \iint d\omega_1\, d\omega_2\, \phi_0(\omega_1, \omega_2)\, a_1^\dagger(\omega_1) a_2^\dagger(\omega_2)\, |0\rangle\,. \tag{2.1}$$

The complex function $\phi_0(\omega_1, \omega_2)$ is called the *joint spectral amplitude* (JSA) of the state, and completely describes the spectral and temporal properties of the state. The squared quantity $|\phi_0(\omega_1, \omega_2)|^2$ is called

the *joint spectral intensity* (JSI). We require that

$$\iint d\omega_1\, d\omega_2\, |\phi_0(\omega_1, \omega_2)|^2 = 1 \tag{2.2}$$

so that $|\psi_0\rangle$ is normalized. The photon in each spatial mode is subject to respective delays τ_1 and τ_2 (see Figure 2.1), which can be described by a unitary evolution given by

$$\begin{aligned} U(\tau_1, \tau_2) &= \exp\left(-i\Omega_1\tau_1 - i\Omega_2\tau_2\right) \\ &= \exp\left(-i\Omega_+\tau_+ - i\Omega_-\tau_-\right). \end{aligned} \tag{2.3}$$

Here, $\tau_\pm = (\tau_1 \pm \tau_2)/2$ gives the mean and relative delays of the two photons. The operator

$$\Omega_i = \int d\omega\, \omega\, a_i^\dagger(\omega) a_i(\omega) \tag{2.4}$$

generate the delays τ_i, and $\Omega_\pm = \Omega_1 \pm \Omega_2$ are the generators of $\tau_\pm$. The effect of this unitary is to transform the probe's state from $|\psi_0\rangle$ into the state

$$|\psi(\tau_1, \tau_2)\rangle = U(\tau_1, \tau_2)\,|\psi_0\rangle = \iint d\omega_1\, d\omega_2\, \phi(\omega_1, \omega_2; \tau_1, \tau_2)\, a_1^\dagger(\omega_1) a_2^\dagger(\omega_2)\,|0\rangle\,, \tag{2.5}$$

where

$$\phi(\omega_1, \omega_2; \tau_1, \tau_2) = \phi_0(\omega_1, \omega_2) e^{-i\omega_1\tau_1 - i\omega_2\tau_2}. \tag{2.6}$$

As discussed in Subsection 1.3.4, the quantum Fisher information for the parameters τ_1 and τ_2 are then determined by the generators and the initial probe state.

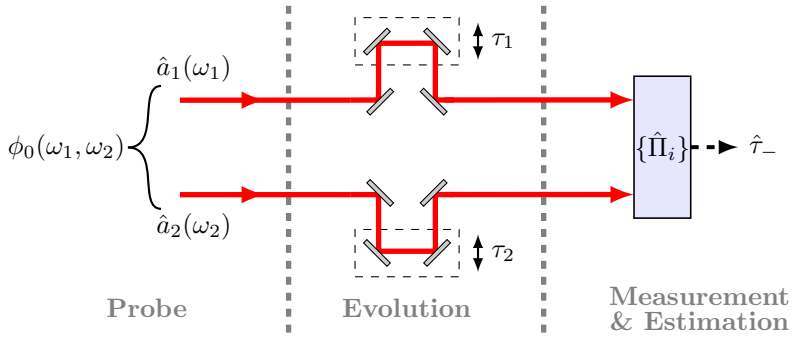

Figure 2.1: Schematic diagram of a two-photon measurement of delay. Incident photon pairs have a joint spectral amplitude $\phi_0(\omega_1, \omega_2)$. The two photons undergo separate variable delays. An arbitrary measurement is made, from which the delay values are estimated.

2.3.1 Estimation with a single unknown delay

For completeness, we first review the bounds that apply when a single delay is estimated. That is, we assume that the delay τ_2 is fixed from one measurement to the next, so that any change in the distribution of measurement outcomes can be fully attributed to changes in τ_1. This bound has been previously derived in [71]. We are then left with a single variable estimation problem, with the achievable precision taking the form

$$(\Delta\tau_1)^2 \geq \frac{1}{N\mathcal{Q}_{\tau_1}}, \tag{2.7}$$

where $(\Delta x)^2$ denotes the variance of x, $\mathcal{Q}_{\tau_1}$ is the corresponding quantum Fisher information for a single trial, and N independent trials are conducted. From (1.53), we have

$$\mathcal{Q}_{\tau_1} = 4\langle\Omega_1^2\rangle_0 - 4\langle\Omega_1\rangle_0^2 = 4(\Delta\omega_1)^2, \tag{2.8}$$

where $\langle\cdot\rangle_0$ denotes an expectation value calculated for the initial probe state $|\psi_0\rangle$. Here, $(\Delta\omega_1)^2$ denotes the variance of the marginal distribution for ω_1,

$$(\Delta\omega_1)^2 \equiv \iint d\omega_1\, d\omega_2\, |\phi_0(\omega_1,\omega_2)|^2\, \omega_1^2 - \left[\iint d\omega_1\, d\omega_2\, |\phi_0(\omega_1,\omega_2)|^2\, \omega_1\right]^2. \tag{2.9}$$

This result can be written in the form of a Heisenberg-like inequality,

$$\Delta\tau_1 \Delta\omega_1 \geq \frac{1}{2}. \tag{2.10}$$

In this case the achievable precision is determined entirely by the spectral properties of the photon in the first spatial mode, and the second photon plays no role.

2.3.2 Estimation with two unknown delays

We now turn to the situation in which both delays τ_1 and τ_2 are unknown. This is the case, for example, in clock synchronization protocols in which an intermediary which sends a single photon to each of two parties. In this case the probability distribution describing the measurement outcomes is parameterized by two unknown parameters, although only one of them is of practical interest.

The quantum Cramér-Rao bound on the precision takes the form of the matrix inequality (1.59). The diagonal elements of this inequality can be written in the form

$$(\Delta\tau_i)^2 \geq \frac{1}{N\mathcal{Q}_{\text{eff}}^{(i)}}, \tag{2.11}$$

where

$$\mathcal{Q}_{\text{eff}}^{(i)} \equiv \frac{1}{(\boldsymbol{\mathcal{Q}}^{-1})_{ii}}, \tag{2.12}$$

with $\boldsymbol{\mathcal{Q}}$ denoting the quantum Fisher information matrix. The quantities $\boldsymbol{\mathcal{Q}}_{\text{eff}}^{(i)}$ bounds the variance in a

similar manner to the single parameter quantum Fisher information. Explicitly, using the fact that the matrix $\boldsymbol{\mathcal{Q}}$ is symmetric, we have

$$\mathcal{Q}_{\text{eff}}^{(1)} = \boldsymbol{\mathcal{Q}}_{11} - \frac{(\boldsymbol{\mathcal{Q}}_{12})^2}{\boldsymbol{\mathcal{Q}}_{22}}, \qquad \mathcal{Q}_{\text{eff}}^{(2)} = \boldsymbol{\mathcal{Q}}_{22} - \frac{(\boldsymbol{\mathcal{Q}}_{12})^2}{\boldsymbol{\mathcal{Q}}_{11}}. \tag{2.13}$$

A similar relationship holds if we instead parameterize by the mean and relative delays $\tau_{\pm}$. The diagonal elements $\boldsymbol{\mathcal{Q}}_{ii} > 0$ are just the single parameter quantum Fisher information. The presence of an additional unknown parameter reduces the information available about any individual parameter, except in the case that the off-diagonal elements $\boldsymbol{\mathcal{Q}}_{12}$ vanish. This is a general property of the quantum Fisher information matrix than can be proven for the any n-parameter estimation problem.

Note that the commutator of the generators vanishes,

$$[\Omega_1, \Omega_2] = 0, \qquad [\Omega_+, \Omega_-] = 0, \tag{2.14}$$

as a result of the orthogonality of the two spatial modes. As mentioned in Subsection 1.3.4, it follows that the quantum Cramér-Rao bound is a tight bound on the variance; that is, a measurement exists that saturates the bound. We may therefore interpret $\mathcal{Q}_{\text{eff}}^{(i)}$ as being the amount of information about τ_i contained in the probe state.

A calculation analogous to the one leading to (1.53) shows that the quantum Fisher information matrix for a probe prepared in a pure state $|\psi_0\rangle$ undergoing unitary evolution has the elements

$$\boldsymbol{\mathcal{Q}}_{ij} = 2\langle\{h_i, h_j\}\rangle_0 - 4\langle h_i\rangle_0\langle h_j\rangle_0, \tag{2.15}$$

where h_i is the generator corresponding to the i^{th} parameter, $\{\cdot, \cdot\}$ denotes the anticommutator, and $\langle\cdot\rangle_0$ denotes the expectation value calculated for the initial probe state. For the state and evolution defined

above, the QFI matrix for the parameters $\tau_\pm$ has the elements

$$\boldsymbol{\mathcal{Q}}_{++} = 4(\Delta\omega_1)^2 + 4(\Delta\omega_2)^2 + 8C, \tag{2.16a}$$

$$\boldsymbol{\mathcal{Q}}_{--} = 4(\Delta\omega_1)^2 + 4(\Delta\omega_2)^2 - 8C, \tag{2.16b}$$

$$\boldsymbol{\mathcal{Q}}_{+-} = \boldsymbol{\mathcal{Q}}_{-+} = 4(\Delta\omega_1)^2 - 4(\Delta\omega_2). \tag{2.16c}$$

Here $(\Delta\omega_i)^2$ again refers to the variance of the marginal distribution for parameter ω_j, obtained after integrating out one variable from $|\phi_0(\omega_1, \omega_2)|^2$. The parameter C is defined as

$$C = \langle \Omega_1 \Omega_2 \rangle_0 - \langle \Omega_1 \rangle_0 \langle \Omega_2 \rangle_0, \tag{2.17}$$

and quantifies the correlations between frequencies ω_1 and ω_2 for the distribution $|\phi_0(\omega_1, \omega_2)|^2$. Note that the off-diagonal element $\boldsymbol{\mathcal{Q}}_{+-}$ vanishes only when the probe state has equal bandwidths in both arms. In this case, estimation of τ_- and τ_+ can be regarded as separate problems, and the quantum Cramér-Rao bound for either parameter is given by the corresponding single parameter QFI. In any case, the effective QFI determining the precision bound is given by

$$\mathcal{Q}_{\text{eff}}^{(\pm)} = \frac{(\Delta\omega_1)^2(\Delta\omega_2)^2 - C^2}{(\Delta\omega_1)^2 + (\Delta\omega_2)^2 \mp 2C}. \tag{2.18}$$

For fixed bandwidths $\Delta\omega_1$ and $\Delta\omega_2$, the maximum value of $\mathcal{Q}_{\text{eff}}^{\pm}$ occurs for $C = \pm\min\left[(\Delta\omega_1)^2, (\Delta\omega_2)^2\right]$, in which case the quantum Cramér-Rao bound takes the form

$$\Delta\tau_\pm \geq \frac{1}{4\sqrt{N}} \max\left[(\Delta\omega_1)^{-1}, (\Delta\omega_2)^{-1}\right]. \tag{2.19}$$

The precision bound is always limited by the smaller of the two photon bandwidths. The factor of two difference between this bound and the bound (2.10) is due to the factor of two in the definition of $\tau_\pm$, so that the mean and relative delays are always bounded by the stricter of the two Heisenberg-like bounds

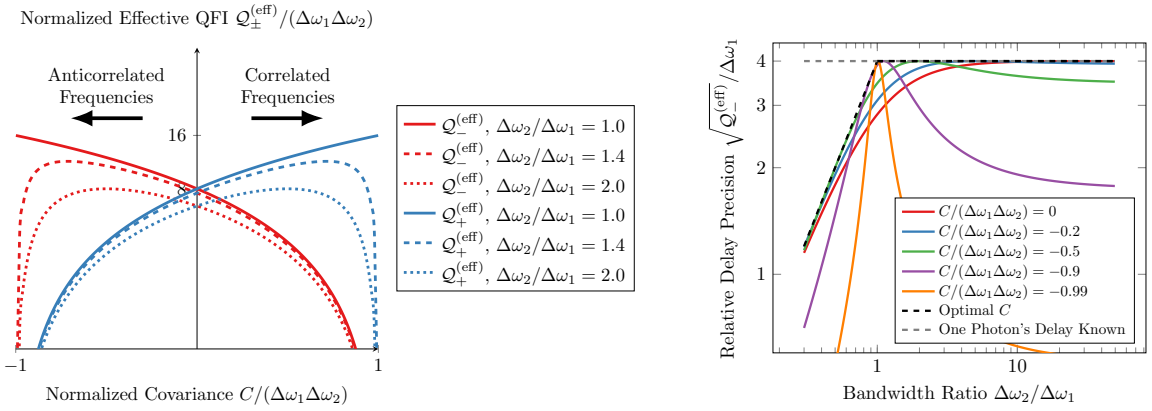

Figure 2.2: (a) The effective quantum Fisher information for estimation of relative (τ_-) and mean (τ_+) delays. (b) The effective quantum Fisher information for estimation of τ_-, normalized to the bandwidth of one photon.

$\Delta\tau_i \geq 1/2\Delta\omega_i$. Estimation of the delays $\tau_\pm$ is more challenging than estimation of either of the two delays τ_1 or τ_2. Not only are $\tau_\pm$ limited by the bandwidths of each arm, but optimal estimation of these delays requires that the frequency correlations be tuned to obtain the optimal value of C. By comparison, in simultaneous estimation of τ_1 and τ_2 the off-diagonal element $\boldsymbol{\mathcal{Q}}_{12}$ is proportional to C, so that the precision bound is optimal whenever the frequencies of the photons are uncorrelated.

The effective QFI values for estimation of $\tau_\pm$ are plotted in Figure 2.2(a), normalized to the product of the bandwidths $\Delta\omega_1\,\Delta\omega_2$. The correlation parameter $C/(\Delta\omega_1\Delta\omega_2)$ is normalized to the range $[-1, 1]$, with a value of $+1$ signifying complete correlation and a value of -1 corresponding to complete anticorrelation. It is seen that correlated frequencies are best for estimation of the mean delay, while anticorrelated frequencies are best for estimation of the relative delay.

We now consider estimation of the relative delay τ_-. Many sources of photon pairs used in practice, in particular cw-pumped SPDC, naturally produce photons with highly anticorrelated frequencies. It is evident from the plot that in this case, the achievable precision in estimating τ_- is highly dependent on the bandwidth mismatch between the two photons; in the ideal scenario of perfect frequency anticorrelations,

$\mathcal{Q}_{\text{eff}}^{(-)}$ vanishes unless $\Delta\omega_1 = \Delta\omega_2$. This statement is not a consequence of any particular measurement scheme, but is due to the nature of the probe state itself. By comparison, while uncorrelated photon frequencies are not optimal for either delay $\tau_\pm$, they are also much less sensitive to any mismatch in the photon bandwidths.

Figure 2.2(b) considers the case where one of the photons (here the photon with frequency ω_1) has a fixed bandwidth, while the other photon's bandwidth is allowed to vary. The optimal precision for τ_- is the same as the precision bound for estimation of τ_1 alone whenever $\Delta\omega_2 \geq \Delta\omega_1$, in which case the precision is limited solely by $\Delta\omega_1$. By considering different values of the correlation coefficient, one sees that this optimal bound is achievable regardless of the amount of frequency correlations in the probe state. However, as the frequency correlations decrease, the necessary bandwidth $\Delta\omega_2$ increases, so that in this constrained situation anticorrelated frequencies are still preferable as they allow for precise estimation without a large bandwidth $\Delta\omega_2$. Note that this figure is plotted on a log-log axis, so that the precision bound has a slow variation with $\Delta\omega_2/\Delta\omega_1$.

2.4 Timing measurements based on two-photon interference

We now turn to the specific case of estimation of τ_- using a Hong-Ou-Mandel interferometer. For simplicity, we consider the case of time- and frequency-non-resolving detectors; the case of frequency-resolved has been addressed in [107]. The detection scheme is illustrated in Figure 2.3. The beamsplitter mixes the two spatial modes, performing the transformation

$$a_1^\dagger(\omega) \to \sqrt{\eta}a_1^\dagger(\omega) + i\sqrt{1-\eta}a_2^\dagger(\omega), \tag{2.20a}$$

$$a_2^\dagger(\omega) \to i\sqrt{1-\eta}a_2^\dagger(\omega) + \sqrt{\eta}a_1^\dagger(\omega), \tag{2.20b}$$

where η is the reflection coefficient of the beamsplitter, assumed here to be frequency-independent. Note that the phase convention used here differs from that in Section 1.2; one can verify that this convention

also satisfies the necessary commutation relations. After the beamsplitter, the state of the photon pair is

$$|\psi(\tau_1,\tau_2)\rangle = i\sqrt{\eta(1-\eta)}\,|\psi_{11}(\tau_1,\tau_2)\rangle + i\sqrt{\eta(1-\eta)}\,|\psi_{22}(\tau_1,\tau_2)\rangle + |\psi_{12}(\tau_1,\tau_2)\rangle\,, \tag{2.21}$$

where we have defined the (not necessarily normalized) state vectors

$$|\psi_{ii}(\tau_1,\tau_2)\rangle = \iint d\omega_1\, d\omega_2\, \phi(\omega_1,\omega_2;\tau_1,\tau_2)\, a_i^\dagger(\omega_1)a_i^\dagger(\omega_2)\,|0\rangle\,, \tag{2.22a}$$

$$|\psi_{12}(\tau_1,\tau_2)\rangle = \iint d\omega_1\, d\omega_2\, \left[\eta\phi(\omega_1,\omega_2;\tau_1,\tau_2) - (1-\eta)\phi(\omega_2,\omega_1;\tau_1,\tau_2)\right]\, a_1^\dagger(\omega_1)a_2^\dagger(\omega_2)\,|0\rangle\,. \tag{2.22b}$$

The probability of detecting a coincidence is calculated using the projection operator

$$\Pi_{12} = \iint d\omega_1\, d\omega_2\, a_1^\dagger(\omega_1)a_2^\dagger(\omega_2)\,|0\rangle\,\langle 0|\, a_1(\omega_1)a_2(\omega_2). \tag{2.23}$$

The coincidence probability is found to be

$$\begin{aligned} P_c &\equiv \langle\psi(\tau_1,\tau_2)|\,\Pi_{12}\,|\psi(\tau_1,\tau_2)\rangle \\ &= \eta^2 + (1-\eta)^2 - 2\eta(1-\eta)\,\mathrm{Re}\iint d\omega_1\, d\omega_2\, \phi_0(\omega_1,\omega_2)\phi_0^*(\omega_2,\omega_1)e^{-2i(\omega_1-\omega_2)\tau_-}. \end{aligned} \tag{2.24}$$

The final term can be viewed as an inner product between the joint spectral amplitude $\phi_0(\omega_1,\omega_2)e^{i(\omega_2-\omega_1)\tau_-}$ and its transpose, obtained by interchanging ω_1 and ω_2. Since the JSA is normalized, this overlap integral has a maximum value of unity, so that the final term is bounded in magnitude by $2\eta(1-\eta)$. Only this term is sensitive to delays; the optimal interference visibility occurs for $\eta = 1/2$ (*i.e.*, a 50:50 beamsplitter), which we shall assume in the rest of the analysis. At $\tau_- \to 0$, the interference visibility V, defined so that

$$P_c|_{\tau=0} = (1-V)P_c|_{\tau\to\infty}, \tag{2.25}$$

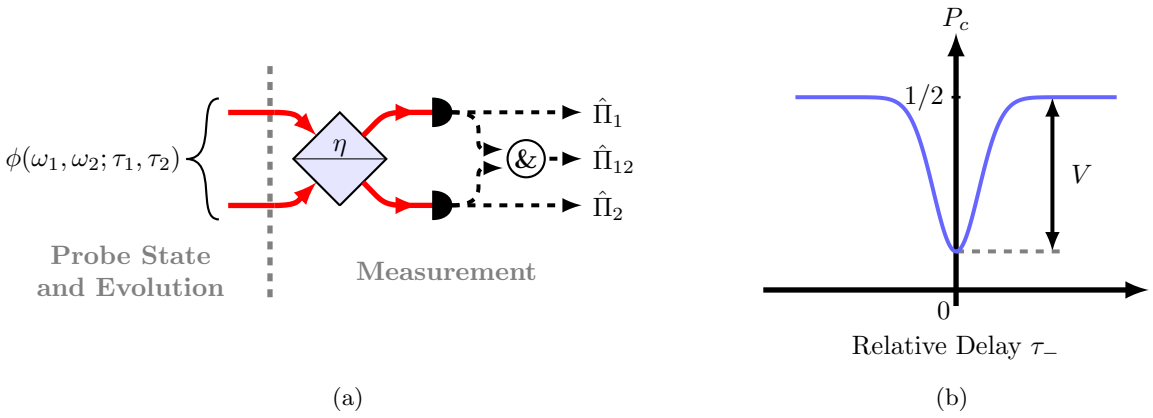

Figure 2.3: (a) Measurement of relative delay using a Hong-Ou-Mandel interferometer. After encoding the delays (Figure 2.1), the two photons interfere at a beamsplitter. The coincidence rate is used to estimate the unknown delay τ_-. (b) The HOM dip measured for a biphoton with a Gaussian joint spectral amplitude.

is

$$V = \iint d\omega_1 \, d\omega_2 \, \phi_0(\omega_1, \omega_2) \phi_0^*(\omega_2, \omega_1), \tag{2.26}$$

which is just the overlap integral of the incident JSA $\phi_0(\omega_1, \omega_2)$ and its transpose. Since ϕ_0 is normalized to unity, the Cauchy-Schwarz inequality shows that $V = 1$ only when the state is symmetric, $\phi_0(\omega_1, \omega_2) = \phi_0(\omega_2, \omega_1)$. Note that the restriction to $\tau_- = 0$ does not place any fundamental restrictions on the analysis, since any finite relative delay can be included in the definition of ϕ_0.

In the model developed so far, the Hong-Ou-Mandel interference pattern appears in the probability of a coincidence detection, and a complementary interference pattern appears in the probability of measuring no coincidence (*i.e.*, a single detector clicks). In practice, the exact number of pairs sent into the interferometer is not known in advance. At the same time, losses in the interferometer mean that the exact intensity correlations between the two arms is degraded, so that a single detector click does not necessarily correspond to a photon pair that has bunched at the beamsplitter. Typically, the Hong-Ou-Mandel interferogram is measured only from a change in the rate of observed coincidences, which arrive

stochastically at the detectors (an example of an experiment which can detect the rate of both bunched and "antibunched" pairs appears in Chapter 3). If an estimate of τ_- is made from both the coincidence probability P_c and from the probability of no coincidence $1 - P_c$, then the classical Fisher information per input pair takes the form

$$\begin{aligned}\mathcal{F}_{\tau_-} &= \frac{1}{P_c}\left(\frac{\partial P_c}{\partial \tau_-}\right)^2 + \frac{1}{1-P_c}\left(\frac{\partial (1-P_c)}{\partial \tau_-}\right)^2 \\ &= \frac{1}{P_c(1-P_c)}\left(\frac{\partial P_c}{\partial \tau_-}\right)^2 .\end{aligned} \tag{2.27}$$

Including the probability $1 - P_c$ in the CFI overestimates the precision that is possible for measurements which record only the rate of coincidence detections. This can be made rigorous if we assume that pairs arrive at the beamsplitter with a mean rate R, so that the rate of coincidences is RP_c. Supposing that coincidence detections are distributed in time according to a Poisson distribution, the CFI should be calculated from the distribution of coincidences which are detected in a fixed time interval. In this case, one can show that the CFI takes the form

$$\frac{1}{RP_c}\left(\frac{\partial RP_c}{\partial \tau_-}\right)^2 = \frac{R}{P_c}\left(\frac{\partial P_c}{\partial \tau_-}\right)^2 , \tag{2.28}$$

assuming that the mean rate R does not depend on the delay. The information per photon pair is then

$$\mathcal{F}_{\tau_-} = \frac{1}{P_c}\left(\frac{\partial P_c}{\partial \tau_-}\right)^2 , \tag{2.29}$$

which is what one would get if the second term in (2.27), corresponding to a no-coincidence detection, were neglected. This is the expression for the CFI used in some other analyses of the Hong-Ou-Mandel interferometer [108].

Based on the expression (2.29), two aspects of the probability P_c contribute to maximizing the CFI for a given probe state. The first is that $P \to 0$ as $\tau_- \to 0$. The second is that the derivative $\partial P_c/\partial \tau_-$ is large. The first condition is met when $V \to 1$, which occurs when $\phi_0(\omega_1, \omega_2)$ has a high overlap with its

transpose $\phi_0(\omega_2, \omega_1)$. In the limit that $\tau_- \to 0$ with $V \to 1$, the CFI takes the form

$$\mathcal{F}_{\tau_-} = 4 \iint d\omega_1 \, d\omega_2 \, (\omega_1 - \omega_2)^2 \, \phi_0(\omega_1, \omega_2) \phi_0^*(\omega_2, \omega_1). \tag{2.30}$$

Recalling that $\phi_0(\omega_1, \omega_2) \propto \phi_0(\omega_2, \omega_1)$ whenever $V \to 1$, this is just the average of the squared frequency difference $(\omega_1 - \omega_2)^2$. We see that a large CFI requires that $|\omega_1 - \omega_2|$ is large, so that the state should have strong frequency anticorrelations.

2.4.1 States with Gaussian joint spectral amplitudes

We now focus on a specific class of JSAs that approximate the states created in practice. These are the states which have a JSA that is a two-dimensional Gaussian distribution. More specifically, we assume that the JSA takes the form

$$\phi_0(\omega_1, \omega_2) = N \exp\left[-\frac{1}{4} \sum_{i,j=1}^{2} (\omega_i - \overline{\omega}_i)(\mathbf{\Sigma}^{-1})_{ij} (\omega_j - \overline{\omega}_j) \right]. \tag{2.31}$$

Here, $\overline{\omega}_i$ is the mean of the marginal distribution for ω_i,

$$\mathbf{\Sigma} = \begin{pmatrix} (\Delta\omega_1)^2 & C \\ C & (\Delta\omega_2)^2 \end{pmatrix} \tag{2.32}$$

is the covariance matrix, and $N = (2\pi\sqrt{\det \mathbf{\Sigma}})^{-1/2}$ is a normalization constant. Most sources of photon pairs result in JSIs which possess sinc-like lobes in addition to a central peak; this Gaussian approximation serves to model the main peak while neglecting the smaller side lobes. States of this form result in a Gaussian Hong-Ou-Mandel dip,

$$P_c = \frac{1}{2} \left[1 - V \exp\left(-\frac{\tau_-^2}{2T^2} \right) \right], \tag{2.33}$$

which has a width

$$T = \frac{1}{4}\sqrt{\frac{(\Delta\omega_1)^2 + (\Delta\omega_2)^2 + 2C}{(\Delta\omega_1)^2(\Delta\omega_2)^2 - C^2}} \tag{2.34}$$

and a visibility

$$V = 2\sqrt{\frac{(\Delta\omega_1)^2(\Delta\omega_2)^2 - C^2}{\left[(\Delta\omega_1)^2 + (\Delta\omega_2)^2\right]^2 - 4C^2}} \exp\left(-\frac{(\overline{\omega}_1 - \overline{\omega}_2)^2}{2\left[(\Delta\omega_1)^2 + (\Delta\omega_2)^2 - 2C\right]}\right). \tag{2.35}$$

The center frequencies play a role only in determining the interference visibility; optimal visibility requires that the mean frequencies are equal, $\overline{\omega}_1 = \overline{\omega}_2$. The bandwidths $\Delta\omega_i$ and the frequency covariance C affect both the visibility and the width T of the interferogram. The visibility is maximal ($V = 1$) whenever $\Delta\omega_1 = \Delta\omega_2$ and $\overline{\omega}_1 = \overline{\omega}_2$, regardless of C; as discussed earlier, this is due to the fact that such a JSA is symmetric for any choice of C. In this case, $T \propto [(\Delta\omega)^2 - C]^{-1/2}$, so that anticorrelated frequencies produce a minimum width of $T = 1/4\Delta\omega$, and correlated frequencies can produce arbitrarily large values of T.

The CFI calculated from (2.29) (*i.e.*, neglecting no-coincidence outcomes) is

$$\mathcal{F}_{\tau_-} = \frac{1}{T^2}\left[\frac{\tau_-^2}{2T^2}\frac{(Ve^{-\tau_-^2/2T^2})^2}{1 - Ve^{-\tau_-^2/2T^2}}\right]. \tag{2.36}$$

Since the CFI is calculated from the functional form of P_c, this expression holds for any Gaussian-shaped HOM dip, regardless of the physical mechanism determining the finite visibility V and width T. By comparison, the CFI including bunching outcomes (calculated using (2.27)) is

$$\widetilde{\mathcal{F}}_{\tau_-} = \frac{1}{T^2}\left[\frac{\tau_-^2}{2T^2}\frac{(Ve^{-\tau_-^2/2T^2})^2}{\left(1 - Ve^{-\tau_-^2/2T^2}\right)^2}\right]. \tag{2.37}$$

This functional form is similar to the one used in [109], which used both the rate of coincidences and the rate of single clicks to estimate the delay. In this case, the finite visibility was due primarily to a

polarization mismatch between the photons. Due to optical losses in this experiment, the CFI due to the coincidence rate exceeded that due to the singles rate by a factor of ~ 30, which justifies our neglect of the second term in (2.29).

The effective QFI governing estimation of τ_- is, from (2.18),

$$\mathcal{Q}_{\tau_-} = \frac{(\Delta\omega_1)^2(\Delta\omega_2)^2 - C^2}{(\Delta\omega_1)^2 + (\Delta\omega_2)^2 + 2C^2} = \frac{1}{T^2}. \tag{2.38}$$

The HOM measurement saturates the quantum Cramér-Rao bound whenever the term in brackets in (2.36) approaches one. This occurs only when $V \to 1$ and $\tau_- \to 0$. For finite V, the optimal value of the CFI is achieved for a pair of τ_- values displaced equally in the positive and negative directions from zero, which can be obtained numerically, as discussed in [109].

2.4.2 Delay estimation when one bandwidth is constrained

We now consider the problem of optimizing the estimation of τ_- when the bandwidth $\Delta\omega_1$ is constrained to lie below some value. This occurs when one photon must traverse a channel that is transparent only over some spectral window, as would occur in measurements of the group delay induced by a material sample or in clock synchronization where the channel connecting the source to one party has a finite transmission. One is then left with the task of optimizing the spectral properties of the other photon, as well as the frequency correlations, to maximize the measurement precision. Since the maximum precision is bounded by the smaller of the two bandwidths, we assume that $\Delta\omega_1$ takes on its maximum value, and furthermore assume that $\overline{\omega}_1 = \overline{\omega}_2$. We then consider the optimal precision as a function of $\Delta\omega_2$ and C.

Figure 2.4(a) shows a numerical evaluation of the CFI, normalized to the fixed value of $\Delta\omega_1$, for different values of $\Delta\omega_2$ and C. At each point, the CFI is calculated for the value of τ_- which maximizes the measurement precision. The maximum precision occurs when $\Delta\omega_1 = \Delta\omega_2$. In this case, the optimal precision occurs for maximally anticorrelated states, $C \to -1$, which are produced naturally by most sources. When the bandwidths are not equal, highly anticorrelated states rapidly lose their precision,

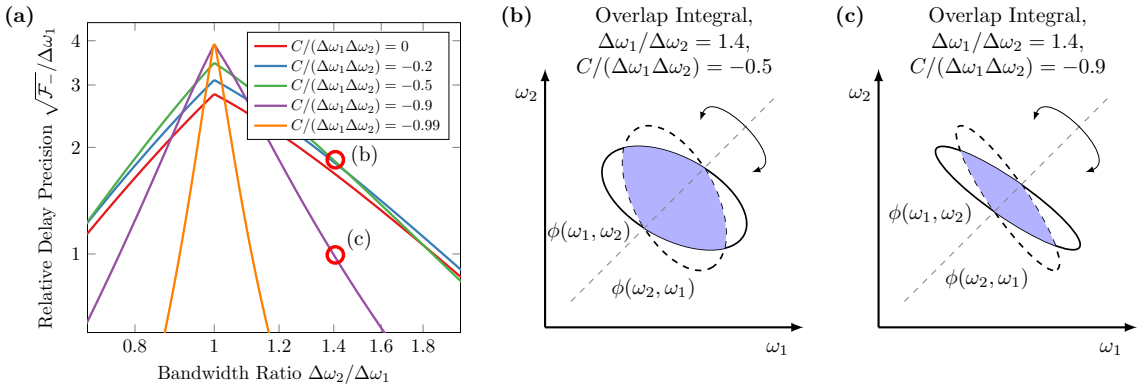

Figure 2.4: (a) The classical Fisher information for measurement of the relative delay τ_-, normalized to the bandwidth of one photon (compare Figure 2.2(b)). Circles mark the state parameters used in (b) and (c). (b) and (c) Overlap of the initial and transposed joint spectral amplitudes when the photons have unequal bandwidths. The overlap is greater when the frequency anticorrelations are weaker (b) than it is when the anticorrelations are stronger (c).

whereas less correlated states lose sensitivity more gradually. This can be explained by considering the interference visibility, which is given by the overlap integral of $\phi_0(\omega_1, \omega_2)$ and its transpose $\phi_0(\omega_2, \omega_1)$. Figures 2.4(b) and 2.4(c) depicts the covariance ellipses for two points with $\Delta\omega_2 = 1.4\Delta\omega_1$ but different values of C, as well as the ellipse for the transposed states. When the bandwidths are not equal, the ellipse is at an oblique angle relative to the diagonal, so that the state no longer completely overlaps with its transpose. As a result, the interference visibility is decreased. Reducing the frequency correlations for a given pair of bandwidths tends to broaden the covariance ellipse, which in turn results in a smaller change to the visibility.

Comparing Figure 2.4(a) to the quantum bound (Figure 2.2(b)), we see that the CFI saturates the bound ($\sqrt{\mathcal{F}_{\tau_-}} = 4\Delta\omega_1$) only when $\Delta\omega_1 = \Delta\omega_2$. The quantum bound shows a similar trade-off in which highly correlated states are more sensitive to bandwidth mismatch; however, in the general case this cannot be attributed to any interference visibility, and is a consequence of the choice of probe state itself. As well, the horizontal axes in Figures 2.2(b) and 2.4(a) have largely different scales, so that the HOM measurement degrades more quickly for $\Delta\omega_2 \neq \Delta\omega_1$ than is required by the general bounds.

2.4.3 The role of mean delay sensitivity in estimation of the relative delay

Interestingly, despite the fact that the HOM measurement as described is entirely insensitive to τ_+, the ultimate measurement precision is bounded not only by the single-parameter quantum Cramér-Rao bound determined by (2.7), but also by the stricter multiparameter bound for estimates of both τ_+ and τ_-. This can be understood as follows: the measurement probabilities P_c are the same regardless of whether the probe state is parameterized by a single delay or by two delays. Consequently, the CFI, which depends only on the probability distribution of the measured outcomes, must have the same value for both the single-parameter and multiparameter problems. It follows that $\mathcal{F}_{\tau_-}$ is bounded by both the single parameter QFI ($\boldsymbol{\mathcal{Q}}_{--}$ in (2.16)) and the multiparameter effective QFI $\mathcal{Q}_{\text{eff}}^{(-)}$. This illustrates a general property by which the maximum precision of a measurement is determined not only by those parameters which it is sensitive to, but also by those which it is entirely *insensitive* to. This is ultimately a consequence of the nonzero off-diagonal components of $\boldsymbol{\mathcal{Q}}$, which makes the multiparameter matrix bound stricter than the single parameter bound. Any two-photon measurement of the relative delay which is insensitive to τ_+ can be expected to follow the stricter bound $\mathcal{Q}_{\text{eff}}^{(-)}$.

One may argue that a Hong-Ou-Mandel interferometer in fact is sensitive to the mean time delay τ_+; any photodetector is capable of resolving time-of-arrival to some extent, even if this resolution is far worse than the time resolution of an optical interferometer. Appendix A discusses a more elaborate model which includes a poor, but finite, detector time resolution. In this context, one finds that as the detector's response time becomes large relative to the biphoton coherence time, the multiparameter information for estimation of τ_- approaches (2.29), plus corrections which vanish in the limit of a long detector response time. This confirms the intuition that a poor detector time response is essentially negligible in determining the metrological performance of a Hong-Ou-Mandel interferometer.

2.5 Conclusion

Our analysis has considered the theoretical measurement limits governing the estimation of the time delays affecting a photon pair. In general, this involves estimation of two unknown delays, τ_1 and τ_2 or τ_- and τ_+. In many laboratory experiments the only variable delay is that of a single photon, say τ_1. Any variation in measured signals may be attributed entirely to changes in τ_1, whose precision is then limited by the inverse of the same photon's bandwidth (*i.e.*, to the coherence time of the photon being delayed).

Variations in both delays occurs when the source and detectors are each located in different laboratories. This situation arises in clock synchronization protocols based on distribution of a photon pair [101]. Similar considerations also apply to measurement-device-independent quantum key distribution [110] if the same photon pairs used for key distribution are also used to stabilize the relative pulse delay. In this case, we show that the achievable precision of τ_- is limited by the smaller of the two photon bandwidths. With one bandwidth $\Delta\omega_1$ fixed, maximizing the other bandwidth is not always optimal, however. The optimal value of $\Delta\omega_2$ then depends on the amount of frequency correlation between the two photons. For equal bandwidths, maximal frequency anticorrelations yield the most information about τ_-. Highly anticorrelated frequencies also lead to a very rapid deterioration in τ_--precision when the bandwidths are not equal, which can be attributed to a strong correlation between estimates of τ_- and τ_+, with the probe state being highly insensitive to the latter.

A similar behaviour occurs in Hong-Ou-Mandel-based measurements of τ_-: highly anticorrelated frequencies are optimal when the photon bandwidths are equal, but the same anticorrelations also lead to a rapid deterioration in precision when one bandwidth differs slightly from the other. In this case, the deterioration can be understood in terms of the decreased overlap between the two spectral amplitudes leading to the interference, which tends to decrease the interference visibility (see Figure 2.4).

It is interesting to note that the effective multiparameter information for τ_- in the case of a general measurement also acts as an upper bound on the single-parameter information of a HOM measurement.

This feature can be understood as a consequence of the HOM interferometer's relative insensitivity to τ_+ as well as the interdependency of τ_+ and τ_- estimation for unequal bandwidths. As shown in Appendix A, the single-parameter and multiparameter estimation problems become identical when the detector time resolution, which determines τ_+-sensitivity, is much worse than the coherence time of the biphoton. Similar conclusions are expected to hold in other two-photon measurements of the relative delay.

It should be noted that the conclusions made about Hong-Ou-Mandel interference are based on a Gaussian approximation of the joint spectral amplitude, and so do not fully describe the behaviour of more structured frequency distributions. Another case of great practical interest involves a JSA which consists of two narrow but well-separated peaks; in this case it is the peak separation that determines the bandwidth of the state, and hence the overall timing precision. The metrological performance of such states is discussed in [71], and the phase sensitivity of a similar scheme is discussed in Chapter 4.

3

Quantum spectroscopy using Hong-Ou-Mandel interference

3.1 Introduction

The linear interaction between a material sample and light is characterized by two real-valued spectra. First, the absorption spectrum of the sample describes the change in intensity of the incoming beam at each frequency. Second, the phase spectrum (*i.e.*, the frequency-dependent phase imparted by the sample) relates the phase of a monochromatic incoming beam to the phase of the outgoing beam. Quantum-enhanced measurements of each quantity have been proposed. Classical absorption spectroscopy, whose quantum noise is determined by the intensity fluctuations of a classical beam of light (*e.g.*, one emitted from a laser), can be improved by preparing Fock states (photon-number eigenstates) of the field. Experimentally, one replaces the incident beam of a standard absorption spectrometer by one of the two beams emerging from a SPDC source — this beam, the probe beam, interacts with the sample, while the other beam, the herald, is directed to a reference photodetector. Photons in each arm are always created in pairs, so that the intensities of the probe and herald beam are (in principle, perfectly) correlated. Measurement of the herald beam allows one to gain knowledge about the particular intensity of the probe beam, beyond what is possible for unentangled, classical states of light, and hence reduce the uncertainty in the inferred absorption parameter. Quantum-enhanced measurements of absorption using heralded single photons [111]

have demonstrated reductions in noise of more than 30%.

Phase spectroscopy, on the other hand, can be enhanced through the use of entangled-state interferometry, for example using N00N states. In this form of interferometer, the probe state has the form $(|N,0\rangle + |0,N\rangle)/\sqrt{2}$, where $|a,b\rangle$ denotes a state with a photons in one interferometer arm and b photons in the other. A phase shift ϕ transforms this to a state $(e^{iN\phi}|N,0\rangle + |0,N\rangle)/\sqrt{2}$, which shows N times the phase shift of a single photon. The phase fringes of this measurement are then N times finer, leading to a reduction in phase uncertainty by a factor of N; this is an improvement over the $1/\sqrt{N}$-like scaling that one obtains by measuring the phase with an equal number of uncorrelated photons, as in the case of a classical interferometer.

Each method leads to a reduction in absorption or phase uncertainty, respectively, when one is limited to a fixed number of probe photons. This situation is increasingly important in measurements of photosensitive samples [112], which include materials of current interest such as perovskite crystals [113] and quantum dot emitters [114]. In many common systems (in particular, systems which do not involve cavities), absorption and phase are interrelated quantities: the Kramers-Kronig relations relate the phase shift at any frequency to the full absorption spectrum, and vice versa. This type of one-way inference of one parameter from the other has been studied by Gianani *et al.* [115]. In the context of spectroscopy, however, the end goal is usually not measurement of the absorption or phase profile of a sample; rather, one would like to infer some information about the electronic behaviour using properties such as the center frequency, linewidth, and oscillator strength of the various transitions. Thus, one should consider not the metrological estimation of the absorption or phase shifts for a fixed number of probe photons, but rather estimation of these electronic parameters. Information about resonance features is imprinted in both the absorption and phase spectra of a sample. It is reasonable therefore to ask which measurements are optimal for joint estimation of both absorption and phase. This problem is examined from the perspective of the theoretical precision bounds in Chapter 4.

The present chapter discusses an experimental demonstration of joint absorption and phase measurement using quantum-correlated photon pairs. The absorption measurement is performed in a manner simi-

lar to heralded-photon methods, while the phase measurement occurs via a frequency-entangled Hong-Ou-Mandel interferometer, of the type introduced in Subsection 1.2.3. We demonstrate through spectroscopic measurement of an absorbing dye that the heralding statistics and Hong-Ou-Mandel interferogram can be used for quantitative absorption and phase spectroscopy. As discussed in Chapter 4, this method provides per-probe-photon absorption information which is close to the quantum limit, while also providing shot noise-limited phase estimation. The additional phase information does not come at great expense to the absorption information, allowing this method to extract more information about the joint amplitude-and-phase response than existing methods. If one is concerned with estimation of a parameter which affects both the absorption and phase shift of a sample, then, this method may provide more information than even a quantum-optimal measurement of absorption alone.

Hong-Ou-Mandel interferometers of this type have been investigated in previous theoretical and experimental studies. Frequency-entangled HOM interferometers result in an interferogram containing a rapid oscillation [8], whose delay sensitivity is determined by the beat frequency of the two spectral components [71]. Photon pairs which are in a superposition of two widely-separated, narrow spectral lines can be for delay sensing at the scale of tens of attoseconds without requiring broadband transmission [71, 116]. In the context of spectroscopy, HOM interferometers have been proposed as a means of overcoming time-bandwidth limitations [77, 117] and as a method of separating different contributions to the spectroscopic signal [76]. Another approach relies on the low probe intensities of a typical HOM interferometer [118], which reduces the influence of probe-driven dynamics in nonlinear pump-probe spectroscopies. A phase-sensitive Hong-Ou-Mandel interferogram similar to the one discussed in this chapter is measured in Ref [119], who use the technique for single photon holography. The same authors suggest application of the method to low-flux spectroscopy. However, they do not consider the possibility of performing a simultaneous heralded absorption measurement, nor do they attempt to quantify the information content of the measurement. So far, there has been little investigation of Hong-Ou-Mandel spectroscopy from the perspective of quantum metrology. The work of the next two chapters demonstrates the great potential of such nonclassical interferometers in measurements of the spectral properties of photosensitive samples.

This chapter begins with a high-level description of the measurement technique in Section 3.2. Section 3.3 gives a more detailed description of the measurement apparatus. This is followed in Section 3.4 by a model of the interferometer, which allows us to relate the measured count rates to spectroscopic parameters of the sample. As we show, the phase profile can be estimated quite simply using the measured interferogram. When it comes to absorption, however, the problem is more complicated: the measured coincidence spectrum is necessarily symmetrized due to the indistinguishability of probe and herald photons, so that quantitative absorption estimation requires the use of calibration measurements. A workaround to this problem is presented in Section 3.5. Finally, the observed two-photon interferograms along with the measured absorption and phase spectra are discussed in Section 3.6.

3.2 Spectroscopic measurements of absorption and phase

A conceptual schematic of the measurement is shown in Figure 3.1. The probe state consists of two photons, where one photon is incident on a spectroscopic sample and the other travels through a reference arm. A measurement step (detailed below) counts the number of photons exiting the setup. The signal photon is either transmitted or absorbed; if it is transmitted, then two photons are detected, and if it is absorbed then a single photon is detected. If the setup has negligible optical loss apart from the sample, then this measurement can count the exact number of photons which were incident on the sample, as well as the exact number of photons which were absorbed. As described so far, this measurement is identical to a measurement of absorption with heralded single photons, which was shown in previous experiments to beat the shot noise limit.

The novelty of our work lies in our introduction of phase sensitivity to the measurement scheme in a manner that preserves much of the intensity correlations used for absorption measurements. It does this by incorporating a broadband two-photon interferometer before the detectors. Before discussing in detail this interferometer, it is useful to discuss a basic constraint on the possible probe states if this measurement is to be phase-sensitive. Let $|\omega_s\rangle_s$ denote a signal photon with frequency ω_s and $|\omega_h\rangle_h$ denote a herald

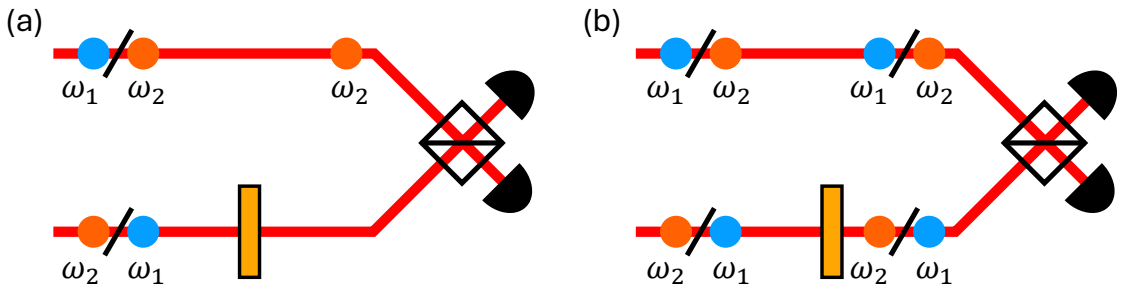

Figure 3.1: Schematic of the HOM-based measurement of absorption and phase. One photon from a frequency-entangled pair is incident on a sample. Absorption by the sample (a) is identified by a single detector click, with the detected frequency indicating the frequency of the absorbed photon. Transmitted photons (b) lead to two-photon interference, which is used to measure the phase shift.

photon with frequency ω_h. After transmission through the sample, the signal photon picks up a phase shift $\phi(\omega_s)$, resulting in the state $e^{i\phi(\omega_s)} |\omega_s\rangle_s$. If the probe and herald are prepared in a separable state, then the total state after transmission is $e^{i\phi(\omega_s)} |\omega_s\rangle_s |\omega_h\rangle_h$. The phase shift imparted by the sample appears as a global phase and so is not measurable. It follows that any phase-sensitive measurement using a heralded photon must use an entangled state. This is a consequence of the well-known adage that "a single photon has no phase". Considering a frequency-entangled state, the transmitted state will have the form

$$e^{i\phi(\omega_1)} |\omega_1\rangle_s |\omega_2\rangle_h + e^{i\phi(\omega_2)} |\omega_2\rangle_s |\omega_1\rangle_h . \tag{3.1}$$

The measurable (relative) phase is $\phi(\omega_1) - \phi(\omega_2)$; in any case, the phase measured using this scheme will be the relative phase corresponding to two possible values of some degree of freedom of the signal photon.

We use a frequency-entangled probe state, which allows for a measurement of $\phi(\omega_1) - \phi(\omega_2)$ through two photon interference. The absorption of the sample can be determined from the ratio of two-photon coincidence detections to single photon detections. For those pairs that are detected, the distribution of pairs between the two output ports of a beamsplitter provides a measurement of $\phi(\omega_1) - \phi(\omega_2)$. The next subsection describes this interference in more detail.

3.2.1 Hong-Ou-Mandel interference of frequency-entangled photons

As discussed in the paragraphs above, we consider a probe state of the form (3.1). Hong-Ou-Mandel interference with this state is a special case of the entangled-state interference discussed in Subsection 1.2.3. Specifically, we consider probe states which have phases imparted both by the sample and by a controllable delay line. If the delay line imparts a delay τ on the herald photon, then the state (3.1) instead has the form

$$\frac{1}{\sqrt{2}}\left[e^{i\phi(\omega_1)-i\omega_2\tau}a_1^\dagger b_2^\dagger\left|0\right\rangle + e^{i\phi(\omega_2)-i\omega_1\tau}a_2^\dagger b_1^\dagger\left|0\right\rangle\right], \tag{3.2}$$

where we now include the proper normalization of the state, and where a and b are the spatial modes of the signal and herald photons, respectively. Comparing with (1.20) and (1.21), we can immediately conclude that the post-beamsplitter state is of the form

$$\frac{1}{\sqrt{2}}\left[\cos\frac{\delta}{2}c_1^\dagger c_2^\dagger - \cos\frac{\delta}{2}d_1^\dagger d_2^\dagger - i\sin\frac{\delta}{2}c_1^\dagger d_2^\dagger + i\sin\frac{\delta}{2}c_2^\dagger d_1^\dagger\right]\left|0\right\rangle. \tag{3.3}$$

Here,

$$\delta \equiv \phi(\omega_1) - \phi(\omega_2) + (\omega_1 - \omega_2)\tau \tag{3.4}$$

is the relative phase between the two terms in the superposition state (3.2).

The probability of detecting a coincidence after the beamsplitter (*i.e.*, of detecting either $c_1^\dagger d_2^\dagger\left|0\right\rangle$ or $c_2^\dagger d_1^\dagger\left|0\right\rangle$) is

$$\sin^2\frac{\delta}{2} = \frac{1}{2} - \frac{1}{2}\cos\Big(\phi(\omega_1) - \phi(\omega_2) + (\omega_1 - \omega_2)\tau\Big), \tag{3.5}$$

which oscillates at the beat frequency $|\omega_1 - \omega_2|$ as τ is varied. Beat-frequency HOM interference of this type was first observed by Ou and Mandel [8]. More recently, it has been studied in the context of delay

sensitivity by Chen *et al.* [71].

If one knows τ, then the phase difference $\phi(\omega_1) - \phi(\omega_2)$ can be determined from the phase offset of the resulting sinusoid. We also note that in the post-beamsplitter state, the two photons always reside in distinct spatio-spectral modes. If the detectors at c and d can resolve the two frequencies ω_1 and ω_2, then it is possible to distinguish between single clicks and bunched pairs without the need for number-resolving detectors. Frequency-entangled Hong-Ou-Mandel interference, together with frequency-resolving detectors, allows for separate measurement of the interferograms for antibunched pairs (probability $\sin^2(\delta/2)$) and bunched pairs (probability $\cos^2(\delta/2)$), unlike in traditional HOM interferometers.

3.3 Spectrally-resolved Hong-Ou-Mandel interference

As discussed in the previous section, the measurement consists of three main components. The first stage consists of a source of broadband pairs of photons which are separated into two beams. The second introduces a sample to one arm, and implements a controllable relative delay between the two photons. The measurement stage consists of a beamsplitter which interferes the two photons, followed by spatial filtering of the pairs using single-mode fibers, and finally a time-tagging biphoton spectrometer.

3.3.1 A broadband source of photon pairs

Photon pairs are produced using type-0 SPDC. The source uses a 1 mm long periodically poled potassium titanyl phosphate (PPKTP) in a non-colinear geometry, pumped by a 405 nm continuous wave laser. This results in a measured bandwidth of 155 nm, centered at 810 nm; the measured bandwidth is detector-limited, and is likely larger. The resulting photons have identical linear polarization but exit the crystal with opposite transverse momenta. A $f = 10$ cm achromatic lens is used to collimate the cone of photons emerging from the crystal, and a D-shaped knife-edge mirror is placed $2f$ from the center of the crystal, at the momentum plane of the down-converted photons. Due to the strong anticorrelations in the transverse

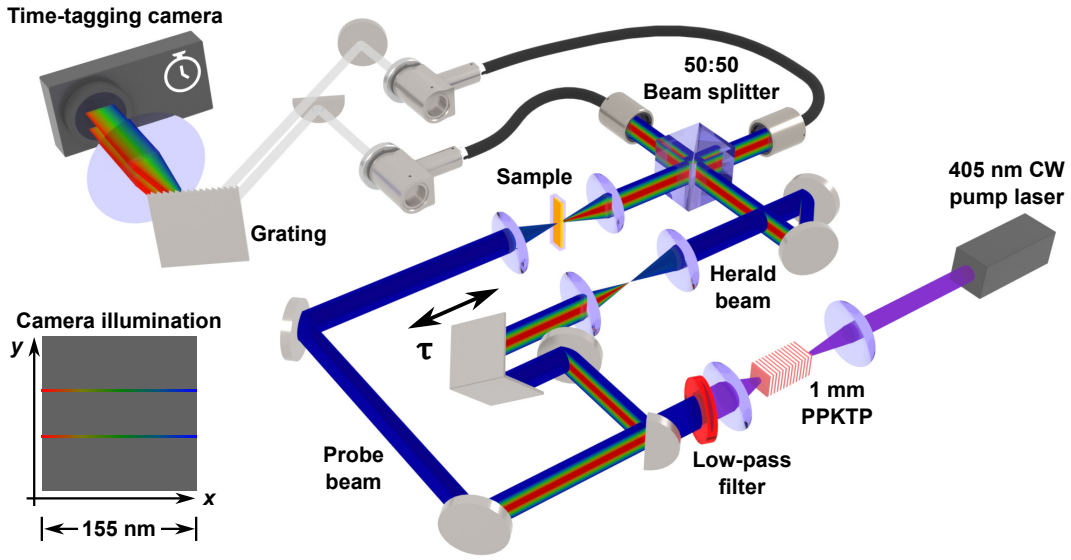

Figure 3.2: Experimental implementation of the Hong-Ou-Mandel spectrometer. A source of broadband photon pairs is generated using cw-pumped SPDC. One photon interacts with a sample; the other photon experiences a variable delay. The photons interfere at a beamsplitter, and then are collected into single mode fibers and sent to a biphoton spectrometer. The spectrometer uses a time-tagging camera, which can determine both the frequency and time-of-arrival of each detected photon.

momenta, photons appear on opposite sides of the momentum plane, so that one photon of each pair is reflected by the mirror. This results in two D-shaped beams, which propagate through the two arms of the interferometer. The positions of the photons in these beams are strongly anticorrelated due to the momentum anticorrelations in the original SPDC cone. Each point in one beam has strong intensity and frequency correlations with a corresponding point in the other beam, which is at an equal radial distance and opposite azimuthal angle.

3.3.2 The spectroscopic sample

One of the beams passes through a cuvette holder containing the spectroscopic sample. We use two chemical samples in our measurements: one contains only a toluene solvent; the other is a solution consisting of toluene and silicon 2,3-naphthalocyanine (SiNC) dye (Sigma Aldrich). The SiNC dye features a primary absorption peak centered at 774 nm [120]. This dye is chemically stable, and features an isolated absorption peak which is well suited to our spectrometer's bandwidth and resolution. For calibration purposes discussed later, measurements are also made with no sample placed in the cuvette holder, and also with the sample and reference arms blocked.

Each of the cuvettes used features a slightly wedged shape, due to manufacturing error. This wedge tends to deflect the beam passing through the sample arm. As discussed later in this chapter, the beams are spatially filtered before detection to improve interferometric visibility; this deflection changes the part of the beam which transmits through the spatial filters. Furthermore, the phase matching condition (1.62b) couples angle and frequency in SPDC, so that photon pairs produced through this mechanism generally feature spatial-spectral correlations. Deflection of the beam therefore also affects the JSI of measured photons, in addition to the overall intensity of counts. In the setup described so far, this wedge is sufficient to entirely deflect the correlated photons outside of the region collected by the spatial filters, so that no coincidence counts are observed after inserting a sample. In order to reduce the sensitivity of the interferometer to this wedge, a pair of $f = 5\,\mathrm{cm}$ lenses are placed one focal length away from the cuvette holder in either direction. These lenses bring the beam to a focus at the sample and collimate it again

afterwards; this increases the numerical aperture of the beam at the point of the cuvette so that small deflections in the beam's direction due to the wedge have a smaller impact on the rate of coincidences. Nevertheless, small changes in the JSI of the probe beam due to the combination of spectral-spatial correlations and the spatial filter persist, and are a source of uncontrolled error in the experiment.

This pair of lenses results in a spatial inversion of the beam in the transverse direction; to maintain the correct relative position of the photons, a second pair of identical lenses is added to the reference arm. Small misalignment in the positions of each lens pair results in aberration in the transmitted beam; this further necessitates the use of spatial filtering, since only a small region of either beam can be brought into suitable alignment at a time. Though these lens pairs reduce the impact of the wedge on the total rate of measured coincidences, differences in the spectrum of the collected light is observed when comparing measurements with and without a cuvette.

3.3.3 The Hong-Ou-Mandel interferometer

The interferometer consists of two D-shaped correlated beams, described in Subsection 3.3.1 above, which form the two arms of a Hong-Ou-Mandel interferometer. The incident beams show intensity and frequency correlations at points which are diametrically opposed relative to the center of the down-converted cone. To ensure that photon pairs enter the beamsplitter at identical transverse positions, a retroreflector is added to one of the two arms to implement a spatial inversion, turning the anticorrelated transverse positions into correlated transverse positions. This retroreflector is also used to add a variable delay τ to one photon. In non-spectrally-resolved HOM interference, this delay introduces distinguishability between the two photons. As discussed in Subsection 3.2.1, the same delay adds a controllable phase shift to the interferometric oscillation in frequency-entangled HOM interference.

Interference occurs at a 50:50 nonpolarizing beamsplitter. Unlike a traditional Mach-Zehnder interferometer, the mean intensity of light exiting each beamsplitter port does not change as the delay is varied; rather, the photons preferentially "bunch" (*i.e.*, both photons exit a single beamsplitter port) or "an-

tibunch" (*i.e.*, both photons exit different beamsplitter ports), which can be measured using time- and frequency-resolved photodetection, discussed in the next subsection.

3.3.4 Biphoton spectroscopy using a time-tagging camera

Central to this spectroscopic method is the ability to spectrally resolve the two-photon interference effect. Since this interference appears only in the relative positions of the two photons at the beamsplitter output ports — whether they emerge from a single port or from opposing ports — simple intensity measurements are unable to detect this type of interference, and so a standard spectrometer is not sufficient. Instead, the spectrometer must be able to identify pairs of correlated photons, originating from the same SPDC event, which arrive at the beamsplitter within the biphoton coherence time and hence showing the interference. This is accomplished using a spectrometer which tags each detected photon with a nanosecond-scale time of arrival. The pair source we use produces pairs at a relatively low rate of thousands of pairs per second, so that two photons arriving within a few-nanosecond window may be assumed to belong to a correlated pair.

The spectrometer consists of two rows of time-tagging pixels providing a full set of spectral bins for each of the two beamsplitter outputs. The bandwidth of the pairs spans hundreds of spectral bins, so that photons in a pair almost always arrive at different spectral bins, due to the conservation of energy in SPDC. This detector is therefore capable of distinguishing five possible categories of detection events: a single photon may arrive in one of the two rows; a pair of photons may arrive with a single photon in each of the two rows; or a pair of photons may arrive with both photons in one of the two rows. Detection of a single photon is described by a single wavelength λ, resulting in a one-dimensional spectrum. Detection of two photons is described by a pair of wavelengths (λ_1, λ_2), resulting in a two-dimensional spectrum. The two-photon interference pattern can be resolved by comparing the relative rates of pairs arriving in a single spectrometer row to that of pairs arriving at opposing spectrometer rows.

The description so far is independent of any specific detector technology. Our experiment relies on a

time-tagging camera (Timepix3, Amsterdam Scientific), providing a 256-by-256 pixel CMOS sensor with per-pixel time-tagging. Single-photon sensitivity is provided by the use of an image intensifier, which uses optical-to-electrical-to-optical transduction to amplify a single incident photon into a cluster of many incident detector clicks, allowing the camera to overcome the noise inherent to CMOS detectors. Biphoton measurements using this intensified camera were pioneered by Nomerotski *et al.* [121, 122]; application of this camera to spectrally-resolved measurements of Hong-Ou-Mandel interference originated in the work of Zhang *et al.* [123]. These measurements are also possible using a linear array of single-photon avalanche diodes [124]. A similar technique, relying on a pair of time-of-flight spectrometers, has been demonstrated in [125]

Our detector follows the setup used by Zhang *et al.* [123]. We couple the two beamsplitter outputs into single-mode fiber to allow for spatial filtering. Off-axis parabolic collimators direct the beams from the fibers towards a blazed grating, which is imaged using a $f = 20\,\mathrm{cm}$ lens onto the intensifier. The resulting spectrometer has a bandwidth of 155 nm centered at 810 nm, a pixel-limited wavelength resolution of 0.6 nm, and a timing resolution of about 7 ns. The spectrometer was calibrated using the emission spectrum of an argon gas lamp, and the pixel-to-wavelength relationship was found to be linear to within the pixel resolution of the camera. The primary limiting factors of this spectrometer are a low overall quantum efficiency, due to fiber coupling losses, grating reflectance, and the intensified camera efficiency of about 10%. As shown in Chapter 4, this is one of the primary factors preventing the demonstration of a true per-photon quantum advantage in our spectroscopy measurement.

3.4 A simple model of the experiment

3.4.1 Optical state

We now discuss a model of the spectroscopic measurement including the effects of sample absorption and the finite optical efficiencies of the setup. This model is later used to justify the calibration procedure and

estimators used when performing spectroscopy. Since the detector involves a projection onto well-defined spatial modes through the use of single-mode fiber, it is sufficient to consider only two spatial modes in the interferometer; likewise, since the down-converted photons are produced by type-0 SPDC, we assume all photons have the same linear polarization. We also assume that the pump power is low enough for the two-mode squeezed light produced by the crystal to be considered a stream of independent photon pairs, with simultaneous emission of more than two photons being negligible. The state of the field then has the form

$$|\psi_0\rangle = \sqrt{1-g}\,|0\rangle + \sqrt{g}\sum_{i,j=1}^{N} \Psi_{ij} a_i^\dagger b_j^\dagger\,|0\rangle\,, \tag{3.6}$$

where g, related to the amount of squeezing, describes the probability of producing a pair in a given trial. Here, the indices $i, j = 1, \ldots, N$ label the spectral bins ω_i and ω_j, Ψ_{ij} is the joint spectral amplitude of the light, normalized so that $\sum_{ij}|\Psi_{ij}|^2 = 1$, and, $a_i^\dagger$ and $b_i^\dagger$ are creation operators for the i^{th} spectral bin in one of two orthogonal spatial modes (the two arms of the interferometer). These operators obey

$$\left[a_i,\, a_j^\dagger\right] = \left[b_i,\, b_j^\dagger\right] = \delta_{ij}, \qquad \left[a_i,\, b_j^\dagger\right] = 0. \tag{3.7}$$

Our use of discretized spectral bins is largely one of mathematical convenience. As shown in Subsection 3.4.2, the spectrometer's action consists of a simultaneous click/no-click measurement in each spectral bin, which is expressed as a tensor product over all frequency bins. The use of discrete bins avoids much of the mathematical subtleties associated with uncountably large tensor products.

The state (3.6) is propagated through the two interferometer arms and the sample, before being mixed at a beamsplitter and detected by the spectrometer. Each of the two arms is assumed to have a finite transmittance; the transmittance at frequency ω_i through the sample arm (including any sample) is denoted by T_i, and the transmittance at ω_i through the reference arm by R_i. It must be emphasized that R_i denotes a transmittance; reflectances, when required, are denoted by $1 - T_i$ and $1 - R_i$. We also place any relative phase shifts, including those due to the sample and due to changes in the relative path length, in the phase

of the sample arm. Transmission through the two arms is described by the transformations

$$a_i^\dagger \to \sqrt{T_i} e^{-i\phi_i} a_i^\dagger + \sqrt{1-T_i}\, a_i'^\dagger, \qquad b_i^\dagger \to \sqrt{R_i} b_i^\dagger + \sqrt{1-R_i}\, b_i'^\dagger, \tag{3.8}$$

where any light lost during transmission is assumed to scatter into modes a_i' and b_i'. The state after transmission through the arms is obtained by substituting these expressions into the density operator $|\psi_0\rangle\langle\psi_0|$ and tracing out the auxiliary modes a_i' and b_i'. The 50:50 beamsplitter, meanwhile, performs the transformation

$$a_i^\dagger \to \frac{1}{\sqrt{2}} c_i^\dagger + \frac{1}{\sqrt{2}} d_i^\dagger, \qquad b_i^\dagger \to \frac{1}{\sqrt{2}} c_i^\dagger - \frac{1}{\sqrt{2}} d_i^\dagger. \tag{3.9}$$

With this substitution, we obtain the post-beamsplitter state

$$\begin{aligned}
\rho = {} & g \sum_{ij} |\Psi_{ij}|^2 (1-T_i)(1-R_j) \,|0\rangle\langle 0| \\
& + \frac{g}{2} \sum_i (1-T_i) \left[\sum_j \Psi_{ij} \sqrt{R_j} (c_j^\dagger - d_j^\dagger) \,|0\rangle \right] \left[\sum_j \Psi_{ij}^* \sqrt{R_j} \,\langle 0| \,(c_j - d_j) \right] \\
& + \frac{g}{2} \sum_j (1-R_j) \left[\sum_i \Psi_{ij} \sqrt{T_i} e^{-i\phi_i} (c_i^\dagger + d_i^\dagger) \,|0\rangle \right] \left[\sum_i \Psi_{ij}^* \sqrt{T_i} e^{i\phi_i} \,\langle 0| \,(c_i + d_i) \right] \\
& + |\psi'\rangle\langle\psi'| \,,
\end{aligned} \tag{3.10}$$

where we have defined the non-normalized state

$$|\psi'\rangle \equiv \sqrt{1-g}\,|0\rangle + \frac{\sqrt{g}}{2} \sum_{ij} \Psi_{ij} \sqrt{T_i R_j} e^{-i\phi_i} (c_i^\dagger + d_i^\dagger)(c_j^\dagger - d_j^\dagger)\,|0\rangle \,. \tag{3.11}$$

This state consists of four terms. The first involves no photons appearing after the beamsplitter; this occurs either when no photons are produced by the crystal, with probability $(1-g)$, or when photons are produced but are both lost during transmission through the arms. The second and third describe a pair

which enters the interferometer, after which one of the two photons is lost. The state of the remaining photon depends on the frequency of the photon which was absorbed. The final state describes a pair which transmits through the beamsplitter with neither photon being absorbed; this term describes a pair which is left in a pure state and which exhibits Hong-Ou-Mandel interference.

3.4.2 Detection probabilities

There is one more important source of loss in the experiment, which is due to the finite detector efficiency, including any coupling losses into single mode fiber. Let η_{c_i} and η_{d_i} be the effective quantum efficiencies of the spectrometer pixels corresponding to modes c_i and d_i, respectively. We assume these efficiencies include also any losses due to the coupling into single-mode fiber. The POVM elements for a single-mode non-number-resolving detector are

$$\Pi^{(nc)} = \sum_{m=0}^{\infty} \frac{(1-\eta)^m}{m!} (a^\dagger)^m \left|0\right\rangle \left\langle 0\right| a^m, \tag{3.12a}$$

$$\Pi^{(c)} = \mathbb{1} - \Pi^{(nc)}, \tag{3.12b}$$

where $\Pi^{(c)}$ describes a click and $\Pi^{(nc)}$ describes no click.

The spectrometer is modeled as a simultaneous click/no-click measurement of each mode c_i and d_i. This model ignores dark counts, which are observed to play a minor role in the measured intensities — dark counts make up roughly 1% of the measured photon counts. In this approximation, we may assume that at most two photons arrive at the detector in a given time bin. The relevant POVM elements are

then

$$\Pi_{c_i} = \Pi_{c_i}^{(c)} \otimes \bigotimes_{k\neq i} \Pi_{c_k}^{(nc)} \otimes \bigotimes_{k} \Pi_{d_k}^{(nc)}, \tag{3.13a}$$

$$\Pi_{d_i} = \Pi_{d_i}^{(c)} \otimes \bigotimes_{k} \Pi_{c_k}^{(nc)} \otimes \bigotimes_{k\neq i} \Pi_{d_k}^{(nc)}, \tag{3.13b}$$

$$\Pi_{c_i c_j} = \Pi_{c_i}^{(c)} \otimes \Pi_{c_j}^{(c)} \otimes \bigotimes_{k\neq i, k\neq j} \Pi_{c_k}^{(nc)} \otimes \bigotimes_{k} \Pi_{d_k}^{(nc)}, \qquad (i \neq j) \tag{3.13c}$$

$$\Pi_{d_i d_j} = \Pi_{d_i}^{(c)} \otimes \Pi_{d_j}^{(c)} \otimes \bigotimes_{k} \Pi_{c_k}^{(nc)} \otimes \bigotimes_{k\neq i, k\neq j} \Pi_{d_k}^{(nc)}, \qquad (i \neq j) \tag{3.13d}$$

$$\Pi_{c_i d_j} = \Pi_{c_i}^{(c)} \otimes \Pi_{d_j}^{(c)} \otimes \bigotimes_{k\neq i} \Pi_{c_k}^{(nc)} \otimes \bigotimes_{k\neq j} \Pi_{d_k}^{(nc)}, \tag{3.13e}$$

$$\Pi_0 = \mathbb{1} - \sum_i \Pi_{c_i} - \sum_i \Pi_{d_i} - \sum_{i\neq j} \Pi_{c_i c_j} - \sum_{i\neq j} \Pi_{d_i d_j} - \sum_{ij} \Pi_{c_i d_j}. \tag{3.13f}$$

The first two POVM elements correspond to a single click in modes c_i and d_i, respectively. The third and fourth operators correspond to two clicks in a single spatial mode but different spectral bins. The fifth operator describes two clicks in different spatial modes. The final operator describes no click. These expressions may be expanded using the relations (3.12); truncating to the subspace of states with zero,

one, or two photons results in the expressions

$$\Pi_{c_i} = \eta_{c_i} c_i^\dagger |0\rangle \langle 0| c_i + \frac{1}{2}\eta_{c_i}(2-\eta_{c_i})(c_i^\dagger)^2 |0\rangle \langle 0| c_i^2 + \eta_{c_i} \sum_{j\neq i}(1-\eta_{c_j}) c_i^\dagger c_j^\dagger |0\rangle \langle 0| c_i c_j + \eta_{c_i} \sum_j (1-\eta_{d_j}) c_i^\dagger d_j^\dagger |0\rangle \langle 0| c_i d_j, \tag{3.14a}$$

$$\Pi_{d_i} = \eta_{d_i} d_i^\dagger |0\rangle \langle 0| d_i + \frac{1}{2}\eta_{d_i}(2-\eta_{d_i})(d_i^\dagger)^2 |0\rangle \langle 0| d_i^2 + \eta_{d_i} \sum_j (1-\eta_{c_j}) d_i^\dagger c_j^\dagger |0\rangle \langle 0| d_i c_j + \eta_{d_i} \sum_{j\neq i}(1-\eta_{d_j}) d_i^\dagger d_j^\dagger |0\rangle \langle 0| d_i d_j, \tag{3.14b}$$

$$\Pi_{c_i c_j} = \eta_{c_i}\eta_{c_j} c_i^\dagger c_j^\dagger |0\rangle \langle 0| c_i c_j, \tag{3.14c}$$

$$\Pi_{d_i d_j} = \eta_{d_i}\eta_{d_j} d_i^\dagger d_j^\dagger |0\rangle \langle 0| d_i d_j, \tag{3.14d}$$

$$\Pi_{c_i d_j} = \eta_{c_i}\eta_{d_j} c_i^\dagger d_j^\dagger |0\rangle \langle 0| c_i d_j. \tag{3.14e}$$

In practice, it is more useful to consider the total rate of photon clicks, which includes clicks that arrive both individually and also as part of a pair. We therefore define operators corresponding to these unconditioned clicks,

$$\Pi_{c_i}^{(s)} = \Pi_{c_i} + \sum_{j\neq i} \Pi_{c_i c_j} + \sum_j \Pi_{c_i d_j}, \tag{3.15a}$$

$$\Pi_{d_i}^{(s)} = \Pi_{d_i} + \sum_{j\neq i} \Pi_{d_i d_j} + \sum_j \Pi_{c_j d_i}. \tag{3.15b}$$

These have the approximate expressions

$$\Pi_{c_i}^{(s)} = \eta_{c_i} c_i^\dagger |0\rangle \langle 0| c_i + \eta_{c_i} \sum_{j\neq i} c_i^\dagger c_j^\dagger |0\rangle \langle 0| c_i c_j + \eta_{c_i} \sum_j c_i^\dagger d_j^\dagger |0\rangle \langle 0| c_i d_j, \tag{3.16a}$$

$$\Pi_{d_i}^{(s)} = \eta_{d_i} d_i^\dagger |0\rangle \langle 0| d_i + \eta_{d_i} \sum_{j\neq i} d_i^\dagger d_j^\dagger |0\rangle \langle 0| d_i d_j + \eta_{d_i} \sum_j c_j^\dagger d_i^\dagger |0\rangle \langle 0| c_j d_i. \tag{3.16b}$$

We have neglected in each expression those outcomes in which two photons arrive in the same spatial mode and in the same spectral bin. When the photon frequencies are strongly anticorrelated, this corresponds

to a negligible fraction of the total counts.

At this stage we assume that the photon frequencies are perfectly anticorrelated, so that $\Psi_{ij} = \psi_i \delta_{i,N+1-i}$ for some ψ_i, and also that the joint spectral amplitude is symmetric, so that $\psi_i = \psi_{N+1-i}$. This is reasonable so long as the photons are produced by cw-pumped SPDC in a crystal which is aligned with the optic axis; in this case, nothing distinguishes photons in one arm from the other, so that the spectrum is necessarily symmetric. The probabilities for observing a single unconditioned click is then

$$\mathrm{Tr}\left[\rho\,\Pi_{c_i}^{(s)}\right] = \frac{g}{2}\eta_{c_i}(T_i + R_i)|\psi_i|^2, \tag{3.17a}$$

$$\mathrm{Tr}\left[\rho\,\Pi_{d_i}^{(s)}\right] = \frac{g}{2}\eta_{d_i}(T_i + R_i)|\psi_i|^2, \tag{3.17b}$$

and the probabilities of observing each type of coincidence is

$$\mathrm{Tr}\left[\rho\,\Pi_{c_i c_{N+1-i}}\right] = \frac{g}{4}\eta_{c_i}\eta_{c_{N+1-i}}\left|\sqrt{T_i R_{N+1-i}}e^{i\phi_i} + \sqrt{T_{N+1-i}R_i}e^{i\phi_{N+1-i}}\right|^2|\psi_i|^2, \tag{3.18a}$$

$$\mathrm{Tr}\left[\rho\,\Pi_{d_i d_{N+1-i}}\right] = \frac{g}{4}\eta_{d_i}\eta_{d_{N+1-i}}\left|\sqrt{T_i R_{N+1-i}}e^{i\phi_i} + \sqrt{T_{N+1-i}R_i}e^{i\phi_{N+1-i}}\right|^2|\psi_i|^2, \tag{3.18b}$$

$$\mathrm{Tr}\left[\rho\,\Pi_{c_i d_{N+1-i}}\right] = \frac{g}{4}\eta_{c_i}\eta_{d_{N+1-i}}\left|\sqrt{T_i R_{N+1-i}}e^{i\phi_i} - \sqrt{T_{N+1-i}R_i}e^{i\phi_{N+1-i}}\right|^2|\psi_i|^2. \tag{3.18c}$$

The coincidence probabilities are evaluated only for pairs of spectral bins $(i, N+1-i)$ due to our assumption of tight frequency anticorrelations. This expression generalizes the simple model considered in Subsection 3.2.1 to include the effects of finite transmission through each arm. This leads to a change in the interference visibility, but otherwise the same beat-frequency oscillations are observed.

Neglecting the possibility of multiple down-converted pairs in a single pair of spectral bins, the total number of single and coincidence counts of each type is a Poisson-distributed random variable with a mean equal to the rate of production, times the integration time, times the probability g. The expressions above can therefore be used in place of the mean number of counts so long as g is now interpreted as being the total number of pairs produced during the measurement interval. Subsequent sections describe how the optical absorption and phase shift imparted by a spectroscopic sample may be estimated from these rates.

3.5 Calibration procedure

The goal of our spectroscopic method is to determine the absorption spectrum of a sample by means of heralded (*i.e.*, coincidence) counts, and to determine its phase spectrum from the two-photon interference pattern. This is complicated by the presence in (3.17) and (3.18) of various parameters which are not of primary interest. This section describes the procedure by which these unwanted parameters are eliminated, leaving only the absorption and phase values.

The simplest parameters to correct for are the detector efficiencies η_{c_i} and η_{d_i} for each spectral bin i. From the expressions (3.17) for the rate of unconditioned single clicks, we have that

$$\frac{\mathrm{Tr}\left[\rho\,\Pi_{c_i}^{(s)}\right]}{\mathrm{Tr}\left[\rho\,\Pi_{d_i}^{(s)}\right]} = \frac{\eta_{c_i}}{\eta_{d_i}}. \tag{3.19}$$

The ratio of unconditioned click rates at each pair of spectrometer pixels can be used to estimate the ratio of the corresponding efficiencies. By multiplying or dividing by this ratio, one of the two detector efficiencies can be eliminated from (3.17) and (3.18), leaving factors of the as-yet-undetermined efficiency of a single spectrometer arm; for definiteness, we take this arm to be the c arm.

Explicitly, we calculate the quantities

$$\begin{aligned} S_i &= \mathrm{Tr}\left[\rho\,\Pi_{c_i}^{(s)}\right] + \frac{\eta_{c_i}}{\eta_{d_i}}\mathrm{Tr}\left[\rho\,\Pi_{d_i}^{(s)}\right] \\ &= g\eta_i(T_i + R_i)|\psi_i|^2, \qquad (3.20a) \\ C_i^+ &= \mathrm{Tr}\left[\rho\,\Pi_{c_i c_{N+1-i}}\right] + \frac{\eta_{c_i}\eta_{c_{N+1-i}}}{\eta_{d_i}\eta_{d_{N+1-i}}}\mathrm{Tr}\left[\rho\,\Pi_{d_i d_{N+1-i}}\right] \\ &\quad + \frac{\eta_{c_{N+1-i}}}{\eta_{d_{N+1-i}}}\mathrm{Tr}\left[\rho\,\Pi_{c_i d_{N+1-i}}\right] + \frac{\eta_{c_i}}{\eta_{d_i}}\mathrm{Tr}\left[\rho\,\Pi_{c_{N+1-i} d_i}\right] \\ &= g\eta_i\eta_{N+1-i}(T_i R_{N+1-i} + T_{N+1-i}R_i)|\psi_i|^2 \qquad (3.20b) \\ C_i^- &= \mathrm{Tr}\left[\rho\,\Pi_{c_i c_{N+1-i}}\right] + \frac{\eta_{c_i}\eta_{c_{N+1-i}}}{\eta_{d_i}\eta_{d_{N+1-i}}}\mathrm{Tr}\left[\rho\,\Pi_{d_i d_{N+1-i}}\right] \\ &\quad - \frac{\eta_{c_{N+1-i}}}{\eta_{d_{N+1-i}}}\mathrm{Tr}\left[\rho\,\Pi_{c_i d_{N+1-i}}\right] - \frac{\eta_{c_i}}{\eta_{d_i}}\mathrm{Tr}\left[\rho\,\Pi_{c_{N+1-i} d_i}\right] \\ &= 2g\eta_i\eta_{N+1-i}\sqrt{T_i T_{N+1-i} R_i R_{N+1-i}}|\psi_i|^2 \cos\left(\phi_i - \phi_{N+1-i}\right), \qquad (3.20c) \end{aligned}$$

where the corresponding expressions have been obtained from (3.17) and (3.18). The rate S_i corresponds to the total rate of unconditioned single clicks, weighted by the ratio of detector efficiencies. The two rates C_i^+ and C_i^- similarly combine the corrected coincidence rates. The rate C_i^+ quantifies the total number of coincidences, irrespective of whether the photons bunched or antibunched; the rate C_i^- describes the difference between the bunching and antibunching rates. The total single and coincidence rates S_i and C_i^+ are insensitive to the bunching statistics of the photons, and their ratio C_i^+/S_i can be viewed as the equivalent of the heralding ratio in a traditional quantum absorption spectrometer, which we discuss further in Subsection 3.5.1. These two rates are used to calculate the absorption of the sample. The rate C_i^-, meanwhile, exhibits phase-sensitive oscillations, and can be used to estimate the phase spectrum imparted by the sample on the transmitted light.

3.5.1 Calculating the sample absorption

Earlier quantum spectroscopy experiments rely on the heralding ratio C_i/S_i to determine the absorption of a sample. This ratio has a simple physical interpretation, in that it measures the proportion of single clicks in a given arm which also make up part of a coincidence detection. In repeated measurements, the joint intensity will take on a range of values due to the spontaneous nature of the down-conversion process, so that $g|\psi_i|^2$ can be considered a thermal (Bose-Einstein)-distributed random variable. Both C_i and S_i are proportional to the joint spectral intensity $g|\psi_i|^2$ of the probe beam, so that estimates of the absorption from either the coincidence C_i or singles S_i rate alone will have limited precision as a result of this stochastic joint intensity. The minimum per-photon uncertainty of such an estimate occurs for $g \to 0$, when the intensity is approximately Poisson-distributed and the measurement becomes shot noise limited. The heralding ratio, however, is independent of the joint spectral intensity — it still exhibits random fluctuations due to the stochastic absorption process, but ideally will not depend on noise in the probe intensity. This may be regarded as the origin of the improved precision in traditional quantum-enhanced absorption spectroscopy.

In essence, this improvement is due to the strong intensity correlations which exist between the two beams, so that detection of one photon alerts the experimenter to the presence of ("heralds") the other. The two beams in a heralded absorption measurement both derive from the same intensity $g|\psi_i|^2$. This is in contrast to the classical-like states of light which are produced by lasers, in which the quantum shot noise of any two beams is uncorrelated. Heralded sources of light allow measurement of the intensity of one beam to reduce uncertainty of the other below this shot noise limit.

By analogy, we seek to estimate the absorption of a spectroscopic sample using the ratio of coincidences to singles. In our frequency-entangled experiment, a photon at frequency ω_i is heralded by a photon at frequency ω_{N+1-i}. We therefore define the heralding ratio in this experiment to be C_i^+/S_{N+1-i}. Using

(3.20), we have that

$$\frac{C_i^+}{S_{N+1-i}} = \frac{g\eta_i\eta_{N+1-i}(T_iR_{N+1-i} + T_{N+1-i}R_i)|\psi_i|^2}{g\eta_{N+1-i}(T_{N+1-i} + R_{N+1-i})|\psi_i|^2}$$
$$= \eta_i \frac{T_iR_{N+1-i} + T_{N+1-i}R_i}{T_{N+1-i} + R_{N+1-i}}. \tag{3.21}$$

Here we have used the symmetry of the joint spectral intensity, $|\psi_i| = |\psi_{N+1-i}|$, which is appropriate for photon pairs possessing the same polarization in the nonlinear crystal. Note that both C_i^+ and S_{N+1-i} are measured in a single trial of the experiment. The random variable $g|\psi_i|^2$, describing the number of photon pairs produced during this trial, takes the same value in each expression, so that random fluctuations in the number of incident pairs do not affect the measurement. However, the heralding ratio still shows statistical fluctuations which arise from the transmittance factors T and R. These fluctuations arise from the stochastic nature of photon absorption and optical loss.

The properties of heralding ratio in this experiment are therefore similar to those in previous heralded absorption measurements, with the important difference that the transmittance factors for the herald arm do not cancel each other. Physically, this is due to the indistinguishability of the probe and herald photons after the beamsplitter — the rate of coincidence detections at bins $(i, N+1-i)$ contains information about the transmission of the sample at both ω_i and ω_{N+1-i}, and these contributions cannot be separated. By comparison, in a traditional heralded absorption measurement, there is no ambiguity about the path of the two detected photons. Any decrease in the probe arm's intensity can then be attributed entirely to the sample's absorption at the corresponding frequency. Suitable calibration of the experiment is needed to eliminate the contribution of the unwanted second term in the numerator and denominator of (3.21).

We now consider a differential measurement, in which the goal is to estimate the relative absorption $T_i^{(s)}/T_i^{(r)}$ of a sample of interest (s) to a reference sample (r). Our calculation assumes that the detector efficiencies η_i and the transmittance of the reference arm R_i remain unchanged between the two

measurements. The relative absorption can then be calculated in terms of the relative heralding ratio,

$$\frac{C_i^{+(s)}/S_{N+1-i}^{(s)}}{C_i^{+(r)}/S_{N+1-i}^{(r)}} = \left(\frac{1+T_{N+1-i}^{(r)}/R_{N+1-i}}{1+T_{N+1-i}^{(s)}/R_{N+1-i}}\right)\left(\frac{T_i^{(s)}+T_{N+1-i}^{(s)}R_i/R_{N+1-i}}{T_i^{(r)}+T_{N+1-i}^{(r)}R_i/R_{N+1-i}}\right). \tag{3.22}$$

As shown in (3.21), the heralding ratio itself is almost symmetric under a reflection of the spectrum ($i \to N+1-i$), since only the detector efficiency η_i appears asymmetrically in the ratio. As a consequence, calculations relying only on the heralding ratio cannot distinguish absorption at the low frequency from that at the correlated high frequency. Fundamentally, this is due to the symmetrization imposed by the beamsplitter. This symmetry can be broken by considering the spectrum of single clicks, which is not symmetric, allowing for unambiguous absorption spectroscopy. The two samples used in this experiment are known to be almost completely transmissive on one side of the degeneracy frequency $\omega_p/2$. It is therefore reasonable to assume that the transmittance T_{N+1-i} is the same for all measurements, where $i \leq N/2$. In this case,

$$\begin{aligned}\frac{C_i^{+(s)}/S_{N+1-i}^{(s)}}{C_i^{+(r)}/S_{N+1-i}^{(r)}} &= \frac{T_i^{(s)}+T_{N+1-i}R_i/R_{N+1-i}}{T_i^{(r)}+T_{N+1-i}R_i/R_{N+1-i}} \\ &= \frac{T_i^{(s)}/T_i^{(r)}+T_{N+1-i}R_i/T_i^{(r)}R_{N+1-i}}{1+T_{N+1-i}R_i/T_i^{(r)}R_{N+1-i}}.\end{aligned} \tag{3.23}$$

Extraction of the relative absorption $T_i^{(s)}/T_i^{(r)}$ from the heralding ratios requires we correct for the terms $T_{N+1-i}R_i/T_i^{(r)}R_{N+1-i}$. We now examine how this correction can be estimated from the measured data.

For calibration purposes, two more measurements are made with the setup. In one, the sample arm is blocked, and in the other the reference arm is blocked. In each case, the singles spectrum is measured. We use $S_i^{(0)}$ to denote the spectrum with the reference arm blocked, and $S_i^{(0')}$ to denote the spectrum with the sample arm blocked. We now use $T_i^{(0)}$ to denote the transmittance through the sample arm, and write

$$T_i^{(r)} = T_i^{(0)}e^{-\chi_i^{(r)}}, \qquad T_i^{(s)} = T_i^{(0)}e^{-\chi_i^{(s)}}. \tag{3.24}$$

From (3.20),

$$S_i^{(0)} = g\eta_i T_i^{(0)} |\psi_i|^2, \qquad S_i^{(0')} = g\eta_i R_i |\psi_i|^2. \tag{3.25}$$

From these, we calculate

$$\frac{S_i^{(0)}}{S_i^{(0')}} = \frac{T_i^{(0)}}{R_i}, \qquad \frac{S_{N+1-i}^{(0)}}{S_{N+1-i}^{(0')}} = \frac{T_{N+1-i}}{R_{N+1-i}}. \tag{3.26}$$

These provide the necessary correction factors, apart from the additional factor $e^{-\chi_i^{(r)}}$ needed to account for absorption by the reference sample. This factor can be estimated using the singles rates,

$$\frac{S_i^{(r)} - S_i^{(0')}}{S_i^{(0)}} = \frac{T_i^{(r)}}{T_i^{(0)}} = e^{-\chi_i^{(r)}}. \tag{3.27}$$

Using (3.26) and (3.27), the transmittance ratio is found from

$$\frac{T_i^{(s)}}{T_i^{(r)}} = \left(1 + \frac{S_{N+1-i}^{(0)}}{S_{N+1-i}^{(0')}} \frac{S_i^{(0')}}{S_i^{(0)}} \frac{S_i^{(0)}}{S_i^{(r)} - S_i^{(0')}}\right) \frac{C_i^{+(s)}/S_{N+1-i}^{(s)}}{C_i^{+(r)}/S_{N+1-i}^{(r)}} - \frac{S_{N+1-i}^{(0)}}{S_{N+1-i}^{(0')}} \frac{S_i^{(0')}}{S_i^{(0)}} \frac{S_i^{(0)}}{S_i^{(r)} - S_i^{(0')}}. \tag{3.28}$$

This quantity is calculated below as an estimate of the absolute transmission of the sample of interest.

Replacing the reference singles rate $S_i^{(r)}$ by the corresponding quantity for the sample of interest, (3.27) yields an estimate of the sample transmittance which is independent of the coincidence count rates. This can be compared directly to the transmission spectrum calculated from (3.28) to check for consistency. Assuming our model sufficiently describes the measured count rates, the two spectra should be the same. A comparison of this type is presented in the following section.

3.6 Results of spectroscopic measurements

As discussed in Section 3.3, we perform an experiment which uses this two photon spectroscopy method to measure the absorption and phase of SiNC dye molecules. This dye is measured in solution (concentration of 0.15 mM), so that the absorption spectrum of the dye is determined via differential measurements with a reference sample containing only the toluene solvent. The dye-in-solvent and solvent-only samples play the role of the sample of interest and reference sample in the procedure described in the previous section.

3.6.1 The measured interferograms

Spectroscopic measurements are conducted on each sample by measuring the rate of single and coincidence counts at each of the two beamsplitter outputs using the biphoton spectrometer described in Subsection 3.3.4. These spectra are measured at a range of relative delays τ extending symmetrically on either side of the HOM dip. These counts, after suitable calibration of the detector efficiencies as discussed in Section 3.5, yield a singles spectrum S_i along with total and difference coincidence spectra C_i^+ and C_i^-. The total coincidences and singles counts are phase-insensitive, and are not observed to vary with delay; these counts are integrated over the range of delays to obtain a single spectrum of each type for each sample. The ratio of total coincidences to singles at each frequency bin are used to determine the absorption spectrum, in analogy to previous heralded absorption measurements. This procedure was discussed in detail in Subsection 3.5.1.

The phase-sensitivity of the measurement appears in the difference coincidence rate C_i^-. From (3.20), including the phase shifts due to the relative delay τ imposed by a delay line, the coincidence rate is

$$C_i^- = 2g\eta_i\eta_{N+1-i}\sqrt{T_iT_{N+1-i}R_iR_{N+1-i}}|\psi_i|^2\cos\left[(\omega_i-\omega_{N+1-i})\tau+\phi_i-\phi_{N+1-i}\right]. \tag{3.29}$$

For each of the two samples, the difference coincidence spectrum is measured as a function of delay; the interferograms obtained in this way are shown in Figure 3.3 and Figure 3.4. Each spectrum is symmetric

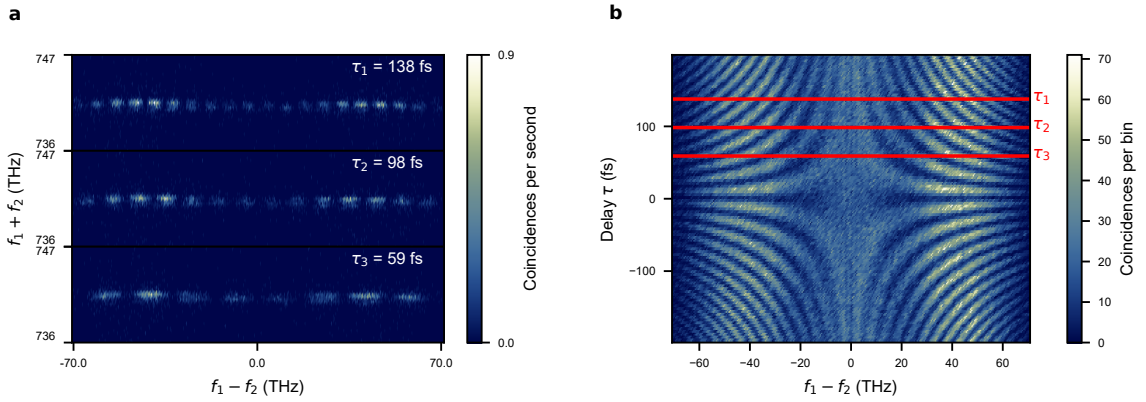

Figure 3.3: The measured HOM interferogram for the reference (toluene) sample. (a) Joint spectral intensity of coincidence counts measured at three values of the relative delay. (b) Measured interferogram for all delay values. Each row of (b) is obtained by summing a JSI measurement over one axis (the vertical axis, in (a)). The resulting interferogram shows oscillations with τ for each value of the frequency difference $f_1 - f_2$. The interferogram shows a left-right symmetry due to the indistinguishability of the two photons after the beamsplitter.

under reflection across the center frequency $\omega_p/2$. At a particular spectral bin, corresponding to pairs at frequencies ω_i and ω_{N+1-i}, the count rate varies sinusoidally as a function of time with a known frequency $\omega_i - \omega_{N+1-i}$. The relative phase shift $\phi_i - \phi_{N+1-i}$ acts to shift the position of fringe peaks. The relative phase shift can therefore determined by fitting the oscillation at each pair of frequencies. The phase shifts obtained in this manner can be used to reconstruct the phase spectrum $\phi(\omega)$ imparted by the sample on transmitted photons. This method is sensitive only to the relative phase spectrum $\phi(\omega) - \phi(\omega_p/2 - \omega)$, which is a consequence of our particular probe state; any measurement of this type using a narrowband pump shows a similar restriction. As in the absorption measurement, the phase shift at frequencies below $\omega_p/2$ is assumed to be negligible, so that this relative phase spectrum can be associated with the absolute phase shift $\phi(\omega)$ for $\omega > \omega_p/2$.

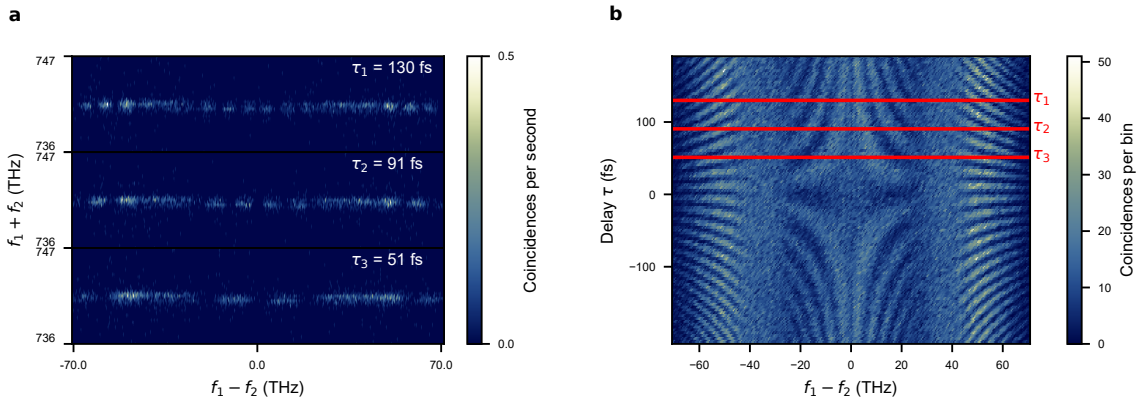

Figure 3.4: The measured HOM interferogram for the SiNC dye sample. The interferogram has the same interpretation as in Figure 3.3. The addition of the sample causes two main differences. Absorption leads to a decrease in the amplitude of oscillations at some frequencies; due to photon indistinguishability, a single absorption peak appears symmetrically on both sides of the interferogram. The phase shift imparted by the sample appears as a phase offset in each vertical oscillation.

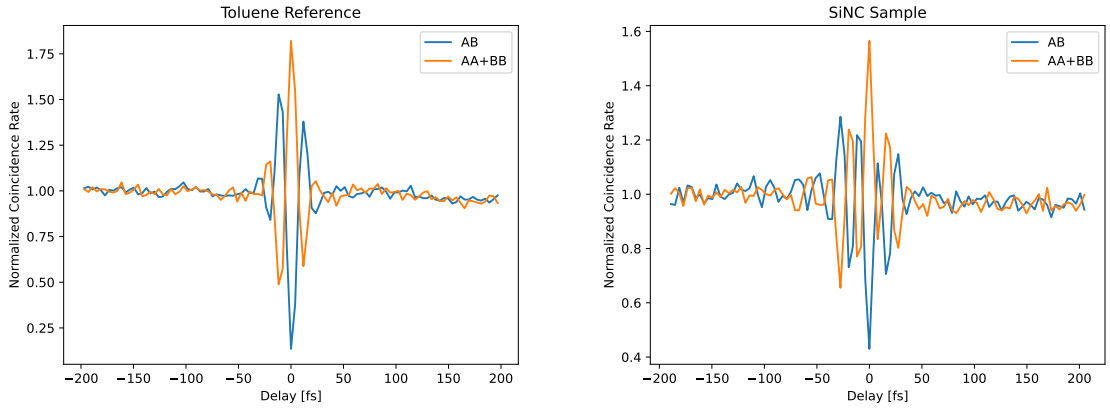

(a) (b)

Figure 3.5: Measured HOM dips for both the reference (a) and dye (b) samples. Each curve is obtained by summing over the horizontal frequency axis in interferograms of the type shown in Figures 3.3 and 3.4. The curves labeled "AB" are those obtained from the JSIs for antibunched pairs, involving a single detection from each beamsplitter port. The curves labeled "AA+BB" are obtained from JSIs for bunched pairs, in which both photons are observed at the same output port of the beamsplitter. These JSIs show complementary two-photon interference fringes.

3.6.2 The absorption spectrum

Raw rates of single clicks are first used to estimate the ratio of the quantum efficiencies of the two spectrometer arms using (3.19). Single and coincidence rates are then scaled by this ratio so as to correct for this imbalance. (That is, a single factor of this ratio is used to scale the singles rates; two factors are used to scale the coincidence rates.) This eliminates one of the two efficiencies η_{c_i}, η_{d_i} in favour of the other, so that all count rates are proportional to a single frequency-dependent detection efficiency, as discussed at the start of Section 3.5. An estimate of the transmission spectrum is obtained from the scaled coincidence and singles rates using the expression (3.28).

The measured transmission spectrum for the SiNC dye is presented in Figure 3.6, which shows results based on both the heralded method and on the singles rates alone. The same figure also shows the transmission spectrum as measured with a conventional spectrometer.

The transmission profile shows qualitative agreement with the conventionally-determined spectra, but in each case quantitative disagreements are observed. The disagreement in the absorption profile is believed to be due to changes in the signal beam's direction upon passage through the cuvette. The glass cuvettes containing the two samples were observed to have slightly different wedges, so that insertion of a cuvette into the spectrometer changed the portion of the down-converted beam which is later coupled into single-mode fibers. A pair of $f = 5$ cm planoconvex lenses were placed one focal length before and after the sample, which increased the numerical aperture of the beam at the location of the sample and reduced this effect. Nevertheless, it was observed that significant reductions in the count rates were introduced when adding cuvettes even with these lenses present, which could not be explained by the known absorption of the sample. Since the calibration, reference sample, and sample-of-interest measurements were made with different cuvettes present, this introduced a source of variation which is not accounted for in the simple model of Section 3.4, and which cannot be corrected for without significant additional characterization. The molecular absorption profile was measured using a commercial spectrometer containing a separate optical setup, and so does not suffer from alignment issues to the same extent.

Considering the model of Section 3.4, addition of a glass wedge in the sample arm acts to change the spatial mode of the field which couples into the single mode fibers. Due to optical reciprocity, this fiber mode can be traced backwards through the interferometer; after transmission through the cuvette, part of the optical mode will terminate at the nonlinear crystal, and part will exit the interferometer due to scattering outside of the beam's aperture. The portion of the fiber mode which intersects the nonlinear crystal will contribute optical photons, which will show some correlation with the photons contained in the reference mode. Due to unitarity, the portion of the fiber mode which scatters outside of the aperture will appear as result in additional optical loss between the crystal and the detector. Since the cone of down-converted photons contains a large number of spatial modes, it is possible that the probe spectrum $|\psi_i|$ observed with the cuvette in place is not the same spectrum observed with the cuvette removed; ultimately, this is due to the spatial-spectral correlations that exist in the down-converted beam as a result of the phase matching conditions. The second effect, leading to additional optical loss, will lead to a sample transmission spectrum T_i which is lower than would be the case if loss only occurred due to sample transmission. In a classical spectrometer, the only variable of interest is the field amplitude $\sqrt{T_i}\psi_i$ leaving the sample arm. In the HOM interferometer, these two variables contribute distinct errors to the measured spectrum due to the measurement's reliance on correlations.

The heralding ratios, which are ratios of spectra obtained from a single measurement of a fixed cuvette, is not affected by changes to $|\psi_i|$. The correction factor used in the heralded measurement also involves ratios of intensities obtained from different cuvettes. The absorption estimate using the heralding ratios will therefore be sensitive to changes in $|\psi_i|$ arising from the reference cuvette, but will not be affected by similar changes arising from the sample cuvette. By comparison, additional loss included in $T_i^{(s)}$ is expected to affect both the heralded and singles measurements of absorption similarly. The systematic errors observed in the heralded and singles-based measurements in Figure 3.6 are similar and appear only as an additional reduction in the measured transmission, which suggests that scattering of light out of the beam path by the wedge may be the dominant source of error in the present experiment.

3.6.3 The phase spectrum

The phase spectrum of the sample is obtained by fitting a sinusoid to each column of Figure 3.4(b). The resulting phase function has a large linear component due to the group delay imparted by the cuvette. To correct for this delay, we calculate the shift τ_{dip} in the HOM dip's peak (Figure 3.5) due to the sample, and subtract the corresponding phase gradient $\omega\tau_{\text{dip}}$. The resulting profile is shown in Figure 3.7, together with a phase profile calculated by applying the Kramers-Kronig relations to the conventionally-measured absorption profile. The spectrum of each sample is measured ten times, and error bars indicate the standard deviation of the measurements. Each plot shows only those wavelengths below the degeneracy point (810 nm); as discussed earlier, the SiNC molecules are expected to have negligible absorption and phase profiles at measured wavelengths larger than this. Due to differences in the thickness of the different glass cuvettes used, a substantial group delay is found when comparing phase measurements between the two samples. As our method is sensitive to the absolute phase shift, this group delay appears as a gradient in the phase spectrum; this should be contrasted with the Kramers-Kronig calculation, which is inherently insensitive to any delay-related phases. The magnitude of this delay is estimated based on the shift in the (non-frequency-resolved) HOM dip, obtained by summing over all frequency bins (Figure 3.5), and a corresponding phase correction has been applied.

In the phase measurement, changes in $|\psi_i|$ lead only to a change in the amplitude of the observed coincidence oscillations, so that a change in the probe spectrum due to the cuvette is not expected to lead to systematic errors in the phase spectrum. Deflections due to the cuvette may introduced an additional group delay in the cuvette measurements; this group delay is expected to be much smaller than that due to propagation through the cuvette glass. Additional group delay between different measurements has been estimated based on the position of the HOM interferogram, and this group delay has been removed from the phase shift shown in Figure 3.7. Changes to the transmission spectrum T_i due to scattering by the cuvette are also expected to lead to additional measured phase shifts. This may be the cause of the systematic errors seen in the phase measurements. Since the cuvette-related losses extend outside of

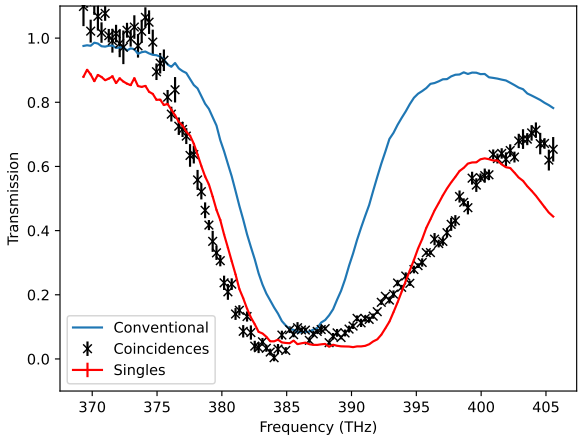

Figure 3.6: Estimated absorption profile for the SiNC dye. The blue curve shows the absorption profile measured with a commercial spectrometer. Black points indicate the absorption profile estimated from the coincidence-to-singles ratio, as discussed in Subsection 3.5.1. Error bars on these points are the standard error calculated from ten repeated measurements. The red curve shows the absorption profile estimated from the ratio of singles counts measured with the reference and dye samples. Error bars on the red curve are too small to be visible.

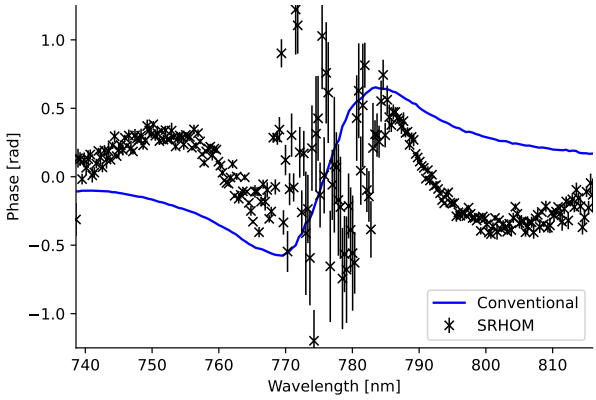

Figure 3.7: Estimated phase profile for the SiNC dye. The blue curve shows the profile predicted from the Kramers-Kronig relations applied to the conventional absorption profile shown in Figure 3.6. The black points show the phase profile estimated from shifts in the positions of oscillations in the interferogram Figure 3.4. Error bars on these points are the standard error calculated from ten repeated measurements.

the measured bandwidth in Figure 3.6, it is not possible to correct for these phase shifts using the data available at present.

Errors of the types previously mentioned can be reduced by suitable changes to the method of collection of light out of the sample. One option is to fiber-couple the light both before and after each sample; this allows for an independent measurement of transmission through the sample which nevertheless experiences identical losses due to scattering by the cuvette. Alignment through the cuvette can be optimized using a commercial spectrometer to ensure that scattering by the glass has minimal effect, which should in turn reduce errors in the heralded measurement. A second option is to increase the numerical aperture of the lenses before and after the sample, to further minimize scattering losses; this was avoided due to the increased aberrations coming from optical misalignment. A third option is to avoid the use of single-mode fiber altogether, which would also reduce sensitivity to misalignment. This is the approach taken by many practical spectrometers. At the same time, removing single-mode fibers may act to reduce the interferometric visibility due to a reduction in spatial overlap between the two beams. Fourier-transform spectrometry techniques, however, typically do not involve any spatial filtering. Entirely free-space quantum interferometric spectroscopy may therefore be a viable practical technique.

3.7 Conclusions

This method of spectrally-resolved Hong-Ou-Mandel interference allows one to perform simultaneous measurement of the linear-optical absorption and phase spectra imparted by a sample. Crucially, the absorption measurement relies on heralding information — that is, on the ratio of coincidence counts to single counts — which is not affected by the HOM-based phase measurement. If the only source of loss in the experiment comes from the sample, then the unpaired single detections allows one to determine the exact number of photons absorbed by the sample at each frequency. In traditional heralded measurements, the number of coincidence detections allows one to also determine the exact number of transmitted pairs, which results in an optimal measurement of the sample absorption. The situation is more complicated here, however,

due to the presence of the beamsplitter. As discussed in Subsection 3.5.1, coincidence clicks involving transmission through the sample of a photon at ω_i are indistinguishable from clicks involving transmission at the correlated frequency ω_{N+1-i}. The HOM method therefore provides less absorption information per coincidence click than a traditional heralded measurement. This issue is examined in more detail in Chapter 4, which examines the classical Fisher information for a model of the experiment. By this method, one finds that the HOM-based spectroscopy saturates the quantum limit for absorption measurement when loss in the experiment is low. In this limit, the majority of the absorption information comes from the relatively rare instances in which a photon is absorbed, so that the degraded coincidence information is unimportant.

The same indistinguishability also introduces a practical challenge since the absorption is no longer simply related to the heralding ratio. Our demonstration relies on a correction factor (3.28) which must be determined using calibration measurements. We have not examined the uncertainty arising from the absorption estimator (3.28), which is necessary for proper metrological demonstrations. In fact, from Figure 3.6, it is expected that our estimator is not optimal, since the estimator which includes heralding information has much larger uncertainty than the simple estimator based only on the rate of single detections. A better method would use the singles-only estimator as a prior estimate, which could then be updated to an appropriate extent using the heralding information. More generally, it is not necessary to rely on analytic estimators; maximum likelihood estimation saturates the classical Fisher information in the limit of a large number of samples [38]. Another option is to use machine learning algorithms to approximate the optimal estimator [126]; here, the challenge is to build a large database of measurement results to allow for training.

It is useful to also consider the properties of the HOM measurement from the perspective of practical chemical spectroscopy. Here, the method performs well. The interferometer is quite phase-stable since the phase of the interference pattern depends on the path length L through a term $\Delta\omega L/c$, which depends on the difference of two optical frequencies; this is to be contrasted with the $\omega L/c$ dependence of classical (*e.g.* Michelson) interferometers. The current measurements were made on a timescale of a few minutes, but

the interferometer was observed to be stable over many hours without the use of active phase stabilization. The use of SPDC provides continuous bandwidths exceeding 100 nm using only a narrowband cw pulse. The introduction of time-tagged detection also automatically provides a coarse time resolution on the order of a few nanoseconds, which allows one to easily incorporate signal modulation techniques at frequencies up to hundreds of megahertz.

The early stage of development of these time-tagging cameras does place some restrictions on the measurement, however. The most serious of these is the relatively low quantum efficiency of the intensifier and sensor, which in this experiment was about 10%. As mentioned above, and discussed in more detail in Chapter 4, this method is most useful when system losses are low, since any additional (non-sample) losses tend to degrade the quantum correlations upon which the method relies. Image intensifiers with quantum efficiencies of up to 50% are commercially available, but at the cost of much longer phosphor decay times. The development of high-efficiency photocathodes and fast phosphors therefore seems vital if this method is to find practical application. Less serious concerns involve the pixel-limited spectral resolution and the exposure limits of the camera. The spectral resolution, which is currently limited to about 250 bins due to the sensor resolution, can be improved by "wrapping" the dispersed beam of photons across multiple camera rows; currently, only two rows of the camera sensor are used, whereas it may be possible to illuminate dozens of rows, which would increase the spectral resolution by a similar factor. The spectrometer's throughput is currently constrained by saturation of the camera, which limits the exposure to about 200 photons per pixel per second; exposing more camera pixels would similarly lower the necessary exposure time. Alternatively, linear arrays of avalanche diodes are now available, offering 512 pixels per package with improved time resolution and quantum efficiency compared to time-tagging cameras [124]. At very high exposures, one will encounter signal-to-noise difficulties associated with "accidental" coincidence counts. In a fixed time interval, two independent, randomly-distributed streams of photons have some chance of containing a click, which will lead to an erroneous coincidence detection. This probability increases quadratically with the rate of single clicks, whereas the true coincidence rate increases linearly. For sufficiently high photon fluxes, then, a large fraction of detected coincidences will

be due to these uncorrelated "accidental" clicks. This can be partially improved through the use of better filtering methods, such as the time-frequency correlation-based filtering we use in this experiment. Ultimately, given a fixed detector time response and spectral resolution, this problem will set the ultimate limit to the allowable photon flux, and hence will set a minimum exposure time.

Having discussed the fundamental concerns limiting the usefulness of the method, it should be noted that the absorption and phase estimates shown in Figures 3.6 and 3.7 are not limited by the available precision, but instead by large systematic errors. These errors are believed to be due to beam deflections introduced by the sample cuvette, which lead to unaccounted-for changes in the measured spectra., as discussed in Section 3.6. Future experiments aim to reduce these errors, allowing for truly quantitative spectroscopy. One approach forgoes the use of fiber coupling altogether, so that beam deflections do not introduce large losses; this also greatly decreases the system losses, which in the current experiment are due in large part to the fiber coupling. This introduces a new challenge, since beam alignment must be maintained to preserve a high interference visibility. The beam alignment can be tracked and corrected using the single-photon-sensitive camera, however. Another method uses a fiber-coupled SPDC source, with one photon being fed through a sample holder which is also has fiber-coupled input and output. The sample fibers can be connected to either the quantum spectroscopy setup, or to a classical white light source and spectrometer; the classical spectrometer can be used to measure the transmission of the entire fiber-sample-fiber stage, which can then be quantitatively compared to the estimates obtained from the quantum spectrometer. After addressing the systematic errors, it becomes possible to pursue a demonstration of a true per-photon quantum advantage.

Experimental quantum metrology has so far focused on separate optimization of absorption and phase information. In the context of material spectroscopy, these tasks become intertwined, so that one is instead concerned with maximizing the information about electronic parameters that is jointly expressed through the absorption and phase spectra. The Hong-Ou-Mandel method we have demonstrated is one avenue by which this information can be improved; notably, it introduces phase sensitivity to the already optimal heralded-photon absorption measurement, with, at least for low losses, little degradation in absorption in-

formation. It is not the only means by which one can estimate absorption and phase — any interferometric phase measurement will of course be sensitive to absorption, since one can measure also the decrease in total measured intensity. In this way, one can consider other well-known interferometric methods, such as the N00N state interferometer, from the perspective of joint estimation. More broadly, the recognition that many spectroscopic tasks are indeed an example of this parameter estimation should lead to greater focus on improving low-light spectroscopy through a joint measurement of both absorption and phase.

4

Metrological performance of Hong-Ou-Mandel-based spectroscopy

4.1 Introduction

The experiment discussed in the previous chapter was motivated by a desire to introduce phase sensitivity to existing heralded absorption measurements. This phase sensitivity arises from the indistinguishability of pairs for which the probe is at ω_1 and the herald at ω_2, and pairs for which the probe is at ω_2 and the herald at ω_1. In traditional heralded absorption measurements, the exact number of photons transmitted by the sample arm is (ideally) equal to the number of coincidence detections. By introducing indistinguishability between transmissions at two possible frequencies, the Hong-Ou-Mandel-based spectroscopy is unable to distinguish transmission at ω_1 from transmission at ω_2, which somewhat degrades the absorption information compared to standard heralding methods. It is therefore necessary to quantify the amount of absorption information available using the HOM method to determine the circumstances under which it surpasses classical spectroscopic methods.

This chapter examines the exact precision bounds governing absorption and phase measurement with the HOM method. It does this by evaluating the classical multiparameter Cramér-Rao bounds for the

absorption and phase at each frequency. The key parameters determining the precision of each variable are the various losses experienced by the photon pair. We first consider the lossless case, in which any photon loss is due to absorption by the sample. Following this discussion, we examine the impact of various losses on the absorption and phase precision bounds.

This line of research is motivated in large part by the view that spectroscopic measurement can be viewed as estimation of the various model parameters describing a sample's optical response. As discussed in Chapter 3, a sample's absorption and phase spectra can be parameterized by a set of variables describing the electronic response of the sample, such as resonance wavelengths, oscillator strengths, and line widths, as well as environment parameters such as the temperature of the bath. The same set of variables determine both the absorption and phase response of the sample, and conversely, both the absorption and phase spectra yield information about the values of these parameters.

It is interesting to ask: to what extent does phase information improve in estimation of these parameters? A complete calculation of the precision bounds for this parameter estimation problem requires a detailed model of the parameters of interest and of their relation to the absorption and phase at each frequency — it is then difficult to extrapolate from the results of such a calculation due to the many problem-specific details that must be included. Section 4.4 discusses a somewhat heuristic approach to this question based on a single figure-of-merit describing both absorption and phase estimation. This allows direct comparison between the HOM method, classical spectroscopy, and heralded absorption measurement in the context of this joint estimation task.

While experimental investigation into joint absorption-and-phase measurements is still in early stages, recent years have seen a steady increase in the theoretical interest of such a task. The idea that absorption and phase variables may be based on a common set of parameters was first identified in a metrological context by Birchall *et al.* [127]. They consider estimation of a single unknown parameter which is jointly encoded in both spectral variables, showing that the quantum Fisher information of such a variable is (up to some prefactors) the sum of the absorption information and the phase information. They also show that squeezed coherent states can have precision exceeding that of a classical state with a similar number of

probe photons. Other work on absorption-and-phase measurements considers independent measurement of both parameters, rather than any relation to a set of underlying variables. Gianani *et al.* [115] consider the relationship between precision in absorption measurements and precision in phase measurements when the two quantities are linked by the Kramers-Kronig relations. Other research has focused on the role of incompatibility in measurements of absorption and phase [128, 129], which generally introduces a trade-off between precision in one and precision in the other. Of note, these investigations have recently revealed that the quantum Fisher information for phase and absorption only shows incompatibility at small numbers of photons; as the number of probe photons increases, a single probe state can be optimal for both variables [130, 50]. Specifically, Ref. [50] distinguishes between "probe incompatibility" (the ability of a single probe state to be optimally sensitive to both parameters) and "measurement incompatibility" (the ability of a single measurement to optimally extract information about both parameters). For large photon numbers, the probe incompatibility vanishes, whereas the measurement incompatibility does not — a single state is optimally sensitive to absorption and phase, but no measurement saturates the precision bound for both variables. The same work shows that entanglement between the sample beam and an auxiliary beam can reduce the amount of measurement incompatibility between the two variables, and in fact a second auxiliary mode is necessary if one wishes to have a Gaussian state (which includes any coherent displacement, squeezing, or thermal noise) that saturates the quantum bounds. It should be noted that the current work, which relies on two spatial modes and two frequencies, is a four-mode measurement, and so does not fall under their framework.

This chapter is organized as follows. Section 4.2 makes some general remarks about the calculation of the classical Cramér-Rao bound. In particular, it relates spectroscopic measurements involving a large number N of frequencies to a simplified model involving only pairs of correlated frequencies. It argues that, under some mild assumptions, the metrological performance of the HOM measurement can be analyzed by considering only two frequencies at a time. It then discusses the mathematical model of the measurement, which is largely similar to that of Section 3.4. Section 4.3 considers first the lossless limit of phase and absorption estimation, and shows that the absorption measurement in this case approaches the optimal

quantum bound, while the phase measurement is shot noise-limited. It then considers the various types of loss that might exist in the measurement, and compares the absorption and phase precision with classical methods and (in the case of absorption) with the heralded measurement. Finally, Section 4.4 discusses the relationship between the absorption and phase bounds and the problem of estimating parameters which affect both types of spectra. It provides a heuristic figure of merit, and with it compares the overall performance of the HOM method to that of a Mach-Zehnder interferometer, a heralded absorption measurement, and a two-photon N00N-state interferometer, which serves as an alternative method of quantum interferometric spectroscopy.

Throughout this chapter, a general benchmark in comparisons is the shot noise limit. In all discussions, this refers to a classical measurement which experiences the same losses and detector inefficiencies as the quantum method in question. In the case of absorption, this optimal classical measurement is a measurement of transmitted power with a coherent state as input; for phase measurements, the optimal classical measurement is a shot noise-limited interferometer. Performance is generally characterized in terms of the precision (*i.e.*, inverse Cramér-Rao bound) divided by the average number of probe photons incident on the sample at the frequency of interest. For interferometric phase measurements, this is not the same as the precision-per-input photon, since not all photons interact with the sample.

Even in the classical case, there is generally a trade-off between per-photon sensitivity to absorption and phase. As we discuss in Section 4.3, the optimal classical phase measurement uses a highly imbalanced interferometer with a tiny fraction of the incident power being transmitted through the sample. This same measurement gives almost zero information about absorption, since a similarly tiny amount of power is actually absorbed. The discussion in Section 4.3, which considers separately the bounds for absorption and phase, makes comparisons with both the optimal classical single-parameter measurements of absorption and phase (the shot noise limit), and also with the case of a balanced classical interferometer. Section 4.4, which considers the total information for both absorption and phase, defines the shot noise limit to be the precision a classical interferometer, where all beamsplitter reflectivities have been chosen so as to optimize the figure-of-merit in question.

4.2 Description of the problem

This section describes a simplified model of the experiment which is used for further calculations. As in the previous chapter, we assume that the probe beam can be described by a photon pair, with one photon propagating in each of two spatial modes. We also assume perfect frequency anticorrelations in the state, which corresponds to the assumption of a narrowband pump beam.

Denoting annihilation operators for frequency bin ω_i in the two spatial modes by a_i and b_i, the probe state has the form

$$\sqrt{1-g}\,|0\rangle + \sqrt{g}\sum_{i=1}^{N}\psi_i a_i^\dagger b_{N+1-i}^\dagger\,|0\rangle\,. \tag{4.1}$$

Here g is some parameter describing the probability of possessing a photon pair in a given trial. Normalization of the state requires that $\sum_i|\psi_i|^2=1$.

The photodetectors used at the end of the experiment are assumed to be frequency-resolving. In principle, for N spectral bins monitoring each of the two output ports of the interferometer, there are 2^{2N} possible experimental outcomes, since dark counts allow any combination of detector bins to click in a given trial. This leads to an analytically and numerically intractable problem, since calculation of the corresponding Fisher information involves summation over 2^{2N} terms for each matrix element. We therefore neglect the effect of dark counts at the detector. A given trial therefore involves zero, one, or two detector clicks. By assumption, two simultaneous clicks must belong to frequency-anticorrelated bins.

We will determine the sensitivity of the spectroscopic method by calculating the relevant classical Fisher information matrix. The effect of an arbitrary spectroscopic sample is described by N absorption parameters α and N phase shifts ϕ acting on one spatial mode. The complete estimation problem therefore involves $2N$ unknown parameters, and the corresponding classical Cramér-Rao bound is determined by a

$2N$ by $2N$ real symmetric matrix $\boldsymbol{\mathcal{F}}$ whose elements are given by (1.57),

$$\mathcal{F}_{\zeta\zeta'} = \sum_k \frac{1}{p_k} \left(\frac{\partial p_k}{\partial \zeta}\right) \left(\frac{\partial p_k}{\partial \zeta'}\right), \tag{4.2}$$

where ζ, ζ' are each one of the $2N$ unknown parameters. After neglecting dark counts, each matrix element is determined by a sum over all measurement outcomes, of which there are $5N + 1$: one outcome corresponding to no detector clicks, $2N$ possible clicks for a single photon, and $4N$ possible paired clicks ($2N$ possible positions for the first click, which determines the position of the second click up to a choice of one of two spatial modes).

Due to the assumption of perfect frequency anticorrelations, the probability of a single or coincidence click involving the frequency ω_i can depend only on the absorption and phase parameters at frequencies ω_i and ω_{N+1-i}. Each spectral bin therefore relates to four parameters, which are the absorption and phase parameters at ω_i and ω_{N+1-i}. Conversely, consider the calculation of some fixed element of the Fisher information matrix. If the element is in a row or column related to parameter ζ, then every term in the summation (4.2) involves a derivative with respect to ζ. If ζ is one of the four parameters related to the frequency pair ω_i and ω_{N+1-i}, then every term which involves clicks at an unrelated frequency vanishes. It should be noted here that the term corresponding no-click outcome, whose probability depends on all absorption coefficients, does not vanish whenever ζ is an absorption parameter. It follows that when ζ and ζ' are parameters relating to distinct frequency pairs, every term in the calculation except for the no-click

term necessarily vanishes, and $\boldsymbol{\mathcal{F}}$ takes the form

$$\boldsymbol{\mathcal{F}} = \begin{pmatrix} \mathcal{F}_{\alpha_1\alpha_1} & \mathcal{F}_{\alpha_1\alpha_N} & \mathcal{F}_{\alpha_1\phi_1} & \mathcal{F}_{\alpha_1\phi_N} & & & & \\ \mathcal{F}_{\alpha_N\alpha_1} & \mathcal{F}_{\alpha_N\alpha_N} & \mathcal{F}_{\alpha_N\phi_1} & \mathcal{F}_{\alpha_N\phi_N} & & & & \\ \mathcal{F}_{\phi_1\alpha_1} & \mathcal{F}_{\phi_1\alpha_N} & \mathcal{F}_{\phi_1\phi_1} & \mathcal{F}_{\phi_1\phi_N} & & & & \\ \mathcal{F}_{\phi_N\alpha_1} & \mathcal{F}_{\phi_N\alpha_N} & \mathcal{F}_{\phi_N\phi_1} & \mathcal{F}_{\phi_N\phi_N} & & & & \\ & & & & \mathcal{F}_{\alpha_2\alpha_2} & \mathcal{F}_{\alpha_2\alpha_{N-1}} & \mathcal{F}_{\alpha_2\phi_2} & \mathcal{F}_{\alpha_2\phi_{N-1}} \\ & & & & \mathcal{F}_{\alpha_{N-1}\alpha_2} & \mathcal{F}_{\alpha_{N-1}\alpha_{N-1}} & \mathcal{F}_{\alpha_{N-1}\phi_2} & \mathcal{F}_{\alpha_{N-1}\phi_{N-1}} \\ & & & & \mathcal{F}_{\phi_2\alpha_2} & \mathcal{F}_{\phi_2\alpha_{N-1}} & \mathcal{F}_{\phi_2\phi_2} & \mathcal{F}_{\phi_2\phi_{N-1}} \\ & & & & \mathcal{F}_{\phi_{N-1}\alpha_2} & \mathcal{F}_{\phi_{N-1}\alpha_{N-1}} & \mathcal{F}_{\phi_{N-1}\phi_2} & \mathcal{F}_{\phi_{N-1}\phi_{N-1}} \\ & & & & & & & \ddots \end{pmatrix} + \boldsymbol{\mathcal{F}}^{(\mathbf{0})}, \tag{4.3}$$

where $\boldsymbol{\mathcal{F}}^{(\mathbf{0})}$ is the contribution due to the no-click outcomes,

$$\mathcal{F}^{(0)}_{\zeta\zeta'} = \frac{1}{p_0}\left(\frac{\partial p_0}{\partial \zeta}\right)\left(\frac{\partial p_0}{\partial \zeta'}\right) \tag{4.4}$$

If not for this no-click contribution, the classical Fisher information matrix takes the form of a block-diagonal matrix, with each block describing the four parameters relating to a pair of anticorrelated frequencies.

The absence of a click is typically not recorded in practice. Rather, many trials of the measurement are performed, and the total number of clicks of each type are recorded. This distinction is important to note in calculations of the Fisher information — as noted in Section 2.4, measurements which count only the number of clicks have access to less metrological information than those which also know the total number of trials (equivalently, the number of copies of the state (4.1)). The number of clicks of a fixed type in N trials is then a Poisson-distributed random variable whose mean is N times the probability of the same click pattern in a single trial. The random variables describing different click patterns are

related only in that the total number of clicks of all types (including the no-click pattern) must sum to the number of trials N. If one records only those experimental outcomes in which a detector click is observed, the various Poisson-distributed counts can be regarded as independent variables, so that each Fisher information matrix element is just the sum of the contributions from each individual click count. (Strictly speaking, this neglects the remaining constraint that the sum of all counts cannot exceed N. We restrict our analysis to the limit $g \to 0$ in which photon pairs are rarely produced, so that the probability of a click in a given trial is small; it follows that the probability of N or more clicks in N trials is negligible). Under this assumption, the classical Fisher information determined by the distribution of counts for clicks of all types, but excluding trials leading to no click, is equal to the number of trials N times a matrix which is the same as (4.3), but now excluding terms related to the no-click outcome. Appendix B presents a short proof that this neglect of the no-click outcome results in an effective Fisher information which always lower bounds the true value, so that this procedure results in a useful (*i.e.*, saturable) metrological bound. Under this assumption, then, the classical Fisher information matrix breaks into a block-diagonal form.

Under the conditions described above, the problem of determining the precision of the spectroscopic measurement can be analyzed by considering a single pair of correlated frequencies which involves four unknown parameters, consisting of two absorption and two phase variables. The complete classical Cramér-Rao bound is determined by the inverse of a block-diagonal classical Fisher information matrix which consists of one block for each pair of frequencies; since the inverse of a block-diagonal matrix is also block-diagonal, the precision limits for a given variable depends only on the matrix block associated with the related pair of frequencies. The problem can then be analyzed entirely using a model which includes only two frequencies and four unknown parameters.

4.2.1 A two-frequency model of spectrally-resolved HOM

Based on the preceding discussion, the probe state for the simplified model can be written in the form

$$\sqrt{1-g}\,|0\rangle + \sqrt{g}\psi_1 a_1^\dagger b_2^\dagger\,|0\rangle + \sqrt{g}\psi_2 a_2^\dagger b_1^\dagger\,|0\rangle\,. \tag{4.5}$$

This state is used to probe a spectroscopic sample (in spatial mode a), and a relative delay τ is placed on the reference photon (in spatial mode b). The action of these two components can be written in the form

$$a_i^\dagger \longmapsto e^{-\alpha_i/2+i\phi_i}a_i^\dagger + \sqrt{1-e^{-\alpha_i}}\,s_i^\dagger, \qquad b_i^\dagger \to e^{-i\omega_i\tau}b_i^\dagger, \tag{4.6}$$

where absorption by the sample is described by scattering into an auxiliary pair of modes s_i. We also introduce additional losses into each arm, described by transmittances T_i for the sample arm and R_i for the reference arm, using similar auxiliary modes. The modes a and b are inputs to a 50:50 beamsplitter with output ports c and d. The four modes after the beamsplitter (two frequencies in each of the spatial modes c and d) are detected at four corresponding photodetectors with efficiencies η_{c_i} and η_{d_i} which may depend on frequency. This model is essentially the same one described in Section 3.4, and the state prior to detection has the form

$$\begin{aligned}
\rho_{\text{out}} = g\left[|\psi_1|^2(1-T_1e^{-\alpha_1})(1-R_2) + |\psi_2|^2(1-T_2e^{-\alpha_2})(1-R_1)\right]|0\rangle\langle 0| \\
+ \frac{g}{2}(1-T_1e^{-\alpha_1})R_2|\psi_1|^2(c_2^\dagger - d_2^\dagger)\,|0\rangle\langle 0|\,(c_2-d_2) \\
+ \frac{g}{2}(1-T_2e^{-\alpha_2})R_1|\psi_2|^2(c_1^\dagger - d_1^\dagger)\,|0\rangle\langle 0|\,(c_1-d_1) \\
+ \frac{g}{2}(1-R_2)T_1e^{-\alpha_1}|\psi_1|^2(c_1^\dagger + d_1^\dagger)\,|0\rangle\langle 0|\,(c_1+d_1) \\
+ \frac{g}{2}(1-R_1)T_2e^{-\alpha_2}|\psi_2|^2(c_2^\dagger + d_2^\dagger)\,|0\rangle\langle 0|\,(c_2+d_2) \\
+ |\psi_{\text{out}}\rangle\langle\psi_{\text{out}}|\,,
\end{aligned} \tag{4.7}$$

where $|\psi_{\text{out}}\rangle$ is the (unnormalized) state vector

$$\begin{aligned}|\psi_{\text{out}}\rangle = &\sqrt{1-g}\,|0\rangle \\ &+ \frac{\sqrt{g}}{2}\psi_1\sqrt{T_1R_2}e^{-\alpha_1/2+i\phi_1-i\omega_2\tau}(c_1^\dagger + d_1^\dagger)(c_2^\dagger - d_2^\dagger)\,|0\rangle \\ &+ \frac{\sqrt{g}}{2}\psi_2\sqrt{T_2R_1}e^{-\alpha_2/2+i\phi_2-i\omega_1\tau}(c_2^\dagger + d_2^\dagger)(c_1^\dagger - d_1^\dagger)\,|0\rangle\,. \end{aligned} \tag{4.8}$$

Unlike the previous chapter, we consider the raw count rates of each type, rather than the rates corrected for detector efficiency. We therefore consider the POVM given by (3.13), which has been truncated to consider only the zero-, one-, and two-photon subspaces. It is helpful to first define the quantities

$$q_0 = \text{Tr}\left[\rho_{\text{out}}\ |0\rangle\langle 0|\right], \tag{4.9a}$$

$$q_1 = \text{Tr}\left[\rho_{\text{out}}\, c_1^\dagger\,|0\rangle\langle 0|\, c_1\right] = \text{Tr}\left[\rho\, d_1^\dagger\,|0\rangle\langle 0|\, d_1\right], \tag{4.9b}$$

$$q_2 = \text{Tr}\left[\rho_{\text{out}}\, c_2^\dagger\,|0\rangle\langle 0|\, c_2\right] = \text{Tr}\left[\rho\, d_2^\dagger\,|0\rangle\langle 0|\, d_2\right], \tag{4.9c}$$

$$q_{12}^{(b)} = \text{Tr}\left[\rho_{\text{out}}\, c_1^\dagger c_2^\dagger\,|0\rangle\langle 0|\, c_1c_2\right] = \text{Tr}\left[\rho\, d_1^\dagger d_2^\dagger\,|0\rangle\langle 0|\, d_1d_2\right], \tag{4.9d}$$

$$q_{12}^{(ab)} = \text{Tr}\left[\rho_{\text{out}}\, c_1^\dagger d_2^\dagger\,|0\rangle\langle 0|\, c_1d_2\right] = \text{Tr}\left[\rho\, d_1^\dagger c_2^\dagger\,|0\rangle\langle 0|\, d_1c_2\right], \tag{4.9e}$$

which are given by

$$q_0 = (1-g) + g|\psi_1|^2(1-T_1e^{-\alpha_1})(1-R_2) + g|\psi_2|^2(1-T_2e^{-\alpha_2})(1-R_1), \tag{4.10a}$$

$$q_1 = \frac{g}{2}T_1e^{-\alpha_1}(1-R_2)|\psi_1|^2 + \frac{g}{2}(1-T_2e^{-\alpha_2})R_1|\psi_2|^2, \tag{4.10b}$$

$$q_2 = \frac{g}{2}T_2e^{-\alpha_2}(1-R_1)|\psi_2|^2 + \frac{g}{2}(1-T_1e^{-\alpha_1})R_2|\psi_1|^2, \tag{4.10c}$$

$$q_{12}^{(b)} = \frac{g}{4}T_1R_2e^{-\alpha_1}|\psi_1|^2 + \frac{g}{4}T_2R_1e^{-\alpha_2}|\psi_2|^2 + \frac{g}{2}\sqrt{T_1T_2R_1R_2}e^{-\alpha_1/2-\alpha_2/2}\text{Re}\left[\psi_1\psi_2^*e^{i(\phi_1-\phi_2)-i(\omega_2-\omega_1)\tau}\right], \tag{4.10d}$$

$$q_{12}^{(a)} = \frac{g}{4}T_1R_2e^{-\alpha_1}|\psi_1|^2 + \frac{g}{4}T_2R_1e^{-\alpha_2}|\psi_2|^2 - \frac{g}{2}\sqrt{T_1T_2R_1R_2}e^{-\alpha_1/2-\alpha_2/2}\text{Re}\left[\psi_1\psi_2^*e^{i(\phi_1-\phi_2)-i(\omega_2-\omega_1)\tau}\right]. \tag{4.10e}$$

The detection probabilities then have the form

$$\begin{aligned} p_0 = \mathrm{Tr}\left[\rho_{\mathrm{out}}\,\Pi_0\right] &= q_0 + (2-\eta_{c_1}-\eta_{d_1})q_1 + (2-\eta_{c_2}-\eta_{d_2})q_2 \\ &\quad + \left[(1-\eta_{c_1})(1-\eta_{c_2}) + (1-\eta_{d_1})(1-\eta_{d_2})\right] q_{12}^{(b)} \\ &\quad + \left[(1-\eta_{c_1})(1-\eta_{d_2}) + (1-\eta_{d_1})(1-\eta_{c_2})\right] q_{12}^{(ab)}, \end{aligned} \tag{4.11a}$$

$$p_{c_1} = \mathrm{Tr}\left[\rho_{\mathrm{out}}\,\Pi_{c_1}\right] = \eta_{c_1} q_1 + \eta_{c_1}(1-\eta_{c_2}) q_{12}^{(b)} + \eta_{c_1}(1-\eta_{d_2}) q_{12}^{(ab)}, \tag{4.11b}$$

$$p_{c_2} = \mathrm{Tr}\left[\rho_{\mathrm{out}}\,\Pi_{c_2}\right] = \eta_{c_2} q_2 + \eta_{c_2}(1-\eta_{c_1}) q_{12}^{(b)} + \eta_{c_2}(1-\eta_{d_1}) q_{12}^{(ab)}, \tag{4.11c}$$

$$p_{d_1} = \mathrm{Tr}\left[\rho_{\mathrm{out}}\,\Pi_{d_1}\right] = \eta_{d_1} q_1 + \eta_{d_1}(1-\eta_{d_2}) q_{12}^{(b)} + \eta_{d_1}(1-\eta_{c_2}) q_{12}^{(ab)}, \tag{4.11d}$$

$$p_{d_2} = \mathrm{Tr}\left[\rho_{\mathrm{out}}\,\Pi_{d_2}\right] = \eta_{d_2} q_2 + \eta_{d_2}(1-\eta_{d_1}) q_{12}^{(b)} + \eta_{d_2}(1-\eta_{c_1}) q_{12}^{(ab)}, \tag{4.11e}$$

$$p_{c_1 c_2} = \mathrm{Tr}\left[\rho_{\mathrm{out}}\,\Pi_{c_1 c_2}\right] = \eta_{c_1}\eta_{c_2} q_{12}^{(b)}, \tag{4.11f}$$

$$p_{d_1 d_2} = \mathrm{Tr}\left[\rho_{\mathrm{out}}\,\Pi_{d_1 d_2}\right] = \eta_{d_1}\eta_{d_2} q_{12}^{(b)}, \tag{4.11g}$$

$$p_{c_1 d_2} = \mathrm{Tr}\left[\rho_{\mathrm{out}}\,\Pi_{c_1 d_2}\right] = \eta_{c_1}\eta_{d_2} q_{12}^{(ab)}, \tag{4.11h}$$

$$p_{d_1 c_2} = \mathrm{Tr}\left[\rho_{\mathrm{out}}\,\Pi_{d_1 c_2}\right] = \eta_{d_1}\eta_{c_2} q_{12}^{(ab)}. \tag{4.11i}$$

This probability distribution determines the metrological performance of the spectroscopic method, which is given formally by the relevant classical Cramér-Rao bounds.

As described above, the classical Fisher information matrix related to a given pair of correlated frequencies ω_1 and ω_2 has the form of a four-by-four real symmetric matrix,

$$\mathcal{F} = \begin{pmatrix} \mathcal{F}_{\alpha_1\alpha_1} & \mathcal{F}_{\alpha_1\phi_1} & \mathcal{F}_{\alpha_1\alpha_2} & \mathcal{F}_{\alpha_1\phi_2} \\ \mathcal{F}_{\alpha_1\phi_1} & \mathcal{F}_{\phi_1\phi_1} & \mathcal{F}_{\phi_1\alpha_2} & \mathcal{F}_{\phi_1\phi_2} \\ \mathcal{F}_{\alpha_1\alpha_2} & \mathcal{F}_{\phi_1\alpha_2} & \mathcal{F}_{\alpha_2\alpha_2} & \mathcal{F}_{\alpha_2\phi_2} \\ \mathcal{F}_{\alpha_1\phi_2} & \mathcal{F}_{\phi_1\phi_2} & \mathcal{F}_{\alpha_2\phi_2} & \mathcal{F}_{\phi_2\phi_2} \end{pmatrix}. \tag{4.12}$$

Each element of the matrix is given by

$$\mathcal{F}_{\zeta\zeta'} = \sum_{p\in\mathcal{P}} \frac{1}{p}\frac{\partial p}{\partial \zeta}\frac{\partial p}{\partial \zeta'}, \tag{4.13}$$

where the sum is over the set $\mathcal{P} \equiv \{p_0, p_{c_1}, p_{c_2}, p_{d_1}, p_{d_2}, p_{c_1c_2}, p_{d_1d_2}, p_{c_1d_2}, p_{d_1c_2}\}$. The pair of parameters ϕ_1 and ϕ_2 appear in the distribution only in the combination $\phi_1 - \phi_2$. This is a consequence of the fact that the biphoton is a superposition of two terms, with one term acquiring a phase shift ϕ_1 and the other ϕ_2; the absolute phase $\phi_1 + \phi_2$ then appears as an unmeasurable global phase in the biphoton state, and only the relative phase can be measured. This is a consequence not of the spectroscopic measurement, but rather of the probe state itself. The consequence for the Fisher information is that the ϕ_1 and ϕ_2 rows (and similarly the corresponding columns) are linearly dependent, so that the matrix cannot be inverted, and the Cramér-Rao bound is undefined. To obtain a well-defined statistical problem, we can only consider estimation of the relative phase

$$\delta \equiv \phi_1 - \phi_2 \tag{4.14}$$

together with the two absorption parameters. The estimation problem therefore involves three unknown parameters, and the corresponding classical Fisher information matrix has the form

$$\mathcal{F} = \begin{pmatrix} \mathcal{F}_{\alpha_1\alpha_1} & \mathcal{F}_{\alpha_1\alpha_2} & \mathcal{F}_{\alpha_1\delta} \\ \mathcal{F}_{\alpha_1\alpha_2} & \mathcal{F}_{\alpha_2\alpha_2} & \mathcal{F}_{\alpha_2\delta} \\ \mathcal{F}_{\alpha_1\delta} & \mathcal{F}_{\alpha_2\delta} & \mathcal{F}_{\delta\delta} \end{pmatrix}. \tag{4.15}$$

Each derivative appearing in this matrix can in turn be written in terms of derivatives of the q_i, which are given in terms of the optical parameters of the measurement.

Due to the large number of terms involved in the calculation, explicit expressions for the matrix elements are not useful. Symbolic calculations using Mathematica have been used for analytical calculation of the

classical Cramér-Rao bounds, which after simplification can be used for numerical calculations. This approach has the advantage over purely numerical techniques in that difficulties associated with numeric stability of the matrix inversion can be handled by symbolic cancellation and limiting processes.

4.3 Evaluation of the precision bounds

We now consider the evaluation of the bounds described in the previous section. For simplicity, we first consider the lossless limit, in which the optical transmissions through each arm (apart from the unavoidable loss due to interactions with the sample) and the detector efficiencies are each unity. After this, we turn to the question of loss tolerance in the measurement, which may occur in the sample arm, the reference arm, or due to finite detector efficiency.

For concreteness, we focus on estimation of the absorption parameter α_1 and the relative phase shift δ. The bounds for α_2 are obtained upon relabeling of the spectral bin indices. In discussing the phase difference, we include the known phase $(\omega_1 - \omega_2)\tau$ in the definition of δ, which does not change the metrological information but does simplify the resulting expressions. In all cases, the quantity of interest for a given parameter is the multiparameter information per incident photon, of which there are $g|\psi_1|^2$ (we assume any loss in the sample arm occurs after the beam interacts with the sample). In counting the photons that interact with the sample, we only include those at the frequency of interest (ω_1 in this case), which implicitly assumes that the phase shift δ can be entirely attributed to one frequency; this is the case in the experiment of the previous chapter, where the spectral response of the sample was confined to one half of the probe's bandwidth. We always consider the limit of weak two-mode squeezing, for which the probability of producing a pair on a given trial $g \to 0$. The per-photon information in the multiparameter

case is then given by

$$\begin{aligned} C_{\alpha_1} &\equiv \lim_{g\to 0} \frac{1}{g|\psi_1|^2} \left((\mathcal{F}^{-1})_{\alpha_1\alpha_1}\right)^{-1} \\ &= \lim_{g\to 0} \frac{1}{g|\psi_1|^2} \left(\mathcal{F}_{\alpha_1\alpha_1} - \frac{\mathcal{F}_{\alpha_2\alpha_2}\mathcal{F}_{\alpha_1\delta}^2 + \mathcal{F}_{\delta\delta}\mathcal{F}_{\alpha_1\alpha_2}^2 - 2\mathcal{F}_{\alpha_1\alpha_2}\mathcal{F}_{\alpha_1\delta}\mathcal{F}_{\alpha_2\delta}}{\mathcal{F}_{\alpha_2\alpha_2}\mathcal{F}_{\delta\delta} - \mathcal{F}_{\alpha_2\delta}^2} \right), \end{aligned} \tag{4.16a}$$

$$\begin{aligned} C_{\delta} &\equiv \lim_{g\to 0} \frac{1}{g|\psi_1|^2} \left((\mathcal{F}^{-1})_{\delta\delta}\right)^{-1} \\ &= \lim_{g\to 0} \frac{1}{g|\psi_1|^2} \left(\mathcal{F}_{\delta\delta} - \frac{\mathcal{F}_{\alpha_1\alpha_1}\mathcal{F}_{\alpha_2\delta}^2 + \mathcal{F}_{\alpha_2\alpha_2}\mathcal{F}_{\alpha_1\delta}^2 - 2\mathcal{F}_{\alpha_1\alpha_2}\mathcal{F}_{\alpha_1\delta}\mathcal{F}_{\alpha_2\delta}}{\mathcal{F}_{\alpha_1\alpha_1}\mathcal{F}_{\alpha_2\alpha_2} - \mathcal{F}_{\alpha_1\alpha_2}^2} \right). \end{aligned} \tag{4.16b}$$

These have been defined so as to be the inverse of the corresponding classical Cramér-Rao bound, after normalizing by the number of photons.

4.3.1 Precision in the lossless limit

The lossless limit consists of the case $T_i \to 1, R_i \to 1, \eta \to 0$. In terms of the two amplitudes ψ_1 and ψ_2 in the frequency-entangled state (4.5), the per-photon absorption information takes the form

$$C_{\alpha_1} = \frac{e^{-\alpha_1}}{1-e^{-\alpha_1}} - \frac{e^{-\alpha_1}|\psi_2|^2}{e^{-\alpha_1}|\psi_1|^2+|\psi_2|^2}. \tag{4.17}$$

For arbitrary values of α_1, this is optimized when $|\psi_1|^2 \to 1$; in this limit, the scheme becomes a standard heralded absorption measurement (see Section C.3), and the multiparameter absorption information tends to the value $e^{-\alpha_1}/(1-e^{-\alpha_1})$, which saturates the quantum bound for single parameter absorption measurements. However, the phase information, which depends upon interference between the two terms in the state (4.5), vanishes in the same limit. If we instead suppose an equal superposition,

$$|\psi_1|^2 = |\psi_2|^2 = \frac{1}{2}, \tag{4.18}$$

then the multiparameter absorption information tends to the value

$$C_{\alpha_1} = \frac{2e^{-2\alpha_1}}{1-e^{-2\alpha_1}} = \coth\alpha_1 - 1. \tag{4.19}$$

This is a factor $(1+e^{-\alpha_1})/2$ smaller than the quantum bound.

When the sample absorption is low ($\alpha_1 \to 0$), the HOM measurement's absorption information approaches the optimal limit. Unlike a traditional heralded measurement, however, the HOM measurement performs worse than the shot noise limit when the sample loss is sufficiently large: for values of $\alpha_1 > \ln(1+\sqrt{2})$, or $e^{-\alpha_1} < 1/(1+\sqrt{2})$, the value of C_{α_1} falls below the information for a single-parameter, shot noise-limited absorption measurement of $e^{-\alpha_1}$.

The phase sensitivity in the same lossless limit is

$$C_\delta = \frac{8e^{-2\alpha}|\psi_2|^2\sin^2\delta}{2e^{-2\alpha}|\psi_1|^4 + (1+T+\cos 2\delta)\,|\psi_2|^4 - T\,(1-T+(2+T)\cos 2\delta)\,|\psi_1|^2|\psi_2|^2}, \tag{4.20}$$

which is maximum for phases near $\delta \approx \pi/2, 3\pi/2$. In this case, the phase information is

$$C_\delta = \frac{4e^{-\alpha}(1-|\psi_1|^2)}{1-(1-e^{-\alpha})|\psi_1|^2}. \tag{4.21}$$

The maximum per-photon phase information occurs in the limit $|\psi_1| \to 0$; this is analogous to a classical Mach Zehnder interferometer, in which the maximum per-photon sensitivity comes in the limit of vanishing probe intensity (see Section C.2). The phase information tends to zero in this limit, but the number of probe photons tends to zero in the same way, so that the information per probe photon approaches an asymptotic limit of $4e^{-\alpha}$, which is the same shot noise limit as occurs in a classical interferometer. In contrast to measurement of the sample absorption, which shows a near-optimal enhancement in sensitivity as compared to classical techniques, the phase sensitivity of the measurement shows the same shot noise-limited behaviour that is seen in classical interferometers. In a classical interferometer, this is due to the Poissonian statistics governing the number of photons emitted in a given time interval; in the case of the

HOM measurement, this is due to the Poissonian statistics governing the creation of biphotons at the nonlinear crystal. In this limit the absorption information vanishes, since no photons at the frequency of interest ω_1 interact with the sample. In all later analysis, we will assume a value of $|\psi_1| = |\psi_2| = \frac{1}{\sqrt{2}}$, which allows for estimation of both phase and absorption.

4.3.2 Loss-tolerance

A persistent challenge in applications of quantum metrology is the sensitivity of entangled probes to noise; in optical experiments, the main source of noise is usually due to optical losses. Optical losses tend to degrade nonclassical states of light, reducing quantum enhancements to measurement sensitivity [131]. When using entangled probe states, one often encounters a loss threshold, with excessive losses leading to *less* precision with the quantum strategy than with a comparable classical technique. The origin of this behaviour is simple to understand: optical losses tend to entangle the probe state with additional, unmeasured optical modes. In measurements of the probe state alone, this entanglement appears to cause decoherence, turning the initial pure probe state into a mixed state. The quantum technique then effectively uses this mixed state as a probe; under excessive losses, the probe state typically approaches a mixture of coherent states, which for many metrological tasks (such as phase measurement) is outperformed by a pure coherent state. A salient feature of heralded absorption measurements is that the technique outperforms classical measurements for any amount of loss. The shot noise limit for absorption acts as an asymptotic limit for the heralded measurement's precision as the loss increases, but at no point does the heralded measurement perform worse than the shot noise limit. As was shown in the previous subsection, this is not true for the HOM measurement; sample transmission below $1/(1+\sqrt{2})$ results in a precision that is below the shot noise limit. The rest of this section considers similar thresholds arising from other sources of loss in the measurement.

In the HOM method, three inequivalent forms of loss can occur: the loss can appear in the sample arm, in the herald arm, or after the beamsplitter. We generally denote sample arm transmission by T_i, reference arm transmission by R_i, and describe post-beamsplitter loss using a detector efficiency η_i. We

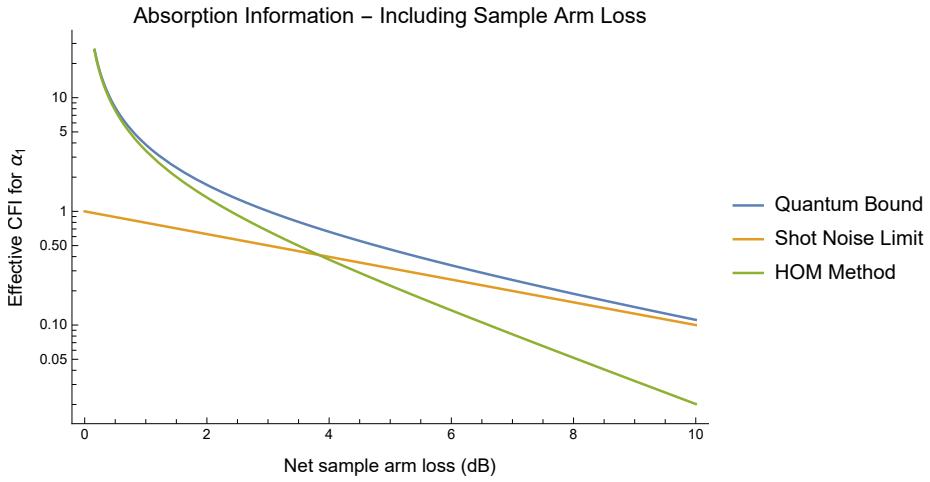

Figure 4.1: Effective classical Fisher information for absorption (loss only in the sample arm).

will consider each in turn.

Losses due to finite transmission T_1, T_2 in the sample arm affect the probe state in the same manner as losses due to sample absorption $e^{-\alpha_1}, e^{-\alpha_2}$. We therefore consider the affect of the net transmission $T_i e^{-\alpha_i}$ on the measurement precision. Figure 4.1 shows the multiparameter per-photon absorption information as a function of the sample arm's net transmission $T_1 e^{-\alpha_1}$, alongside the quantum and shot noise limits for single-parameter absorption measurements. As discussed in the previous subsection, the HOM measurement approaches the quantum bound for low losses. Excessive loss leads to performance worse than classical absorption spectroscopy. The multiparameter phase information is shown in Figure 4.2. If there are no losses at the correlated frequency ω_2, then the HOM method has the same performance as a balanced Mach-Zehnder interferometer. Sample arm losses at the correlated frequency ω_2 degrade the HOM measurement but not a Mach-Zehnder measurement.

The case of losses in the reference arm is shown in Figures 4.3 and 4.4. The behaviour of the absorption information is very different depending on which frequency experiences loss. Loss at ω_2 (*i.e.*, loss in the frequency correlated with the frequency of interest) decreases the heralding efficiency of the probe, and

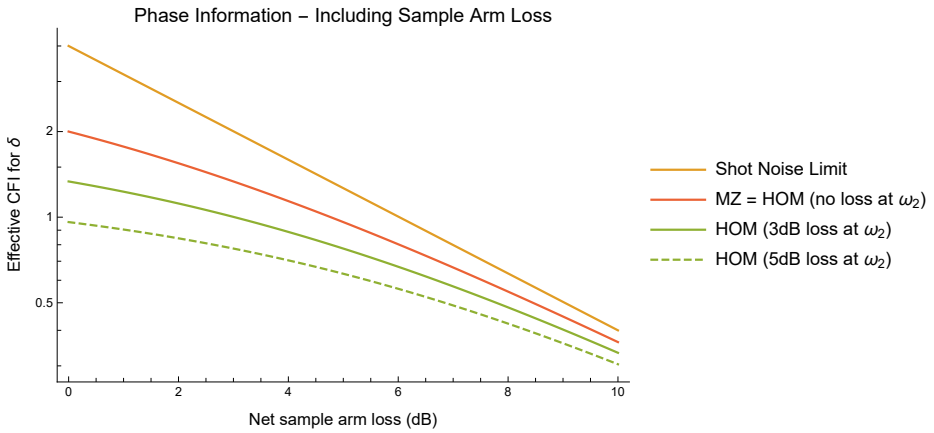

Figure 4.2: Effective classical Fisher information for phase (loss only in the sample arm).

leads to decreased performance when the sample also induces a large amount of loss. However, it still allows for an unbounded advantage over the shot noise limit when the sample arm's loss approaches zero. This is similar to a traditional heralded measurement, in which any amount of heralding allows for a large quantum advantage. By contrast, loss at ω_1, which does not affect the heralding of the frequency ω_1 of interest in the sample arm, has a lesser impact when the sample arm's transmission is low but a much greater impact when the sample arm's transmission is high. Ignoring all other sources of loss, the absorption information for arbitrary R_1 is $2/(1-R_1^2)$, so that even in the limit $R_1 \to 0$ the absorption measurement still shows a factor of 2 advantage over the shot noise limit. In fact, as $R_1 \to 0$, the absorption information, calculated for arbitrary $T_1 e^{-\alpha_1}$ but ignoring all other losses, has the form

$$C_{\alpha_1} = \frac{T_1 e^{-\alpha_1}}{1 - T_1 e^{-\alpha_1}/2}, \tag{4.22}$$

which outperforms the shot noise limit for all values of the sample arm transmission. That is, completely attenuating the frequency ω_1 in the reference arm returns the HOM measurement to one whose performance qualitatively resembles the traditional heralded measurement. This shows that the poor performance of the HOM measurement for strongly absorbing samples is a consequence of the additional detections at ω_1

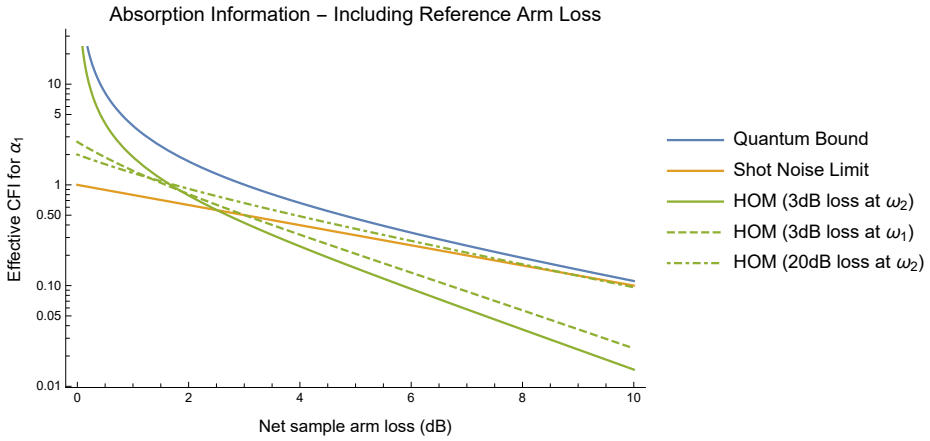

Figure 4.3: Effective classical Fisher information for absorption, including reference arm loss.

due to the reference beam. Of course, in the same limit the phase information completely vanishes, and we return to a phase-insensitive heralded measurement.

The degradation of the phase information is shown in Figure 4.4. Loss at either ω_1 or ω_2 reduces the phase sensitivity for all values of the sample transmission $Te^{-\alpha}$. Losses at ω_1 in the reference arm has an identical effect to loss in a classical Mach Zehnder interferometer. Unlike the classical interferometer, reference arm losses at ω_2 also degrade the performance of the HOM measurement, since absorption of a photon at this frequency also leads to decoherence of the probe state (4.5). Since the HOM measurement is degraded by absorption at both frequencies, in contrast to a Mach-Zehnder interferometer which is degraded only by absorption at a single frequency, the HOM measurement will generally perform worse than a classical interferometer once finite losses are introduced at both frequencies.

We finally consider the effects of detector loss. In all cases, we assume uniform detector loss at all frequencies and for both beamsplitter outputs. Figure 4.5 shows the per-probe photon absorption information for three values of η. Detector loss leads to a decrease in absorption precision for all values of sample arm transmission $T_1 e^{-\alpha_1}$. In the absence of any other losses in the setup, the absorption information has the

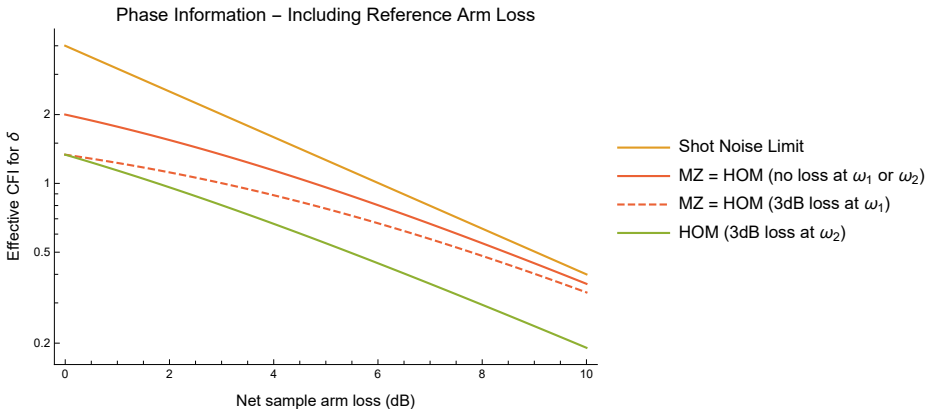

Figure 4.4: Effective classical Fisher information for phase, including reference arm loss.

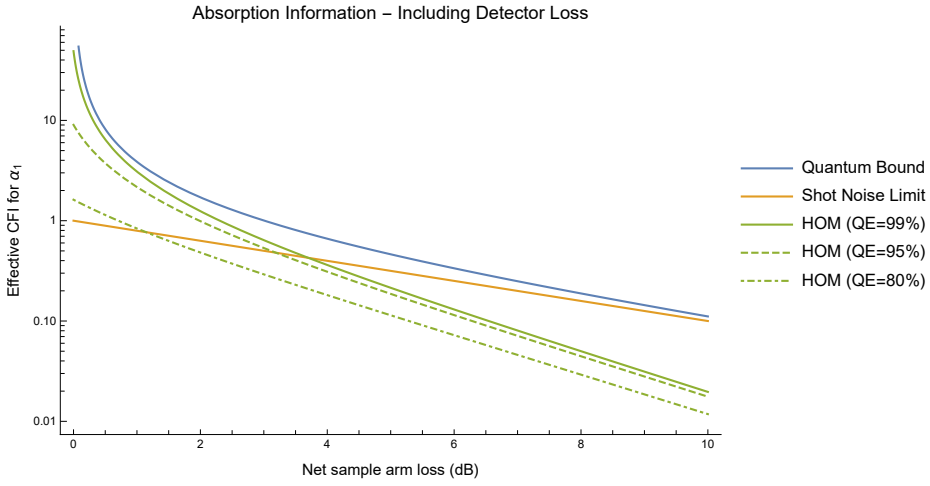

Figure 4.5: Effective classical Fisher information for absorption, including finite detector efficiency.

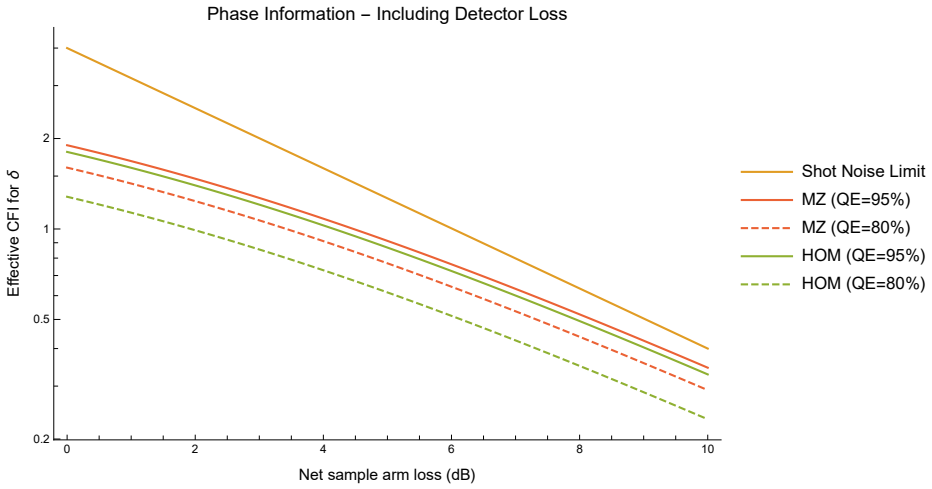

Figure 4.6: Effective classical Fisher information for phase, including finite detector efficiency.

form

$$C_{\alpha_1} = \frac{\eta}{2}\left(1 + \frac{\eta^2}{1 - 2\eta + 2\eta^2 - \eta^3}\right). \tag{4.23}$$

For detector efficiencies below $\eta \approx 0.727$, any quantum advantage in the absorption measurement is lost. Unlike the case of losses in the sample arm, no amount of loss in the reference arm is capable of restoring an advantage that is lost due to detector inefficiency.

The effect of detector efficiency on phase precision is shown in Figure 4.6. Phase sensitivity of the HOM measurement is the same as that for a classical Mach-Zehnder interferometer, except that classical interferometer's information is proportional to η whereas the HOM measurement's information is proportional to η^2. The extra factor of η is due to the phase information appearing in paired photon detection probabilities for a HOM interferometer, as opposed to single photon detection probabilities for a classical interferometer.

In summary, the HOM measurement shows a per-photon absorption precision which approaches the

quantum bound in the absence of losses. This quantum advantage persists even in the presence of low amounts of loss. In phase measurements, however, the HOM measurement shows a precision that equals a classical Mach Zehnder in the lossless limit, with the classical measurement generally showing better performance once losses are included. As a result, any metrological advantage that the HOM measurement shows over a classical interferometer must come from its advantage in absorption information; for sufficiently low losses, the HOM measurement may outperform both traditional heralded measurements and classical interferometry in estimating a single parameter which is encoded in both the absorption and phase response. This is the case in linear spectroscopy, in which both absorption and phase encode the parameters describing the electronic response of a sample.

4.4 Comparison with other spectroscopic methods

This section discusses the HOM measurement in the context of three other possible strategies for linear spectroscopy. These are the classical Mach Zehnder interferometer, which has been discussed to a small extent above; the heralded absorption measurement; and the two-photon N00N state. The three techniques have varying degrees of feasibility for short-term applications. Mach Zehnder-type interferometers form the basis of white light interferometry, which has been used for spectroscopic measurements in which the phase response of a sample is of interest, one example being in the design of ultrafast optical components [132]. Heralded interferometry has been implemented in proof-of-principle experiments; it is an attractive method of low-light absorption spectroscopy due to potential for sub-shot noise sensitivity without the need for tight tolerances on optical losses or the need for expensive detectors. We discuss also N00N state interferometry as an example of a technique which is capable of achieving a quantum advantage in both absorption and phase sensitivity, though at the cost of tight tolerances on net optical losses. Details of the three measurements discussed here are provided in Appendix C.

As discussed in the previous section, the HOM measurement is primarily useful when it is used for measurement of some parameters of interest which are encoded in both the absorption and phase shift

imparted by a sample. For instance, in linear spectroscopy, both the absorption and phase are determined by the same set of electronic parameters (resonance frequencies, line widths, ...). Rather than independent estimation of absorption and phase, one is usually concerned with estimating these electronic parameters, from which both amplitude and phase can be calculated. In Subsection 4.4.1, we first discuss some general features of the relationship between the multiparameter phase and absorption bounds and estimation of shared parameters which relate to both quantities. We then define an approximate figure of merit which includes both absorption and phase information. This figure of merit is then used in Subsections 4.4.2, 4.4.3, 4.4.4, and 4.4.5 as the basis of a comparison between HOM spectroscopy and other possible measurement techniques.

4.4.1 Linear spectroscopy as a parameter estimation problem

The task of a typical linear interferometry measurement, as applied to chemical, biological, and material science, may be phrased in the following terms. An unknown spectroscopic sample is placed in a spectrometer, which measures either the absorption spectrum, the phase spectrum, or both. The measured spectrum is compared to an analytic model describing the properties of the sample, which itself is parameterized by a series of parameters χ_i quantifying some features of the model. For instance, these parameters may be the resonant wavelengths, line widths, and oscillator strengths of a typical Lorentzian resonance, which in turn convey information of interest about some properties of the sample such as its electronic transitions. The goal of the experiment is therefore to estimate from the measured spectrum the values of the χ_i. If the sample is photosensitive, then one seeks to optimize the precision of these estimates for a fixed allowable number of probe photons.

As a consequence of the Kramers-Kronig relations, resonance parameters which are encoded in the absorption profile of the sample are also encoded in its phase spectrum. We can therefore parameterize the measured absorption and phase as $\alpha(\chi_i)$ and $\phi(\chi_i)$. Estimation of the χ_i is determined by a classical

Fisher information matrix $\widetilde{\mathcal{F}}$ with parameters

$$\begin{aligned}\widetilde{\mathcal{F}}_{ij} &= \sum_p \frac{1}{p}\frac{\partial p}{\partial \chi_i}\frac{\partial p}{\partial \chi_j} \\ &= \sum_{k\ell}\sum_p \frac{1}{p}\frac{\partial p}{\partial f_k}\frac{\partial p}{\partial f_\ell}\frac{\partial f_k}{\partial \chi_i}\frac{\partial f_\ell}{\partial \chi_j} \\ &= \sum_{k\ell}\frac{\partial f_k}{\partial \chi_i}\frac{\partial f_\ell}{\partial \chi_j}\mathcal{F}_{k\ell} \end{aligned} \tag{4.24}$$

For simplicity, we suppose the approximate the continuous absorption and phase profiles may be approximated by their values at a discrete set of frequencies. These discretized absorption and phase parameters form the elements of the vector f_k. The classical Fisher information matrix describing the χ is therefore related to the matrix describing the phase and absorption parameters by the Jacobian matrix connecting the two sets of variables. Denoting the Jacobian by $J_{ki} = \partial f_k/\partial \chi_i$, we have

$$\widetilde{\mathcal{F}} = J^T \mathcal{F} J. \tag{4.25}$$

The classical Cramér-Rao bounds then take the form

$$(\Delta\chi_i)^2 \geq (\widetilde{\mathcal{F}}^{-1})_{ii} = [J^{-1}\mathcal{F}^{-1}(J^T)^{-1}]_{ii}, \tag{4.26}$$

or

$$(\Delta\chi_i)^2 \geq \sum_{k\ell}(\mathcal{F}^{-1})_{k\ell}\frac{\partial \chi_i}{\partial f_k}\frac{\partial \chi_i}{\partial f_\ell}. \tag{4.27}$$

The classical Fisher information matrix calculated for the absorption and phase can therefore be used to directly determine the bounds on the spectroscopic parameters.

We now consider the case of a sample spectrum which contains a single resonance peak. Both the absorption and phase response of the sample will be proportional to a single oscillator strength; the precise

relationship between the χ_i and the spectrum parameters α and ϕ will depend on the detailed shape of the line as well as the detuning, but it is reasonable to assume that $\frac{\partial \chi_i}{\partial \alpha}$ and $\frac{\partial \chi_i}{\partial \phi}$ will be of comparable magnitude. For instance, in the case of a Lorenz oscillator, the absorption and phase are given by

$$\alpha(\omega) = \frac{\sigma z}{2c} \frac{\omega^2 \gamma}{(\omega_0^2 - \omega^2)^2 + \omega^2 \gamma^2}, \tag{4.28}$$

$$\phi(\omega) = \frac{\sigma z}{2c} \frac{\omega(\omega_0^2 - \omega^2)}{(\omega_0^2 - \omega^2)^2 + \omega^2 \gamma^2}, \tag{4.29}$$

where ω_0 is the resonant frequency, γ the damping constant, z the thickness of the medium, and σ set the oscillator strength. Measuring the absorption and phase at a single frequency is sufficient to estimate any two parameters, which we take to be $\chi_1 = \omega_0$ and $\chi_2 = \gamma$. We suppose that $2\pi c/\omega_0 = 810$ nm, $z = 0.1$ mm, take σ equal to Avogadro's constant, and set $\alpha = 1$ and $\phi = 0.5$ rad. In this case, all four of the Jacobian elements relating ω_0 and γ to α and ϕ lie within the range [240 GHz, 640 GHz], which is reasonable agreement given the level of detail in our discussion. The precision bound on the χ_i will be the sum of three terms, where two relate to the bounds for α and ϕ, given by the diagonal elements of an inverse CFI matrix $\mathcal{F}^{-1}$, and the third is associated with the off-diagonal element of $\mathcal{F}^{-1}$ which may be positive or negative. By our discussion above, we may assume that the proportionality factors associated with the diagonal elements have similar magnitude For simplicity, we will take the trace of $\mathcal{F}^{-1}$ to be a measure of the sensitivity of the spectroscopic measurement to the given electronic parameter χ. This ignores the relationship between the parameter χ_i and correlations between α and ϕ, but does include the effect of these correlations on the measurement precision for absorption and phase.

The next few subsections make a comparison between alternative spectroscopic measurements and the HOM measurement discussed above. As described above, the natural performance metric of a given measurement technique is the inverse of the sum of the precision bounds for α and ϕ; that is, the quantity

$$\frac{1}{(\mathcal{F}^{-1})_{\alpha\alpha} + (\mathcal{F}^{-1})_{\phi\phi}}. \tag{4.30}$$

However, our analysis involves comparison between joint measurements of absorption and phase. For the heralded measurement $(\mathcal{F}^{-1})_{\phi\phi}$ is not well-defined, since the technique is insensitive to phase. We therefore use instead the figure of merit

$$\mathcal{B} = \frac{1}{(\mathcal{F}^{-1})'_{\alpha\alpha}} + \frac{1}{(\mathcal{F}^{-1})'_{\phi\phi}}, \tag{4.31}$$

which (up to a constant factor) is an upper bound for the expression above; the prime indicates that the precision bounds have been normalized by the number of photons incident on the sample, as in the earlier discussion. This figure of merit is reasonable if we consider the absorption and phase measurements to provide independent estimates of χ (and we assume $\partial\chi/\partial\alpha$ and $\partial\chi/\partial\phi$ have the same magnitude); then $\mathcal{B}$ is proportional to the inverse of the variance that is obtained after doing a suitable weighted average of the two measurement results. This figure of merit also has the advantage that for phase-insensitive measures, we may set $(\mathcal{F}^{-1})_{\phi\phi} = \infty$ (that is, the effective information is zero) and still get reasonable results.

For each of the measurements we consider, we make as a first approximation the assumption that all losses are equal; that is, the transmission of each spatial mode and the quantum efficiency of each detector is equal to the same value, which we denote by η. We do not, however, include the effect of the sample's absorption in the definition of η. Our task is then to see which measurement performs the best for given values of α and η.

4.4.2 Spectrally-resolved Hong-Ou-Mandel interferometer

Figure 4.7 shows the value of the metric $\mathcal{B}$ for various values of α and η. Two cases are considered: in the first, the probe state is assumed to be an equal superposition of the two paths, $|\psi_1| = |\psi_2| = 2^{-1/2}$; in the second, the ratio of the two amplitudes is optimized so as to maximize the value of $\mathcal{B}$. For low values of sample absorption α, the optimization has little effect. As the sample absorption increases, optimization of the probe state becomes increasingly important. Optimization of the probe state shows minor improvements in sensitivity when the optical efficiency η is above a value of about 0.5. For efficiencies

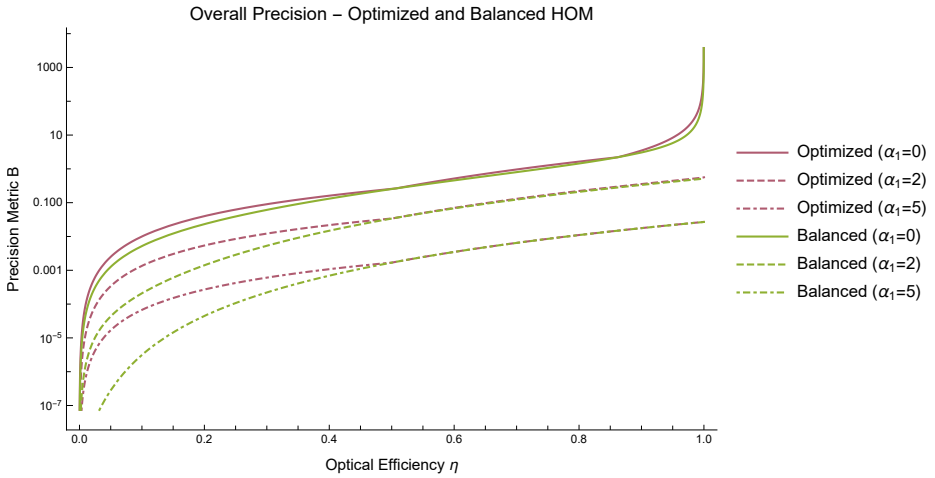

Figure 4.7: Total information in optimized and balanced Hong-Ou-Mandel measurements.

below this value, probe optimization can greatly improve the sensitivity of the interferometer, particularly when the sample absorption is large. The limiting behaviour of the interferometer as the optical efficiency η approaches unity is mostly unchanged by optimization of the probe state.

4.4.3 Classical interferometer

A plot of the performance of a classical Mach Zehnder interferometer is shown in Figure 4.8. The curves corresponding to HOM measurement with a non-optimized probe state are shown for comparison. In all three Mach Zehnder curves, the precision of the interferometer has been maximized over the range of possible beamsplitter reflectivities; as a result, these results also include the special case of a classical non-interferometric absorption measurement. Similar to the HOM measurement, sample absorption degrades the performance of the interferometer for all values of the optical efficiency η. The HOM measurement generally outperforms a Mach Zehnder interferometer for this joint amplitude-and-phase measurement when the efficiency η is sufficiently large; the range of η over which the HOM measurement shows an advantage increases as the sample absorption becomes large. Despite the rapid decrease of HOM measurement per-

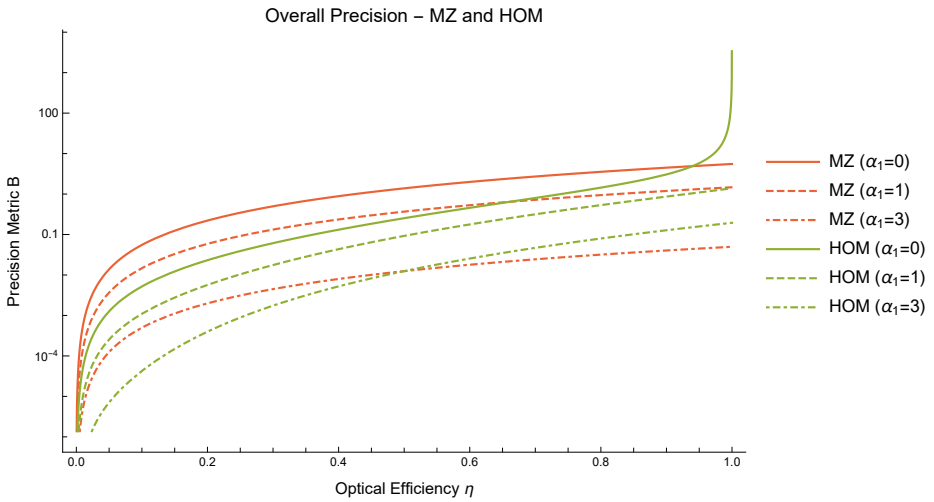

Figure 4.8: Total information in balanced Hong-Ou-Mandel and optimized classical measurements.

formance for highly absorbing samples, the similar decrease in classical interferometer precision means that the relative performance of the HOM measurement actually increases as the sample loss becomes large. By this metric, then, the quantum advantage improves as the sample's absorption becomes the dominant source of noise in the measurement.

4.4.4 Heralded absorption measurements

Figure 4.9 compares a traditional heralded measurement to a HOM measurement with a non-optimized probe state. Since the HOM measurement's absorption information degrades more quickly with loss compared to a heralded absorption measurement, at low sample losses and for high optical efficiency the overall performance of the heralded interferometer is better than that of the more complicated HOM measurement. Once a finite amount of sample absorption is introduced, the HOM measurement shows an improvement in overall precision for $\eta \gtrsim 0.5$. For these cases, the additional phase information provided by the HOM measurement allows for greater estimation of the joint parameter χ than is possible using

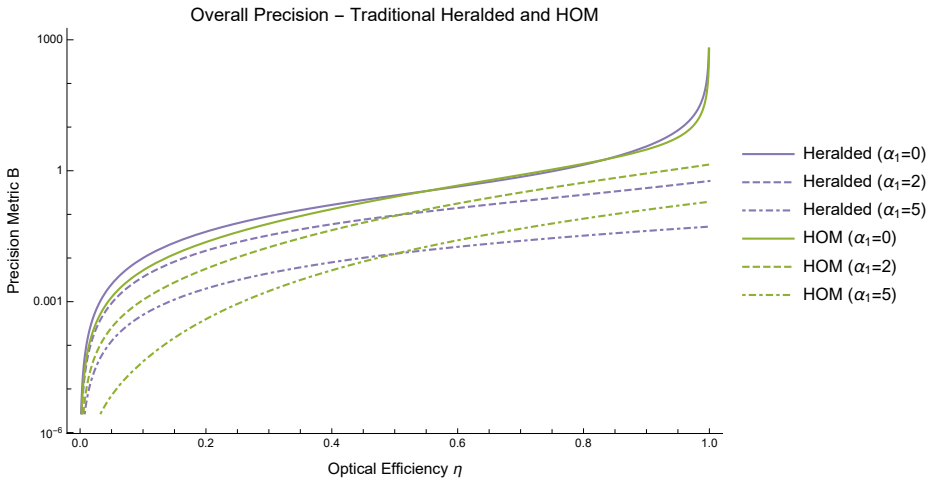

Figure 4.9: Total information in balanced Hong-Ou-Mandel and heralded absorption measurements.

only the improved absorption estimate of the heralded measurement.

4.4.5 Two-photon N00N state interferometry

The performance of a two-photon N00N state is shown alongside that of the non-optimized HOM measurement in Figure 4.10. The N00N measurement is optimized over all values of the final beamsplitter's reflectivity. For small values of sample absorption, the N00N measurement, which shows both a phase and absorption enhancement, outperforms the HOM measurement for all values of the optical efficiency η. The HOM measurement again outperforms the N00N state interferometer once sample absorption becomes large compared to other optical losses, with the threshold sample absorption above which the HOM measurement can show a comparative advantage being $\alpha \gtrsim 1$.

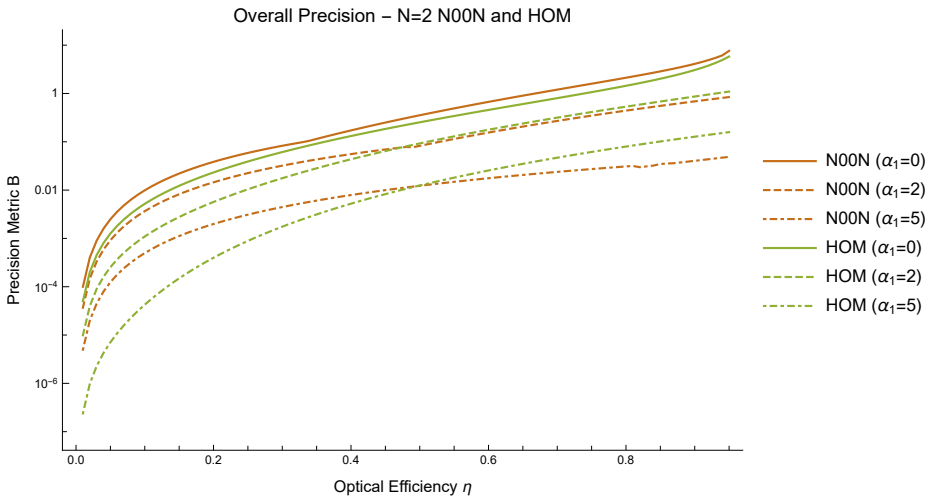

Figure 4.10: Total information in balanced Hong-Ou-Mandel and optimized $N = 2$ N00N-state measurements.

4.5 Conclusions

This chapter has examined the precision limits relevant for Hong-Ou-Mandel-based spectroscopy from two viewpoints: first, from the perspective of simultaneous estimation of two unknown parameters (the sample's absorption and phase shift) at each wavelength; and second, from the perspective of estimation of a single unknown parameter which influences both absorption and phase. This problem is approached through an analysis that considers each pair of correlated frequencies separately, so that the problem involves four modes (two spatial modes at two frequencies each) and three unknown parameters (two absorption parameters, and a relative phase). In short, we show that the HOM measurement is capable of sub-shot-noise absorption spectroscopy, though there is no enhancement in phase sensitivity compared to classical interferometry. In the problem of estimating a single parameter from both absorption and phase, the HOM measurement performs quite well: when the sample absorption is large relative to other optical losses, this measurement achieves significantly higher precision than any other technique we consider.

For separate absorption and phase estimation, the main classical benchmarks are the classical (*e.g.* Mach-Zehnder) interferometric phase measurement, and the shot noise-limited absorption measurement. In the limit of low system losses (not related to the sample), phase measurement is identical to that of the classical interferometer. There is some subtlety here: classical phase measurements provide the most per-probe-photon information when the fraction of light directed through the sample arm decreases to zero. The equivalent situation for the HOM measurement involves low sample exposure at the frequency of interest, but high exposure at the correlated frequency. The HOM measurement is less practically useful in this situation; furthermore, the same scenario leads to very low absorption information at the same frequency. A more practical situation uses a probe state with an equal probability of each frequency in each arm, which shows the same phase sensitivity as a balanced (50:50) Mach-Zehnder interferometer; this falls below the classical precision bound by a factor of two. The low-system-loss absorption measurement is more straightforward: if the sample transmits more than 41.4% of the incident light at the frequency of interest, then the HOM measurement yields more absorption information than a shot noise-limited measurement. As the sample's transmission increases above this value, the quantum advantage grows; in the limit of very low losses, the HOM method's precision approaches that of an optimal quantum measurement. It should be noted that the absorption and phase information do not detract from each other; for low losses, the method yields a near-optimal absorption measurement while still providing the phase information of a balanced Mach-Zehnder interferometer.

Since the HOM interferometer involves quite a few modes, losses can enter the setup in a few inequivalent ways. Loss in the sample arm affects the absorption information in the same way that sample absorption does; since the HOM interference visibility is related to the spectral indistinguishability of the two possible biphoton paths, absorption in the sample arm generally degrades phase information to a greater extent than the equivalent classical interferometer. Loss in the reference arm similarly degrades the phase information. Interestingly, high loss in the reference arm at one frequency actually improves the absorption precision for highly lossy samples — when the reference arm has low transmission at a frequency ω, any coincidence detection involving ω must be due to a transmission of a ω-photon through

the sample. The loss therefore removes the indistinguishability between the two biphoton paths leading to a coincidence, which generally degrades the absorption information relative to a traditional heralded measurement. Nevertheless, this reference arm loss only restores the absorption information to the shot noise level, and never leads to a quantum advantage. Finally, detector loss tends to degrade the HOM interferometer's phase precision more than a Mach-Zehnder, and degrades absorption information more than in a traditional heralded measurement.

Overall, then, the HOM method's performance for simultaneous absorption and phase estimation is mixed; it is capable of a quantum-enhanced absorption measurement at low losses, but at the cost of a phase measurement which scales poorly with loss compared to a classical interferometer. If only the absorption information is of interest, a traditional heralded technique is better. If only the phase information is needed, a classical interferometer is more robust against loss, and if the interferometer is made to be highly unbalanced one even gains a factor of $\sqrt{2}$ in per-probe-photon-precision compared to a typical balanced HOM interferometer. The use case of the HOM interferometer is then limited to scenarios in which both the absorption and phase of the sample are of interest. As we have argued, this is exactly the problem of low-light linear spectroscopy.

The final section of this chapter has considered the performance of each method in estimating a single parameter whose value determines both the phase and absorption spectra. To avoid introducing unnecessary detail about the exact dependence of the spectra on this parameter, we have considered the problem in terms of a figure of merit (4.31) which combines the multiparameter absorption and phase information without any regard for how correlations in the two estimates impact the precision of the unknown parameter. Here, we reach a surprising conclusion. If the sample is highly transmissive, the HOM interferometer is outperformed by an optimized classical interferometer except at very low system losses. At the same time, any improvement compared to a heralded measurement is minimal. However, once the sample absorption becomes the dominating source of loss in the interferometer, the HOM method outperforms classical and heralded measurements even in the presence of significant system losses. With a sample transmission of approximately 50%, for instance, the HOM method shows enhanced precision compared

to both classical and heralded measurements when losses of 50% are introduced into both arms and into both detectors. The HOM interferometer similarly outperforms a two-photon N00N-state interferometer, which is taken as an example of a measurement showing quantum enhancements for both absorption and phase. Demonstration of a quantum advantage in HOM-based measurement of such a joint parameter is therefore possible under quite realistic levels of loss, so long as one considers a sample which absorbs a significant fraction of incident light.

In summary, this HOM-based measurement is neither optimal for absorption nor for phase measurement, though the presence of intensity correlations do enable a quantum enhancement in absorption sensitivity. Rather, the primary application of such a measurement is likely to be in a problem such as spectroscopy, where one is concerned not with making a particularly good measurement of absorption, or of phase, but rather of inferring from one or both of these quantities the value of some variable of interest. This interferometric measurement performs quite well even compared to other quantum-enhanced measurement techniques so long as the sample absorption is larger than the system losses. Of course, we have not conducted a thorough survey of all possible quantum strategies; it is possible that an alternative measurement exists that outperforms the HOM measurement in any given circumstance. Nevertheless, the experimental ease with which spectrally-resolved HOM interferometry can be implemented may make it a promising approach for practical applications. A demonstration of genuine quantum advantage will require future research that firstly identifies a specific light-sensitive material sample, whose absorption is such that the HOM measurement can show a definite improvement in precision, and secondly constructs a HOM measurement with sufficiently low optical loss such that suitable quantum correlations are maintained throughout the measurement. In the experiment of Chapter 3, the ultimate bottleneck dictating the system efficiency is the relatively high loss introduced by the fast image intensifier. The prospect of practical quantum technologies relying on such detectors may serve as additional motivation for their future development.

5

Quantum optical coherence tomography

5.1 Introduction

In many contexts, one possesses an unknown material sample. The basic problem is then to identify the composition of the sample in order to understand its properties. In contexts such as biological imaging and device engineering, samples can be composed of many microscopic structures, so that one would like to identify the shape and spatial distribution of the various materials forming the larger sample. Optical coherence tomography (OCT) is an attractive option due to its nondestructive nature. In this method, a probe pulse is sent into the sample; every discontinuity in the refractive index will cause a small fraction of the power to reflect, so that a train of reflected pulses returns from the sample. This pulse train is compared with a reference pulse by means of linear interferometry, and the measured interferogram can be used to estimate the relative delay of each reflected pulse in the pulse train. From this information, one can infer the depths of the various material interfaces in the sample. Measurement of the interface positions at a fixed transverse position is called an *A-scan*. Usually, one performs an A-scan at various transverse positions across the sample, and the map of interface depth z versus transverse position (x, y) allows for three-dimensional reconstruction of the sample's structure. The OCT technique is regularly used in medical imaging, for instance in diagnostic imaging of the structure of the retina.

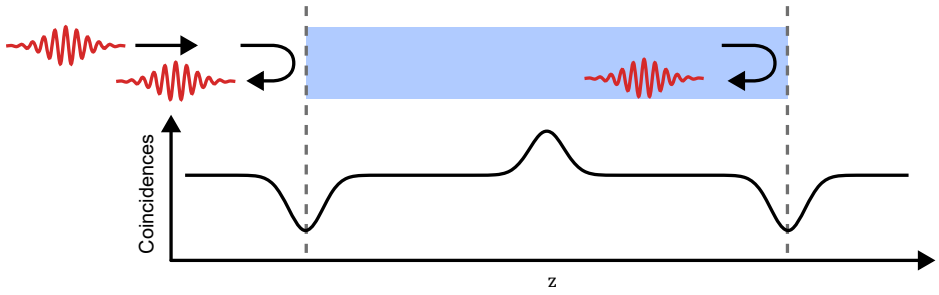

Figure 5.1: Schematic diagram of quantum optical coherence tomography. A photon is incident on an unknown sample. Each discontinuity in refractive index leads to partial reflection of the photon, so that the photon exits the sample in the form of a pulse train. Interference with a reference photon leads to a HOM dip at the position of each interface, plus an artifact (cross-interference) peak halfway between each pair of interfaces.

The classical implementation of OCT uses a probe and reference pulse which both originate at a single broadband source. Interference between the probe and reference only occurs if the relative delay between the two pulses is within the coherence time of the optical source. By scanning the delay of the reference pulse, then, the interference envelope can be used to identify the delay of each pulse in the reflected pulse train. Modern implementations replace a static broadband source with a narrowband swept-frequency laser to improve the scan speed, but otherwise rely on the same principle.

Hong-Ou-Mandel interference can be used for the same purpose. In this type of measurement, called quantum optical coherence tomography (QOCT), one photon enters the sample. This probe photon returns from the sample in a temporal mode consisting of a train of pulses, analogous to the classical case. A reference photon, meanwhile, is given a controllable delay; if the temporal modes of the reference and probe photons overlap, then Hong-Ou-Mandel interference leads to an increase in the probability of bunching. When one scans the reference photon's delay, the measured coincidence rate shows a sequence of partial Hong-Ou-Mandel dips, with the locations of the dips indicating the relative delays of the various pulses in the probe photon's waveform (see Figure 5.1).

A few possible practical advantages of QOCT have been identified. In the original proposal by Abouraddy *et al.*, it was noted that the width of a HOM dip is unaffected by group velocity dispersion

[10], and also that the quantum interference is narrower by a factor of two than the classical interference [66], so that the resolution of QOCT is double that of a classical OCT measurement with the same probe bandwidth. The quantum interferogram also excludes a background term that is seen in the classical OCT signal, which may lead to higher sensitivity for a fixed number of probe photons [66].

At the same time, the quantum method inspired advances in classical OCT. Classical measurements which mimic coincidence detection, either experimentally [133, 134, 135, 136] or in post-processing [137], also allow for cancellation of group velocity dispersion. Similarly, classical analogues to the HOM interferometer show a $\sqrt{2}$-enhancement in resolution, in contrast to the factor of two enhancement of QOCT. These methods allow one to use much greater fluxes of photons, which generally results in better signal-to-noise ratios than the quantum measurements.

A further issue arises when one tries to perform coherence tomography using measurement of intensity correlations. The measured signal in both quantum OCT and its classical analogues is the autocorrelation of the transfer function describing the sample reflections. The signal then involves the convolution of each reflected amplitude with itself, which leads to the dispersion cancellation, but also the convolution of the amplitude from one reflecting interface with that of another [66, 138]. A sample with N interfaces then leads to N HOM dips centered at the interface positions, as well as approximately $N^2/2$ so-called artifact peaks which lie halfway between each pair of interfaces (see Figure 5.1). In complicated samples the number of artifacts is much greater than the number of interface-related HOM dips, so that the correspondence between measured signal and sample structure becomes quite complicated. These artifacts can be removed via both numerical algorithms [139] and by modifying the pump beam [66, 134, 138].

This chapter considers application of spectrally-resolved detection to QOCT as a means of alleviating two problems. Section 5.2 first considers the role of the heralding ratio in quantum interferometry. The quantum OCT signal appears in the measured coincidence rate at a pair of photodetectors. Generally, the measured rate not only includes coincidences due to correlated photon pairs, but also "accidental" coincidences due to near-simultaneous detection of one photon from each of two pairs. In realistic measurements, such as in measurements involving biological tissues, only a small fraction of incident photons

are reflected from the sample. The vast majority of detections then come from reference-arm photons whose correlated probe-arm partner has been lost. The rate of accidental counts then greatly exceeds the rate of genuine coincidences, which greatly degrades the measured interferogram. Existing application of QOCT has involved samples with a relatively large reflectance so as to maintain a reasonable coincidence-to-accidental ratio. Indeed, previous reports on measurements of biological samples (onion skins) required the sample first be coated in gold to enhance reflection [140]. Section 5.2 takes a different approach; using spectrally-resolved detection and frequency-domain filtering, we are able to measure HOM interference from a tissue-like sample even at very low photon fluxes and with poor coincidence-to-accidental ratios.

Separately, we also consider the value of spectrally-resolved detection for removal of artifacts in the QOCT interferogram. Spectrally-resolved QOCT has been used for artifact removal in previous work [139]. However, removal of all artifacts requires extremely broadband pump beams, which make these methods difficult to implement in a phase matched quantum interferometer. We discuss an alternative method relying on distinct timing information in the biphoton state after the beamsplitter, which allows one to distinguish the HOM and artifact interferences in the measured signal. This timing information can be accessed through a frequency-domain quantum interference analogous to digital holography, allowing for removal of all resolvable artifacts with current biphoton sources. Section 5.3 discusses the behaviour of QOCT interference from the perspective of a time-domain model. This perspective shows that artifacts arise from an interferometric effect distinct from Hong-Ou-Mandel interference. This effect, which we refer to as cross-interference (following Ref. [66]), has properties which are in some ways hybrid between HOM and Franson interference. Nevertheless, this cross-interference has a time-domain behaviour which is qualitatively distinct from either of these effects. This behaviour forms the basis of an artifact removal method which is described in Section 5.4. Appendix D discusses a possible implementation of this method in a modified QOCT interferometer.

5.2 Progress towards QOCT measurement of a tissue-like sample

Much of the practical value of OCT is in its nondestructive measurement of biological samples. Coherence tomography allows for micron-scale resolution at low optical powers, and so is an essential tool in modern biological and medical imaging. Quantum OCT offers enhanced resolution compared to classical techniques, and has been the focus of dozens of laboratory demonstrations since being proposed. Nevertheless, all measurements to date have involved artificially-constructed samples, featuring highly reflective dielectric or metallic interfaces. Measurements of biological samples [140] have in fact relied upon reflection from deposited gold nanoparticles. This is suitable for laboratory demonstration, but cannot be used in *in-situ* imaging of biological tissue. The reason for this lack of *in-situ* imaging is the reliance of QOCT on intensity correlations. The number of measured coincidences decreases in proportion to the reflectance from the sample, so that samples with low reflectance result in a very low rate of measured coincidences. In principle, this is partially offset by the increased visibility of HOM interference, which does not depend on sample reflectance; by comparison, the classical interference visibility decreases with the square root of the reflectance. In practice, at very low coincidence rates, one finds that only a small fraction of recorded coincidences are due to correlated pairs, with the rest of the rate coming from accidental coincidences which do not show interference.

More specifically, suppose the flux of photon pairs generated by the source is R. Let η_s and η_r be the net transmission through the sample and reference arms of the interferometer, including detector efficiencies, so that $\eta_s \ll \eta_r$ on account of low sample reflectance. In a measurement time T, the number of biphotons which result in coincidence counts is $N_c = \eta_s \eta_r RT$. If coincidences are defined to be pairs of detector clicks which arrive within a short time interval T_c, then the average number of "accidental" coincidences involving detection of a single photon each from two different biphotons is $N_a = \frac{1}{4}(\eta_s + \eta_r)^2 R^2 T T_c$. For sufficiently low values of R both N_c and N_a are approximately Poisson-distributed; the fluctuations in

the total number of recorded coincidences is then $\sqrt{N_a + N_c}$. The signal of interest is the number of true coincidence counts, for which the signal-to-noise ratio is

$$\frac{N_c}{\sqrt{N_a + N_c}} = \frac{\eta_s \eta_r RT}{\sqrt{\frac{1}{4}(\eta_s + \eta_r)^2 R^2 T T_c + \eta_s \eta_r RT}} \approx 2\eta_s \sqrt{\frac{T}{T_c}}. \tag{5.1}$$

The final expression holds when $\eta_s \ll \eta_r$ and $\eta_s \ll \eta_r RT_c$. Due to the quadratic increase in accidental counts with photon flux, the signal-to-noise ratio in this limit does not vary with R, and for highly lossy samples is directly proportional to η_s. The only experimentally-accessible parameters are the coincidence window T_c and the measurement time T; the former is limited by the detector's time resolution, and practical considerations limit the latter.

The discussion so far has considered coincidence measurements using non-spectrally-resolved detectors. If spectrally-resolved detectors are used, then "true" coincidences can be identified on the basis of the strong frequency correlations between the two photons. If each detector resolves N different frequency bins, then each coincidence detection can be associated with one of N^2 joint-spectrum bins. If the biphotons possess maximal frequency anticorrelations, then "true" coincidences will fall into one of the N bins along the antidiagonal of the joint spectrum. Accidental coincidences, on the other hand, do not show frequency correlations, and will be distributed across all N^2 bins. If the measured joint spectrum is filtered so as to remove coincidences which are not along the antidiagonal, then the coincidence-to-accidental ratio is improved by a factor of roughly N, corresponding to a $\sim \sqrt{N}$-fold improvement in signal-to-noise.

The remainder of this section describes an ongoing experiment to demonstrate the use of such spectral filtering in QOCT measurements of a highly lossy tissue-like sample. We present preliminary results showing reliable reconstruction of the HOM interferogram using a small number of detected biphotons and with coincidence-to-accidental ratios on the order of 1 : 100.

5.2.1 Description of the experiment

The experimental apparatus consists of four stages, shown in Figure 5.2. First, broadband photon pairs are produced using non-colinear type-0 SPDC in a periodically-poled potassium titanyl phosphate crystal pumped by a 405 nm continuous-wave laser. The down-converted beam is collimated, and the photons are separated into two beams by a knife-edge mirror placed one focal length away from the lens. The second stage consists of two identical sample arms, one for each photon, consisting of a polarizing beamsplitter (PBS), quarter wave plate, 40x objective lens (OBJ), and sample holder. One sample holder contains the tomographic sample, which we describe below; the other contains a reference mirror. Back-scattered radiation in each arm is collected by the objective and exits via the reflection port of the PBS. A controllable delay is imparted on the reference arm using a retroreflector. The two beams are then mixed at a 50:50 non-polarizing beamsplitter (NPBS). Finally, the two beams exiting the beamsplitter are collected into fibers and sent to detectors. These fibers are connected to a pair of Excelitas avalanche photodiodes for non-frequency-resolved measurement. They can also be connected to a biphoton spectrometer, which is build using a time-tagging camera as described in Subsection 3.3.4.

As a stand-in for a biological sample, we use a multilayer OCT phantom (BioPixS). This sample consists of FeO nanoparticles ($1\,\mu$m diameter) embedded in a polymer substrate. The absorption coefficient ($\mu_a = 5\,\mathrm{m}^{-1}$) and reduced scattering coefficient ($\mu_s' = 300\,\mathrm{m}^{-1}$) of the sample are similar to those of fatty tissue ($\mu_a \approx 5\,\mathrm{m}^{-1}$, $\mu_s' \approx 370 - 650\,\mathrm{m}^{-1}$ [141]). This phantom therefore serves as a reasonable stand-in for a biological tissue, and is shelf-stable over long time periods. Due to the low amount of back-scattering from the sample and the poor quantum efficiency of the biphoton spectrometer, current measurements rely on a 40x, NA = 0.8 objective to increase the measured coincidence rate. This leads to a relatively short, micron-scale depth-of-field at the sample, so that the current measurement is unable to simultaneously resolve multiple scattering centers at different sample depths. We find that reliable reconstruction of the HOM interferogram is possible using only a small fraction of the biphotons which are measured in the current experimental setup. It should then be possible to repeat these measurements with a lower-NA

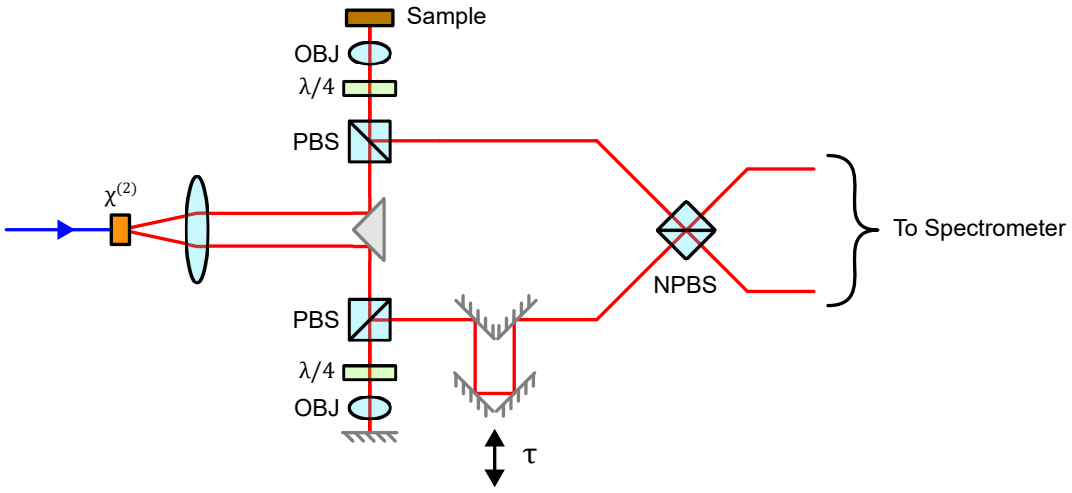

Figure 5.2: Diagram of the quantum optical coherence tomography experiment. Broadband photon pairs are generated using cw-pumped SPDC in a short nonlinear crystal. The photons are separated using a knife edge mirror into two arms. One photon reflects from a tomographic sample, while the other is given a controllable delay τ. The photons interfere at a beamsplitter, and are measured using a biphoton spectrometer similar to the one shown in Figure 3.2.

objective, which will in turn allow for measurements which extend deeper into the sample.

Measurements using this sample are performed as in traditional QOCT experiments. In non-spectrally-resolved measurements, the observed coincidence rate is recorded for a range of delay line positions τ. This coincidence rate shows a Hong-Ou-Mandel interferogram; the dip in coincidences can be used to estimate the position of the scattering center responsible for reflection. The spectrally-resolved measurement records the joint spectral intensity of pairs after the beamsplitter. This JSI shows frequency-domain fringes, similar to those described in Section 3.6. We perform frequency-domain filtering of the measured coincidences to improve the signal-to-noise ratio of the Hong-Ou-Mandel interferogram. Summing the coincidences recorded in all spectral bins results in a reconstructed coincidence dip which can be compared to the non-spectrally-resolved case.

5.2.2 Preliminary results

The current experiment has been used to demonstrate non-spectrally-resolved HOM interference arising from a single sample reflection. A corresponding spectrally-resolved measurement has also been performed. Due to failure of the camera's image intensifier during the spectrally-resolved measurement, interference has been measured only over a small range of delays far from the position of the HOM dip. Nevertheless, the measured interferogram can be used to estimate the phase offset and amplitude of the interference oscillation at each pair of frequencies (f_1, f_2), which can then be extrapolated so as to reconstruct the entire HOM dip.

The measured joint spectral intensity, summed over all delay line positions, is shown in Figure 5.3. The JSI includes only coincidences in which one photon is detected at each of the two beamsplitter output ports; similar JSIs are also obtained from pairs which bunch at the beamsplitter. Using a coincidence window of $T_c = 10\,\text{ns}$, which is determined by the timing resolution of the camera, a total of 9.75×10^5 coincidences are measured. Accidental counts are distributed almost uniformly across all spectral bins. In addition, approximately 9.65×10^3 excess counts lie along an antidiagonal line passing through the point $(\lambda_1, \lambda_2) = (810\,\text{nm}, 810\,\text{nm})$. These excess points are due to detection of correlated biphotons; only these counts display Hong-Ou-Mandel interference. The total coincidence-to-accidentals ratio is 1 : 100 before any spectral filtering. Excluding counts that lie at points not on this antidiagonal line, we instead arrive at a coincidence-to-accidentals ratio of approximately 1 : 1.

The joint spectral intensity was measured at a total of 18 relative delay values τ, all of which lie far away from the position of the non-frequency-resolved HOM dip. At this point, the camera's image intensifier failed, preventing further measurements. This partial measurement still shows fringes in the joint spectral intensity, however, which are due to frequency-entangled HOM interference between biphotons. These fringes are visualized using a method similar to that of Chapter 3. The measured counts shown in Figure 5.3 are filtered according to their frequencies, so that only counts along the antidiagonal line are included. These counts are separated into 18 JSIs, one for each position of the delay line. The

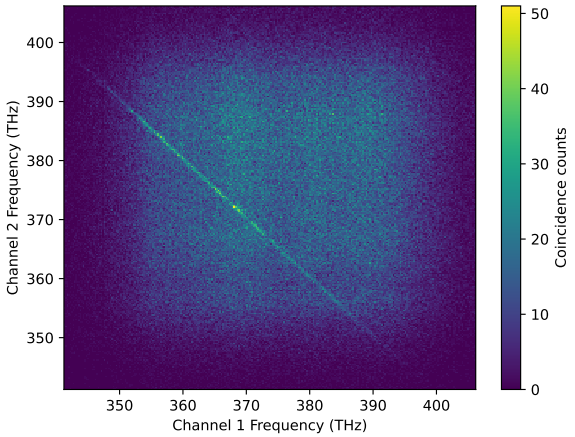

Figure 5.3: The measured joint spectral intensity, summed over all values of the delay τ. Correlated photon pairs appear as a sharp antidiagonal line due to their strong frequency anticorrelations. Accidental counts appear as a diffuse background spread over all pairs of frequencies.

expected number of accidentals are subtracted. Since interference fringes appearing in the bunched-pair JSIs are inverted compared to those in the antibunched-pair JSI, we subtract the bunched JSIs from the antibunched JSI. We then plot the distribution of counts along the antidiagonal for each of the 18 delay steps. Stacking these distributions on top of each other, ordered by delay value, leads to the interferogram shown in Figure 5.4a, which is similar to the interferograms measured in [123] and [125].

Further analysis is applied to this measured interferogram. We fit the oscillation at each pair of measured frequencies (*i.e.,* of each column of Figure 5.4a) to a sinusoid, obtaining the amplitude and phase offset of the oscillation. These oscillations are then extrapolated to later times on the basis of these parameters. The period of oscillation is known exactly from the frequency difference $f_1 - f_2$ between the two measured photons. The extrapolation to larger delays uses this exact oscillation period; the extrapolation is therefore not limited by the poor Nyquist resolution of frequency arising from the small number of delay positions used in the measurements. The extrapolated interferogram is shown in Figure 5.4b. Despite using a small number of correlated pairs, this reconstruction results in smooth interference fringes.

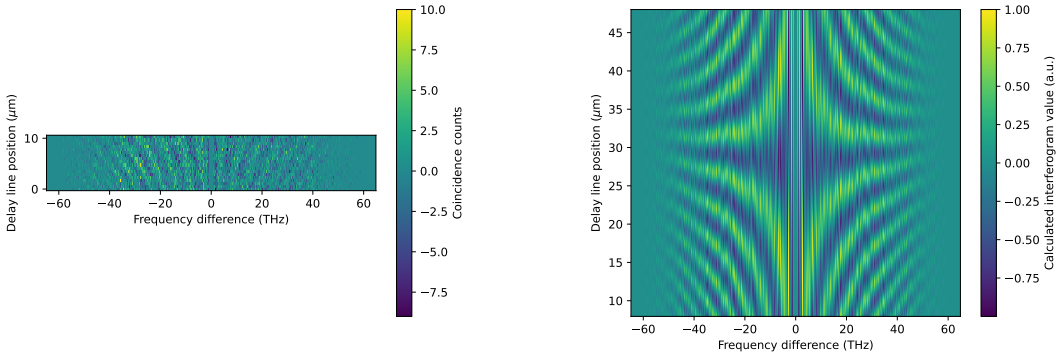

(a) (b)

Figure 5.4: (a) The measured two-photon interferogram, obtained after filtering out all photon pairs which do not lie on the antidiagonal line in Figure 5.3. The interferogram is constructed in the same way as shown in Figure 3.3: the antidiagonal line at each delay is extracted from the corresponding JSI, and these lines make up the rows of the interferogram. In this plot, we subtract the interferogram obtained for bunched pairs from that obtained for antibunched pairs, since the two interferograms show complementary fringes. (b) The result of extrapolating the interferogram in (a) to larger delays. The asymmetry between negative and positive delays is caused by third order dispersion, which is due to the two arms having unequal path lengths through the polarizing beamsplitters.

To test the accuracy of the reconstruction we can sum each row of the interferogram Figure 5.4b, which corresponds to summing over all frequencies. The interferogram then reduces to a standard non-frequency-resolved HOM dip. This HOM dip has been separately measured using avalanche photodiodes. Figure 5.5 shows the HOM dip measured using the avalanche photodiodes, and the HOM dip obtained from the extrapolated frequency-domain interferogram Figure 5.4b. The frequency-domain analysis described above discards the constant term in the interferogram, so the two HOM dips are normalized to have the same minima and the same values at large delays. The APD-based measurement, due to its much greater detection efficiency, has a coincidence-to-accidental ratio of approximately 1 : 3, and involves measurement of 37 times more correlated pairs than the frequency-resolved measurement. The spectrally-resolved measurement yields a HOM dip with similar width and position to the APD measurement, and also captures qualitatively similar oscillations arising from third-order dispersion in the interferometer. The biphoton spectrometer therefore allows for suitable reconstruction of the HOM dip given far fewer measured pairs, far worse quantum efficiency, and using measurements at only a small number of delay line positions.

Finally, we test the reliability of the frequency-domain reconstruction method at smaller numbers of photons. The measured coincidences used in the analysis above are divided into M different subsets with equal exposure times. Each subset therefore contains approximately M times fewer pairs than the measurement shown in Figure 5.4b. We calculate the standard deviation in the estimated position of the HOM dip (*i.e.*, the minimum of the interferogram) as a function of M to estimate the precision of the delay measurement for low numbers of measured pairs. The results are shown in Table 5.1. Our results show that even with extremely low numbers of detected biphotons, involving only hundreds of correlated pairs and at coincidence-to-accidental ratios near 1 : 100, reliable reconstruction of the HOM dip is possible. These trials involve less than one correlated pair per frequency bin (along the antidiagonal) per delay step, and yet are capable of estimating the position of the HOM dip to within 100 nm.

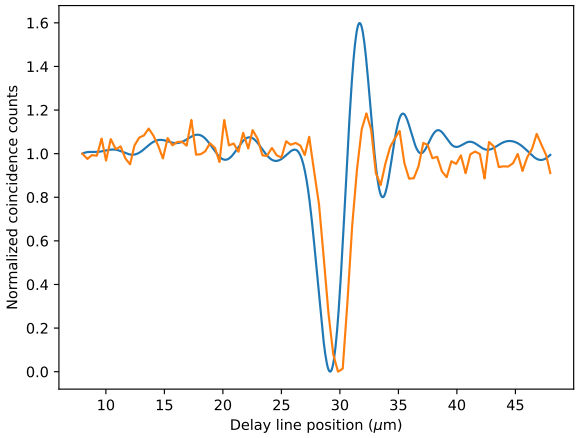

Figure 5.5: Hong-Ou-Mandel dips obtained through direct measurement with non-spectrally-resolving avalanche photodiodes (orange), and reconstructed using the measured frequency-domain interferogram (blue). The $\sim 1\,\mu$m shift in dip position is consistent with an observed day-to-day variation of about $\sim 2\,\mu$m.

M	Average Accidentals N_a	Average Correlated Pairs N_c	St. Dev. Dip Position (nm)
2	2.3×10^5	2124	29
3	1.5×10^5	1416	32
4	1.2×10^5	1062	48
5	9.7×10^4	882	99
6	7.7×10^4	708	51
8	5.8×10^4	531	69
12	3.9×10^4	354	120
25	1.9×10^4	176	174

Table 5.1: Precision in estimates of the HOM dip's position. Estimates are made by dividing the collection of all detector clicks into M disjoint sets which have equal exposure times. For each value of M, the average number of accidental coincidences N_a and the average number of correlated pairs N_c obtained in spectrally-resolved coincidence measurements are given. The precision of the dip estimate is taken to be the standard deviation in the position of the dip.

5.2.3 Discussion

We have reported on an experiment in progress which aims to demonstrate QOCT measurement of the structure of a tissue-like sample. Ordinary HOM measurements struggle in this regime due to the poor coincidence-to-accidental ratio found with for lossy samples, which makes it difficult to distinguish genuine HOM dips from statistical fluctuations in the number of coincidences. Our results demonstrate that the strong frequency correlations arising from cw-pumped SPDC, together with spectrally-resolved detection, can enable reliable positioning of HOM dips even in the presence of large amounts of noise. These results form a first step towards biological applications of QOCT.

Two major limitations exist in the current experiment. First is the use of a high-NA objective to collect diffusely-scattered radiation from the sample. The 40x objective used in current measurements greatly limits the depth of field of the measurement, limiting us to measurement of a single scattering center at a time. One option is to translate the sample through this small focal region in order to perform full tomography at all depths. A more practical approach replaces the current objective lens with a lens of smaller numerical aperture. This allows a single HOM scan to resolve multiple reflections in the sample, but comes at the cost of greatly decreased collection efficiency, which in turn leads to a degraded coincidence-to-accidental ratio. As we discuss above, this coincidence-to-accidental ratio ultimately limits the signal-to-noise ratio of any tomographic measurement. Our success in resolving a single reflection with very few photon pairs indicates that our spectrally-resolved technique is highly resilient to noise, so that further measurements at lower collection efficiencies may be viable.

A second limitation comes from the poor quantum efficiency of our detector (approximately 1%, including fiber coupling efficiency). A similar concern was identified in the context of spectroscopic measurements in Chapter 3 which discussed possible improvements to the overall efficiency of the optical system, particularly regarding fiber coupling. Some advantage may be found in the use of linear SPAD arrays, which have a slightly improved quantum efficiency compared to time-tagging cameras [124]. Even more useful in the context of QOCT, these detectors feature a timing resolution that is hundreds of times faster than

that of image-intensified cameras. As noted by (5.1), the detector timing resolution is the key parameter determining the signal-to-noise ratio in coincidence measurements using lossy samples, so that these detectors may result in noise reductions of more than ten decibels. Ultimately, it may be the case that the practical utility of quantum OCT is determined mainly by the performance of available detectors - in the form of efficiency and timing resolution, and also through measurement of additional degrees of freedom such as frequency.

5.3 Cross-interference in the QOCT interferogram

The previous section dealt with one practical concern of QOCT, namely the problem of statistical noise. We now change focus to the second major source of error in these measurements, which comes from the numerous artifacts which occur in QOCT interferograms.

Quantum optical coherence tomography is typically considered using a frequency-domain picture [66, 142, 138]. This is convenient as cw-pumped SPDC produces photon pairs with near-perfect frequency anticorrelations. As well, the time resolution of the best modern photodetectors is on the order of many tens of picoseconds, far beyond the femtosecond scale set by the sample structures of interest, making time-domain descriptions inaccessible to most experiments. The recent introduction of frequency-resolved QOCT experiments further reinforces this frequency-based view of QOCT experiments.

This section discusses QOCT from a time-domain perspective. This viewpoint is useful for two reasons: first, it gives physical insight into some of the well-known features of QOCT, such as the origin of the factor-of-two enhancement in resolution compared to classical OCT measurement with equivalent bandwidth. More importantly, this analysis shows that the biphoton state after the beamsplitter contains timing information which can be used to distinguish features in the interferogram corresponding to genuine physical interfaces in the sample from false "artifact" peaks which tend to clutter the signal. As we discuss in Section 5.4, this timing information resides in the phase of the joint spectral amplitude, which has been ignored in existing analysis. This phase can be recovered by means of interferometry, leading to a new

method of artifact removal which has practical advantages over existing techniques.

The current section presents the time-domain analysis at two levels of abstraction. First, in Subsection 5.3.1, we present a simple picture of the interferometer in terms of space-time diagrams. A more detailed discussion in terms of the joint temporal amplitude of the biphoton state is given in Subsection 5.3.3. Finally, Subsection 5.3.4 uses this time-domain model to discuss the origins of the resolution enhancement of QOCT.

5.3.1 Representing interferometry using space-time diagrams

We first give a simple pictorial representation of QOCT using space-time diagrams. These diagrams treat each photon as a localized particle with a well-defined trajectory. Two paths interfere if they lead to identical outcomes; that is, they will interfere if they result in the same set of detectors clicking at the same time. For pedagogical reasons, we consider first the diagrammatic representation of Michelson, Hong-Ou-Mandel, and Franson interferometers. The diagrams relevant to QOCT are then discussed.

As we show, QOCT is described using two distinct sets of diagrams. The first set corresponds to Hong-Ou-Mandel interference, and leads to a dip in the coincidence rate whenever the delay line's position matches the position of a reflecting interface in the sample. The second set of diagrams explains the appearance of artifact peaks halfway between each pair of sample interfaces. Following Abouraddy *et al.* [66] we refer to this effect as *cross-interference*. Our diagrammatic representation of cross-interference is similar to that of Ou [143], who discussed the effect as an example of non-local interference due to the position of the interference pattern halfway between two physical interfaces. Likewise, Pittman [144] considers a similar form of interference in order to draw fundamental conclusions about the nature of two-photon interference. Despite this earlier work, this description has not yet been applied to the problem of coherence tomography itself. We show that these diagrams reveal important information about the biphoton state after the beamsplitter, enabling improved methods of artifact removal.

It should be noted that in assigning an exact position to each photon, we are implicitly considering

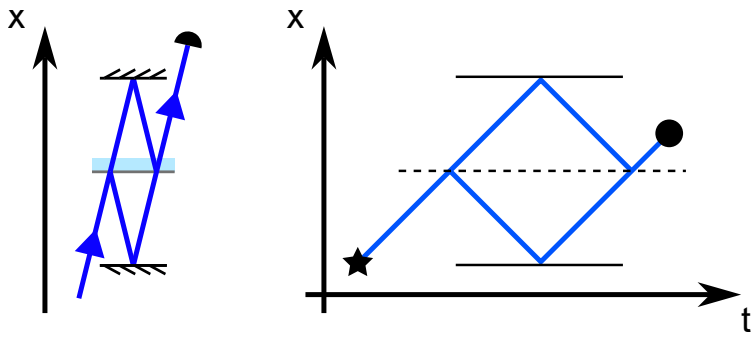

Figure 5.6: Space-time representation of Michelson interference. Left: the path of rays through space. For clarity, the beam has been drawn with a slight tilt; the horizontal spatial axis should not be confused with the temporal axis. Right: the corresponding paths along one spatial dimension (vertical) as a function of time (horizontal).

the large-bandwidth limit. Subsection 5.3.3 presents a more complete mathematical description that takes into account the finite bandwidth and coherence time of a biphoton.

Michelson interferometer

A Michelson interferometer begins with a single beam emerging from a light source. A beamsplitter divides this input beam into two beams, each of which reflect off of a mirror before returning to the beamsplitter. The two resulting beams show first-order optical interference. From the perspective of quantum optics, a Michelson interferometer relies on single photon interference — each input photon is placed in a superposition of two paths, which experience a relative delay before being recombined. The corresponding space-time diagram is shown in Figure 5.6. For simplicity, we display only a single spatial dimension along the vertical axis, with time along the horizontal axis. A star marks the optical source. The beamsplitter, which has a fixed position at all times, is depicted by a dashed line, and solid lines show the positions of the two mirrors. A circle denotes a detector placed at one output arm. A blue line marks the two possible paths a photon may take from source to detector.

Interference occurs if the two paths shown on the diagram cannot be distinguished after the final beamsplitter. This requires that the outgoing photon reaches any given position (for instance, the location

of the detector) at the same time, regardless of the path taken prior to that point. If the round-trip path lengths along the two arms of the interferometer are equal, then the path of the photon after the final beamsplitter is the same regardless of the path through the interferometer. The two paths then cannot be distinguished at the detector, and the probability of a single detection (or, equivalently, the optical intensity) will contain a contribution arising from interference between the two possible paths.

Hong-Ou-Mandel interferometer

The diagrammatic representation of a HOM interferometer is shown in Figure 5.7. In contrast to the Michelson interferometer, interference now occurs between two different biphoton paths, and involves two detector clicks. The space-time diagram must then include the possible paths of each photon. In Figure 5.7, one photon's path is shown in red, and the other photon's path is in blue. Each photon reflects off of a mirror before arriving at a beamsplitter. A click is registered at each output port of the beamsplitter; this can happen if both photons reflect at the beamsplitter, or if both photons are transmitted, so that these are the two biphoton paths of interest. In order for these two paths to be indistinguishable after the beamsplitter, it is necessary that the path length from the source to the beamsplitter is equal for each photon. In this case, the reflect-reflect and transmit-transmit biphoton paths overlap in space and in time after the beamsplitter (depicted by alternating red-blue dashed lines), and the probability of a coincidence detection contains a contribution due to interference between the two possible paths. Furthermore, any additional degrees of freedom of the two photons, such as their polarization, must be identical; otherwise, the value of this degree of freedom in each of the two beams leaving the beamsplitter will distinguish between the two paths and prevent interference.

Franson interferometer

The space-time diagram for a Franson interferometer is shown in Figure 5.8. This type of interference involves a biphoton that can be created at one of two possible times [14]. Each photon encounters a

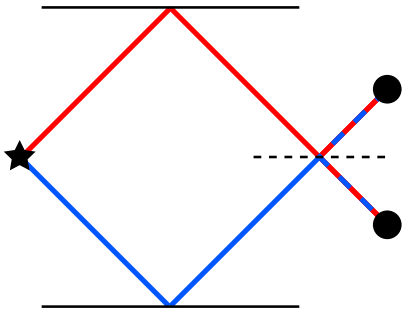

Figure 5.7: Space-time representation of Hong-Ou-Mandel interference. A single biphoton path consists of two traces, corresponding to the paths of the two photons. One photon's path is in red; the other is in blue. After the beamsplitter, two possible paths corresponding to two possible beamsplitter scatterings overlap (red-blue dashed lines), leading to interference.

beamsplitter and a mirror. Each reflected beam arrives at a detector; likewise, the transmitted beam reflects off of the mirror, and may transmit through the beamsplitter once again to also arrive at the detector. Each photon can therefore take two possible paths to the detector, with one path having a shorter path length and the other a longer path length. A coincidence detection occurs at a particular moment in time; a biphoton leading to this pair of clicks may have taken the two short paths, or the two long paths. Necessarily, this requires that the biphoton had one of two possible creation times: an early creation time taking the two long paths and a late creation time taking the two short paths will result in the same pair of detector clicks. Note that this diagram represents two paths of a *single* biphoton, involving a total of two photons; one should not confuse this with an interference between two pairs of photons.

Franson interference does not require that the two photons be identical in all degrees of freedom; if the photon represented by the red path possesses a horizontal polarization, and the photon taking the blue path has a vertical polarization, then the two possible biphoton paths are still indistinguishable. This interference will vanish, however, if one creates the biphoton using a pump pulse with a very short duration. If the pulse duration is much shorter than the difference in optical delay between the short and long paths, then each of the two photons will be created in a correspondingly short temporal mode. After

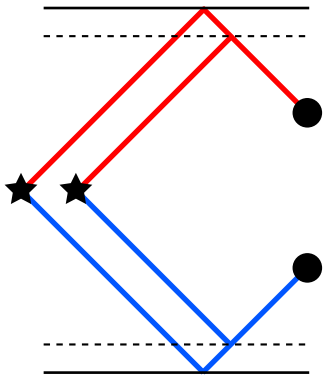

Figure 5.8: Space-time representation of a Franson interferometer. Interference occurs between two possible biphoton paths which leave the crystal at different times. One biphoton path involves both photons traveling a longer distance, which allows both biphoton paths to end with the same pair of detector clicks.

the beamsplitter, the temporal modes corresponding to the two possible paths of each photon will not overlap, and no interference will occur.

5.3.2 A description of QOCT in terms of space-time diagrams

Having discussed the representation of interference effects using these diagrams, we now consider the specific problem of quantum optical coherence tomography.

It is well-known that the QOCT interferogram contains two different types of contributions. One component of the interferogram consists of a single Hong-Ou-Mandel dip in coincidences from each of the reflecting interfaces in a sample. This contribution is the simplest to understand, and so we consider it first. For definiteness, we consider a sample which contains two interfaces, leading to two HOM dips.

Figure 5.9 depicts a typical QOCT interferometer. A biphoton is created; one photon is incident on the sample, and can reflect from one of two interfaces. The second photon is directed towards a delay line. After reflection, the two photons mix at a beamsplitter, and the coincidence rate is recorded. When the delay imposed by the movable mirror is equal to the round-trip delay for reflection from one of the sample interfaces, we obtain the diagrams of Figure 5.9, where the left and right paths differ only in which sample

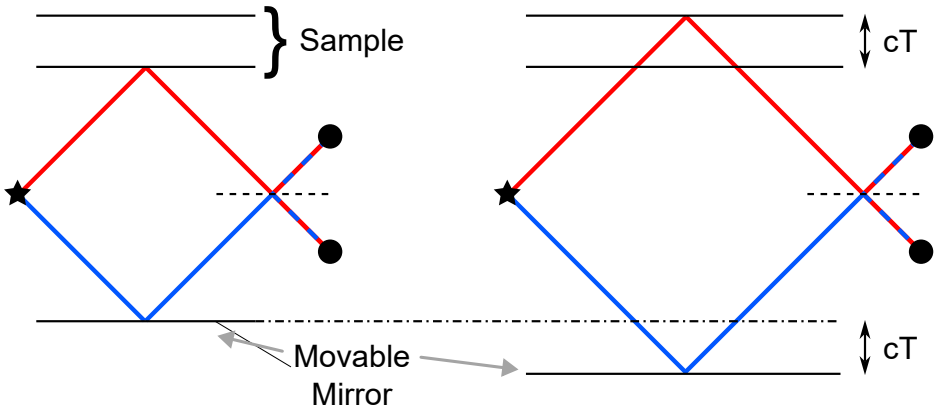

Figure 5.9: Space-time representation of HOM dips in a QOCT interferometer. Hong-Ou-Mandel interference can occur for two possible positions of the movable mirror. In either case, the interpretation of the diagram is the same as in Figure 5.7.

interface leads to the interference. The situation here is identical to that of a standard Hong-Ou-Mandel interferometer discussed above, apart from a decrease in the interference visibility of each HOM dip; this is because only a fraction of the photons incident on the sample reflects from each interface. The properties of these dips are the same as those of a traditional HOM interferometer, and do not need to be discussed further.

The second contribution to the QOCT interferogram is cross-interference between a pair of distinct interfaces; these contributions lead to artifacts in the tomographic signal. The artifact peaks appear at delays halfway between the delays of the related interfaces; they are phase-sensitive (*i.e.*, the paths can interfere either constructively or destructively); and the interference visibility of a given artifact depends on the reflectivities of both interfaces. The relevant space-time diagrams are shown in Figure 5.10, where the delay line is set to an arbitrary position $c\tau$, defined so that the first interface's HOM dip occurs at $\tau = 0$. To simplify the diagram, we use a square to represent a beamsplitter followed by a pair of detectors. As before, interference requires that the two paths arrive at each beamsplitter at the same time.

If the photon incident on the sample reflects from the nearest interface, then the arrival times of the two photons at the beamsplitter are separated by the round-trip delay 2τ of the photon traversing the

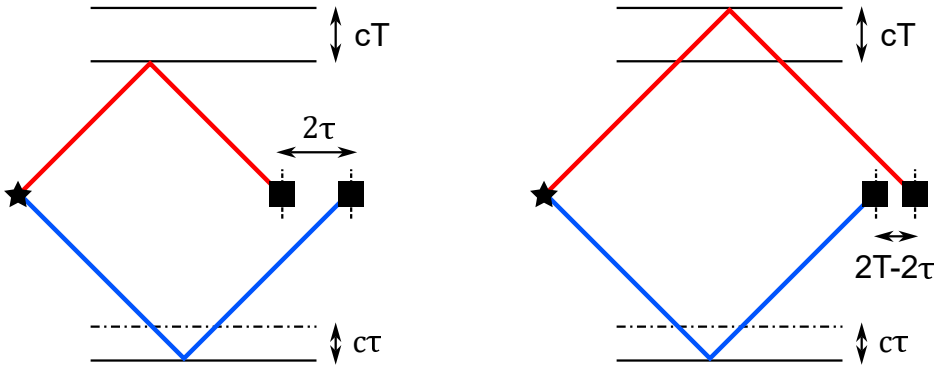

Figure 5.10: The two possible two-photon paths in an imbalanced QOCT setup. To avoid cluttering the diagrams, solid squares now indicate a beamsplitter followed by a pair of detectors.

delay line. Likewise, if the sample-arm photon reflects from the farthest interface, then the different in arrival times at the beamsplitter is $2T - 2\tau$, where $2T$ is the round-trip delay between the two interfaces. Each biphoton will lead to a definite pair of detector clicks separated by some time interval. If we require that these two paths each result in the same pair of clicks, then the arrival time differences must be equal, so that

$$2\tau = 2T - 2\tau \qquad \Longrightarrow \qquad \tau = T/2. \tag{5.2}$$

This explains the appearance of the cross-interference artifact at mirror positions halfway between the two interface HOM dips, which are located at $\tau = 0$ and $\tau = T$.

Figure 5.11 shows the two paths of Figure 5.10 in the special case where $\tau = T/2$. In order for the arrival times at the beamsplitters to match, the two biphoton paths must begin at different creation times, similar to the Franson interferometer. If the one-way delay between the two sample interfaces is T, then the two creation times are separated by a time interval T. Likewise, in both paths the two photons arrive at the beamsplitter at different moments in time, with the difference in arrival times also being T.

Comparison of Figures 5.9 and 5.11 shows that there are two timing features that distinguish the Hong-

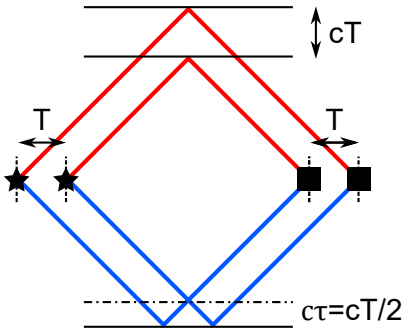

Figure 5.11: The space-time diagram describing the cross-interference effect. Cross-interference occurs when the two biphoton paths in Figure 5.10 are indistinguishable, which requires photons arrive at the beamsplitter at the same pair of times regardless of which path is taken. The interference occurs then between paths in which the photon pair is created at different times. Photon pairs undergoing this interference effect necessarily leave the beamsplitter at different times.

Ou-Mandel and cross-interference components of the QOCT interferogram. First, in Hong-Ou-Mandel interference the two biphoton paths originate at the same creation time, whereas the two biphoton paths leading to cross-interference originate at distinct creation times similar to Franson interference. Second, Hong-Ou-Mandel interference requires that the two photons leave the beamsplitter at the same time; in contrast, cross-interference only occurs if the two photons leave the beamsplitter at different times. The two interferogram contributions can therefore be distinguished based on the difference in creation time, or based on the difference in detection time. This distinction plays a key role in Section 5.4, where it allows one to separate the two contributions to the QOCT signal.

Remarks on the physical properties of the cross-interference

It is helpful to briefly consider the physical properties of the cross-interference effect as they relate to Hong-Ou-Mandel interference and Franson interference. First, consider the creation times. HOM interference involves two biphoton paths originating at a single creation time, so that it depends on the pump field only at a single moment in time. Franson interference requires coherence between the two distinct biphoton creation times leading to the two biphoton paths. It follows that Franson interference vanishes if the pump

coherence time is made sufficiently short, while HOM interference does not. Second, consider the role of auxiliary degrees of freedom. HOM interference, which involves interchange of the two photons at the beamsplitter, requires that any auxiliary degrees of freedom, such as polarization, must be identical for the two photons; if they are not, then the two biphoton paths are distinguishable, and interference does not occur. In Franson interference a given photon always arrives at the same detector regardless of the particular biphoton path; because of this, the two photons can differ in polarization (or other degrees of freedom) and still show interference.

The cross-interference effect involves both two distinct creation times and interchange at a beamsplitter. Similar to a Franson interferometer, interference only occurs if the pump coherence time is sufficiently long since the two paths must be coherent regardless of creation time. Similar to a Hong-Ou-Mandel interferometer, indistinguishability between the two biphoton paths requires that the two photons not be distinguishable on the basis of auxiliary degrees of freedom. The cross-interference effect therefore has properties that are in some ways similar to HOM interference, and in some ways similar to Franson interference.

Nevertheless, cross-interference cannot be regarded as just a hybrid between Hong-Ou-Mandel and Franson interferences. Figure 5.11 makes it clear that cross-interference only occurs between pairs of photons which leave the beamsplitter at different times. If detectors are placed at the two beamsplitter output ports and one examines the distribution of relative arrival times, then three peaks will be observed, in the simplest case of a two-interface sample. One peak will correspond to pairs which leave the beamsplitter at the same time — as indicated by Figure 5.9, this peak will show Hong-Ou-Mandel interference. The other two histogram peaks will be positioned symmetrically on either side, corresponding to a pairs in which one detection occurs slightly before the other, and those in which the same detector clicks slightly later than the other. These side peaks will show cross-interference, but no HOM interference. There is then a physical distinction between pair detections which show HOM interference and those that show cross-interference, if one's detectors have sufficiently good time resolution. Comparing with Figure 5.8, one sees that Franson interference also occurs between pairs which leave the beamsplitter at the same time. This

timing difference *after the beamsplitter* distinguishes cross-interference from the more well-known HOM and Franson effects.

5.3.3 The joint temporal amplitude after the beamsplitter

The discussion so far has focused on a simple diagrammatic representation of biphoton interference. This section provides a more detailed mathematical description of the interferometer which incorporates a finite bandwidth. The results of this section are used to understand the enhanced resolution of QOCT in Subsection 5.3.4, and they form the basis of Section 5.4's artifact removal method.

We consider a biphoton state which has an approximately Gaussian joint spectral amplitude of the form

$$\phi(\omega_1,\omega_2) = \frac{1}{\sqrt{2\pi\Omega_-\Omega_+}} \exp\left(-\frac{(\omega_1-\omega_2)^2}{8\Omega_-^2}\right) \exp\left(-\frac{(\omega_1+\omega_2-2\omega_0)^2}{8\Omega_+^2}\right). \tag{5.3}$$

Here $2\omega_0$ is the pump frequency, and Ω_- (Ω_+) denotes the bandwidth along the antidiagonal (diagonal) of the joint spectral intensity. It is sometimes helpful to write this in terms of the frequencies $\omega_\pm = (\omega_1 \pm \omega_2)/\sqrt{2}$, so that

$$\phi(\omega_+,\omega_-) = \frac{1}{\sqrt{2\pi\Omega_-\Omega_+}} \exp\left(-\frac{\omega_-^2}{4\Omega_-^2}\right) \exp\left(-\frac{(\omega_+-\sqrt{2}\omega_0)^2}{4\Omega_+^2}\right), \tag{5.4}$$

so that $\Omega_\pm$ is the variance of the distribution along the $\omega_\pm$-axis. The corresponding joint temporal amplitude is given by the two-dimensional Fourier transform of this function,

$$\widetilde{\phi}(t_1,t_2) = \frac{1}{\sqrt{2\pi\tau_-\tau_+}} e^{i\omega_0(t_1+t_2)} \exp\left(-\frac{(t_1-t_2)^2}{8\tau_-^2}\right) \exp\left(-\frac{(t_1+t_2)^2}{8\tau_+^2}\right), \tag{5.5a}$$

$$\widetilde{\phi}(t_+,t_-) = \frac{1}{\sqrt{2\pi\tau_-\tau_+}} e^{i\sqrt{2}\omega_0 t_+} \exp\left(-\frac{t_-^2}{4\tau_-^2}\right) \exp\left(-\frac{t_+^2}{4\tau_+^2}\right), \tag{5.5b}$$

where $\tau_\pm \equiv 1/\sqrt{8}\Omega_\pm$ is the variance of the distribution along the $t_\pm$-axis, where $t_\pm = (t_1 \pm t_2)/\sqrt{2}$.

The delay line imposes a delay τ on the photon with frequency ω_2, while each interface in the sample imposes some delay T on the photon with frequency ω_1. If we neglect group delay dispersion in the sample, then the action of the sample can be described by a transfer function

$$H(\omega_1) = \int dT\, r(T)\, e^{i\omega_1 T}. \tag{5.6}$$

This is a Riemann-Stieltjes integral over the delay T; the relationship between T and the sample depth z depends on the different group indices in the sample. The function $r(T)$ gives the reflection coefficient for the interface with round-trip group delay T. The joint spectral amplitude before the beamsplitter is $\phi(\omega_1, \omega_2)H(\omega_1)e^{i\omega_2\tau}$, and the corresponding joint temporal amplitude is

$$\widetilde{\phi}(t_+, t_-) = \int dT\, \frac{r(T)}{\sqrt{2\pi\tau_-\tau_+}} e^{i\omega_0(\sqrt{2}t_+ + T + \tau)} \exp\left(-\frac{(\sqrt{2}t_+ + T + \tau)^2}{8\tau_+^2}\right) \exp\left(-\frac{(\sqrt{2}t_- + T - \tau)^2}{8\tau_-^2}\right). \tag{5.7}$$

The state after the beamsplitter will be described by two amplitudes, describing bunching and antibunching pairs, respectively. Antibunching may occur either when the photons both reflect at the beamsplitter, or when the photons both transmit. Mathematically, the antibunching amplitude is equal to the difference of two terms, which are the incident JSA with the original frequency ordering (ω_1, ω_2), as well as the same JSA with the frequencies swapped (ω_2, ω_1). Equivalently, the first term of the JTA will be the incident JTA, while the second term will be the incident JTA where the delays have been transformed as $\tau_\pm \to \pm\tau_\pm$. To preserve unitarity, the bunching amplitude must have a similar form, with the second term possessing the opposite sign. After the beamsplitter, then, the joint temporal amplitude is

$$\begin{aligned}\widetilde{\phi}_\pm(t_+, t_-) = \int dT\, \frac{r(T)}{\sqrt{8\pi\tau_-\tau_+}} e^{i\omega_0(\sqrt{2}t_+ + T + \tau)} \exp\left(-\frac{(\sqrt{2}t_+ + T + \tau)^2}{8\tau_+^2}\right) \dots \\ \dots \left[\exp\left(-\frac{(\sqrt{2}t_- + T - \tau)^2}{8\tau_-^2}\right) \pm \exp\left(-\frac{(\sqrt{2}t_- - T + \tau)^2}{8\tau_-^2}\right)\right].\end{aligned} \tag{5.8}$$

Here, $\widetilde{\phi}_+(t_+, t_-)$ describes the joint temporal amplitude of photon pairs which bunch at the beamsplitter,

and $\widetilde{\phi}_-(t_+, t_-)$ describes pairs which antibunch at the beamsplitter.

This state has a simple interpretation. Suppose that the sample consists of a discrete set of reflections at delays $T = \tau_j, j = 1, \ldots, N$, so that

$$r(T) = \sum_j r_j \delta(T - \tau_j). \tag{5.9}$$

Then

$$\widetilde{\phi}_\pm(t_+, t_-) = \sum_j \frac{r_j}{\sqrt{8\pi\tau_-\tau_+}} e^{i\omega_0(\sqrt{2}t_+ + \tau_j + \tau)} \exp\left(-\frac{(\sqrt{2}t_+ + \tau_j + \tau)^2}{8\tau_+^2}\right) \ldots$$
$$\ldots \left[\exp\left(-\frac{(\sqrt{2}t_- + \tau_j - \tau)^2}{8\tau_-^2}\right) \pm \exp\left(-\frac{(\sqrt{2}t_- - \tau_j + \tau)^2}{8\tau_-^2}\right)\right]. \tag{5.10}$$

The joint temporal amplitude consists of $2N$ two-dimension Gaussian functions, two from each interface. These Gaussian functions consist of two sets; one set of N peaks is centered at the points $(t_1, t_2) = (\tau_j, \tau)$, and the other N peaks are centered at the points $(t_1, t_2) = (\tau, \tau_j)$. As τ is varied, then, one set of peaks translates along the t_1-axis, while the other set translates along the t_2-axis.

Interference occurs when two peaks overlap in the (t_1, t_2) plane — if the distance between the different τ_j is larger than both τ_- and τ_+, then two peaks can overlap only if one is from the set translating along t_1 and one is from the set translating along t_2. Figure 5.12 depicts this situation in the common case where $\Omega_- \gg \Omega_+$ ($\tau_- \ll \tau_+$). Note that overlap between peaks can occur in two ways; if $\tau = \tau_j$ for some j, then the τ_j-peak of one set will overlap with the τ_j-peak of the other, which leads to Hong-Ou-Mandel interference (Figure 5.12(b)). If, instead, $\tau = (\tau_i + \tau_j)/2$ for $i \neq j$, then the τ_i-peak of the first set will have the position

$$(t_1, t_2) = \left(\tau_i, \frac{\tau_i + \tau_j}{2}\right) = \left(\frac{\tau_i}{2}, \frac{\tau_j}{2}\right) + \left(\frac{\tau_i}{2}, \frac{\tau_i}{2}\right), \tag{5.11}$$

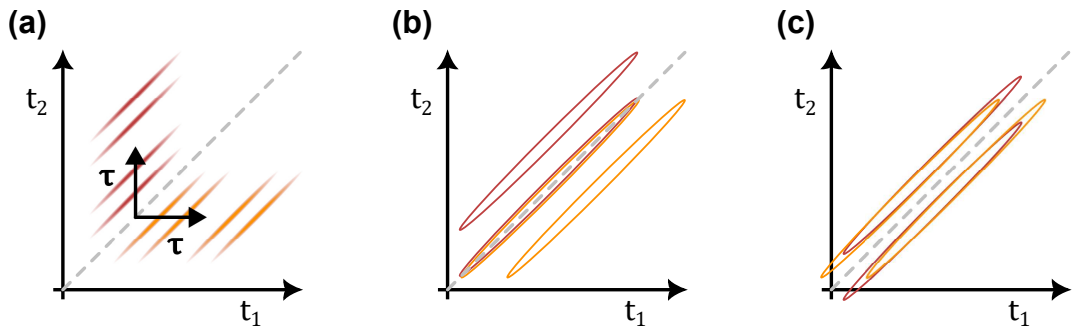

Figure 5.12: (a) Depiction of the joint temporal intensity after the beamsplitter. Four sample reflections lead to eight peaks in the post-beamsplitter JTI. One set of peaks (orange) translates along the t_1 axis when τ is varied, while the other (red) translates along the t_2 axis. (b) Hong-Ou-Mandel interference occurs when both peaks arising from a single reflection overlap along the $t_1 = t_2$ diagonal. (c) Cross-interference occurs when a pair of peaks corresponding to two distinct interfaces overlap each other. This necessarily requires an initial JTI which extends sufficiently far in the diagonal $t_1 + t_2$-direction. This interference always occurs at off-diagonal points $t_1 \neq t_2$.

while the τ_j peak of the second set will have the position

$$(t_1, t_2) = \left(\frac{\tau_i + \tau_j}{2}, \tau_j\right) = \left(\frac{\tau_i}{2}, \frac{\tau_j}{2}\right) + \left(\frac{\tau_j}{2}, \frac{\tau_j}{2}\right). \tag{5.12}$$

The two peaks are offset from each other along the diagonal t_+-direction. If the width of the temporal distribution τ_+ along this direction is much larger than $|t_i - t_j|$, however, then the two Gaussians will still have significant overlap and lead to interference; a similar calculation shows that the other τ_i-peak and τ_j-peak will also overlap each other near the point $(\tau_j/2, \tau_i/2)$, so that the four peaks (two from τ_i, two from τ_j) together result in cross-interference (Figure 5.12(c)). Noting that the relative-time histogram discussed at the end of Subsection 5.3.2 is just the marginal distribution of the joint temporal intensity $|\widetilde{\phi}(t_+, t_-)|$ along the t_--axis, we see that Hong-Ou-Mandel interference occurs when $t_1 \approx t_2$, or $\tau_- \approx 0$, while cross-interference occurs when $|t_1 - t_2| = |\tau_-| \approx |\tau_i - \tau_j|/2$. This confirms our earlier statement that HOM interference and cross-interference occur at different peaks of the relative time histogram.

5.3.4 Time-bandwidth product and tomographic resolution

We now apply the model of the previous section to understand the improved resolution of QOCT compared to a classical OCT measurement with equal bandwidth. We show that this resolution enhancement consists of two factors: one factor is related to the relationship between the variable delay τ and the measured signal, and can be replicated using a pair of separable (unentangled) beams; the other factor comes from the relationship between coherence time and bandwidth, which is different for entangled and separable states of light.

It is well-known that the Hong-Ou-Mandel dip of a single interface in quantum optical coherence tomography has a temporal width which is half that of the interference envelope of a traditional OCT interferometer [66]. The width of the interference pattern τ_0 arising from a single reflection sets the resolution limit of the interferometer; as the delay between two reflections becomes smaller than τ_0, the interferograms overlap, and one's ability to infer the positions of the two reflecting interfaces quickly deteriorates [145]. When considering the resolution of the QOCT measurement, then, it is sufficient to consider a sample with a single reflecting interface. In this case, only Hong-Ou-Mandel interference occurs.

As discussed in Subsection 5.3.3, Hong-Ou-Mandel interference occurs when two terms in the post-beamsplitter joint temporal amplitude overlap along the line $t_1 = t_2$. The resolution of the interferometer can be defined to be the standard deviation of one of the two Gaussian amplitudes which overlap in the (t_1, t_2) plane. Figure 5.13(a) depicts this situation when the reference mirror imposes an arbitrary delay τ, where $\tau = 0$ is the location of the HOM dip. One of the two Gaussian peaks in the JTA is translated along the t_1-direction by τ, while the other is translated along the t_2-direction by τ. The total separation between the two peaks is then $\sqrt{2}\tau$ directed along the t_--direction. This can be contrasted with a traditional OCT interferometer, in which the pulse passing through the sample is unaffected by the delay line, while the other pulse is delayed by τ. The effect of the delay line in the QOCT interferometer is enhanced by a factor of $\sqrt{2}$ compared to a classical interferometer — this $\sqrt{2}$ increase occurs regardless of the quantum state of the two photons, and is merely a consequence of the beamsplitter on a biphoton state. The

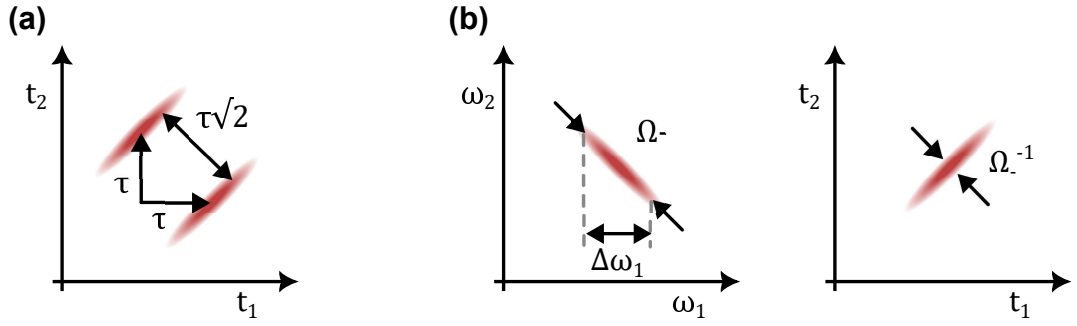

Figure 5.13: Temporal resolution in the QOCT interferometer. (a) Delay by a factor of τ causes a given pair of peaks receding from the diagonal. If the peaks overlap on the diagonal at $\tau = 0$, then the total difference is $\sqrt{2}\tau$. This leads to one $\sqrt{2}$-enhancement in interferometer resolution. (b) A second $\sqrt{2}$-enhancement in resolution occurs for highly entangled photon pairs. Interference occurs along the antidiagonal line of the JTI, so that the relevant width of the JTI is the antidiagonal width (rightmost figure). This width is in turn determined by the antidiagonal width of the JSI (leftmost figure), which is $\sqrt{2}$ times the bandwidth of a single photon.

additional factor of $\sqrt{2}$ means that any interferogram measured as a factor of τ is automatically a factor of $\sqrt{2}$ narrower than would be the case in a classical interferometer. An experiment by Lavoie *et al.* has found this $\sqrt{2}$ increase in resolution when using a pair of oppositely-chirped pulses and a sum-frequency measurement, which is analogous to a coincidence detection [134].

In addition to this measurement-related $\sqrt{2}$-enhancement, QOCT features a second $\sqrt{2}$-improvement in resolution due to the use of an entangled biphoton state, giving an overall resolution enhancement of two. Figure 5.13(b) shows the joint spectral amplitude of the probe state, along with the corresponding joint temporal amplitude. As noted above, the two peaks leading to HOM interference approach each other along the t_--direction when τ is varied. The relevant parameter determining the width of the HOM dip is then the width τ_- along the t_--direction. The JTA and JSA are related by a two-dimensional Fourier transform; it follows that the width τ_- is inversely proportional to the bandwidth Ω_- along the antidiagonal of the JSA. When discussing the bandwidth of the optical state, however, one is concerned with the bandwidth $\Delta\omega_1$ passing through the sample. If $\Delta\omega_1 = \Delta\omega_2$ (other situations are discussed in

Chapter 2), then

$$\Omega_- = \sqrt{2}\Delta\omega_1, \tag{5.13}$$

so that τ_- is a factor of $\sqrt{2}$ smaller than the coherence time $\sim (\Delta\omega_1)^{-1}$ that would be anticipated from classical optics. Stated another way, the biphoton coherence time (sometimes called the *entanglement time*), defined to be the width of the joint temporal intensity along the t_--direction, is a factor $\sqrt{2}$ shorter than the coherence time of a classical pulse of light with the same bandwidth $\Delta\omega_1$. This is a uniquely quantum-mechanical feature of entangled photon pairs — the joint spectral amplitude of a separable state is just the product of the two spectral amplitudes of the two photons, so that the minimum width along t_-, which occurs for $\Delta\omega_1 = \Delta\omega_2$, is just the classical coherence time $(\Delta\omega_1)^{-1}$.

In summary, then, the resolution enhancement of QOCT comes from two distinct places. The use of the beamsplitter together with two-photon detection leads to a factor of $\sqrt{2}$ — this factor can be reproduced using entirely classical states of light, as in [134]. A second factor of $\sqrt{2}$ requires the use of entangled photon pairs, which have a coherence time which is shorter by a factor $\sqrt{2}$ than that of a separable state.

One should note that just using entangled pairs is not enough; if one considers an interferometer consisting of a Mach-Zehnder in one arm and no beamsplitter in the other, then interference occurs between two peaks in the JTA, one of which translates along t_1 and the other of which is stationary. The relevant width is then just $\Delta t_1 = (\Delta\omega_1)^{-1}$, *i.e.* the classical coherence length. The improved sensitivity of the biphoton state occurs only along the t_--direction. Hong-Ou-Mandel interference occurs along this direction of the JTA, so that entanglement can lead to a resolution enhancement.

5.4 A proposal for interferometric removal of artifacts

The QOCT interferogram consists of a single HOM dip for each reflecting interface in the sample, and a cross-interference artifact for each pair of interfaces. When the number of interfaces in a sample is

large, the artifact peaks greatly outnumber the HOM dips; the correspondence between the measured interferogram and the sample structure is then quite poor. Subsection 5.3.2 showed that dips corresponding to HOM interference can be distinguished from those due to cross-interference by two means. First, cross-interference relies on the pump field at two moments in time; if one uses a pulsed pump or a pump with a short coherence time, then the artifact peaks vanish. Second, the relative arrival time of pairs is different in the two cases. Hong-Ou-Mandel interference only occurs for pairs that leave the beamsplitter at the same time, whereas cross-interference occurs for pairs that leave the beamsplitter at different times. Each of these physical distinctions can be used to separate the HOM and artifact peaks in the interferogram.

Existing techniques for artifact-removal largely rely on modification of the pump beam. If a monochromatic pump is used, then the artifact peaks alternate from constructive to destructive interference as the pump frequency is varied. By sweeping the frequency of a narrowband pump, the average contribution of the artifacts washes out [138, 134]. A similar method relies upon a pulsed pump beam [146]. Another proposal relies upon an electro-optic phase modulator to generate the pump incoherence [147]. These methods encounter a common difficulty: removal of artifact peaks requires that the coherence length of the pump pulse be less than the round-trip delay between the two related reflecting interfaces. For samples of interest, this is on the order of a few microns (tens of femtoseconds). If one is performing measurements of samples near the resolution limit of the interferometer, then the pump bandwidth required to remove all artifacts is extremely large — on the order of 100 nanometers, for typical experiments. Swept-source lasers with similar bandwidths are common in classical OCT, but nonlinear phasematching requirements (see Section 1.4) make the use of such broadband pumps extremely difficult in biphoton experiments.

On the other hand, one can try to distinguish artifacts on the basis of the time-of-arrival information after the beamsplitter. The timescale of question is again on the order of ten femtoseconds, so that direct measurement of this time difference is not possible with current photodetectors. Only the spectral intensity of the biphoton after the beamsplitter is easily measured, whereas this timing information resides in the phase of the joint spectral amplitude. An alternative strategy is then to perform an interferometric measurement of the complete post-beamsplitter biphoton state, including the JSA's phase. The complex

JSA can then be Fourier transformed to obtain the JTA, from which artifacts and HOM dips can be separated.

This scheme has practical benefits. Interferometric measurement of the complex JSA occurs via interference between the biphoton amplitude leaving the QOCT interferometer and a reference biphoton amplitude, in a manner analogous to classical digital holography. Measurements of this type have been demonstrated recently in order to perform tomographic reconstruction of the spatial component of the biphoton amplitude [148]. A similar type of interference occurs in the experiment of [103]. Here, the two biphoton amplitudes are associated with different orders of the perturbation expansion. The relative weights of the amplitudes are controlled by tuning the pump power, and the net effect of the two interfering amplitudes is a gain-dependent group delay between the two photons. Another recent experiment, Ref [149], demonstrates this phase-sensitive interference between biphoton amplitudes which originate in different nonlinear crystals. In each of these measurements, the bandwidth of the biphoton state determines the possible time resolution. In contrast to the use of broadband pump beams, biphoton bandwidths greater than 100 nanometers are easily obtained. Furthermore, since the biphoton bandwidth determines both the resolution of the QOCT interferogram and the timing resolution of the artifact removal technique, it follows that all resolvable artifacts can be removed by such a technique.

The rest of this chapter discusses the proposed scheme in more detail. The basic outline of the scheme is as follows. A single pump beam is divided into two components; one component generates a probe biphoton amplitude which enters the QOCT interferometer; the other component generates a reference biphoton amplitude which does not encounter the sample. The probe biphoton is mixed at a beamsplitter, resulting in a joint temporal amplitude of the kind considered in Subsection 5.3.3. After the beamsplitter, the probe and reference amplitudes are recombined at beamsplitters. The joint spectral intensity of the combined amplitude is measured — as in the case of digital holography, it will feature fringes which are sensitive to the phase difference between the probe and reference amplitudes. As this relative phase is varied, then, one can reconstruct the complex joint spectral amplitude of the probe biphoton. Fourier transforming the joint spectral amplitude yields the joint temporal amplitude; by removing the off-diagonal

($t_- \neq 0$) components and performing the inverse transform, the artifact peaks can be removed, resulting in an interferogram consisting of a single HOM dip for each sample interface.

5.4.1 The biphoton interferometry scheme

We now consider the scheme in more detail. This discussion focuses on the conceptual implementation of the method. Appendix D discusses a simple modification of existing spectrally-resolved QOCT interferometers that can be used to perform such a measurement.

We suppose that a pair of SPDC sources has been constructed; these sources are driven by the same pump beam (Figure 5.14) resulting in a two-photon state which is a superposition of a pair leaving the first source (denoted the *probe*) and a pair leaving the second source (denoted the *reference*): $|\phi_0\rangle_s + e^{i\theta} |\phi_0\rangle_r$. We assume that the pair has the same initial joint spectral amplitude ϕ_0 in either case. The relative phase θ can be controlled via a phase modulator acting on one part of the pump beam. As in Subsection 5.3.2, we consider a state which consists of only a single photon pair, which may come from either of the two sources. In the discussions that follow, we sometimes refer to a "probe biphoton" or a "reference biphoton" — these terms are used to refer to biphoton paths which originate at the probe or reference sources, and are not meant to imply that multiple pairs are created simultaneously.

The two beams of the probe biphoton are sent through a typical QOCT interferometer; after leaving the beamsplitter, the probe pair is left in a state of the form (5.8), which includes amplitudes for bunched and antibunched pairs. The reference biphoton, meanwhile, is prepared in a biphoton state $\phi_r(\omega_1, \omega_2)$; the form of this reference state is discussed below.

At this point, the probe and reference states interfere at a second beamsplitter, shown in Figure 5.14. As discussed above, the point of this interference is to allow for separation of the HOM interference, which occurs along the diagonal line $t_- \approx 0$ of the JTA, and cross-interference, which occurs at off-diagonal positions in the (t_1, t_2) plane. Due to destructive HOM interference, the JTA of antibunched probe biphotons is always zero along the diagonal line $t_- \approx 0$. The JTA of bunched probe biphotons,

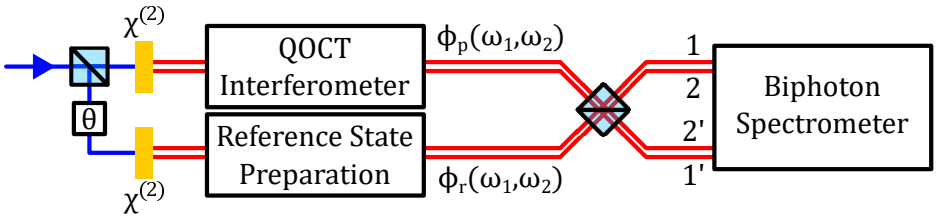

Figure 5.14: Schematic diagram of the artifact removal method. Two biphoton amplitudes are generated by two different nonlinear crystals; one amplitude enters a QOCT interferometer, while the other acts as a timing reference. Each beam in the reference biphoton interferes with a beam in the QOCT-biphoton, leading to interference. The measured interferogram can be used to reconstruct the complex joint temporal amplitude of the QOCT-biphoton, from which artifacts and HOM interference can be distinguished.

on the other hand, shows constructive HOM interference along the same diagonal line; we therefore wish to measure the amplitude of bunched probe biphotons, since this JTA will contain both HOM and cross-interference components. We denote the JSA of bunched probe biphotons by $\phi_p(\omega_1, \omega_2)$.

The beamsplitter shown in Figure 5.14 mixes each beam of the probe biphoton with one beam of the reference biphoton. After this beamsplitter, we are left with four beams (1, 2, $1'$, and $2'$), each of which is subject to a spectrally-resolving detection. Each probe beam contributes to two of the beams after this beamsplitter; a coincidence detection between two output beams associated with the same probe beam (1 and $1'$, or 2 and $2'$) indicate a pair which was bunched prior to the beamsplitter. Such a detection may come from a pair which was bunched in the corresponding beam of the probe biphoton, or one which was bunched in the corresponding beam of the reference biphoton. Interference then occurs between the amplitude describing a bunched probe biphoton and the amplitude describing a bunched reference biphoton. Similar considerations shown that the antibunched amplitudes interfere with each other.

Based on these considerations, the desired state of the reference biphoton is a bunched state; a bunched reference amplitude will interfere with a bunched probe amplitude, allowing for interferometric measurement of the bunched probe amplitude $\phi_p(\omega_1, \omega_2)$. The reference state preparation stage should therefore consist of a third beamsplitter; when the reference biphoton is incident on this beamsplitter, it will undergo Hong-Ou-Mandel bunching. We therefore let $\phi_r(\omega_1, \omega_2)$ refer to the JSA describing a bunched reference

biphoton.

The measured signal consists of coincidence counts which are distributed between four measurement channels, with each channel being spectrally resolved. A coincidence detection between channels 1 and $1'$, or between 2 and $2'$, can only come from a biphoton which was bunched before the beamsplitter. The probability of such a detection is proportional to

$$p(\omega_1,\omega_2) = |\phi_p(\omega_1,\omega_2) + e^{i\theta}\phi_r(\omega_1,\omega_2)|^2 = |\phi_p(\omega_1,\omega_2)|^2 + |\phi_r(\omega_1,\omega_2)|^2 + 2\mathrm{Re}\left[\phi_p^*(\omega_1,\omega_2)\phi_r(\omega_1,\omega_2)e^{i\theta}\right]. \tag{5.14}$$

As in classical digital holography, measurement of this probability distribution for various relative phases θ, together with knowledge of the reference amplitude $\phi_r(\omega_1,\omega_2)$, allows for reconstruction of the complex JSA $\phi_p(\omega_1,\omega_2)$ for bunched probe biphotons. This JSA can be Fourier transformed to obtain a probe JTA of the kind shown in Figure 5.12(a). In practice, it is only necessary to transform along the antidiagonal direction ω_-; this is also the direction in which the JSA's bandwidth is largest, corresponding to the maximum timing precision.

Numerical simulations

We now assume that such an interferometric measurement has been performed. We simulate the results of such a measurement, based on the probability distribution (5.14). Specifically, we consider Gaussian biphoton states of the form (5.3) with a center wavelength of 810 nm, and with each photon having a bandwidth of 105 nm. The pump beam is assumed to have a 1.2 nm bandwidth. Interference between the probe and reference biphoton amplitudes is used to reconstruct the complex JSA of the probe after the QOCT stage. This JSA is Fourier transformed along the ω_--direction; the transformed function is multiplied by a filter $f(t_-)$; and the inverse transform is then applied. The total number of bunched-pair coincidence counts at all frequencies is then calculated from this filtered JSA, and this number is plotted as a function of the QOCT stage's delay line position. Because we are considering bunched pairs, sample

reflections appear as a HOM peak, rather than the HOM dip seen in antibunched rates.

We first consider a sample consisting of four interfaces of equal reflectance; the phases of the artifact peaks are chosen randomly, and the dispersion of the sample is negligible. Figure 5.15 shows the results of such a calculation when the filter function $f(t_-)$ is taken to have the form

$$f(t_-) = \exp\left(-\frac{t_-^2}{T_-^2}\right), \tag{5.15}$$

for different values of the filter width T_-. This filter acts to suppress off-diagonal peaks of the probe JTA. Since cross-interference occurs at off-diagonal positions in the (t_1, t_2) plane, this filter suppresses the artifact peaks in the QOCT interferogram. As discussed in Subsection 5.3.3, cross-interference between reflections at delays τ_i, τ_j occurs near $t_- \approx \pm|\tau_i - \tau_j|/\sqrt{8}$. Artifact peaks due to closely-spaced pairs of sample interfaces require small filter widths T_- to be removed. Filter bandwidths of $T_- \sim 5\,\text{fs}$ are capable of removing all artifacts in the interferogram, despite the separation between artifacts and HOM peaks being close to the resolution limit of the interferometer.

Once the complex JTA is known, it is possible to also consider more complicated types of filters. For instance, Figure 5.16 shows the interferogram that is obtained using filter functions of the form

$$f(t_-) = 1 - \frac{1}{2}\exp\left(-\frac{t_-^2}{T_-^2}\right). \tag{5.16}$$

This function suppresses the JTA's diagonal by a factor of two; for suitably chosen values of T_-, it therefore removes the contribution of constructive HOM interference along the line $t_- \approx 0$. When the value of T_- is suitably chosen, the filtered interferogram contains only artifact peaks due to cross-interference between interfaces. Such information may be useful in estimating the dispersion of the different sample layers [142].

This method of time-domain filtering does come at a cost, however. Figure 5.17 shows the result of removing the off-diagonal components of the JTA for a sample with very large group velocity dispersion. Ordinarily, HOM interferometers are insensitive to odd orders of dispersion [10]. When the contributions

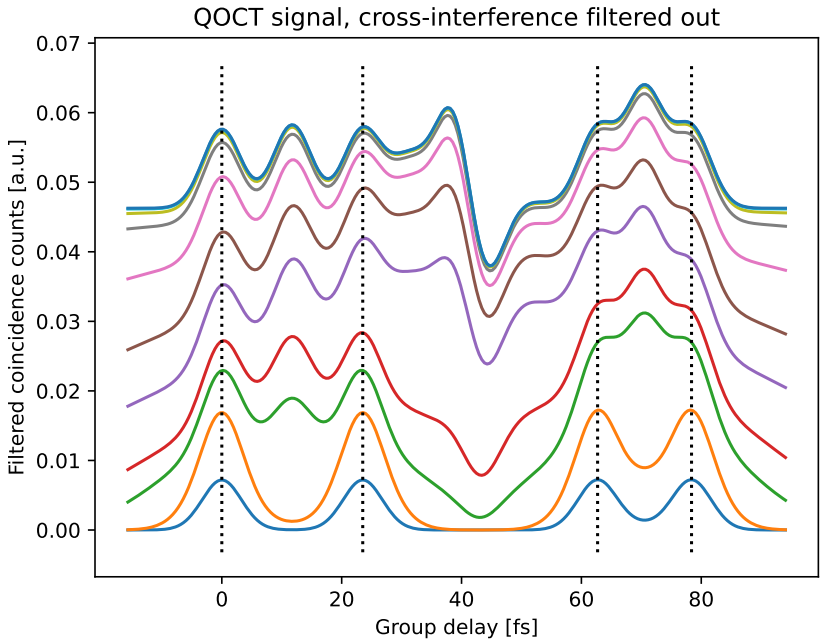

Figure 5.15: Simulated QOCT interferograms after filtering out off-diagonal components of the joint temporal amplitude, for filters of various widths. The filter widths T_- are, from bottom to top, 1.5, 5, 15, 25, 50, 75, 125, 250, 500, 1250, and 5000 femtoseconds. Dashed lines indicate the position of sample interfaces. The simulated sample provides four reflections with randomly-chosen phase shifts at depths of 0.0, 2.4, 6.4, and 8.0 μm from the sample surface, and has a group index (1.48) and GVD ($\beta_2 = 58.9$ fs^2/mm) consistent with cellulose [150].

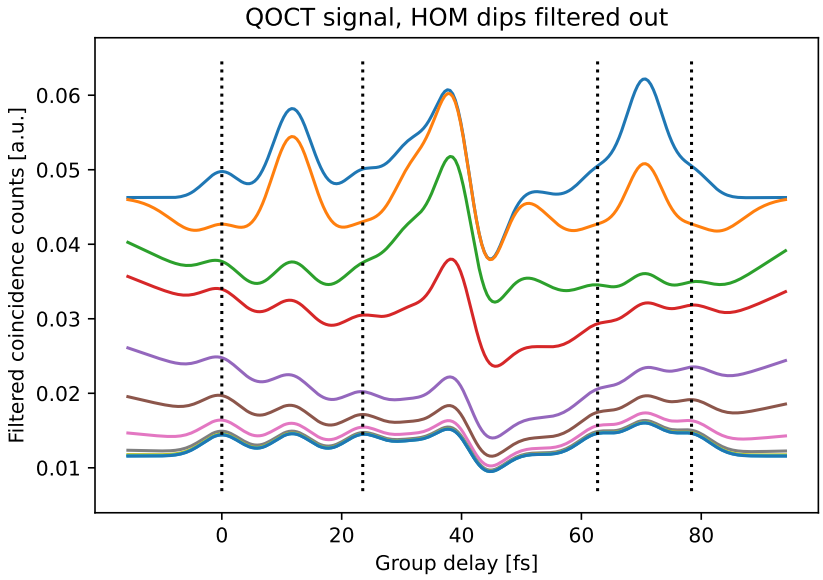

Figure 5.16: Simulated QOCT interferograms after filtering out part of the diagonal components of the joint temporal amplitude, for filters of various widths. The filter widths T_- are 1.5, 5, 15, 25, 50, 75, 125, 250, 500, 1250, and 5000 femtoseconds, from top to bottom. (The order of delays along the vertical axis is inverted compared to Figure 5.15. This is because one filter (5.15) is an increasing function of T_-, while the other (5.16) is a decreasing function of T_-.) Dashed lines indicate the position of sample interfaces. Optical properties are the same as in Figure 5.15.

due to cross-interference are removed, the HOM peaks broaden similar to a classical OCT signal. Since this filtering is performed in post-processing, however, the interferogram for multiple filter widths can be calculated from a single set of measured data. When the off-diagonal components of the JTA are removed, artifact peaks disappear; this allows one to identify the "real" peaks corresponding to sample interfaces. Once these have been identified, one can return to the original, unfiltered interferogram, which shows less dispersive broadening and therefore greater precision in the location of the peaks. By comparing the results of multiple kinds of filters, then, it is possible to avoid both the ambiguity arising from the artifact peaks and also the poor resolution resulting from dispersion. Of course, one is not limited to the kinds of simple filters we have considered here. A more holistic method of post-processing relying on the entire complex JTA may provide the same information without the need for multiple analyses. One can also consider methods which relate the measured JTAs at all delay line positions, rather than the current approach of separately filtering the JTA at each delay.

5.5 Conclusion

Quantum optical coherence tomography holds some promise as a means of enhancing the resolution of tomographic imaging. It is the case in many applications that the sample of interest determines the allowable bandwidth of a probe beam. For instance, tomographic imaging of the choroid, a vascular structure behind the retina, is limited to wavelengths greater than 1050 nm, which results in a reduced imaging resolution. Quantum OCT, which shows resolution enhancements due to both the coincidence measurement and to time-frequency entanglement (see Subsection 5.3.4), can improve resolution without requiring invasive measurements. This resolution enhancement comes at the expense of many practical challenges. Our work addresses two of these, namely the problem of statistical noise and the problem of interference artifacts.

The primary source of statistical noise in QOCT comes from the presence of accidental coincidence counts, which are due to uncorrelated detections and do not show any interference. The number of ac-

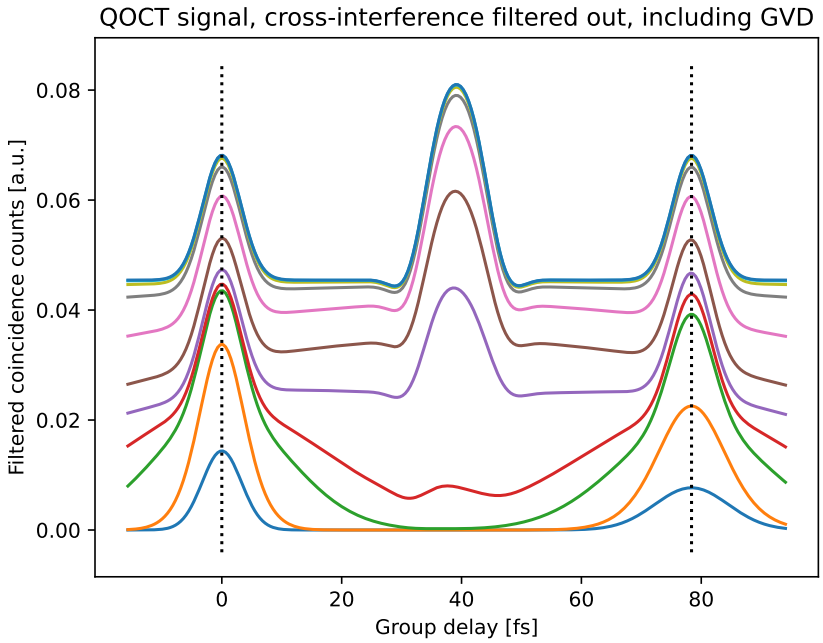

Figure 5.17: Simulated QOCT interferograms after filtering out off-diagonal components of the joint temporal amplitude, for a sample with large group velocity dispersion. The filter function and filter widths are the same as in Figure 5.15. The right peak shows greater broadening than the left, due to its location deeper in the sample. This simulation involves two reflecting interfaces (imparting equal phase shifts) at depths of 0.0 and 8.0 μm and a group index of 1.48. An excessively large GVD of $\beta_2 = 2 \times 10^{12}$ is used to highlight the effect.

cidentals increases quadratically with the source brightness; as a result, measurements of lossy samples are fundamentally limited by the measurement duration and the detector's time resolution. We discuss preliminary experimental results which use frequency correlations to filter out accidental counts, thereby improving the quality of the measured interferogram. Using a biphoton spectrometer, we show an improvement in the coincidence-to-accidentals ratio by a factor of approximately one hundred; furthermore, frequency-domain processing of the measured interferogram allows for accurate reconstruction of a HOM dip using only a few hundred measured biphotons. Ongoing work seeks to use this technique to perform the first tomographic measurement of a tissue-like sample without relying on artificially-enhanced sample reflections.

Artifact interference has long been identified as a fundamental challenge for QOCT. In a measurement involving N HOM dips, there will generally be $N^2/2$ additional artifact peaks which do not correspond simply to the sample structure. Many authors have proposed methods of artifact removal; these methods invariably rely on modification of the pump beam — for large pump bandwidths, the visibility of artifact peaks decreases. In practice, one wishes to image structures near the resolution limit of the interferometer. Removal of all artifacts in this case requires a pump bandwidth similar to the bandwidth of the biphoton probe. Sources of this type are not in common use due to the great challenge in achieving suitable phase-matching for all pump wavelengths. We discuss an alternative interferometric method of artifact removal; this method relies on the bandwidth of the probe photons, not of the pump, and so can automatically remove artifacts near the resolution limit. This method relies on physical differences between HOM interference and artifact (cross-)interference. We show that these effects are physically distinct, so that the two types of interference can be distinguished on the basis of their time-domain behaviour. This work is one of the first to consider the time-domain behaviour of QOCT; as we show, consideration of both the temporal and spectral properties of this interference can yield practical benefits.

6

Conclusions

Quantum metrology as a field of research is currently at an inflection point. Much of the research of past few decades has sought to establish a theoretical legitimacy to the idea of quantum-enhanced measurements. This began in the early development of quantum information theory and the connection between entanglement and sensitivity. Once the theoretical underpinnings of metrology were understood, effort turned to detailed study of a few key measurement problems, such as interferometric measurement of a single unknown phase parameter. In this concrete setting, the problem becomes optimization of the probe state and measurement strategy given various constraints. It quickly became apparent that theoretically-optimal states, such as the N-photon N00N state, were only practically useful in idealized settings. Efficient generation of these probe states and implementation of the optimal measurement scheme remains challenging. Furthermore, these highly-entangled states were not only more sensitive to the parameter of interest but are also more sensitive to experimental imperfections and loss, so that their performance quickly degraded in practical settings. At present, it seems that these experimental imperfections limit the amount of precision enhancement that can be obtained using quantum techniques. Rather than the $\sqrt{M}$-enhancement predicted by Heisenberg scaling, which can be made arbitrarily large by increasing the number M of entangled particles, one instead finds that the quantum precision enhancement scales as $\sqrt{M}$ only for small M, after which only classical-like scaling of the precision with the number of probes is possible.

Despite this large body of theoretical knowledge, the techniques of quantum metrology have only led to practical improvements in a few situations. Most prominent of these has been the use of quadrature-

squeezed light in the LIGO gravitational wave interferometer. This experiment served as the ideal testing ground for practical quantum metrology: the experiment involves measurement of a single unknown phase, one of the most well-studied metrological problems; the generation and detection of squeezed light are relatively straightforward; the experimental precision of the measurement was expected to be quantum-limited; and the great difficulty and scale of the experiment meant that the potential precision enhancements from quantum techniques were well worth the cost of implementation. Few measurements come close to the scale and sensitivity of LIGO, however. Further applications of quantum metrology must therefore provide practical benefits in measurements which are less well-defined, and which may contain larger amounts of experimental imperfection. The resilience of quantum techniques in the face of loss is therefore crucial for practical utility.

This work has largely focused on the measurement of parameters encoded in the temporal and spectral properties of entangled photon pairs. A common theme throughout this work is the presence of many unknown values in problems of interest. For instance, spectroscopic measurements (Chapters 3 and 4) can be described by the many electronic parameters governing the optical resonances of a molecule, or alternatively by an unknown amplitude and phase shift at each frequency. Chapter 2 discusses another role that these additional parameters may play: under certain circumstances, information about one parameter of interest (for instance, the relative delay between photons) may become correlated with information about additional parameters which are not measured (such as the mean delay). Measurements which cannot resolve both parameters are limited in their estimation of either value. In each of these situations, simple models involving a single unknown parameter are insufficient, and a more complete description involving many parameters gives further insight into the metrological performance of the technique. Another example comes from Chapter 4: Hong-Ou-Mandel interferometers provide lower absorption sensitivity than heralded measurements, and lower phase sensitivity than N00N-state interferometers. At the same time, HOM interferometers may outperform both of these more conventional techniques when absorption and phase are used together in the inference of model parameters. Here, consideration of only absorption or phase fails to capture the possible utility of this technique in spectroscopic measurements.

Leaving aside the information-theoretic advantages of entangled photon pairs, the optical properties of these pairs may offer practical advantages. These pairs can be easily generated, possess broad bandwidths, and offer phase-stable interference that is insensitive to some forms of dispersion. Pairs which are generated by down-conversion automatically feature strong time-frequency correlations which can form the basis of powerful denoising techniques. Section 5.2 highlights the use of these frequency correlations in measurements of a highly lossy sample; in this case, filtering the measured signal using this frequency-domain information allows us to reject over 99% of the detected pairs, leaving only a few hundred which contain the information of interest. These remaining pairs in turn allow for sub-micron estimation of the position of a scattering center. These frequency correlations are not uniquely quantum, and can be mimicked using classical sources of light, but the ease with which strongly-correlated quantum pairs can be generated makes them an appealing optical probe.

Many current optical measurements operate in a regime in which the number of probe photons is constrained. This is the case whenever the sample of interest may be damaged by incoming photons, as occurs in measurements involving biological samples and many types of fluorophores. When this is the case, one faces an inherent limit to the possible measurement sensitivity based on the limited information available per probe photon. Quantum-enhanced measurement techniques, which allow one to greatly increase the sensitivity by careful control over the incident photons, may lead to practical improvements in measurements involving small numbers of photons.

APPENDICES

A

Time-resolved detection in Hong-Ou-Mandel measurements of delay

This appendix views the results of Section 2.4 from the perspective of a simple model of time-resolved detection, and shows how the precision bounds described therein appear in the limit of poor timing resolution.

Specifically, we consider a model in which the detectors project onto a set of time-frequency modes ζ_{T_D,ω_D} which are centered at time T_D and frequency ω_D. The time-frequency modes have a Gaussian form

$$\zeta_{T_D,\omega_D}(\omega) = \left(\frac{\tau^2}{2\pi^3}\right)^{1/4} e^{-\tau^2(\omega-\omega_D)^2} e^{i\omega T_D}. \tag{A.1}$$

The single-photon projectors then have the form

$$\Pi_j(T_D,\omega_D) = \left[\int d\omega\, \zeta_{T_D,\omega_D}(\omega)\, a_j^\dagger(\omega)\,|0\rangle\right] \times (\text{h.c.}), \tag{A.2}$$

where $j = 1, 2$ denotes the two spatial modes, and h.c. indicates the Hermitian conjugate of the first factor.

The two-photon projectors have the form

$$\Pi_{ij}(T_D, \omega_D, T'_D, \omega'_D) = \left[\int d\omega \int d\omega' \, \zeta_{T_D,\omega_D}(\omega) \, \zeta_{T'_D,\omega'_D}(\omega') \, a_i^\dagger(\omega) a_j^\dagger(\omega') \, |0\rangle \right] \times \text{(h.c.)}. \tag{A.3}$$

These operators are normalized so that

$$\int dT_D \int d\omega_D \, \Pi_j(T_D, \omega_D) = \int d\omega a_j^\dagger(\omega) \, |0\rangle \, \langle 0| \, a_j(\omega), \tag{A.4a}$$

$$\int dT_D \int d\omega_D \int dT'_D \int d\omega'_D \, \Pi_{12}(T_D, \omega_D, T'_D, \omega'_D) = \int d\omega \int d\omega' a_1^\dagger(\omega) a_2^\dagger(\omega') \, |0\rangle \, \langle 0| \, a_1(\omega) a_2(\omega'), \tag{A.4b}$$

$$\int dT_D \int d\omega_D \int_{T'_D > T_D} dT'_D \int d\omega'_D \, \Pi_{ii}(T_D, \omega_D, T'_D, \omega'_D) = \int d\omega \int_{\omega' > \omega} d\omega' a_i^\dagger(\omega) a_i^\dagger(\omega') \, |0\rangle \, \langle 0| \, a_i(\omega) a_i(\omega'). \tag{A.4c}$$

The requirement that $T'_D > T_D$ ensures that basis vectors $a_i^\dagger(\omega) a_i^\dagger(\omega') \, |0\rangle$ are only counted once, regardless of the permutation of ω and ω'. For completeness, we also define the projector $\Pi_0 = |0\rangle \, \langle 0|$, so that the set of all projectors sum to the identity.

The detection probabilities for each outcome are calculated for a two-photon state with joint spectral amplitude (2.6),

$$\phi_0(\omega_1, \omega_2) e^{-i\omega_1 \tau_1 - i\omega_2 \tau_2}. \tag{A.5}$$

Since we wish to consider both single and coincidence clicks, it is necessary to introduce a source of loss; for simplicity, we give each detector a quantum efficiency of θ. This detector efficiency can be included by introducing beamsplitters with transmission θ in each arm, and tracing out the additional modes. We again consider detectors that resolve neither photon number nor frequency, so that we must add the probability for bunching outcomes to the single detection probabilities, and we must sum over all unobserved variables (corresponding to the two detection frequencies, as well as the later of the two detection times for bunched

pairs). Explicitly, we calculate

$$p_i(T_D) = \int d\omega_D \ \langle\psi|\,\Pi_i(T_D,\omega_D)\,|\psi\rangle + \int_{T'_D>T_D} dT'_D \int d\omega_D \int d\omega'_D \ \langle\psi|\,\Pi_{ii}(T_D,\omega_D,T'_D,\omega'_D)\,|\psi\rangle \tag{A.6a}$$

$$p_{12}(T_D,T'_D) = \int d\omega_D \int d\omega'_D \ \langle\psi|\,\Pi_{12}(T_D,\omega_D,T'_D,\omega'_D)\,|\psi\rangle \tag{A.6b}$$

$$p_0 = 1 - \sum_{i=1}^{2} \int dT_D\, p_i(T_D) + \int dT_D \int dT'_D\, p_{12}(T_D,T'_D). \tag{A.6c}$$

These lead to the probabilities

$$p_0 = (1-\theta)^2, \tag{A.7a}$$

$$p_1(T_D) = \frac{\theta(1-\theta)}{\sqrt{2\pi\tau^2}} \iint dt\,dt' \ \left|\widetilde{\phi}_0(t,t')\right|^2 \left[(1-\eta)e^{-\left[t'+T_D-(\tau_+-\tau_-)\right]^2/2\tau^2} + \eta e^{-[t+T_D-(\tau_++\tau_-)]^2/2\tau^2}\right] + \frac{\eta(1-\eta)\theta^2}{2\sqrt{2\pi\tau^2}} \iint dt\,dt' \ \left|\widetilde{\phi}_0(t+\tau_-,t'-\tau_-) + \widetilde{\phi}_0(t'+\tau_-,t-\tau_-)\right|^2 e^{-(t+T_D-\tau_+)^2/2\tau^2}, \tag{A.7b}$$

$$p_2(T_D) = \frac{\theta(1-\theta)}{\sqrt{2\pi\tau^2}} \iint dt\,dt' \ \left|\widetilde{\phi}_0(t,t')\right|^2 \left[\eta e^{-\left[t'+T_D-(\tau_+-\tau_-)\right]^2/2\tau^2} + (1-\eta)e^{-[t+T_D-(\tau_++\tau_-)]^2/2\tau^2}\right] + \frac{\eta(1-\eta)\theta^2}{2\sqrt{2\pi\tau^2}} \iint dt\,dt' \ \left|\widetilde{\phi}_0(t+\tau_-,t'-\tau_-) + \widetilde{\phi}_0(t'+\tau_-,t-\tau_-)\right|^2 e^{-(t+T_D-\tau_+)^2/2\tau^2}, \tag{A.7c}$$

$$p_{12}(T_D,T'_D) = \frac{\theta^2}{2\pi\tau^2} \iint dt\,dt' \left|\eta\widetilde{\phi}_0(t+\tau_-,t'-\tau_-) - (1-\eta)\widetilde{\phi}_0(t'+\tau_-,t-\tau_-)\right|^2 \ldots \ldots e^{-(t+T_D-\tau_+)^2/2\tau^2-(t'+T'_D-\tau_+)^2/2\tau^2}, \tag{A.7d}$$

where we have defined the joint temporal amplitude

$$\widetilde{\phi}_0(t_1,t_2) = \frac{1}{2\pi} \int d\omega_1 \int d\omega_2\, \phi_0(\omega_1,\omega_2) e^{-i\omega_1 t_1 - i\omega_2 t_2}. \tag{A.8}$$

If the detector time resolution is much larger than the characteristic time over which the joint temporal

amplitude varies, then the exponential functions in each integral may be approximated by a constant. If we suppose that $\widetilde{\phi}_0(t,t')$ is sharply peaked around $t \simeq t' \simeq 0$, then we have

$$p_0 = (1-\theta)^2, \tag{A.9a}$$

$$p_1(T_D) = \frac{\theta(1-\theta)}{\sqrt{2\pi\tau^2}}\left[(1-\eta)e^{-[T_D-(\tau_+-\tau_-)]^2/2\tau^2} + \eta e^{-[T_D-(\tau_++\tau_-)]^2/2\tau^2}\right] + \frac{\eta(1-\eta)\theta^2}{2\sqrt{2\pi\tau^2}} e^{-(T_D-\tau_+)^2/2\tau^2} \iint dt\, dt' \left|\widetilde{\phi}_0(t+\tau_-, t'-\tau_-) + \widetilde{\phi}_0(t'+\tau_-, t-\tau_-)\right|^2, \tag{A.9b}$$

$$p_2(T_D) = \frac{\theta(1-\theta)}{\sqrt{2\pi\tau^2}}\left[\eta e^{-[T_D-(\tau_+-\tau_-)]^2/2\tau^2} + (1-\eta)e^{-[T_D-(\tau_++\tau_-)]^2/2\tau^2}\right] + \frac{\eta(1-\eta)\theta^2}{2\sqrt{2\pi\tau^2}} e^{-(t+T_D-\tau_+)^2/2\tau^2} \iint dt\, dt' \left|\widetilde{\phi}_0(t+\tau_-, t'-\tau_-) + \widetilde{\phi}_0(t'+\tau_-, t-\tau_-)\right|^2, \tag{A.9c}$$

$$p_{12}(T_D, T_D') = \frac{\theta^2}{2\pi\tau^2} e^{-(T_D-\tau_+)^2/2\tau^2 - (T_D'-\tau_+)^2/2\tau^2} H(\tau_-). \tag{A.9d}$$

Here, the function

$$H(\tau_-) = \iint dt\, dt' \left|\eta\widetilde{\phi}_0(t+\tau_-, t'-\tau_-) - (1-\eta)\widetilde{\phi}_0(t'+\tau_-, t-\tau_-)\right|^2 \tag{A.10}$$

describes the two-photon interference pattern. Approximate precision bounds may be calculated directly from this expression.

As discussed in Section 2.3, the precision bounds for measurements of $\tau_\pm$ are described by the classical

Fisher information $\boldsymbol{\mathcal{F}}$, whose elements are given by

$$\begin{aligned}\mathcal{F}_{ij} = &\frac{1}{p_0}\left(\frac{\partial p_0}{\partial \tau_i}\right)\left(\frac{\partial p_0}{\partial \tau_j}\right) \\ &+ \int dT_D\, \frac{1}{p_1(T_D)}\left(\frac{\partial p_1(T_D)}{\partial \tau_i}\right)\left(\frac{\partial p_1(T_D)}{\partial \tau_j}\right) \\ &+ \int dT_D\, \frac{1}{p_2(T_D)}\left(\frac{\partial p_2(T_D)}{\partial \tau_i}\right)\left(\frac{\partial p_2(T_D)}{\partial \tau_j}\right) \\ &+ \iint dT_D\, dT'_D\, \frac{1}{p_{12}(T_D, T'_D)}\left(\frac{\partial p_{12}(T_D, T'_D)}{\partial \tau_i}\right)\left(\frac{\partial p_{12}(T_D, T'_D)}{\partial \tau_j}\right). \end{aligned} \tag{A.11}$$

Here, τ_i, τ_j denote one of the two variables $\tau_\pm$. Analytical evaluation of this matrix is not possible without further restrictions on the form of the joint temporal amplitude. Note, however, that $\mathcal{F}_{ij}$ has the dimensions of an inverse time squared. In the system under consideration, the two relevant timescales are τ, that of the detector response, and T, which characterizes the timescale over which $H(\tau_-)$ varies; as shown in Section 2.4, T is approximately equal to the inverse of the biphoton bandwidth, and is usually much shorter than τ. It is therefore sufficient to consider only the relevant order of each of the matrix elements. By performing a series expansion of (A.11) using the probabilities (A.9), we have

$$\mathcal{F}_{++} = O(\tau^{-2}), \tag{A.12a}$$

$$\mathcal{F}_{+-} = O(\tau^{-2}), \tag{A.12b}$$

$$\mathcal{F}_{--} = \frac{\theta^2}{H(\tau_-)}\left(\frac{dH(\tau_-)}{d\tau_-}\right)^2 + O(T^{-2}) + O(\tau^{-2}). \tag{A.12c}$$

The $O(T^{-2})$ term in $\mathcal{F}_{--}$ denotes a contribution of the approximate form $(dH(\tau_-)/d\tau_-)^2/(1 - H(\tau_-))$ arising from the singles counts. This term was discussed in the context of a no-coincidence event in Section 2.4; in the context of the current discussion, a more detailed calculation shows that for high interference visibility, the prefactor of this term decreases quickly as θ decreases from zero. In experimentally-relevant situations, then, this singles contribution may be safely ignored in comparison to the first term.

The effective precision bound for estimation of τ_- is, from Section 2.3,

$$\frac{1}{(\Delta\tau_-)^2} \leq \mathcal{F}_{--} - \frac{\mathcal{F}_{+-}^2}{\mathcal{F}_{++}} \approx \frac{\theta^2}{H(\tau_-)} \left(\frac{dH(\tau_-)}{d\tau_-} \right)^2 + O(\tau^{-2}). \tag{A.13}$$

When the detector timing resolution τ is negligible in comparison to the biphoton coherence time $T \sim (dH(\tau_-)/d\tau_-)/H(\tau_-)$, we obtain the same expression used in Section 2.4, in which information is obtained only from pair detections and can be calculated from knowledge of the interference pattern $H(\tau_-)$ alone.

It is worthwhile to consider the validity of this model as a description of realistic detectors. Photodetectors typically do not perform time-frequency projections of the type considered here, but rather are described by a POVM which takes into consideration the detector time response. The analysis conducted here follows essentially from the probability distribution (A.9), which makes no mention of a detection frequency, and indeed which is obtained from the state not by a projection onto a pure state but rather by a POVM (since it involves integration over the non-orthonormal time-frequency modes ζ_{T_D,ω_D}). This distribution can be taken as an approximate description of a realistic detector, where the time resolution τ is no longer related to an intrinsic optical bandwidth of the detector, but rather is set by systematic factors such as the electronic response time. The same conclusions about the Fisher information matrix then continue to hold.

B

The relationship between precision bounds calculated with and without the no-click outcome

Chapter 4 calculates the precision bounds for measurement of absorption and phase using a spectrally-resolved Hong-Ou-Mandel interferometer. In principle, some information about the absorption is obtained from the number of incident pairs which do not lead to any detector click. In practice, this rate is not measured; furthermore, this contribution greatly complicates the theoretical discussion, since it prevents one from separating the estimation problem at one frequency from the problem at other, unrelated frequencies. The chapter presents physical arguments allowing for the no-click contribution to be ignored. This appendix presents a mathematical proof that neglect of this contribution serves only to decrease the effective Fisher information that one calculates for each parameter. This neglect therefore leads to precision bounds which are still saturable, and hence describe the true metrological performance of the measurement.

Let $\boldsymbol{\mathcal{F}}$ be the classical Fisher information matrix calculated using some probability distribution $p_k(\{\zeta\})$, where k is an enumeration of some measurement outcomes and $\{\zeta\}$ denotes a set of unknown parameters.

The elements of $\boldsymbol{\mathcal{F}}$ are given by the expression

$$\mathcal{F}_{\zeta\zeta'} = \sum_k \frac{1}{p_k} \left(\frac{\partial p_k}{\partial \zeta} \right) \left(\frac{\partial p_k}{\partial \zeta'} \right). \tag{B.1}$$

We also define the matrix $\boldsymbol{\mathcal{F}'}$ by a similar summation which extends over all outcomes k except for one.

$$\mathcal{F}'_{\zeta\zeta'} = \sum_{k\neq 0} \frac{1}{p_k} \left(\frac{\partial p_k}{\partial \zeta} \right) \left(\frac{\partial p_k}{\partial \zeta'} \right). \tag{B.2}$$

The effective classical Fisher information of a parameter ζ is defined to be $1/(\mathcal{F}^{-1})_{\zeta\zeta}$, *i.e.*, the inverse of a diagonal element of $\boldsymbol{\mathcal{F}}$. We prove that the effective information for ζ calculated from $\boldsymbol{\mathcal{F}}$ is lower bounded by the same effective information calculated from $\boldsymbol{\mathcal{F}'}$.

First, note that $\boldsymbol{\mathcal{F}} - \boldsymbol{\mathcal{F}'}$ is a matrix with components

$$\mathcal{F}_{\zeta\zeta'} - \mathcal{F}'_{\zeta\zeta'} = \frac{1}{p_0} \left(\frac{\partial p_0}{\partial \zeta} \right) \left(\frac{\partial p_0}{\partial \zeta'} \right). \tag{B.3}$$

The matrix $\boldsymbol{\mathcal{F}} - \boldsymbol{\mathcal{F}'}$ is therefore just the outer product of a vector $\boldsymbol{v}$ with itself, where the ζ-component of the $\boldsymbol{v}$ is $(\partial p_0/\partial\zeta)/\sqrt{p_0}$. It follows that $\boldsymbol{\mathcal{F}} - \boldsymbol{\mathcal{F}'}$ is positive semidefinite, so that $\boldsymbol{\mathcal{F}} - \boldsymbol{\mathcal{F}'} \geq 0$, or

$$\boldsymbol{\mathcal{F}} \geq \boldsymbol{\mathcal{F}'}. \tag{B.4}$$

So long as $\mathcal{F}$ is nonsingular, this is equivalent to the statement

$$\boldsymbol{\mathcal{F}}^{-1} \leq \boldsymbol{\mathcal{F}'}^{-1}. \tag{B.5}$$

This implies that the diagonal components of $\boldsymbol{\mathcal{F}}^{-1}$ and $\boldsymbol{\mathcal{F}'}^{-1}$ are related by $(\mathcal{F}^{-1})_{\zeta\zeta} \leq (\mathcal{F}'^{-1})_{\zeta\zeta}$, from which the statement holds.

C

Alternative spectroscopic methods

C.1 Introduction

Chapter 4 makes a comparison between the HOM experiment and other possible spectroscopic measurements of absorption and phase. This appendix describes the different interferometers discussed, and provides details about the precision bounds for each.

C.2 Classical interferometer

The simplest comparison one can make, and the one used as the classical benchmark for the HOM-based spectrometer, is the classical Mach-Zehnder interferometer. This device takes as its input a coherent state $|\alpha\rangle$, which is divided at a beamsplitter into two beams. One beam interacts with the sample, after which it is recombined with the second beam at another beamsplitter. The distribution of intensities at each output port is measured. Since the interferometer relies only on linear optics, any change in intensity of the input beam can be entirely attributed to absorption by the sample. The phase shift, meanwhile, can be determined by the difference in intensities leaving the two output ports.

The input state takes the form $D_a(\alpha)\,|0\rangle$, where $D_a(\alpha)$ is the displacement operator for mode a,

$$D_a(\alpha) = \exp\left(\alpha a^\dagger - \alpha^* a\right). \tag{C.1}$$

The first beamsplitter, whose transmission coefficient is assumed to be tunable, performs the transformation $a^\dagger \longmapsto \sqrt{\zeta}a^\dagger + \sqrt{1-\zeta}b^\dagger$. Since the modes a and b are orthogonal, the displacement operator can be factored to obtain the probe state

$$|\psi_{\text{in}}\rangle = D_a\left(\sqrt{\zeta}\alpha\right) D_b\left(\sqrt{1-\zeta}\alpha\right)|0\rangle\,. \tag{C.2}$$

The effect of the sample is to perform the transformation

$$a^\dagger \longmapsto e^{-\theta/2+i\phi}a^\dagger + \sqrt{1-e^{-\theta}}s^\dagger, \tag{C.3}$$

where s is an auxiliary mode used in place of the sample. After the sample, the state is then

$$D_a\left(\sqrt{\zeta}\alpha e^{-\theta/2+i\phi}\right) D_b\left(\sqrt{1-\zeta}\alpha\right) D_s\left(\sqrt{\zeta}\alpha\sqrt{1-e^{-\theta}}\right)|0\rangle\,, \tag{C.4}$$

and since this is a separable state, the mode s can be easily traced out to obtain

$$D_a\left(\sqrt{\zeta}\alpha e^{-\theta/2+i\phi}\right) D_b\left(\sqrt{1-\zeta}\alpha\right)|0\rangle\,. \tag{C.5}$$

We also allow for additional losses in each arm with respective transmittances T and R, analogous to the similar calculation in Section 3.4. This leads to the pre-beamsplitter state

$$D_a\left(\sqrt{T\zeta}\alpha e^{-\theta/2+i\phi}\right) D_b\left(\sqrt{R(1-\zeta)}\alpha\right)|0\rangle \tag{C.6}$$

The absorption and phase parameters are embedded in the amplitude of the probe arm's coherent state; uncertainty in the amplitude and phase of this coherent state ultimately sets the shot noise-limited sensitivity for both parameters.

The final 50:50 beamsplitter transforms this state into one described by the output modes c and d,

where

$$a^\dagger = \sqrt{\xi}c^\dagger - \sqrt{1-\xi}d^\dagger, \tag{C.7a}$$

$$b^\dagger = \sqrt{1-\xi}c^\dagger + \sqrt{\xi}d^\dagger, \tag{C.7b}$$

leading to the output state

$$\begin{aligned}|\psi_{\text{in}}\rangle &= D_c\left(\sqrt{T\xi\zeta}\alpha e^{-\theta/2+i\phi}\right) D_d\left(-\sqrt{T(1-\xi)\zeta}\alpha e^{-\theta/2+i\phi}\right)\ldots \\ &\qquad D_c\left(\sqrt{R(1-\xi)(1-\zeta)}\alpha\right) D_d\left(\sqrt{R\xi(1-\zeta)}\alpha\right)|0\rangle\,, \\ &\propto D_c\left(\alpha(\sqrt{R(1-\xi)(1-\zeta)} + \sqrt{T\xi\zeta}e^{-\theta/2+i\phi})\right) D_d\left(\alpha(\sqrt{R\xi(1-\zeta)} - \sqrt{T(1-\xi)\zeta}e^{-\theta/2+i\phi})\right)|0\rangle\,.\end{aligned} \tag{C.8}$$

In the final line we have dropped a global phase. The intensity (photon number) at each output port is measured using a photodetector. Detector losses are included via a further factor of η in each coherent state amplitude. Since the state is separable, the probability distribution for the measurement outcomes at the two ports are independent variables. For a coherent state with amplitude γ, the distribution is

$$p(n) = \frac{|\zeta|^{2n}}{n!}e^{-|\zeta|^2}. \tag{C.9}$$

If ζ depends on θ and ϕ, then a simple calculation shows that

$$\begin{aligned}
\mathcal{F}_{\theta\theta} &= \sum_{n=0}^{\infty} \frac{1}{p(n;\theta,\phi)} \left(\frac{\partial p(n;\theta,\phi)}{\partial \theta} \right)^2 \\
&= \frac{1}{|\zeta(\theta,\phi)|^2} \left(\frac{\partial |\zeta(\theta,\phi)|^2}{\partial \theta} \right)^2, \qquad \text{(C.10a)} \\
\mathcal{F}_{\phi\phi} &= \sum_{n=0}^{\infty} \frac{1}{p(n;\theta,\phi)} \left(\frac{\partial p(n;\theta,\phi)}{\partial \phi} \right)^2, \\
&= \frac{1}{|\zeta(\theta,\phi)|^2} \left(\frac{\partial |\zeta(\theta,\phi)|^2}{\partial \phi} \right)^2, \qquad \text{(C.10b)} \\
\mathcal{F}_{\theta\phi} &= \sum_{n=0}^{\infty} \frac{1}{p(n;\theta,\phi)} \frac{\partial p(n;\theta,\phi)}{\partial \theta} \frac{\partial p(n;\theta,\phi)}{\partial \phi} \\
&= \frac{1}{|\zeta(\theta,\phi)|^2} \frac{\partial |\zeta(\theta,\phi)|^2}{\partial \theta} \frac{\partial |\zeta(\theta,\phi)|^2}{\partial \phi}. \qquad \text{(C.10c)}
\end{aligned}$$

Since the measured intensities at the two output ports are statistically independent, the classical Fisher information matrix for the joint probability distribution governing the two intensities is just the sum of the matrices calculated using one output port's intensity. We are interested in the case of a photosensitive sample, so we generally consider the information per incident photon, which we define in the multiparameter case to be $\left[(\mathcal{F}^{-1})_{\theta\theta}\right]/\zeta|\alpha|^2$ and $\left[(\mathcal{F}^{-1})_{\phi\phi}\right]/\zeta|\alpha|^2$ for the respective parameters; that is, the inverse of the classical Cramér-Rao bound, normalized by the number of photons $\zeta|\alpha|^2$ in the probe arm.

The bound on estimation of θ found in this way,

$$(\Delta\theta)^2 \geq \frac{1}{\zeta|\alpha|^2} \frac{Te^{-\theta}\zeta + R(1-\zeta)}{\eta\zeta T^2 e^{-2\theta}}, \qquad \text{(C.11)}$$

is independent of the final beamsplitter transmission ξ. The phase estimation bound generally does depend on ξ; numerical simulations show that the bound is optimized when $\xi = \zeta$. We assume this value of ξ in all future analysis. There is generally a tradeoff between the two parameters when choosing a value of the ζ: the phase information per incident photon is optimal when $\zeta \to 0$, whereas the absorption estimation is optimal when $\zeta \to 1$. The optimal value of ζ for a given problem therefore depends on the relative

importance of phase and absorption estimation.

The phase bound generally has a complicated form. After optimizing the phase bound over ϕ, the phase information per photon is a function of ζ, $Te^{-\theta}$, and R. The multiparameter information per photon approaches the information $\mathcal{F}_{\phi\phi}$ for single-parameter estimation of ϕ whenever $\zeta \to 0$ and $T \leq R$. In this case, the phase bound is

$$(\Delta\phi)^2 \geq \frac{1}{\zeta|\alpha|^2}\frac{1}{4Te^{-\theta}}. \tag{C.12}$$

In this situation, the information per photon (for either the multiparameter or single parameter case) is independent of the exact intensity in the reference arm, so long as $R > T$.

It is important to note that the problems of phase and amplitude estimation are highly dependent on each other with this measurement. Apart from the limit $\zeta \to 0$ discussed above, independent measurements of ϕ and θ have very different metrological precision than the multiparameter case; in the lossless limit $T \to 1, R \to 1, \eta \to 1, \zeta \to 1$, the optimal phase offset for measurements of absorption is π, and the absorption information-per-photon is $\mathcal{F}_{\theta\theta}/|\alpha|^2\zeta \to e^{-\theta}$. The phase estimation has an optimal working point of $\phi \sim \pi/2$, and when we take $\zeta \to 0$ instead, the phase information-per-photon tends to a constant value of $\mathcal{F}_{\phi\phi}/|\alpha|^2\zeta \to 4e^{-\theta}$. These values of $\mathcal{F}_{\theta\theta} = e^{-\theta}$ and $\mathcal{F}_{\phi\phi} = 4e^{-\theta}$ are what define the shot noise limits for absorption and phase estimation, respectively.

C.3 Heralded absorption measurement

The method of heralded measurement of absorption was pioneered by David Klyshko[151], not as a method of precise sensing but rather as a tool to determine detection efficiencies without the need for calibration of the source intensity. Of course, if one puts an absorbing sample between the source and detector, then an absolute measurement of efficiency automatically becomes a measurement of sample absorption. Theoretical calculations [64] based on an optimization of precision over all quantum states have shown

this heralded measurement to be the optimal absorption measurement on a per-probe-photon basis. More specifically, the optimal measurement occurs for any Fock state along with number-resolving detection; heralded single photons are merely the simplest such measurement to implement in practice.

The measurement begins with a photon pair, as may be produced by SPDC.

$$|\psi_{\text{in}}\rangle = \sqrt{1-g}\,|0\rangle + \sqrt{g}a^\dagger b^\dagger\,|0\rangle\,. \tag{C.13}$$

We take mode a to be the probe beam, while mode b is a herald beam. Losses are introduced into each arm: the total transmission of the probe arm is $Te^{-\theta}$, while the herald arm is R. Here, $e^{-\theta}$ is taken to be the transmission of the sample, while T is the transmission of all other optics in the probe arm; both T and R are assumed to include the detector efficiencies as well. After tracing out auxiliary modes associated with the losses, the system is left in a mixed state,

$$\begin{aligned}\rho_{\text{out}} = {} & g(1-Te^{-\theta})(1-R)\,|0\rangle\langle 0| + gT(1-R)e^{-\theta}a^\dagger\,|0\rangle\langle 0|\,a + g(1-Te^{-\theta})Rb^\dagger\,|0\rangle\langle 0|\,b \\ & + \left[\sqrt{1-g} + \sqrt{gTRe^{-\theta}}a^\dagger b^\dagger\right]|0\rangle\langle 0|\left[\sqrt{1-g} + \sqrt{gTRe^{-\theta}}ab\right].\end{aligned} \tag{C.14}$$

The first term describes pairs which are both absorbed or lost; the second and third term describe loss of a single photon in one of the two arms; the final term describes pairs which are both transmitted. This state is measured at two photodetectors — since each arm has at most one photon, number resolution is irrelevant. There are four possible outcomes: no detection, a single detection at one of two arms, or a pair detection. These have respective probabilities

$$p_0 = (1-g) + g(1-Te^{-\theta})(1-R), \tag{C.15a}$$

$$p_a = gT(1-R)e^{-\theta}, \tag{C.15b}$$

$$p_b = g(1-Te^{-\theta})R, \tag{C.15c}$$

$$p_{ab} = gTRe^{-\theta}. \tag{C.15d}$$

As described, this measurement has no phase sensitivity, as any phase shift in the mode a appears as a global phase in the two-photon component of the state (coherent projection onto a combination of the vacuum and two-photon states can, however, detect this phase. This is the basis of phase measurements using squeezed states). We therefore consider a single parameter estimation problem concerning the unknown absorption θ.

The classical Fisher information has the form

$$\begin{aligned}\mathcal{F}_\theta &= \frac{1}{p_0}\left(\frac{\partial p_0}{\partial \theta}\right)^2 + \frac{1}{p_a}\left(\frac{\partial p_a}{\partial \theta}\right)^2 + \frac{1}{p_b}\left(\frac{\partial p_b}{\partial \theta}\right)^2 + \frac{1}{p_{ab}}\left(\frac{\partial p_{ab}}{\partial \theta}\right)^2 \\ &= g\frac{Te^{-\theta}}{1-Te^{-\theta}}\frac{1+T(1-R)e^{-\theta}-gR}{1-gTe^{-\theta}(1-R)-gR}.\end{aligned} \tag{C.16}$$

The information per incident photon (of which there are g per trial) is

$$\frac{1}{g}\mathcal{F}_\theta = \frac{Te^{-\theta}}{1-Te^{-\theta}}\frac{1+T(1-R)e^{-\theta}-gR}{1-gTe^{-\theta}(1-R)-gR}. \tag{C.17}$$

The resulting expression generally increases with g. In the limit $g \to 1$, this model describes deterministic generation of a photon pair; in this case, the presence of a probe photon is always known regardless of whether a herald photon is detected, so the information per probe photon in this case is the same as the limit of perfect heralding, $R \to 0$. In typical experiments, the opposite is true: the pairs are generated by very weak two-mode squeezing which requires $g \ll 1$, so that the creation of pairs is highly stochastic. In this limit, we have

$$\lim_{g\to 0}\frac{1}{g}\mathcal{F}_\theta = \frac{Te^{-\theta}}{1-Te^{-\theta}}\left(1-Te^{-\theta}(1-R)\right). \tag{C.18}$$

In the limit of perfect heralding the final factor drops out, and the information per photon is

$$\lim_{R\to 1}\lim_{g\to 0}\frac{1}{g}\mathcal{F}_\theta = \frac{Te^{-\theta}}{1-Te^{-\theta}}. \tag{C.19}$$

If we instead consider the limit of no heralding, $R \to 0$, then

$$\lim_{R\to 1}\lim_{g\to 0}\frac{1}{g}\mathcal{F}_\theta = Te^{-\theta}. \tag{C.20}$$

This expression, in which the information per photon is just the number of detected photons, is just the shot noise limit for absorption measurements discussed in the previous section. The single-photon absorption measurement performs just as well as a shot noise-limited measurement with a coherent state; *i.e.*, there is no advantage without heralding.

For a finite heralding efficiency, the ratio of the heralded measurement's per-photon absorption information to the shot noise limit is

$$\frac{1-Te^{-\theta}(1-R)}{1-Te^{-\theta}}. \tag{C.21}$$

This is generally greater than unity: any amount of heralding enables a quantum advantage in absorption measurements. For a fixed sample transmission, the advantage increases linearly with the herald arm transmission R, so that the scale of the quantum advantage is proportional to the number of herald photons detected. Furthermore, unlike many other metrological problems, the advantage of the heralded measurement over the classical method is unbounded for even a single photon as the sample beam's overall efficiency $Te^{-\theta}$ increases to unity. Returning to the expression (C.16) for $\mathcal{F}_\theta$, this unbounded advantage comes entirely from the detection outcome p_b. For any finite heralding rate, a click at the herald arm's detector but not the probe arm's detector immediately indicates a photon was lost in the sample arm. When the transmission $Te^{-\theta}$ is close to one, a single absorption is highly informative about size of θ. Mathematically, the large value of $\mathcal{F}_\theta$ is due to the fact that the probability p_b decreases to zero as $Te^{-\theta} \to 1$, while the sensitivity $\partial p_b/\partial\theta$ stays finite. The signal-to-noise ratio for this outcome can therefore grow dramatically as the optical losses approach zero.

C.4 Interferometry using N00N states

Heralded single photons are the optimal probe of absorption; at the same time, high-N N00N states are known to be the optimal probe of phase. Practically, the difficulty associated with these states is due to the fast degradation of the phase sensitivity as the optical losses decrease. Loss of a single photon destroys any coherence in the state, and the probability of a single loss grows quickly as the number of photons is increased. Because of this extreme sensitivity to loss, they also make good probes of sample absorption.

The optimal measurement scheme for phase measurements using a N00N state is generally quite difficult to implement — comparable, in fact, to the difficulty in preparing the state in the first place. We do not consider here the optimal phase measurement. Instead, since the goal is also to obtain a good absorption measurement, we consider a measurement scheme in which the two modes are mixed at a beamsplitter, the outputs of which are monitored by ideal number-resolving detectors. As we show, this leads to absorption precision which approaches that of a heralded measurement, while also enabling enhanced phase sensitivity.

A N-photon N00N state takes the form

$$|\psi_{\text{in}}\rangle = \sqrt{1-g}\,|0\rangle + \sqrt{\frac{g}{2}}\left(\frac{(a^\dagger)^N}{\sqrt{N!}} + \frac{(b^\dagger)^N}{\sqrt{N!}}\right)|0\rangle\,. \tag{C.22}$$

As in other treatments, we take the sample arm to be a and the reference arm to be b. Interaction with the sample, and losses in the two arms, can be described by the transformation

$$a^\dagger \to \sqrt{Te^{-\theta}}e^{-\phi}a^\dagger + \sqrt{1-Te^{-\theta}}a'^\dagger, \tag{C.23a}$$

$$b^\dagger \to \sqrt{R}b^\dagger + \sqrt{1-R}b'^\dagger. \tag{C.23b}$$

After expanding the binomials, this leads to the state

$$\sqrt{1-g}\,|0\rangle + \sqrt{\frac{g}{2N!}}\sum_{k=0}^{N}\binom{N}{k}\Big[\left(Te^{-\theta}\right)^{(N-k)/2}\left(1-Te^{-\theta}\right)^{k/2}e^{i(N-k)\phi}(a^\dagger)^{N-k}(a'^\dagger)^k + R^{(N-k)/2}(1-R)^{k/2}(b^\dagger)^{N-k}(b'^\dagger)^k\Big]|0\rangle\,. \tag{C.24}$$

Tracing out the auxiliary modes, this becomes

$$\rho = \sum_{m=1}^{N}\frac{g}{2(N-m)!}\binom{N}{m}\left(Te^{-\theta}\right)^{N-m}\left(1-Te^{-\theta}\right)^{m}(a^\dagger)^{N-m}\,|0\rangle\langle 0|\,a^{N-m} + \sum_{m=1}^{N}\frac{g}{2(N-m)!}\binom{N}{m}R^{N-m}(1-R)^m(b^\dagger)^{N-m}\,|0\rangle\langle 0|\,b^{N-m} + \frac{g}{2N}\,|\psi_N\rangle\langle\psi_N|\,, \tag{C.25}$$

where

$$|\psi_N\rangle \equiv \left[\sqrt{\frac{1-g}{g}} + \left(Te^{-\theta}\right)^{N/2}e^{iN\phi}(a^\dagger)^N + R^{N/2}(b^\dagger)^N\right]|0\rangle\,. \tag{C.26}$$

The beamsplitter performs the transformation

$$a^\dagger \to \sqrt{\zeta}c^\dagger + \sqrt{1-\zeta}d^\dagger, \tag{C.27a}$$

$$b^\dagger \to \sqrt{1-\zeta}c^\dagger - \sqrt{\zeta}d^\dagger. \tag{C.27b}$$

The probe is detected at a beamsplitter, leading to a probability of having p photons in c and q photons

in d given by

$$p_s(p,q) = \begin{cases} (1-g) + \frac{g}{2}\left[\left(1-Te^{-\theta}\right)^N + (1-R)^N\right], & p=q=0, \\ \frac{g}{2}\binom{N}{p+q}\binom{p+q}{p}\Big[\left(Te^{-\theta}\right)^{p+q}\left(1-Te^{-\theta}\right)^{N-p-q}\zeta^p(1-\zeta)^q & \\ \qquad +R^{p+q}(1-R)^{N-p-q}(1-\zeta)^p\zeta^q\Big], & 0<p+q<N, \\ \frac{g}{2}\binom{N}{p}\left|\left(Te^{-\theta}\right)^{N/2}e^{-iN\phi}\zeta^{p/2}(1-\zeta)^{q/2} + (-1)^q R^{N/2}(1-\zeta)^{p/2}\zeta^{q/2}\right|^2, & p+q=N, \\ 0, & p+q>N. \end{cases}$$

We finally include equal losses η in the two output modes, after which the probability of detecting p photons in c and q in d is

$$p(p,q) = \sum_{\ell=0}^{\infty}\sum_{\ell'=0}^{\infty}\binom{p+\ell}{\ell}\binom{q+\ell'}{\ell'}\eta^{p+q}(1-\eta)^{\ell+\ell'}p_s(p+\ell,q+\ell') \tag{C.28}$$

These probabilities are used to calculate the classical Fisher information matrix in the usual way. We define the absorption and phase information per incident photon by

$$C_\theta = \lim_{g\to 0}\frac{2}{gN}\left(\left(\mathcal{F}^{-1}\right)_{\theta\theta}\right)^{-1}, \qquad C_\phi = \lim_{g\to 0}\frac{2}{gN}\left(\left(\mathcal{F}^{-1}\right)_{\phi\phi}\right)^{-1}, \tag{C.29}$$

which are the inverse of the classical Cramér-Rao bound, normalized by the average number of incident photons $gN/2$. The limit $g \to 0$ is taken to eliminate any information associated with heralding of the state; the resulting information is entirely due to N00N state enhancements to the sensitivity.

Due to the complexity of the resulting classical Fisher information expressions, analytic study of the problem for arbitrary N is not possible. The following conclusions are based on symbolic and numeric evaluation of the expressions for photon numbers N ranging from one to three. The absorption information C_θ is optimal when the phase is near one of $\phi = 0$ or $\phi = \pi$. The phase information C_ϕ is minimal when $\phi = 0$ and $\phi = \pi$. Another tradeoff occurs in the choice of the beamsplitter transmission ζ: the absorption information is maximized when $\zeta \to 0$ or $\zeta \to 1$, while the phase information vanishes in this limit, being

maximized when $\zeta \to 1/2$.

In the limit $\zeta \to 0$, the N00N state probe approaches a heralded Fock state, similar to the one discussed above. The absorption information has a simple expression in this limit. For low numbers of photons, it is given by

$$C_\theta = \begin{cases} \frac{\eta T e^{-\theta}}{\eta R + \eta T e^{-\theta}} \eta T e^{-\theta}, & N = 1, \\ \frac{\eta T e^{-\theta}}{1 - \eta T e^{-\theta}} \left(1 - 2\eta T e^{-\theta} + 2\eta^2 T^2 e^{-2\theta}\right), & N = 2, \\ \frac{\eta T e^{-\theta}}{1 - \eta T e^{-\theta}} \left[1 - 3\eta T e^{-\theta} \left(1 - \eta T e^{-\theta}\right)^2\right], & N = 3. \end{cases} \tag{C.30}$$

It is interesting to note that the $N = 1$ case behaves qualitatively different than other cases, depending on R and also showing different scaling in the per-photon information. The $N = 2$ case performs the best when $\eta T e^{-\theta} < 1/3$. The $N = 3$ case shows the most improvement over $N = 2$ when $\eta T e^{-\theta} \approx 0.678$. However, the multiparameter analysis breaks down in the limit $\zeta \to 0$, since the measurement gives no phase information in this case. A more realistic analysis uses the per-photon information for single-parameter estimation of absorption, which in the limit $\zeta \to 0$ is

$$\lim_{\zeta \to 0} \lim_{g \to 0} \frac{2}{gN} \mathcal{F}_{\theta\theta} = \begin{cases} \eta T e^{-\theta}, & N = 1, \\ \frac{\eta T e^{-\theta}}{1 - \eta T e^{-\theta}} \left(1 - 2\eta T e^{-\theta} + 2\eta^2 T^2 e^{-2\theta}\right), & N = 2, \\ \frac{\eta T e^{-\theta}}{1 - \eta T e^{-\theta}} \left[1 - 3\eta T e^{-\theta} \left(1 - \eta T e^{-\theta}\right)^2\right] & N = 3. \end{cases} \tag{C.31}$$

As may be expected, the $N = 1$ case behaves the same as a classical (shot noise-limited) measurement of absorption, with the information being simply the number of photons detected. This is the same expression found for the heralded measurement when the heralding efficiency decreases to zero. The remaining cases show the same expression in this limit as was given by the multiparameter bound, so that the discussion above still applies. The $N = 1$ case now outperforms higher N when $\eta T e^{-\theta}$ is small (below about 0.4). Ultimately, the $N = 1$ scaling is still much worse in the $\eta T e^{-\theta} \to 1$ limit. The ratio of

the $N > 1$ information to the quantum bound (given by a perfect heralded measurement) is $\eta T e^{-\theta}$ when $\eta T e^{-\theta} \to 1$. The N00N states approach the optimal measurement for high transmittance. This can be understood as a kind of heralding: for high transmittance, it is unlikely for more than one photon to be absorbed by the sample. The remaining photons then trigger the detector, and since we have assumed number resolving detection, this detection "heralds" the existence of the remaining photon which was lost. However, the increased sensitivity of N00N states to loss means that this information degrades much faster than traditional heralded measurements as the transmission decreases, eventually performing worse than the shot noise limit.

We now consider the case $\zeta = 1/2$, which shows both absorption and phase sensitivity. The expressions for C_θ including losses in the herald arm and detectors are very long rational functions in the losses (they do not depend on the particular value of ϕ), and provide no insight. If the only losses come from the sample arm, $R \to 1$ and $\eta \to 1$, then the expressions simplify greatly. In this case, the per-photon absorption information for low values of N is given by

$$C_\theta = \begin{cases} \frac{Te^{-\theta}}{1+Te^{-\theta}} Te^{-\theta}, & N = 1, \\ \frac{Te^{-\theta}}{1-Te^{-\theta}} \frac{1-4Te^{-\theta}+5T^2e^{-2\theta}-2T^3e^{-3\theta}+2T^4e^{-4\theta}}{1+T^2e^{-2\theta}}, & N = 2, \\ \frac{Te^{-\theta}}{1-Te^{-\theta}} \frac{1-3Te^{-\theta}+3T^2e^{-2\theta}+T^3e^{-3\theta}-3T^4e^{-4\theta}+6T^5e^{-5\theta}-3T^6e^{-6\theta}}{(1+Te^{-\theta})(1-Te^{-\theta}+T^2e^{-2\theta})}, & N = 3. \end{cases} \tag{C.32}$$

Qualitatively, the absorption information behaves as discussed earlier. The $N = 1$ state generally performs worse than the shot noise limit. The $N = 2$ and $N = 3$ cases again have the limiting form $Te^{-\theta}/(1-Te^{-\theta})$ due to self-heralding by the probe beam, and these tend to the quantum limit as losses approach zero. The loss tolerance of both states is worse than the $\zeta \to 0$ case, however: the $N = 2$ state falls below the shot noise limit for transmissions below $Te^{-\theta} \approx 0.701$, and the $N = 3$ state does the same for values below 0.621.

The per-photon phase information of an N-photon state is optimized when $\phi \sim \pi/2N$. The multiparameter phase information has a simple form when this phase is chosen as the operating point. In general,

the per-photon information is

$$C_\phi = \frac{4N\eta^N T^N R^N e^{-N\theta}}{R^N + T^N e^{-N\theta}}. \tag{C.33}$$

In the limit of low losses, the phase information approaches $2N$. Even though the measurement under consideration is not optimal from a metrological point of view (an optimal N00N state interferometer shows a per-photon information that is N times the shot noise limit, whereas the information here is $N/2$ times the limit), it still shows the same N-fold scaling. It should be noted, however, that due to this factor of 2, any quantum advantage in phase estimation occurs only when $N > 2$. At the same time, the sensitivity to losses also shows an N-fold enhancement, and in the absence of other losses ($T = R = \eta = 1$), the per-photon phase sensitivity falls below the shot noise limit when $e^{-\theta}$ falls below $N^{-1/(N-1)}$.

The main takeaway here is not that number-resolved N00N state interferometers are a practical avenue towards enhanced spectroscopic sensitivity. N00N states are notoriously difficult to prepare when N exceeds 2, which is required for this scheme to show any enhancement in phase sensitivity (and this ignores the tight loss tolerances that are introduced as N becomes large). At the same time, number-resolving detectors as a technology are still in their infancy, and the prospect of building a number-resolving detector with enough channels to perform practical spectroscopy, though technically feasible, appears to lie in the distant future. Instead, this scheme highlights a surprising aspect of quantum-enhanced linear spectroscopy: even though optical amplitude and phase are traditionally considered complementary observables, it is possible for a single, simultaneous measurement to achieve an arbitrarily large enhancement in per-photon sensitivity of both absorption and phase. That is, enhanced sensitivity to one variable does not necessarily come with any trade off in sensitivity to the other.

D

Implementation of the artifact removal scheme

Section 5.4 provided a high-level description of an interferometric method for removal of QOCT artifact peaks. From Figure 5.14, it may seem that implementation of this method is quite difficult, involving multiple different spatial modes and interference between many beams. This appendix shows how such a scheme may be implemented in existing spectrally-resolved QOCT experiments similar to that of Section 5.2. The basic idea is to prepare the probe and reference biphoton states with orthogonal polarizations; almost all of the scheme can then be implemented in a colinear manner using polarization optics.

A diagram of such an implementation is shown in Figure D.1. The two biphoton amplitudes are generated using a pair of nonlinear crystals which have a relative rotation of 90 degrees about the beam axis; such a geometry is known as a "crossed-crystal" source [152]. Due to phase matching requirements, each crystal generates biphotons only from a particular linear polarization of the pump beam. One therefore prepares a pump beam with an elliptical polarization state

$$|E_p\rangle = \frac{E_0}{\sqrt{2}} |H\rangle + \frac{E_0}{\sqrt{2}} e^{i\theta} |V\rangle , \tag{D.1}$$

where the relative phase θ is encoded using an electro-optic modulator. Assuming type-0 phase matching in each crystal, the output is a superposition of two biphoton states — in one, both photons have horizontal

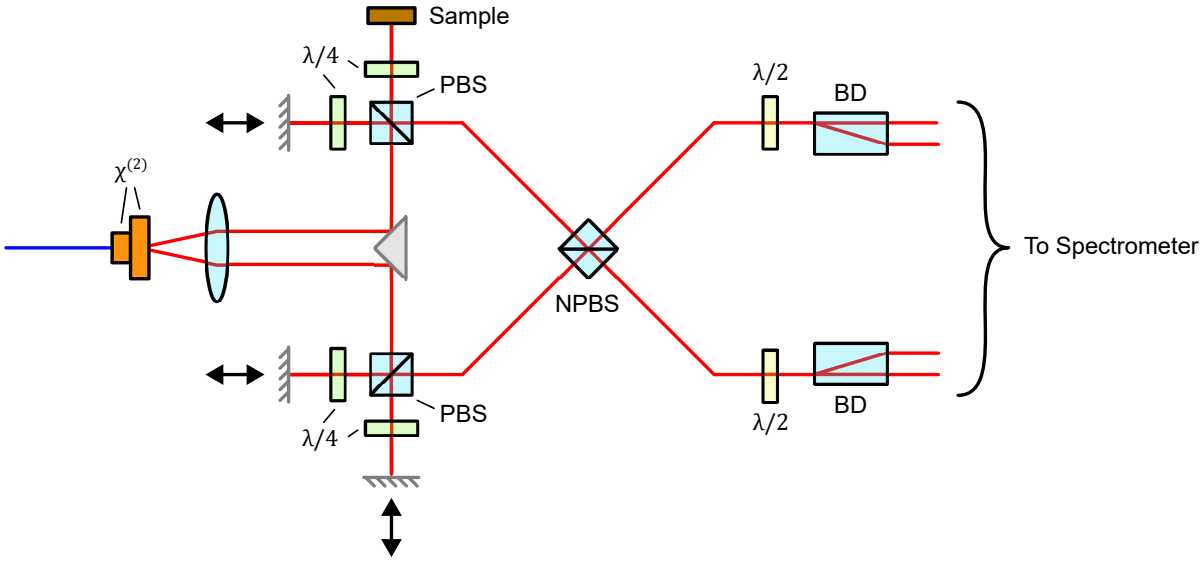

Figure D.1: Schematic diagram of a possible optical implementation of the method of Section 5.4, involving small modifications of the experiment of Figure 5.2. A pair of nonlinear crystals in a crossed-crystal geometry generate two biphoton amplitudes with orthogonal polarizations. A single photon from one of the biphoton amplitudes interacts with the sample. A single non-polarizing beamsplitter implements the QOCT interferometer and also creates a bunched state in the reference biphoton amplitude. Half wave plates and beam displacers (BD) interfere the two different polarizations. Spectrally-resolved detection of the four beams allows for reconstruction of the complex joint temporal amplitude of the QOCT-probing biphoton amplitude.

polarization, and in the other, both photons have vertical polarization:

$$|\phi_0\rangle_{HH} + e^{i\theta} |\phi_0\rangle_{VV} . \tag{D.2}$$

For definiteness, we will take the horizontally polarized pair to be the probe biphoton amplitude, and the vertically polarized pair to be the reference biphoton amplitude.

The two cross-polarized biphoton amplitudes exit the crystals in a colinear beam. A collimating lens and knife-edge mirror separates the photon pairs so that one photon travels down each of the two arms of the interferometer. As in Section 5.2, a polarizing beamsplitter and quarter wave plate are placed in each arm. The polarizing beamsplitter separates the two polarization states of each beam; one of the

polarization components of the sample arm reflects from the tomographic sample, while the remaining three beams reflect from mirrors. The positions of these three mirrors can be used to separately set the relative delays of all four beams.

A non-polarizing beamsplitter serves two purposes. First, it mixes the two horizontally polarized photons; this acts as the QOCT interferometer's beamsplitter. Second, it mixes the two vertically polarized photons; if the relative delay between the vertically polarized photons is set to zero, then the reference biphoton always bunches at this beamsplitter. This beamsplitter thus also serves to prepare the desired reference biphoton state.

After the beamsplitter, it is necessary to interfere the horizontally and vertically polarized components of each output beam; this interference is indicated by the additional beamsplitter in Figure 5.14. This interference can be easily accomplished by placing a half wave plate and a birefringent beam displacer in each arm; the half wave plate rotates the horizontal and vertical polarizations to diagonal and antidiagonal polarizations, and the beam displacer places the horizontal and vertical components of the resulting beam in two spatially-separated beams. This implements a polarization interferometer between the probe and reference biphoton amplitudes.

Finally, detection can be performed using a time-tagging camera, as discussed in Subsection 3.3.4. Existing measurements involve illuminating only two rows of the camera's sensor; it is straightforward to instead use four illuminated rows, which allows for separate spectral resolution of each of the four exiting the two beam displacers.

References

[1] P Grangier, G Roger, and A Aspect. "Experimental Evidence for a Photon Anticorrelation Effect on a Beam Splitter: A New Light on Single-Photon Interferences". In: *Europhys. Lett.* 1.4 (Feb. 15, 1986), pp. 173–179. ISSN: 0295-5075, 1286-4854. DOI: 10.1209/0295-5075/1/4/004.

[2] Leonard Mandel and Emil Wolf. *Optical Coherence and Quantum Optics*. Cambridge: Cambridge University Press, 1995. ISBN: 978-0-521-41711-2. DOI: 10.1017/CBO9781139644105.

[3] Roy Glauber. "Optical Coherence and Photon Statistics". In: *Quantum Optics and Electronics*. Gordon and Breach, 1965, p. 63. ISBN: 978-0-677-10530-7.

[4] H. J. Kimble, M. Dagenais, and L. Mandel. "Photon Antibunching in Resonance Fluorescence". In: *Phys. Rev. Lett.* 39.11 (Sept. 12, 1977), pp. 691–695. ISSN: 0031-9007. DOI: 10.1103/PhysRevLett.39.691.

[5] R. Ghosh et al. "Interference of two photons in parametric down conversion". In: *Phys. Rev. A* 34.5 (Nov. 1, 1986), pp. 3962–3968. ISSN: 0556-2791. DOI: 10.1103/PhysRevA.34.3962.

[6] R. Ghosh and L. Mandel. "Observation of nonclassical effects in the interference of two photons". In: *Phys. Rev. Lett.* 59.17 (Oct. 26, 1987), pp. 1903–1905. ISSN: 0031-9007. DOI: 10.1103/PhysRevLett.59.1903.

[7] C. K. Hong, Z. Y. Ou, and L. Mandel. "Measurement of subpicosecond time intervals between two photons by interference". In: *Phys. Rev. Lett.* 59.18 (Nov. 2, 1987). Publisher: American Physical Society, pp. 2044–2046. DOI: 10.1103/PhysRevLett.59.2044.

[8] Z. Y. Ou and L. Mandel. "Observation of Spatial Quantum Beating with Separated Photodetectors". In: *Phys. Rev. Lett.* 61.1 (July 4, 1988). Publisher: American Physical Society, pp. 54–57. DOI: 10.1103/PhysRevLett.61.54.

[9] J. G. Rarity and P. R. Tapster. "Two-color photons and nonlocality in fourth-order interference". In: *Phys. Rev. A* 41.9 (May 1, 1990), pp. 5139–5146. ISSN: 1050-2947, 1094-1622. DOI: 10.1103/PhysRevA.41.5139.

[10] Aephraim M. Steinberg, Paul G. Kwiat, and Raymond Y. Chiao. "Dispersion cancellation and high-resolution time measurements in a fourth-order optical interferometer". In: *Phys. Rev. A* 45.9 (May 1, 1992). Publisher: American Physical Society, pp. 6659–6665. DOI: 10.1103/PhysRevA.45.6659.

[11] A. M. Steinberg, P. G. Kwiat, and R. Y. Chiao. "Dispersion cancellation in a measurement of the single-photon propagation velocity in glass". In: *Phys. Rev. Lett.* 68.16 (Apr. 20, 1992), pp. 2421–2424. ISSN: 0031-9007. DOI: 10.1103/PhysRevLett.68.2421.

[12] W. P. Grice et al. "Spectral distinguishability in ultrafast parametric down-conversion". In: *Phys. Rev. A* 57.4 (Apr. 1, 1998), R2289–R2292. ISSN: 1050-2947, 1094-1622. DOI: 10.1103/PhysRevA.57.R2289.

[13] X. Y. Zou, L. J. Wang, and L. Mandel. "Induced coherence and indistinguishability in optical interference". In: *Phys. Rev. Lett.* 67.3 (July 15, 1991), pp. 318–321. ISSN: 0031-9007. DOI: 10.1103/PhysRevLett.67.318.

[14] J. D. Franson. "Bell inequality for position and time". In: *Phys. Rev. Lett.* 62.19 (May 8, 1989). Publisher: American Physical Society, pp. 2205–2208. DOI: 10.1103/PhysRevLett.62.2205.

[15] P. G. Kwiat, A. M. Steinberg, and R. Y. Chiao. "High-visibility interference in a Bell-inequality experiment for energy and time". In: *Phys. Rev. A* 47.4 (Apr. 1, 1993), R2472–R2475. ISSN: 1050-2947, 1094-1622. DOI: 10.1103/PhysRevA.47.R2472.

[16] C. Helstrom. "The detection and resolution of optical signals". In: *IEEE Trans. Inform. Theory* 10.4 (Oct. 1964), pp. 275–287. ISSN: 0018-9448, 1557-9654. DOI: 10.1109/TIT.1964.1053702.

[17] Carl W. Helstrom. "Detection theory and quantum mechanics". In: *Information and Control* 10.3 (Mar. 1967), pp. 254–291. ISSN: 00199958. DOI: 10.1016/S0019-9958(67)90302-6.

[18] C.W. Helstrom. "Minimum mean-squared error of estimates in quantum statistics". In: *Physics Letters A* 25.2 (July 1967), pp. 101–102. ISSN: 03759601. DOI: 10.1016/0375-9601(67)90366-0.

[19] C.W. Helstrom, J.W.S. Liu, and J.P. Gordon. "Quantum-mechanical communication theory". In: *Proc. IEEE* 58.10 (1970), pp. 1578–1598. ISSN: 0018-9219. DOI: 10.1109/PROC.1970.7983.

[20] Carlton M. Caves. "Quantum-mechanical noise in an interferometer". In: *Phys. Rev. D* 23.8 (Apr. 15, 1981). Publisher: American Physical Society, pp. 1693–1708. DOI: 10.1103/PhysRevD.23.1693.

[21] Bernard Yurke, Samuel L. McCall, and John R. Klauder. "SU(2) and SU(1,1) interferometers". In: *Phys. Rev. A* 33.6 (June 1, 1986), pp. 4033–4054. ISSN: 0556-2791. DOI: 10.1103/PhysRevA.33.4033.

[22] D.W. Berry and H.M. Wiseman. "Adaptive measurements and optimal states for quantum interferometry". In: *Summaries of papers presented at the Quantum Electronics and Laser Science Conference*. Quantum Electronics and Laser Science Conference. Baltimore, MD, USA: Opt. Soc. America, 2001, pp. 60–61. ISBN: 978-1-55752-663-2. DOI: 10.1109/QELS.2001.961853.

[23] Charles H. Bennett and Stephen J. Wiesner. "Communication via one- and two-particle operators on Einstein-Podolsky-Rosen states". In: *Phys. Rev. Lett.* 69.20 (Nov. 16, 1992), pp. 2881–2884. ISSN: 0031-9007. DOI: 10.1103/PhysRevLett.69.2881.

[24] Charles H. Bennett et al. "Teleporting an unknown quantum state via dual classical and Einstein-Podolsky-Rosen channels". In: *Phys. Rev. Lett.* 70.13 (Mar. 29, 1993), pp. 1895–1899. ISSN: 0031-9007. DOI: 10.1103/PhysRevLett.70.1895.

[25] Charles H. Bennett. "Classical and Quantum Information Transmission and Interactions". In: *Quantum Communication, Computing, and Measurement*. Ed. by O. Hirota, A. S. Holevo, and C. M. Caves. Boston, MA: Springer US, 1997, pp. 25–39. ISBN: 978-1-4613-7716-0. DOI: 10.1007/978-1-4615-5923-8_4.

[26] W. K. Wootters. "Statistical distance and Hilbert space". In: *Phys. Rev. D* 23.2 (Jan. 15, 1981), pp. 357–362. ISSN: 0556-2821. DOI: 10.1103/PhysRevD.23.357.

[27] Samuel L. Braunstein and Carlton M. Caves. "Statistical Distance and the Geometry of Quantum States". In: *Physical Review Letters* 72.22 (May 1994), pp. 3439–3443. ISSN: 0031-9007. DOI: 10.1103/PhysRevLett.72.3439.

[28] D. J. Wineland et al. "Spin squeezing and reduced quantum noise in spectroscopy". In: *Phys. Rev. A* 46.11 (Dec. 1, 1992), R6797–R6800. ISSN: 1050-2947, 1094-1622. DOI: 10.1103/PhysRevA.46.R6797.

[29] Vittorio Giovannetti, Seth Lloyd, and Lorenzo Maccone. "Quantum Metrology". In: *Phys. Rev. Lett.* 96.1 (Jan. 3, 2006), p. 010401. ISSN: 0031-9007, 1079-7114. DOI: 10.1103/PhysRevLett.96.010401.

[30] J. J . Bollinger et al. "Optimal frequency measurements with maximally correlated states". In: *Phys. Rev. A* 54.6 (Dec. 1, 1996), R4649–R4652. ISSN: 1050-2947, 1094-1622. DOI: 10.1103/PhysRevA.54.R4649.

[31] Hwang Lee, Pieter Kok, and Jonathan P. Dowling. "A quantum Rosetta stone for interferometry". In: *Journal of Modern Optics* 49.14 (Nov. 2002), pp. 2325–2338. ISSN: 0950-0340, 1362-3044. DOI: 10.1080/0950034021000011536.

[32] M. W. Mitchell, J. S. Lundeen, and A. M. Steinberg. "Super-resolving phase measurements with a multiphoton entangled state". In: *Nature* 429.6988 (May 2004), pp. 161–164. ISSN: 0028-0836, 1476-4687. DOI: 10.1038/nature02493.

[33] Jonathan P. Dowling. "Quantum optical metrology – the lowdown on high-N00N states". In: *Contemporary Physics* 49.2 (Mar. 2008), pp. 125–143. ISSN: 0010-7514, 1366-5812. DOI: 10.1080/00107510802091298.

[34] U. Dorner et al. "Optimal Quantum Phase Estimation". In: *Phys. Rev. Lett.* 102.4 (Jan. 30, 2009), p. 040403. ISSN: 0031-9007, 1079-7114. DOI: 10.1103/PhysRevLett.102.040403.

[35] Rafał Demkowicz-Dobrzański, Jan Kołodyński, and Mădălin Guţă. "The elusive Heisenberg limit in quantum-enhanced metrology". In: *Nat Commun* 3.1 (Sept. 18, 2012), p. 1063. ISSN: 2041-1723. DOI: 10.1038/ncomms2067.

[36] A. S. Holevo. "Optimal quantum measurements". In: *Theor Math Phys* 17.3 (Dec. 1973), pp. 1172–1177. ISSN: 0040-5779, 1573-9333. DOI: 10.1007/BF01037594.

[37] Carl W. Helstrom. ""Simultaneous measurement" from the standpoint of quantum estimation theory". In: *Found Phys* 4.4 (Dec. 1974), pp. 453–463. ISSN: 0015-9018, 1572-9516. DOI: 10.1007/BF00708521.

[38] Steven M. Kay and Steven M. Kay. "Fundamentals of statistical signal processing. 1: Estimation theory". In: 20. pr. Num Pages: 595. Upper Saddle River, NJ: Prentice Hall PTR, 2013. ISBN: 978-0-13-345711-7.

[39] Helstrom. *Quantum Detection and Estimation Theory*. Google-Books-ID: Ne3iT_QLcsMC. Academic Press, July 6, 1976. 321 pp. ISBN: 978-0-08-095632-9.

[40] Alexander Semenovich Holevo. *Probabilistic and statistical aspects of quantum theory*. North Holland series in statistics and probability 1. Amsterdam u.a: North-Holland Publ. Co, 1982. 312 pp. ISBN: 978-0-444-86333-1.

[41] S. Massar and S. Popescu. "Optimal Extraction of Information from Finite Quantum Ensembles". In: *Phys. Rev. Lett.* 74.8 (Feb. 20, 1995), pp. 1259–1263. ISSN: 0031-9007, 1079-7114. DOI: 10.1103/PhysRevLett.74.1259.

[42] Jasminder S. Sidhu and Pieter Kok. "Geometric perspective on quantum parameter estimation". In: *AVS Quantum Science* 2.1 (Feb. 1, 2020), p. 014701. ISSN: 2639-0213. DOI: 10.1116/1.5119961.

[43] Keiji Matsumoto. "A Geometrical Approach to Quantum Estimation Theory". PhD thesis. University of Tokyo, 1997.

[44] Magdalena Szczykulska, Tillmann Baumgratz, and Animesh Datta. "Multi-parameter quantum metrology". In: *Advances in Physics: X* 1.4 (July 3, 2016), pp. 621–639. ISSN: 2374-6149. DOI: 10.1080/23746149.2016.1230476.

[45] Jing Liu et al. "Quantum Fisher information matrix and multiparameter estimation". In: *J. Phys. A: Math. Theor.* 53.2 (Dec. 2019). Publisher: IOP Publishing, p. 023001. ISSN: 1751-8121. DOI: 10.1088/1751-8121/ab5d4d.

[46] Rafał Demkowicz-Dobrzański, Wojciech Górecki, and Mădălin Guţă. "Multi-parameter estimation beyond quantum Fisher information". In: *J. Phys. A: Math. Theor.* 53.36 (Sept. 11, 2020), p. 363001. ISSN: 1751-8113, 1751-8121. DOI: 10.1088/1751-8121/ab8ef3.

[47] Emanuele Polino et al. "Experimental multiphase estimation on a chip". In: *Optica* 6.3 (Mar. 20, 2019), p. 288. ISSN: 2334-2536. DOI: 10.1364/OPTICA.6.000288.

[48] Aaron Z Goldberg et al. "Rotation sensing at the ultimate limit". In: *J. Phys. Photonics* 3.2 (Apr. 1, 2021), p. 022008. ISSN: 2515-7647. DOI: 10.1088/2515-7647/abeb54.

[49] Hugo Ferretti et al. "Optimal Quantum Multi-Parameter Estimation With Few-Photon States". In: *2024 Conference on Lasers and Electro-Optics (CLEO)*. 2024 Conference on Lasers and Electro-Optics (CLEO). ISSN: 2160-8989. May 2024, pp. 1–2.

[50] Matheus Eiji Ohno Bezerra, Francesco Albarelli, and Rafał Demkowicz-Dobrzanski. "Simultaneous optical phase and loss estimation revisited: measurement and probe incompatibility". In: *J. Phys. A: Math. Theor.* 58.26 (June 2025). Publisher: IOP Publishing, p. 265303. ISSN: 1751-8121. DOI: 10.1088/1751-8121/ade516.

[51] Mankei Tsang. "Quantum limits to optical point-source localization". In: *Optica* 2.7 (July 20, 2015), p. 646. ISSN: 2334-2536. DOI: 10.1364/OPTICA.2.000646.

[52] Jun Suzuki, Yuxiang Yang, and Masahito Hayashi. "Quantum state estimation with nuisance parameters". In: *J. Phys. A: Math. Theor.* 53.45 (Nov. 13, 2020), p. 453001. ISSN: 1751-8113, 1751-8121. DOI: 10.1088/1751-8121/ab8b78.

[53] Leigh S. Martin et al. "Implementation of a canonical phase measurement with quantum feedback". In: *Nat. Phys.* 16.10 (Oct. 2020), pp. 1046–1049. ISSN: 1745-2473, 1745-2481. DOI: 10.1038/s41567-020-0939-0.

[54] Mankei Tsang, Howard M. Wiseman, and Carlton M. Caves. "Fundamental Quantum Limit to Waveform Estimation". In: *Phys. Rev. Lett.* 106.9 (Mar. 3, 2011), p. 090401. ISSN: 0031-9007, 1079-7114. DOI: 10.1103/PhysRevLett.106.090401.

[55] James W. Gardner et al. "Achieving the Fundamental Quantum Limit of Linear Waveform Estimation". In: *Phys. Rev. Lett.* 132.13 (Mar. 28, 2024), p. 130801. ISSN: 0031-9007, 1079-7114. DOI: 10.1103/PhysRevLett.132.130801.

[56] James W. Gardner et al. "Stochastic Waveform Estimation at the Fundamental Quantum Limit". In: *PRX Quantum* 6.3 (July 22, 2025), p. 030311. ISSN: 2691-3399. DOI: 10.1103/h91r-4ws9.

[57] Lin Jiao et al. "Quantum Metrology in the Noisy Intermediate-Scale Quantum Era". In: *Adv Quantum Tech* 8.4 (Apr. 2025), p. 2300218. ISSN: 2511-9044, 2511-9044. DOI: 10.1002/qute.202300218.

[58] Emanuele Polino et al. "Photonic quantum metrology". In: *AVS Quantum Science* 2.2 (June 1, 2020), p. 024703. ISSN: 2639-0213. DOI: 10.1116/5.0007577.

[59] Chuan Xu et al. "Sensing and tracking enhanced by quantum squeezing". In: *Photon. Res.* 7.6 (June 1, 2019), A14. ISSN: 2327-9125. DOI: 10.1364/PRJ.7.000A14.

[60] Henning Vahlbruch et al. "Detection of 15 dB Squeezed States of Light and their Application for the Absolute Calibration of Photoelectric Quantum Efficiency". In: *Phys. Rev. Lett.* 117.11 (Sept. 6, 2016). Publisher: American Physical Society, p. 110801. DOI: 10.1103/PhysRevLett.117.110801.

[61] Rafal Demkowicz-Dobrzański and Lorenzo Maccone. "Using Entanglement Against Noise in Quantum Metrology". In: *Phys. Rev. Lett.* 113.25 (Dec. 19, 2014), p. 250801. ISSN: 0031-9007, 1079-7114. DOI: 10.1103/PhysRevLett.113.250801.

[62] Haocun Yu et al. "Quantum correlations between light and the kilogram-mass mirrors of LIGO". In: *Nature* 583.7814 (July 2, 2020), pp. 43–47. ISSN: 0028-0836, 1476-4687. DOI: 10.1038/s41586-020-2420-8.

[63] Michael A. Taylor et al. "Biological measurement beyond the quantum limit". In: *Nature Photon* 7.3 (Mar. 2013), pp. 229–233. ISSN: 1749-4885, 1749-4893. DOI: 10.1038/nphoton.2012.346.

[64] G. Adesso et al. "Optimal estimation of losses at the ultimate quantum limit with non-Gaussian states". In: *Phys. Rev. A* 79.4 (Apr. 23, 2009). Publisher: American Physical Society, p. 040305. DOI: 10.1103/PhysRevA.79.040305.

[65] G. Brida, M. Genovese, and I. Ruo Berchera. "Experimental realization of sub-shot-noise quantum imaging". In: *Nature Photon* 4.4 (Apr. 2010), pp. 227–230. ISSN: 1749-4885, 1749-4893. DOI: 10.1038/nphoton.2010.29.

[66] Ayman F. Abouraddy et al. "Quantum-optical coherence tomography with dispersion cancellation". In: *Phys. Rev. A* 65.5 (May 8, 2002). Publisher: American Physical Society, p. 053817. DOI: 10.1103/PhysRevA.65.053817.

[67] A. M. Steinberg, P. G. Kwiat, and R. Y. Chiao. "Measurement of the single-photon tunneling time". In: *Phys. Rev. Lett.* 71.5 (Aug. 2, 1993), pp. 708–711. ISSN: 0031-9007. DOI: 10.1103/PhysRevLett.71.708.

[68] Daniel Giovannini et al. "Spatially structured photons that travel in free space slower than the speed of light". In: *Science* 347.6224 (Feb. 20, 2015), pp. 857–860. ISSN: 0036-8075, 1095-9203. DOI: 10.1126/science.aaa3035.

[69] Gabriela Barreto Lemos et al. "Quantum imaging with undetected photons". In: *Nature* 512.7515 (Aug. 2014), pp. 409–412. ISSN: 0028-0836, 1476-4687. DOI: 10.1038/nature13586.

[70] Kevin Lyons et al. "Precision optical displacement measurements using biphotons". In: *Phys. Rev. A* 93.4 (Apr. 22, 2016), p. 043841. ISSN: 2469-9926, 2469-9934. DOI: 10.1103/PhysRevA.93.043841.

[71] Yuanyuan Chen et al. "Hong-Ou-Mandel interferometry on a biphoton beat note". In: *npj Quantum Inf* 5.1 (May 24, 2019). Publisher: Nature Publishing Group, p. 43. ISSN: 2056-6387. DOI: 10.1038/s41534-019-0161-z.

[72] Ranjith Nair. "Quantum-Limited Loss Sensing: Multiparameter Estimation and Bures Distance between Loss Channels". In: *Phys. Rev. Lett.* 121.23 (Dec. 3, 2018), p. 230801. ISSN: 0031-9007, 1079-7114. DOI: 10.1103/PhysRevLett.121.230801.

[73] J. Wang and G. S. Agarwal. "Quantum Fisher information bounds on precision limits of circular dichroism". In: *Phys. Rev. A* 104.6 (Dec. 16, 2021), p. 062613. ISSN: 2469-9926, 2469-9934. DOI: 10.1103/PhysRevA.104.062613.

[74] Laura T. Knoll and Gustavo M. Bosyk. "Simultaneous quantum estimation of phase and indistinguishability in a two-photon interferometer". In: *J. Opt. Soc. Am. B* 40.4 (Apr. 1, 2023), p. C67. ISSN: 0740-3224, 1520-8540. DOI: 10.1364/JOSAB.482301.

[75] Audrey Eshun et al. "Investigations of Molecular Optical Properties Using Quantum Light and Hong–Ou–Mandel Interferometry". In: *J. Am. Chem. Soc.* 143.24 (June 23, 2021). Publisher: American Chemical Society, pp. 9070–9081. ISSN: 0002-7863. DOI: 10.1021/jacs.1c02514.

[76] Shahaf Asban, Konstantin E. Dorfman, and Shaul Mukamel. "Interferometric spectroscopy with quantum light: Revealing out-of-time-ordering correlators". In: *J. Chem. Phys.* 154.21 (June 1, 2021), p. 210901. ISSN: 0021-9606. DOI: 10.1063/5.0047776.

[77] Konstantin E. Dorfman et al. "Hong-Ou-Mandel interferometry and spectroscopy using entangled photons". In: *Commun Phys* 4.1 (Mar. 11, 2021), p. 49. ISSN: 2399-3650. DOI: 10.1038/s42005-021-00542-2.

[78] Sudhakar Prasad, Marlan O. Scully, and Werner Martienssen. "A quantum description of the beam splitter". In: *Optics Communications* 62.3 (May 1, 1987), pp. 139–145. ISSN: 0030-4018. DOI: 10.1016/0030-4018(87)90015-0.

[79] C. Fabre and N. Treps. "Modes and States in Quantum Optics". In: *Reviews of Modern Physics* 92.3 (Sept. 2020), p. 035005. ISSN: 0034-6861, 1539-0756. DOI: 10.1103/RevModPhys.92.035005.

[80] N. Tischler, C. Rockstuhl, and K. Słowik. "Quantum Optical Realization of Arbitrary Linear Transformations Allowing for Loss and Gain". In: *Phys. Rev. X* 8.2 (Apr. 13, 2018). Publisher: American Physical Society, p. 021017. DOI: 10.1103/PhysRevX.8.021017.

[81] P. A. M. Dirac. *The principles of quantum mechanics.* 4th ed. International series of monographs on physics. Oxford: Clarendon Press, 1958.

[82] J. Aasi et al. "Enhanced sensitivity of the LIGO gravitational wave detector by using squeezed states of light". In: *Nature Photon* 7.8 (Aug. 2013). Publisher: Nature Publishing Group, pp. 613–619. ISSN: 1749-4893. DOI: 10.1038/nphoton.2013.177.

[83] R. A. Fisher. "On the mathematical foundations of theoretical statistics". In: *Philosophical Transactions of the Royal Society of London. Series A, Containing Papers of a Mathematical or Physical Character* 222.594 (Jan. 1, 1922), pp. 309–368. ISSN: 0264-3952, 2053-9258. DOI: 10.1098/rsta.1922.0009.

[84] Johannes Jakob Meyer et al. "Quantum Metrology in the Finite-Sample Regime". In: *PRX Quantum* 6.3 (Aug. 27, 2025), p. 030336. ISSN: 2691-3399. DOI: 10.1103/qbn1-p6bq.

[85] Carl W. Helstrom. "Estimation of a displacement parameter of a quantum system". In: *Int J Theor Phys* 11.6 (Dec. 1974), pp. 357–378. ISSN: 0020-7748, 1572-9575. DOI: 10.1007/BF01809715.

[86] Géza Tóth and Iagoba Apellaniz. "Quantum metrology from a quantum information science perspective". In: *J. Phys. A: Math. Theor.* 47.42 (Oct. 2014). Publisher: IOP Publishing, p. 424006. ISSN: 1751-8121. DOI: 10.1088/1751-8113/47/42/424006.

[87] Sammy Ragy, Marcin Jarzyna, and Rafał Demkowicz-Dobrzański. "Compatibility in multiparameter quantum metrology". In: *Phys. Rev. A* 94.5 (Nov. 10, 2016). Publisher: American Physical Society, p. 052108. DOI: 10.1103/PhysRevA.94.052108.

[88] Hiroshi Nagaoka. "A New Approach to Cramér-Rao Bounds for Quantum State Estimation". In: Masahito Hayashi. *Asymptotic Theory of Quantum Statistical Inference*. WORLD SCIENTIFIC, Feb. 2005, pp. 100–112. ISBN: 978-981-256-015-5. DOI: 10.1142/9789812563071_0009.

[89] Mankei Tsang, Francesco Albarelli, and Animesh Datta. "Quantum Semiparametric Estimation". In: *Phys. Rev. X* 10.3 (July 30, 2020). Publisher: American Physical Society, p. 031023. DOI: 10.1103/PhysRevX.10.031023.

[90] Robert W. Boyd. *Nonlinear Optics*. 4th ed. San Diego: Elsevier Science & Technology, 2020. 1 p. ISBN: 978-0-12-811003-4.

[91] Vitaliy Sultanov, Tomás Santiago-Cruz, and Maria V. Chekhova. "Flat-optics generation of broadband photon pairs with tunable polarization entanglement". In: *Opt. Lett.* 47.15 (Aug. 1, 2022), p. 3872. ISSN: 0146-9592, 1539-4794. DOI: 10.1364/OL.458133.

[92] Paul G. Kwiat et al. "New High-Intensity Source of Polarization-Entangled Photon Pairs". In: *Phys. Rev. Lett.* 75.24 (Dec. 11, 1995), pp. 4337–4341. ISSN: 0031-9007, 1079-7114. DOI: 10.1103/PhysRevLett.75.4337.

[93] C. K. Hong and L. Mandel. "Theory of parametric frequency down conversion of light". In: *Phys. Rev. A* 31.4 (Apr. 1, 1985), pp. 2409–2418. ISSN: 0556-2791. DOI: 10.1103/PhysRevA.31.2409.

[94] S.P. Walborn et al. "Spatial correlations in parametric down-conversion". In: *Physics Reports* 495.4 (Oct. 2010), pp. 87–139. ISSN: 03701573. DOI: 10.1016/j.physrep.2010.06.003.

[95] Luis Edgar Vicent et al. "Design of bright, fiber-coupled and fully factorable photon pair sources". In: *New J. Phys.* 12.9 (Sept. 15, 2010), p. 093027. ISSN: 1367-2630. DOI: 10.1088/1367-2630/12/9/093027.

[96] Kyle M. Jordan, Raphael A. Abrahao, and Jeff S. Lundeen. "Quantum metrology timing limits of the Hong-Ou-Mandel interferometer and of general two-photon measurements". In: *Phys. Rev. A* 106.6 (Dec. 22, 2022). Publisher: American Physical Society, p. 063715. DOI: 10.1103/PhysRevA.106.063715.

[97] M. Reisner et al. "Quantum-limited determination of refractive index difference by means of entanglement". In: *npj Quantum Inf* 8.1 (May 16, 2022), p. 58. ISSN: 2056-6387. DOI: 10.1038/s41534-022-00567-7.

[98] Eric Dauler et al. "Tests of a two-photon technique for measuring polarization mode dispersion with subfemtosecond precision". In: *J. Res. Natl. Inst. Stand. Technol.* 104.1 (Jan. 1999), p. 1. ISSN: 1044677X. DOI: 10.6028/jres.104.001.

[99] D. Branning, A. L. Migdall, and A. V. Sergienko. "Simultaneous measurement of group and phase delay between two photons". In: *Phys. Rev. A* 62.6 (Nov. 10, 2000), p. 063808. ISSN: 1050-2947, 1094-1622. DOI: 10.1103/PhysRevA.62.063808.

[100] Stefan Frick, Alex McMillan, and John Rarity. "Quantum rangefinding". In: *Opt. Express* 28.25 (Dec. 7, 2020), p. 37118. ISSN: 1094-4087. DOI: 10.1364/OE.399902.

[101] Christopher Spiess et al. "Clock Synchronization with Correlated Photons". In: *Phys. Rev. Appl.* 19.5 (May 25, 2023). Publisher: American Physical Society, p. 054082. DOI: 10.1103/PhysRevApplied.19.054082.

[102] Kunal K. Dansingani et al. "EN FACE IMAGING OF PACHYCHOROID SPECTRUM DISORDERS WITH SWEPT-SOURCE OPTICAL COHERENCE TOMOGRAPHY". In: *Retina* 36.3 (Mar. 2016), pp. 499–516. ISSN: 1539-2864. DOI: 10.1097/IAE.0000000000000742.

[103] Guillaume Thekkadath et al. "Gain-Induced Group Delay in Spontaneous Parametric Down-Conversion". In: *Phys. Rev. Lett.* 133.20 (Nov. 14, 2024). Publisher: American Physical Society, p. 203601. DOI: 10.1103/PhysRevLett.133.203601.

[104] Yuishi Takeno et al. "Observation of -9 dB quadrature squeezing with improvement of phase stability in homodyne measurement". In: *Opt. Express* 15.7 (2007), p. 4321. ISSN: 1094-4087. DOI: 10.1364/OE.15.004321.

[105] Sandeep Singh et al. "Near-Video Frame Rate Quantum Sensing Using Hong–Ou–Mandel Interferometry". In: *Advanced Quantum Technologies* 6.11 (2023), p. 2300177. ISSN: 2511-9044. DOI: 10.1002/qute.202300177.

[106] Bienvenu Ndagano et al. "Quantum microscopy based on Hong–Ou–Mandel interference". In: *Nat. Photon.* 16.5 (May 2022). Publisher: Nature Publishing Group, pp. 384–389. ISSN: 1749-4893. DOI: 10.1038/s41566-022-00980-6.

[107] Danilo Triggiani, Giorgos Psaroudis, and Vincenzo Tamma. "Ultimate Quantum Sensitivity in the Estimation of the Delay between two Interfering Photons through Frequency-Resolving Sampling". In: *Phys. Rev. Appl.* 19.4 (Apr. 24, 2023). Publisher: American Physical Society, p. 044068. DOI: 10.1103/PhysRevApplied.19.044068.

[108] O. Meskine et al. "Approaching Maximal Precision of Hong-Ou-Mandel Interferometry with Nonperfect Visibility". In: *Phys. Rev. Lett.* 132.19 (May 7, 2024). Publisher: American Physical Society, p. 193603. DOI: 10.1103/PhysRevLett.132.193603.

[109] Ashley Lyons et al. "Attosecond-resolution Hong-Ou-Mandel interferometry". In: *Science Advances* 4.5 (May 4, 2018). Publisher: American Association for the Advancement of Science, eaap9416. DOI: 10.1126/sciadv.aap9416.

[110] Yuan Cao et al. "Long-Distance Free-Space Measurement-Device-Independent Quantum Key Distribution". In: *Phys. Rev. Lett.* 125.26 (Dec. 23, 2020). Publisher: American Physical Society, p. 260503. DOI: 10.1103/PhysRevLett.125.260503.

[111] Korenobu Matsuzaki and Tahei Tahara. "Superresolution concentration measurement realized by sub-shot-noise absorption spectroscopy". In: *Nat Commun* 13.1 (Feb. 17, 2022). Publisher: Nature Publishing Group, p. 953. ISSN: 2041-1723. DOI: 10.1038/s41467-022-28617-w.

[112] Sanguk Woo, Hyein Jung, and Yohan Yoon. "Real-Time UV/VIS Spectroscopy to Observe Photocatalytic Degradation". In: *Catalysts* 13.4 (Apr. 2023). Publisher: Multidisciplinary Digital Publishing Institute, p. 683. ISSN: 2073-4344. DOI: 10.3390/catal13040683.

[113] Lige Liu et al. "Photodegradation of Organometal Hybrid Perovskite Nanocrystals: Clarifying the Role of Oxygen by Single-Dot Photoluminescence". In: *J. Phys. Chem. Lett.* 10.4 (Feb. 21, 2019). Publisher: American Chemical Society, pp. 864–869. DOI: 10.1021/acs.jpclett.9b00143.

[114] Young-Shin Park et al. "Room Temperature Single-Photon Emission from Individual Perovskite Quantum Dots". In: *ACS Nano* 9.10 (Oct. 27, 2015). Publisher: American Chemical Society, pp. 10386–10393. ISSN: 1936-0851. DOI: 10.1021/acsnano.5b04584.

[115] Ilaria Gianani et al. "Kramers–Kronig relations and precision limits in quantum phase estimation". In: *Optica, OPTICA* 8.12 (Dec. 20, 2021). Publisher: Optica Publishing Group, pp. 1642–1645. ISSN: 2334-2536. DOI: 10.1364/OPTICA.440438.

[116] Colin P. Lualdi et al. "Fast quantum interferometry at the nanometer and attosecond scales with energy-entangled photons". In: *Science Advances* 11.21 (May 21, 2025). Publisher: American Association for the Advancement of Science, eadw4938. DOI: 10.1126/sciadv.adw4938.

[117] Shahaf Asban and Shaul Mukamel. "Distinguishability and "which pathway" information in multidimensional interferometric spectroscopy with a single entangled photon-pair". In: *Sci. Adv.* 7.39 (Sept. 24, 2021), eabj4566. ISSN: 2375-2548. DOI: 10.1126/sciadv.abj4566.

[118] Luca Moretti et al. "Measurement principles for quantum spectroscopy of molecular materials with entangled photons". In: *J. Chem. Phys.* 159.8 (Aug. 24, 2023), p. 084201. ISSN: 0021-9606. DOI: 10.1063/5.0156598.

[119] Michał Lipka and Michał Parniak. "Single-Photon Hologram of a Zero-Area Pulse". In: *Phys. Rev. Lett.* 127.16 (Oct. 12, 2021). Publisher: American Physical Society, p. 163601. DOI: 10.1103/PhysRevLett.127.163601.

[120] Mitchell J. Duffy et al. "Towards optimized naphthalocyanines as sonochromes for photoacoustic imaging *in vivo*". In: *Photoacoustics* 9 (Mar. 1, 2018), pp. 49–61. ISSN: 2213-5979. DOI: 10.1016/j.pacs.2017.12.001.

[121] Andrei Nomerotski et al. "Characterization of TimepixCam, a fast imager for the time-stamping of optical photons". In: *J. Inst.* 12.1 (Jan. 2017), p. C01017. ISSN: 1748-0221. DOI: 10.1088/1748-0221/12/01/C01017.

[122] A. Nomerotski et al. "Intensified Tpx3Cam, a fast data-driven optical camera with nanosecond timing resolution for single photon detection in quantum applications". In: *J. Inst.* 18.1 (Jan. 2023). Publisher: IOP Publishing, p. C01023. ISSN: 1748-0221. DOI: 10.1088/1748-0221/18/01/C01023.

[123] Yingwen Zhang et al. "High speed imaging of spectral-temporal correlations in Hong-Ou-Mandel interference". In: *Opt. Express, OE* 29.18 (Aug. 30, 2021). Publisher: Optica Publishing Group, pp. 28217–28227. ISSN: 1094-4087. DOI: 10.1364/OE.432191.

[124] Jakub Jirsa et al. "Fast data-driven spectrometer with direct measurement of time and frequency for multiple single photons". In: *Opt. Express, OE* 33.5 (Mar. 10, 2025). Publisher: Optica Publishing Group, pp. 9962–9972. ISSN: 1094-4087. DOI: 10.1364/OE.543511.

[125] Tiemo Landes. "Nonlinear Light-Matter Interactions with Entangled Photons and Bright Squeezed Vacuum". PhD thesis. University of Oregon, 2022.

[126] Andrew H. Proppe et al. *Imaging at the quantum limit with convolutional neural networks*. June 16, 2025. DOI: 10.48550/arXiv.2506.13488. arXiv: 2506.13488[cs].

[127] Patrick M. Birchall et al. "Quantum Optical Metrology of Correlated Phase and Loss". In: *Phys. Rev. Lett.* 124.14 (Apr. 8, 2020). Publisher: American Physical Society, p. 140501. DOI: 10.1103/PhysRevLett.124.140501.

[128] Lorcán O. Conlon et al. "Efficient computation of the Nagaoka–Hayashi bound for multiparameter estimation with separable measurements". In: *npj Quantum Inf* 7.1 (July 15, 2021). Publisher: Nature Publishing Group, p. 110. ISSN: 2056-6387. DOI: 10.1038/s41534-021-00414-1.

[129] Francesco Albarelli, Jamie F. Friel, and Animesh Datta. "Evaluating the Holevo Cram\'er-Rao Bound for Multiparameter Quantum Metrology". In: *Phys. Rev. Lett.* 123.20 (Nov. 15, 2019). Publisher: American Physical Society, p. 200503. DOI: 10.1103/PhysRevLett.123.200503.

[130] Francesco Albarelli and Rafał Demkowicz-Dobrzański. "Probe Incompatibility in Multiparameter Noisy Quantum Metrology". In: *Phys. Rev. X* 12.1 (Mar. 1, 2022). Publisher: American Physical Society, p. 011039. DOI: 10.1103/PhysRevX.12.011039.

[131] Animesh Datta et al. "Quantum metrology with imperfect states and detectors". In: *Phys. Rev. A* 83.6 (June 24, 2011). Publisher: American Physical Society, p. 063836. DOI: 10.1103/PhysRevA.83.063836.

[132] Scott Diddams and Jean-Claude Diels. "Dispersion measurements with white-light interferometry". In: *J. Opt. Soc. Am. B, JOSAB* 13.6 (June 1, 1996). Publisher: Optica Publishing Group, pp. 1120–1129. ISSN: 1520-8540. DOI: 10.1364/JOSAB.13.001120.

[133] R. Kaltenbaek et al. "Quantum-inspired interferometry with chirped laser pulses". In: *Nature Phys* 4.11 (Nov. 2008). Publisher: Nature Publishing Group, pp. 864–868. ISSN: 1745-2481. DOI: 10.1038/nphys1093.

[134] J. Lavoie, R. Kaltenbaek, and K. J. Resch. "Quantum-optical coherence tomography with classical light". In: *Opt. Express, OE* 17.5 (Mar. 2, 2009). Publisher: Optica Publishing Group, pp. 3818–3826. ISSN: 1094-4087. DOI: 10.1364/OE.17.003818.

[135] M. D. Mazurek et al. "Dispersion-cancelled biological imaging with quantum-inspired interferometry". In: *Sci Rep* 3.1 (Apr. 2, 2013), p. 1582. ISSN: 2045-2322. DOI: 10.1038/srep01582.

[136] Kazuhisa Ogawa and Masao Kitano. "Classical realization of dispersion-canceled, artifact-free, and background-free optical coherence tomography". In: *Opt. Express* 24.8 (Apr. 18, 2016), p. 8280. ISSN: 1094-4087. DOI: 10.1364/OE.24.008280.

[137] Mikkel Jensen et al. "All-depth dispersion cancellation in spectral domain optical coherence tomography using numerical intensity correlations". In: *Sci Rep* 8.1 (June 15, 2018), p. 9170. ISSN: 2045-2322. DOI: 10.1038/s41598-018-27388-z.

[138] Pablo Yepiz Graciano et al. "Interference effects in quantum-optical coherence tomography using spectrally engineered photon pairs". In: *Sci Rep* 9.1 (June 20, 2019). Publisher: Nature Publishing Group, p. 8954. ISSN: 2045-2322. DOI: 10.1038/s41598-019-45088-0.

[139] Sylwia M. Kolenderska and Maciej Szkulmowski. "Artefact-removal algorithms for Fourier domain quantum optical coherence tomography". In: *Sci Rep* 11.1 (Sept. 20, 2021), p. 18585. ISSN: 2045-2322. DOI: 10.1038/s41598-021-98106-5.

[140] Magued B. Nasr et al. "Quantum optical coherence tomography of a biological sample". In: *Optics Communications* 282.6 (Mar. 15, 2009), pp. 1154–1159. ISSN: 0030-4018. DOI: 10.1016/j.optcom.2008.11.061.

[141] R. L. P. van Veen et al. "Determination of visible near-IR absorption coefficients of mammalian fat using time- and spatially resolved diffuse reflectance and transmission spectroscopy". In: *JBO* 10.5 (Sept. 2005). Publisher: SPIE, p. 054004. ISSN: 1083-3668, 1560-2281. DOI: 10.1117/1.2085149.

[142] Magued B. Nasr et al. "Dispersion-cancelled and dispersion-sensitive quantum optical coherence tomography". In: *Opt. Express, OE* 12.7 (Apr. 5, 2004). Publisher: Optica Publishing Group, pp. 1353–1362. ISSN: 1094-4087. DOI: 10.1364/OPEX.12.001353.

[143] Zhe-Yu Jeff Ou. *Multi-photon Quantum interference*. New York: Springer, 2007. 268 pp. ISBN: 978-0-387-25532-3.

[144] T. B. Pittman et al. "Can Two-Photon Interference be Considered the Interference of Two Photons?" In: *Phys. Rev. Lett.* 77.10 (Sept. 2, 1996). Publisher: American Physical Society, pp. 1917–1920. DOI: 10.1103/PhysRevLett.77.1917.

[145] Vahid Ansari et al. "Achieving the Ultimate Quantum Timing Resolution". In: *PRX Quantum* 2.1 (Jan. 4, 2021), p. 010301. ISSN: 2691-3399. DOI: 10.1103/PRXQuantum.2.010301.

[146] Pablo Yepiz-Graciano et al. "Spectrally resolved Hong–Ou–Mandel interferometry for quantum-optical coherence tomography". In: *Photon. Res., PRJ* 8.6 (June 1, 2020). Publisher: Optica Publishing Group, pp. 1023–1034. ISSN: 2327-9125. DOI: 10.1364/PRJ.388693.

[147] Li Gomez and Mayte Yinghua. "Artifact removal in Quantum Optical Coherence Tomography". In: (Jan. 17, 2024).

[148] Danilo Zia et al. "Interferometric imaging of amplitude and phase of spatial biphoton states". In: *Nat. Photon.* 17.11 (Nov. 2023). Publisher: Nature Publishing Group, pp. 1009–1016. ISSN: 1749-4893. DOI: 10.1038/s41566-023-01272-3.

[149] Inbar Hurvitz et al. "Phase analysis of biphoton joint spectra by interference between different SPDC sources". In: *Optica Quantum* 2.5 (Oct. 25, 2024), p. 358. ISSN: 2837-6714. DOI: 10.1364/OPTICAQ.537375.

[150] N. Sultanova, S. Kasarova, and I. Nikolov. "Dispersion Properties of Optical Polymers". In: *Acta Phys. Pol. A* 116.4 (Oct. 2009), pp. 585–587. ISSN: 0587-4246, 1898-794X. DOI: 10.12693/APhysPolA.116.585.

[151] D. N. Klyshko. "Use of two-photon light for absolute calibration of photoelectric detectors". In: *Sov. J. Quantum Electron.* 10.9 (Sept. 30, 1980). Publisher: IOP Publishing, p. 1112. ISSN: 0049-1748. DOI: 10.1070/QE1980v010n09ABEH010660.

[152] Fabian Steinlechner et al. "A high-brightness source of polarization-entangled photons optimized for applications in free space". In: *Opt. Express, OE* 20.9 (Apr. 23, 2012). Publisher: Optica Publishing Group, pp. 9640–9649. ISSN: 1094-4087. DOI: 10.1364/OE.20.009640.